Fall 2018

Computational dynamics and virtual dragline simulation for extended rope service life

Muhammad Wardeh

COMPUTATIONAL DYNAMICS AND VIRTUAL DRAGLINE SIMULATION FOR EXTENDED ROPE SERVICE LIFE

by

MUHAMMAD WARDEH

A DISSERTATION

Presented to the Faculty of the Graduate School of the

MISSOURI UNIVERSITY OF SCIENCE AND TECHNOLOGY

In Partial Fulfillment of the Requirements for the Degree

DOCTOR OF PHILOSOPHY

in

MINING ENGINEERING

2018

Approved by:

Samuel Frimpong, Advisor
Kwame Awuah-Offei, Co-advisor
Grzegorz Galecki
K . Chandrashekhara
Elvan Akin

ABSTRACT

The dragline machinery is one of the largest equipment for stripping overburden materials in surface mining operations. Its effectiveness requires rigorous kinematic and dynamic analyses. Current dragline research studies are limited in computational dynamic modeling because they eliminate important structural components from the front-end assembly. Thus, the derived kinematic, dynamic and stress intensity models fail to capture the true response of the dragline under full operating cycle conditions. This research study advances a new and robust computational dynamic model of the dragline front-end assembly using Kane's method. The model is a 3-DOF dynamic model that describes the spatial kinematics and dynamics of the dragline front-end assembly during digging and swinging. A virtual simulator, for a Marion 7800 dragline, is built and used for analyzing the mass and inertia properties of the front-end components.

The models accurately predict the kinematics, dynamics and stress intensity profiles of the front-end assembly. The results showed that the maximum drag force is 1.375 MN, which is within the maximum allowable load of the machine. The maximum cutting resistance of 412.31 KN occurs 5 seconds into digging and the maximum hoist torque of 917. 87 KN occurs 10 seconds into swinging. Stress analyses are carried out on wire ropes using ANSYS Workbench under static and dynamic loading. The FEA results showed that significant stresses develop in the contact areas between the wires, with a maximum von Mises stress equivalent to 7800 MPa. This research study is a pioneering effort toward developing a comprehensive multibody dynamic model of the dragline machinery. The main novelty is incorporating the boom point-sheave, drag-chain and sliding effect of the bucket, excluded from previous research studies, to obtain computationally dynamic efficient models for load predictions.

ACKNOWLEDGMENTS

All praises are due to Allah (God), the almighty, for the strength and wisdom that I am blessed with to complete this research.

I am very thankful to my research advisor, Dr. Samuel Frimpong, for his support, guidance, patience, and encouragements that he has provided to make this research possible. I feel blessed to have a caring advisor like him and great human being. I am deeply thankful to him for giving me the freedom to dig deeper. I am also grateful to my co-advisor, Dr. Kwame Awuah-Offei, for the ideas that he has shared during my research journey. I would like to thank my committee members: Dr. K. Chandrashekhara, Dr. Grzegorz Galecki, and Dr. Elvan Akin for their time and feedback.

I am indebted to my loving wife, Lena Rashoud, who provided a tremendous support during this journey. She typed a large portion of the dissertation report and trusted in me. She has endured many days and nights alone during my PhD research study. I am thankful to her for being in my live. I am thankful to my friend, Salah Al Smairat, who provided a tremendous support. I greatly acknowledge the assistance of the staff members in the Department of Mining and Nuclear Engineering. I am also thankful to the Heavy Mining Machinery Research Group for their time and friendship. This research would not have been possible without the financial support of the Robert H. Quenon Endowment Fund and the funding provided by Missouri S&T for completing the PhD research.

Finally, I am very grateful to my parents, Ali Wardeh and Dalal Wardeh, for their prayers, support and encouragements during the journey. I am also thankful to my siblings, especially my brother Oussama Wardeh, for their thoughts and support.

TABLE OF CONTENTS

Page

LIST OF ILLUSTRATIONS

Page

LIST OF TABLES

Page

NOMENCLATURE

Symbol	Description
W_{Bucket}	Bucket Weight
W_{Rigging}	Weight of Rigging System
W_{Payload}	Weight of Payload
F_i	Resultant Forces Acting on Body i
m_i^R	Mass of the Body (i)
a_i^R	Translational Acceleration of Body (i)
M_i	Resultant Moments Acting on body (i)
I_o	Moment of Inertia w.r.t Center of Mass of Body
$\ddot{\theta}$	Angular Acceleration
S	Functional (the Integral of Lagrangian over Time)
m_b	Bucket Mass
v	Linear Velocity
ω	Angular Velocity
$M_{av}, M_{it}, M_{rw}, N_{av}, N_{it}, N_{}$	Multipliers of Initial Tension
D	Diameter of Sheave
$\emptyset - \emptyset_1$	Angles of Contact in Rope-Sheave
f	Coefficient of Frictions
d	Diameter of Rope
P	Cutting Force
n	Numerical Coefficient
C	Number of Strokes of Densitometer
A	Coefficient Depending on the Cutting
q_i	Generalized Coordinate
u_r	Generalized Speed of Index r
$\dot{q}_s$	Derivative of Generalized Coordinate
$\overrightarrow{v^{k^*}}$	Translational Velocity of Body k

$\tilde{v}_r$	rth Nonholonomic Partial Velocity
$\tilde{\omega}_r$	rth Nonholonomic Partial Angular Velocity
$Z_i,\ X_i$	Intermediate Variable
a^P	Linear Acceleration of Particle P
α^P	Angular Acceleration of Particle P
T_K^*	Inertia Torque Vector of Body K
$\dot{u}_r$	Independent Generalized Speed Derivative (Acceleration)
$\tilde{F}_r^*$	Generalized Inertia Force
$\tilde{F}_r$	Generalized Active Force
$\tilde{v}_r^{P_i}$	Nonholonomic Partial Velocity of a Particle P_i
R_i	Contact Force
$\vec{G}_k$	Gravity Force Vector of Body K
τ_i	Torque (Hoist, Swinging)
σ	Drag Force
F_c	Cutting Resistance Force
k_p	Coefficient of Loosening of the Rock in the Bucket
$K_F,$	Coefficient of Specific Resistance to Digging
K_{nym}	Ratio of the Bucket Filling Path to the Length of the Bucket
J	Jacobian Matrix
F_j	jthe Constraint Equation
α_B, β_B	Baumgarte Parameters
W_D	Dragline Weight
L_K	Length of Body K in the closed Loop
F_{ct}	Digging Force
ca	Carry Angle
q_c	Cutting Angle
q_{60}	Initial Angular Displacement of Drag rope
g	Gravitational Acceleration

1. INTRODUCTION

This section introduces the background and statement of the research problem in dragline machinery kinematics and dynamics, which highlight the limitations of previous research studies. The introduction also outlines the research scope, objectives and methodology for providing solutions to the problems. The broader impact and scientific contributions of this research and the dissertation structure are provided in this section.

1.1. BACKGROUND OF THE PROBLEM

The global energy demand is expected to grow by 30% between 2018 and 2040 (WEO, 2017). According to the International Energy Agency (IEA, 2017), the contributions of India to the energy demand growth is about 30% (WEO, 2017). India and China still have the largest dependence on coal in the primary energy production (IEA, 2017). The projections show that China holds a towering presence in the coal sector between 2018 and 2025 as shown in Figure 1.1. On the other hand, new policies by China will lead to a decline of 15% in the coal market demand from 2018 to 2040. Coal imports have undergone significant reductions in India to boost domestic production targets (WEO, 2017). Indian imports decreased to 200.1 Mt, while China imports increased to 255.6 Mt in 2016 (IEA, 2017). Despite these trends, China and India were the two largest producers and importers of coal.

According to the U.S. Energy Information Administration (EIA), the United States net electricity generation from coal was the largest in history between 2000 and 2010, and it reached a peak of 1,500 billion kWh (EIA, 2017). This reflects a strong dependence on

coal production, which was the largest around 1,190 million short tons in 2008 as illustrated in Figure 1.2.

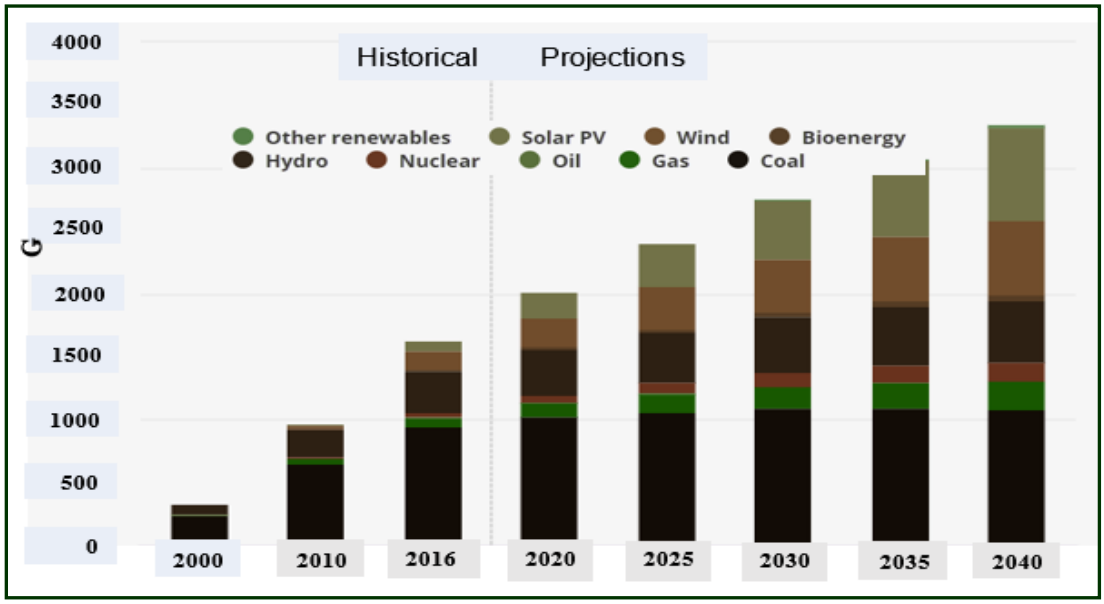

Figure 1.1. Historical and future projections of China's energy production from coal (WEO, 2017)

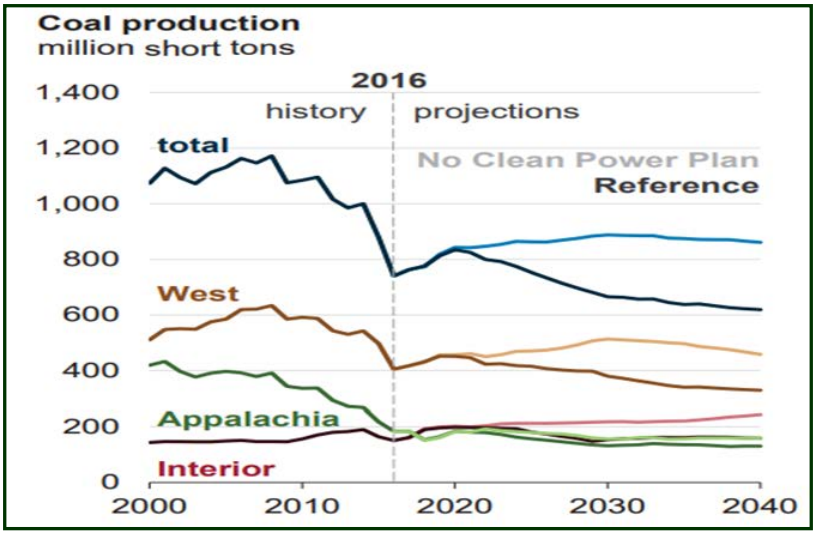

Figure 1.2. Historical and future projections of U.S. coal production (U.S. EIA, 2017)

However, the US total coal production decreased significantly to 660 million short tons in 2016. This decrease is a result of the impact of the Clean Power Plan (CPP) Act (2015), where coal lost market share to natural gas and renewable generation in the electric power sector. Despite the retirement of old, less-efficient coal-fired units, the EIA predicts that the coal-fired units will regain market share from renewables and natural gas in the electricity generation in 2018. The U.S. total coal production is predicted to increase through 2020 to more than 800 million short tons as shown in Figure 1.2 (EIA, 2017).

The coal mining technology started a long time ago and is still going through steady, continuous developments, especially with the advent of new mining methods in the last century. The strip mining method represents the best practice of the coal production techniques. Increased coal demand has pushed for the design of larger draglines for bulk production capacities to achieve economies of scale. Dragline excavators are designed to meet these demands and their productivity peaked between 1994 and 2010. In North America, the median peak productivity for draglines was around 112,000 bank cubic meters per ton (BCM/t) of Rated Suspended Load (RSL), which occurred in 2006 as shown in Figure 1.3 (Lumley and McKee, 2014). The productivity has declined about 5% in North America compared to Australia and Africa. The figure shows that draglines are always favored for use in the U.S mining sector as compared to its use in Australia and Africa.

It is clear that the benefits from large draglines are immense to mining clients, especially for providing quick returns on investment. Each piece of dragline costs between $30 and $100 million and would only be designed and built upon request. However, the use of large-capacity dragline results in a number of challenges in their design, production and use including, but not limited to, mass, volume, flexibility and longevity.

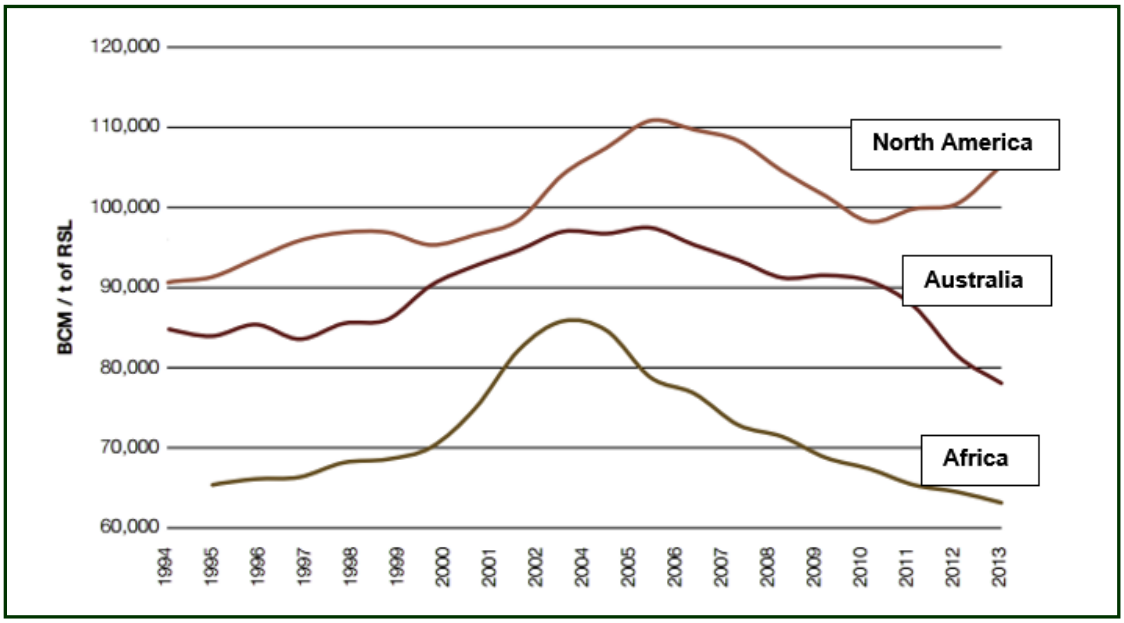

Figure 1.3. Median productivity of draglines by region (Lumley and McKee, 2014)

Caterpillar and Komatsu, the global leaders in the production of these large mining machinery, are working steadily to increase the dragline size to maximize the productivity, reduce cycle time, and improve safety measures. The implemented improvements impacted machine availability, maneuverability, and productivity. However, they do not provide reliable assessment of the effect of increasing the RSL on the overall machine useful life, especially its ropes. It is very challenging to experimentally predict the RSL scenarios on a dragline during its development phase. The random dynamics loading, inertia effects, operator efficiency, and formation characteristics form a significant source of uncertainty to manufacturers for developing new draglines. The design of scaled-down physical models was used in the industry and academia with the aim to improve digging efficiency and bucket pose (Kyle and Costello, 2006). The experimental techniques provided a valuable benchmarking in terms of static loading predictions and RSL, but failed to predict

transient loading scenarios. This drawback can lead to inaccurate designs, unplanned downtimes, and an increase in the cost associated with machine maintenance. As a result, a premature failure of dragline ropes is more likely to happen and best maintenance practices, alone, cannot resolve these issues.

1.2. STATEMENT OF THE PROBLEM

The unique design of the dragline excavators allows for a massive and quick handling of overburden in strip mining operations. With a complex, massive engineered mechanical front-end assembly, the dragline has a bucket capacity range of between 85 and 122 m^3 and can efficiently expose the coal and spoil the waste materials within the pit lengths. The capital investment in draglines in the millions of dollars with operating cost estimate of about US $5 million per year (Corke et al., 2008). The critical task that faces mining clients, who invest in draglines, stems from the right decision of selecting an appropriate model and number of draglines for specific tasks. The best mining practices for using such capital investment are to keep the dragline busy to achieve high productivities subject to operating constraints, and with minimum downtime and maintenance costs. The cyclical operations and irregularities in digging materials can increase the loads on the boom, ropes, and bucket.

The components that are impacted the most from these variable loads are ropes, and the associated maintenance and replacement cost is valued at about 30% of the operating cost (Corke et al., 2008). The dragline usually operates in a cyclic mode and each cycle moves up to about 344,736 kg (760,000 lbs) of Suspended Load Rating (SLR) in about 60 seconds (P&H 9020XPC; Joy Global, 2016). The attractive bulk handling capacity and cost of these draglines may trigger mining clients to invest in a fewer number

of machine. The selection of larger draglines will boost mine productivities as long as machine availability is high enough between about 85 and 95%. It happens sometimes that the peaks in machine productivity can be leveraged when an operator is exceeding the SLR limits of dragline. Cost reduction associated with these practices can generate a quick return in the short-term, but it can be catastrophic in the long term. It is more likely that dragline downtimes and maintenance costs will increase. Thus, as a result of focusing on short-term production targets, the entire project may become unsustainable in the long-term.

In addition to long-term problems, the delays in early inspections of ropes and improper digging trajectories can significantly impact dragline productivity. Poor digging zones require 15% to 40% more power to lift the overburden (WireCo Dragline Guide 9-10, 2018). It means that more loads on the rope electric motors develop and additional stresses will be generated in the ropes. Consequently, the ropes are overloaded resulting in increasing stresses, wear and tear, and the downtime for replacing ropes. Dragline efficiency, availability and utilization are mainly controlled by ropes functionality and their longevity. Any failure can cause significant delays in the mining operations, resulting in increasing maintenance time and costs with adverse impact on the feasibility of using large draglines. Dayawansa et al. (2006) reported that the cost of maintaining wire ropes accounts for 15% of a dragline's total maintenance costs and it is estimated as $300,000 per annum per machine.

Alzheimer et al. (1981) reported that the actual life of dragline ropes varies from few weeks to several months and also stated that the life of drag ropes is only half of that of hoist ropes. They also stated that the cost of operating a dragline of medium size bucket

capacity of 45 to 54 m^3 is about US $2,500 per hour and the capital cost of a pair of drag ropes is about US $15,000. As a result, the total cost of their replacement and downtime can be US $25,000 per hour without accounting for the costs of the time lost and the loss of overburden production. The adverse effect of load fluctuations from improper bucket positioning on the dig face is not well articulated in the literature. These fluctuations can directly reduce the expected life of the rope when they exceed its yield strength. Advanced research initiative is also required to understand the underlying effects of digging scenarios on the dragline ropes endurance and to correlate it to the availability and productivity of dragline and the economic useful life of ropes.

Resistance to failures in the hoist ropes can significantly diminish when ropes run over the deteriorated surfaces (e.g., worn groove of point sheave) and/or misalignments of the fairlead sheaves. The running ropes without impendence from sheaves can reduce metal deformations in the rope strands. The deterioration mechanisms for drag ropes are attributed to the abrasive wear from rope interactions with the digging face. Fragments of gravels with sharp edges may be trapped between strands and can cause premature failure if the operator keeps the drag ropes continuously in contact with the bench. With more, smaller outside wires per strand, this adverse effect can be reduced significantly.

The efficiency and availability of the dragline are the backbone of any strategy to achieve maximum productivity and sustainability of strip mining operations. Breakdowns due to excessive loading and bad mining practices can be minimized through a good engineering understanding of every component capacity and a rigorous kinematic and dynamic analyses of the dragline machinery. The stress analysis of weak components, combined with an appropriate maneuverability of bucket, can increase the dragline

utilization, availability and machine performance. Advanced research initiatives are required to provide understanding into dragline availability, reliability, maintainability and efficiency with focus on its front-end assembly kinematics and dynamics, the subject of this research study.

1.3. RESEARCH SCOPE AND OBJECTIVES OF THE STUDY

Dragline is a massive electrically driven machine and is considered as the primary tool of choice for removing overburden materials in large scale surface strip mining operations. The machine has many electrical and mechanical components that operate in complex geological formations. This research initiative, therefore, focuses on the design, kinematic and dynamic analyses of dragline front-end assembly. To address the problem statement in this research, a dynamic model of the dragline front-end assembly is developed, where important structural components are included to fully describe the dragline dynamic behavior. The design of a 3D CAD model of dragline front-end assembly comprising structural elements: (i) machine house; (ii) boom and boom point sheave; (iii) hoist rope; (iv) dump rope and bucket, and (v) drag rope. The analysis of the front-end assembly focuses on: (i) formulating the kinematics of the dragline with three degrees of freedom (DOF); (ii) formulating the dynamics to predict the loads (forces and torques) in the assembly; and (iii) carrying out finite element analysis of the drag rope-sheave interactions to capture areas of high stresses in the ropes and calculate stress intensity factors.

The primary research objective is to advance research into the kinematics and dynamics of the dragline front-end assembly and to examine in detail maximum stresses and stress intensity factors in the wire ropes. The knowledge from this research could also

be used as basis for improving dragline maintainability, reliability and availability. The elements of this primary objective include the following:

- Formulating complete kinematic and dynamic models of dragline front-end assembly.
- 3D virtual modeling and analysis of a complete dragline front-end assembly.
- Verification and validation of the models.
- Evaluating stresses in wire ropes under static and dynamic loading.

1.4. RESEARCH METHODOLOGY

The nature of this research problem requires a combination of research tools to individually address each of the objectives and to achieve the expected contributions. The combined objectives can be achieved through using an integrated modelling approach. The integrated model includes a critical review of the current body of knowledge in the dynamics and stress analyses of large dragline and lifting machinery. A theoretical formulation of the dragline kinematics and dynamics, which is based on vector mechanics and Kane's method, was developed in order to generate a compact set of kinematic and dynamic equations of motion.

Numerical methods and algorithms are formulated to solve a set of differential algebraic equations (DAE) and ordinary differential equations (ODE). They use constraints handling techniques and Newton-Raphson method to find initial conditions of generalized coordinates and speeds, as well as forces and torques. A 3D CAD model is designed in SolidWorks, with front-end assembly pertaining to a real dragline. The numerical results of the analytical model are compared with real world data from Nikiforuk and Ochitwa (1964) and Frimpong and Demirel (2009). Trajectories are generated to capture any potential hazards resulting in operating the simulator beyond its limits. The validated

mathematical model of the dragline front-end assembly serves as a standalone model for further experimentation.

The final aspect of the integrated approach is based on a finite element analysis (FEA) to capture stresses in the drag ropes of the front-end assembly. Finite element models of ropes with different constructions are tested under static and dynamic loading. ANSYS Workbench is used to recover maximum von Mises stresses generated in the flexible ropes and to determine the stress intensity factors. Stresses are generated at particular points where stress concentrations are high due to wire-wire contacts.

1.5. SIGNIFICANCE AND RESEARCH CONTRIBUTIONS

This research builds on the existing body of knowledge in the area of flexible Multibody Dynamics (MBD) and advance the stress analyses of the dragline machinery. The significance of this research is attributed to an advanced mathematical formulation of the dragline dynamics based on the Kane's Method (KM). The dragline front-end dynamic modeling is a type of closed-loop mechanism that was not properly addressed in previous studies. Most of the closed-loop mechanisms in the literature were cut into two mechanisms to facilitate the kinematic and dynamic analyses. This creates additional unknowns and makes the EOMs more difficult. This study improves on existing models by including all the components in the closed-loop mechanism. In addition to that, dynamic analysis using Kane's Method (KM) was never done before on any dragline. The significance of using KM is attributed to the elimination of the reaction forces. It also centers the dynamic formulation towards finding the solutions for the unknown forces/trajectories.

Moreover, this research expands the limited knowledge about flexible ropes modelling approaches and considers the rope-point sheave interactions. It also takes into

consideration the effect of sliding of bucket on the digging bench. These considerations contribute to mining excavation technology and heavy machines that contain ropes. The analytical dynamic model is manually and symbolically derived using advanced computational techniques in Mathematica. The dynamic model provides reliable estimates of the forces and torques that are used for validation purposes. It also serves as a testbed for several types of closed-loop mechanisms (e.g., cranes, grasping robots, and shovels).

It also pioneers the development of 3D virtual simulator for simulating the dragline machinery performance. Another significance is the optimum control of the dragline digging scenarios by the application of feedforward displacement approach. Optimum trajectories have been well articulated to show its contributions to the efficiency and to the reduction in machine downtime due to better control strategies of the dragline cycles. This leads to a reduction of stresses and increases the useful lives of ropes and the dragline machinery. This research endeavor contributes to the methods of wire ropes stress analysis that can be used as guidelines to the design code of ultra-class heavy duty ropes. The new findings can help companies expand the knowledge of their operators and provide training to increase safety and fidelity in using large mining machines. The results of this research create a safer working environment with a higher trust from public in surface mining technologies and Virtual Reality.

1.6. STRUCTURE OF DISSERTATION

This research advances the kinematics and dynamics of a dragline front-end assembly including stress analysis and stress intensity calculations of the dragline rope system. After an introductory section on the research problem, scope, objectives and methodology, the report discusses the current body of knowledge in the kinematics and

dynamics of closed-loop mechanisms and the benefits of Kane's Method in Section 2. The detailed kinematics and dynamics modeling is provided in Section 3. For accurate numerical simulations of the kinematics and dynamics of a constraint dragline excavator, Section 4 shows different techniques and algorithms for finding the joint forces and torques. This section also entails the verifications and validation of the mathematical models and the virtual simulator and the setup of the FE experiments. Section 5 discusses the experimental results from the mathematical and the FE models. Section 6 provides a summary of the research study with conclusions, contributions and future recommendations. Appendix A is also included and contains Mathematica code for the derivation of the kinematic and dynamic model.

2. LITERATURE SURVEY

This section contains a critical review of previous contributions in advancing the research on dragline machinery and other excavators. The review is divided into four components including: (i) dragline operational performance and control (ii) kinematics and dynamics of dragline closed-loop wire ropes, (iii) dragline virtual modelling and simulation, and (iv) structural integrity analysis. The first part describes the characteristics of the dragline, its modelling and operational control. The second part considers the fundamental theories that are used to develop the dynamic models of the dragline machinery with its intertwined components, bucket-ground interactions, and rope-sheave interactions. The third part addresses the use of simplified virtual dragline and control models. The fourth part of the review highlights the structural integrity of dragline machine. From the limitations of current research efforts, the author's PhD research is placed at the frontiers of dragline front-end assembly to advance the computational dynamics of this assembly.

2.1. DRAGLINE MACHINERY

In large strip mining operations, dragline methods are used to excavate significant amounts of overburden and to expose the orebody efficiently and economically. Coal seams may exist at depths from 20 to 150 feet beneath the ground. Two major stripping tools, therefore, are used to quickly reach out the coal, which are bucket wheel and dragline excavators. Dragline is one of the most economic excavators used to extract overburden materials to expose coal or minerals for extraction. Osgood (1880) invented the dragline and it was first manufactured in 1884 by Osgood Dredge Company (Lovass, 1982). Early

small models of draglines were found in civil engineering applications, such as canal excavation (Lovass, 1982). The bucket capacity has increased from 7 to 168 cubic meters (10 to 220 cubic yards) over the past decades (Stilwell et al., 1979).

Draglines have machine house of welded steel plates mounted on a radial tub using centered king post and tapered high strength rollers. They also have tubular, lattice-design boom filled with pressurized gas to detect cracks, power drive systems for the hoisting and dragging machinery, as well as swing machinery, and massive bucket attached to ropes through rigging system. The boom is anchored to the revolving house at machine-bored mounted lugs and is suspended from its end by the aid of galvanized bridge-strands. The hoist and drag ropes synchronously operate to maneuver the bucket for filling, hoisting, and spoiling purposes. The hoist rope is a single-line run from a hoist drum, which is driven by electric motors, and passes over a gantry sheave, the point sheave and then is attached to the bucket using hoist rope sockets. The drag rope is either a single-line or double-line run, which passes through fairlead sheave located near the operator cabin, and is connected to a drum driven by set of AC motors. The total requirement of wire ropes of dragline is about 3,000 m (2.25 miles) and it weighs about 82.5 tons (Bucyrus, 1974). The wire rope diameter varies from 69 to 125 mm (2.75 to 5 in) and has an approximate weight between 18.9 and 64.7 kg per meter (12.7 and 64.7 lbs per foot) as per (WRI, 2018). These ropes are multi-strand, multi-wire ropes of conventional type (6 strand/rope x 19 wire/strand) or advanced type of (8 strand/rope x 36 wire/strand) with plastic infusion to reduce internal friction. The minimum breaking force of these ropes ranges from 395 to1,383 metric tons (870,825.9 to 3048,993.1 lbs).

The drive system comprises multiple motors rather than larger motors to deliver the power requirement of magnitudes from 8,948.39 to 13,422.59 kW (12,000 to 18,000 hp). Each dragline is equipped with four or five swing motors and several drag and hoist motors to minimize the cycle time and to improve the bucket capacity. Each hoist and drag motor supplies a power of up to 372.85 kW (500 hp), 230 volts, and 480 rpm, whereas each swing motor is rated at 104.39 kW (140 hp), 230 volts, and 480 rpm. All motors, generators, and other electrical machines are securely anchored inside the machine house of a heavy welded steel structure. The machine house also carries an A-shape mast or a tri-structure, which supports the boom of a length ranging from 30 to 132.5 m (100 to 435 foot). The boom is fixed at angle between 30 to 40 degrees using intermediate supporting ropes to handle a Rated Suspended Load (RSL) exceeding 226,000 to 383,000 kg (500,000 to 845,000 lbs). Figure 2.1 shows a dragline in 2D beginning a new cycle of excavation (Nikiforuk and Zoerb, 1966).

Lumley (2014) claimed that the Actual Suspended Load (ASL) equals the total suspended load carried by the boom and it is calculated as in equation (2. 1)

$$\text{ASL} = W_{\text{Bucket}} + W_{\text{Rigging}} + W_{\text{Payload}} \tag{2.1}$$

Equation (2.1) does not account for the weights of the hoist and drag ropes, which are variable during the operation. The hoist and drag ropes exclusion can lead to large errors. If the ASL is equal to 226, 000 kg (498,244.71 lbs) and a hoist rope weighs 64.7 kg/m (43.47 lbs/ft), the hoist rope will have weight of 3,763.98 kg (8,298.15 lbs) if it is laid vertically below the boom tip (for a maximum dumping height of 27.33 m (82 ft) and digging depth of 36.66 m (110 feet) as per Figure 2.1. For this operating condition, the

error is 1.6% and can grow as the rope is reeled out to reduce the effect of passive loading on the bucket during digging motion. An accurate modelling technique is used to rectify the error in this study and considers the effect of ropes extension on the loading.

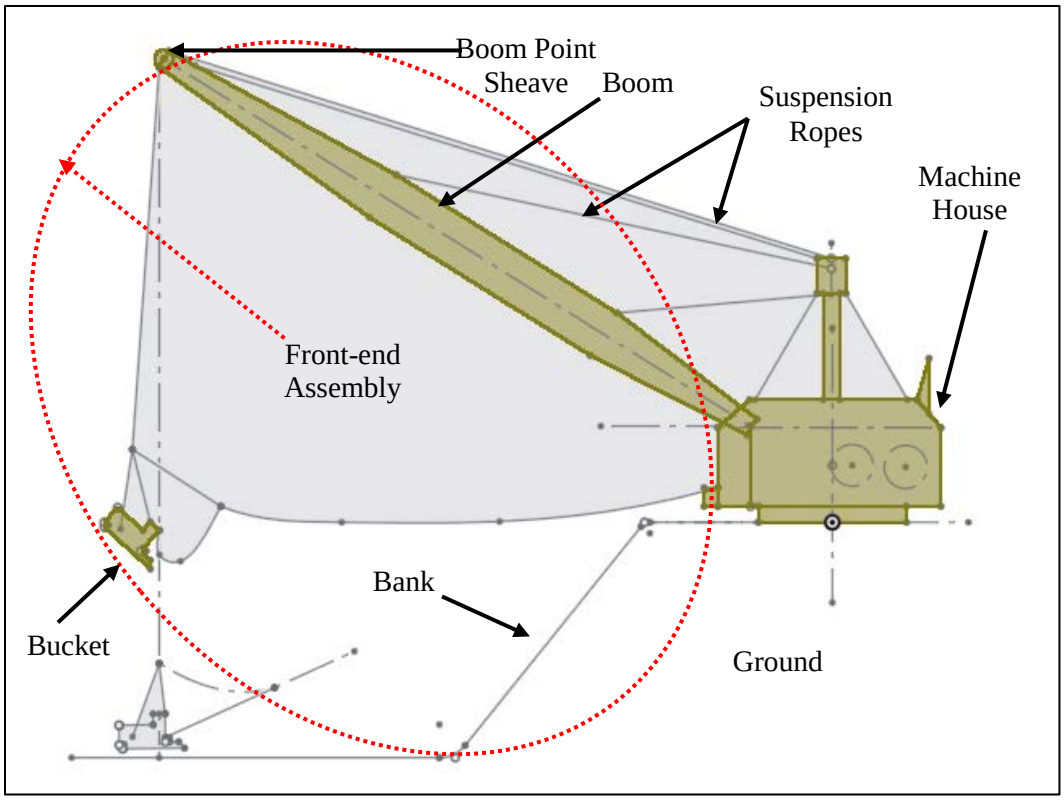

Figure 2.1. Schematic diagram of the Marion 7800 dragline

2.1.1. Operational Characteristics and Performance Monitoring. All draglines operate in a dynamic environment and many variables can affect their functionality, availability, utilization, and reliability. The operational variables include position, digging depth, and dumping height and the dragline radius, as well as its bucket capacity. These variables are cyclic in nature and vary from an operator to another. Other variables are

related to the capacities of the electric drives and the strength of mechanical components, especially the wire ropes, bucket design, and rigging mechanism. Although draglines are engineered from high strength materials (mainly high performance alloy steels), there is a general consensus that a dragline tool cannot last for 50 years (Carter, 2015). Most open-cast mines rely on maximum dragline utilization throughout the year, with a 24 hours a day, 7 days a week schedule. In coal mines, the strip mining activities are entirely driven by the dragline performance (Lovass, 1982). Alzheimer et al. (1981) claimed that a gain of 20 percent in rope life can be obtained when rope load is reduced by 10 percent. The authors mentioned that the gain in rope life could save around US $10,000 per year, but it can result in a net loss of US $510,000 in unremoved overburden due to RSL reductions. The loss in revenues associated with this decrease of rope loading capacity does not include additional losses due to machine downtime and unplanned maintenance, which could total up to $1 million/day (Ebrahimi et al., 2003).

Dragline productivity is controlled by two parameters, the amount of overburden removed (Rated Suspended Load) and cycle time. The bucket plays a central role in defining the productivity of any mining excavator. Bucket manufacturers of draglines provide different designs with increased sizes, and furnish them almost with the same rigging system to address the need of productivity increase. The capability of draglines has increased nonlinearly with the increased sizes of buckets, resulting in increased RSL. Stilwell et al. (1979) developed a rule to define the standard bucket size and related it to the RSL. They indicated that the hoist force in tons, for an empty bucket, is roughly equal to the bucket capacity in cubic yards. However, this claim is inaccurate based on the current review of the dragline manufacturers' specifications. Applying this hypothesis to a dragline

of a bucket capacity of 35 cubic yards yields a hoist load of 35.00 Mt (77,161.8 lbs), which cannot be used to hoist a load of 125.64 Mt (277,000 lbs) (Nikiforuk and Zoerb, 1966).

The design of dragline rigging system did not change for decades until the invention of the Universal Drag and Dump rigging (UDD) by Rowland et al. (2002). The invention of UDD eliminated over two thirds of rigging in a conventional dragline and reduced the carry angle to around 20° (ACARP, 2000). UDD allows bucket hoisting as soon as it is filled with material, and the operator is not required to drag the bucket close to the machine to avoid spillages. The drag time is reduced by about 3 seconds and the payload is increased due to front and rear hoist ropes. A study has shown that UUD's equipped draglines have an increased productivity of about 19% in a chop pass and 29% for high wall pass compared to conventional draglines (Rowland, 2000).

The design of dragline buckets has been refined since 1900s with different models in order to maximize the fill factor and reduce bucket weight while maximizing the digging efficiency and payload retention (Pundari, 1981; Rowlands, 1991; Mclure, 1995; Esterhuyse, 1997; Gentle, 2002; and Lenoard, 2011). Dragline Key Performance Indicators (KPIs) are used as a rule to estimate the performance of the operator and the dragline (Lumley, 2014). These measures include the cycle time, swing angle, payload, and digging rate. The KPIs provide critical information about how the mining practices track the preset goals and guide mine production engineers to achieve them throughout the mine life. It should be pointed out that these KPIs, when combined together, are counterproductive (Lumley, 2014). There are no machines in any database that can achieve the best value for each KPI parameter. The best filling time will most likely lead to a reduction of another important indicator, which is the payload.

Draglines are engineered to last between 20 and 30 years, with many technological developments. Modern draglines began in the late 1960s with the development of digital computers, improvements in AC drive motors, and optimization of structural components. Significant advancements in the dragline monitoring (Chironis, 1978a; McCoy, Jr. and Crowgey, 1980; McCoy Jr. et al., 1983; Scoble and Muftuoglu, 1984; Wu, 1990; Knights and Shanks, 1991; and Scoble et al., 1991) started to develop control techniques to assess production and productivity metrics. These advances created safer working environments by alerting operators of any potential failure or misuse of the mining machine and provided benchmarking for maintenance and training purposes.

Chironis (1978b) highlighted the benefits of using onboard display monitoring system installed in a Marion dragline cabin at the Jim Bridge mine, Wyoming. The system, developed by Douglas Electronics Co., receives inputs from encoders attached to the shafts of hoist and drag drums and swing gearing and it display details about the absolute positions and bucket loads. Additional performance gauge displays the location of the bucket with respect to the bench where the dragline is sitting on. The author claimed that the display systems, with its four performance gauges for visualizing the cycle time, allowed for higher productivity gains from 3,300 to 5,000 cubic yard/hour.

Bucyrus-Erie Co., in collaboration with General Electric Co., developed a static and dynamic anti-tightline control system to avoid collision between the bucket and boom in draglines (McCoy Jr. and Crowgey, 1980). The control system operates using the hoist and drag ropes length signals that are derived from two separate potentiometers driven by the hoist and drag drums. The static limit system uses a voltage signal that is equivalent to the sum drag and hoist lengths and then compares it to a preset value, whereas the dynamic

limit system uses the net velocity of ropes. A regulating amplifier is set to a preset voltage bias and any values that exceed this limit activate the amplifier to drain out the current from the hoist and/or drag rope circuits and reduce its speed. The preset bias voltage is defined by the minimum ellipse zone that the bucket cannot enter for safe operations.

Wu (1990) developed a dynamic monitoring control model of the excavation process under different geological formations. The model provides dynamic output of the simulation process and plots the dragline efficiency versus pit width and digout length. Knights and Shanks (1991) used a short-term monitoring of a dragline bucket and found it to increase the dragline productivity by 2%. Arora et al. (1999) developed a set of symbolic program called “the expert system” that analyzes the vibration levels induced in the dragline bearings due to misalignment or looseness. The expert system was developed on the basis of vibration levels and frequency data collected at bearings of interest. The authors argued that any faults can be traced in three directions and their early diagnosis increased the dragline availability by 6%. Eggers et al. (2007) used computed order tracking to monitor the faults in swing gears of dragline that operate under random rotational speeds and orientations. They mounted an accelerometer with the proximity sensors to measure the amplitude and direction of rotational speed of gear and its vibrations. The online monitoring station on the dragline allowed an early detection of any damage progression in the pinion over its life span.

Increased demands of dragline productivity and reliability have resulted in designing and deploying of larger mining equipment. Most coal mines have dozens of trucks, drillers, shovels, draglines, and many other machines that are operating concurrently. Schiffbauer (2001) stated that on average 13 mining fatalities occur every

year in surface mining operations and around 24 fatalities were related to the underground mining activities. This is due to lack of advanced monitoring systems, interactions among small and big equipment units. The search for additional monitoring techniques that improve safety and eliminate any collision led the National Institute for Occupational Safety and Health (NIOSH) to create an advanced instrument, Hazardous Area Signaling and Ranging Device "HASARD," for proximity warning (Schiffbauer, 2001, and Ruff, 2007). The HASARD device was instrumented on a Joy continuous miner, a highwall launch vehicle, and a Komatsu haul truck (Schiffbauer, 2001).

Complex operations with machine-machine interactions require advanced monitoring systems with high precisions to ensure safety. The Global Positioning Systems (GPS) technology is limited in these applications due to its centimeter precisions (Wusaty and Paulhus, 1995). However, these constraints imposed by U.S. Department of Defense, were removed to allow real-time centimeter precision. The application of GPS technology to locate a mining equipment is very beneficial in terms of safety, availability, utilization and productivity (Wusaty and Paulhus, 1995, Marshall et al., 1998). The benefits of the GPS machine control systems on dragline excavators include reduction in the necessary leveling effort in recent years. The GPS technology has allowed precise definition of the work plans of excavators. Wusaty and Paulhus (1995) at Fording Coal Ltd., introduced a dispatch system on a truck, which resulted in a 4.5% increase in fleet productivity. The authors also used GPS shovel technology to precisely determine the instant position of the shovel dipper.

Tritronics 9000 Series II dragline monitoring and navigation system has been applied to 65 draglines worldwide (Hansen, 2000). The system allows engineers and

managers to track tones of excavated overburden, cycle time, dragline delay times, and bucket positioning. The author claimed that the installation of Tritronics monitors has improved the productivity by 4%. Corke et al. (2000) have designed and tested a 3,500-ton dragline and Roberts et al. (2003) and Winstanley et al. (2007) have used Real Time Kinematic (RTK)-GPS to monitor the operation of a scaled-down dragline using 3D Digital Map Terrain (DTM). The integration of RTK-GPS receiver at the boom tip allowed for real-time 3D visualization of the terrain. Their approach was based on using a single-axis scanning laser mounted at boom-tip directed downward where the angular position of each scan is determined at every rotation from an encoder fixed on the slew drive. According to their study, dragline DTM successfully performed 50 autonomous cycles without the intervention of the operator.

Dragline monitoring systems are vital elements in the development and sustainability of mining operations. Overloading the dragline with payloads above the recommended loads can damage the dragline boom and electric motors (Vynne, 2008). The dragline productivity can be compromised due to unplanned downtime resulting in loss of millions of dollars. Another important KPI indicator, diggability index, has received a great attention due to the implementation of GPS technology. The assessment of dragline diggability index has become more meaningful with accurate measures of dragline bucket position. It can define efficiently the blasting and hole burden and provide possible alternatives for optimizing hole spacing and burden. Vynee (2008) argued that the application of mining monitoring techniques (Thunderbird Mining Systems) safely increased the RSL of Marion dragline 8750 from 306 to 383 tons.

2.1.2. Dragline Simulation and Automatic Control. Dragline simulation greatly helped mine planning engineers, operators, and management to precisely schedule and visualize the digging and dumping processes, as well the topography of mine geological features and equipment. Bandopadhyay and Ramani (1979, 1985) developed computer models to quantify the interrelationship between the mine geological conditions, equipment, and methods. The models accept input data of materials (swell factor, highwall angle, bucket fill factor, angle of repose) and mining parameters (height and width of chopdown bench, mining block length, overburden and interburden height). According to the authors, the model fidelity was established from the 99% confidence interval of production rate per hour and delay time per shift with a small error of 1.87 % and 5%, respectively.

Wu (1990) developed a 3D dragline simulation model for a multi-seam pit that has Graphical User Interphase (GUI) and validated it using field data from two mines. The model was based on a single digout for each coal seam and a Monte Carlo integration method was used as simulation experiment. Mirabediny (1998) developed a computer simulation model of dragline operations that incorporates seven stripping methods. These methods are simple side casting, standard extended bench, split bench, chop cut in pit bench, extended key cut, single highwall and double longwall passing, and double high wall and single lowwall multi-pass. The author argued that the model can provide an optimum solution to the dragline mining methods and planning. Most of these research models have resulted in increased dragline productivity, reduced mine planning time and improved utilization (Baafi et al., 1995; Mirabediny, 1998; Erdem et al., 2004). These

dragline simulation models focused on mine planning and operations, with no discussions on how productivity improvements affect dragline longevity.

The use of computer models for planning dragline operations improves the existing automatic control models and establishes new modelling approaches. The dragline operates in a cyclic, repetitive mode and its cycle lasts about 60 seconds. Two-thirds of the cycle time, 40 seconds, is devoted to swinging after digging with the loaded bucket towards the spoil area. Thus, this area of research is given a greater attention with the improvements of computational tools and computer capabilities. Very early simulations of the dragline dynamics, on analog and digital computers, started in the mid-1960s and accelerated at slow rates until the early 1990s (Nikiforuk and Ochitwa, 1964; Nikiforuk and Zoerb, 1966; Jones, 1974a; Kemp, 1977; McCoy Jr. and Crowgey, 1980; Godfrey and Susanto, 1989; Shannon, 1990; and Roberts et al., 1999). Current computational software with robust capabilities has advanced the analysis of complex machines and made it more manageable. Physical modelling of excavators for experimental purposes has become secondary, especially given the rapid emergence of virtual simulation (VS) (Frimpong and Li, 2006; Frimpong et al., 2007; Frimpong et al., 2008).

2.2. EXCAVATION METHODOLOGY AND MODELLING TECHNIQUES

In strip mining operations, depending on the depth of the overburden layer, the exposure of coal or minerals may require the excavation of large amounts of overburden materials. The type of overburden and its geological features dictate the type of excavation technique, equipment type, and cycle of operations. If the deposits are coal seams lying near the surface less than 60 m (200 feet), the stripping method will be the preferred method. Open-cast (stripping) method is characterized by casting the excavated overburden

to the spoil area. The advantage of the stripping method is the associated high productivity resulting from the deployment of a large mining excavator (dragline, rope shovel, or bucket wheel excavator). Rope shovels are favorable for digging hard rocks, while bucket wheel excavators and draglines are favored for the long reach and higher capacity.

Hartman (1987) compared the productivity of mining equipment under similar conditions of operations. The author claimed that a bucket wheel excavator (BWE) of bucket size 4 m^3 (5.23 yd^3) can achieve an output 8,490 m^3 per hour (11,000 yd^3 per hour). The productivities of a dragline and a shovel of equal bucket size of 57 m^3 (75 yd^3) are 1,990 m^3 per hour (2,600 yd^3 per hour) and 2,180 m^3 per hour (2,850 yd^3 per hour), respectively. However, the productivities of these machines (bucket size/hr) should not be the only basis for equipment selection; it should also include the unit ownership and operating cost per ton ($/tons). In these terms, the dragline is the most economic piece of equipment for stripping of overburden material (Hartman, 1987) as shown in Figure 2. 2.

BWE and dragline quickly spoil the overburden and allow for an immediate reclamation, which is another advantage associated with the strip mining method. Another advantage of the dragline machinery is its long digging and dumping reach. However, the use of few dragline units has the disadvantage for tying large production capacities to one equipment unit. Any breakdown in the dragline unit will cause significant delays and production losses. Another disadvantage associated with the dragline use is the variations in digging and dumping that makes it suitable only for large scale overburden removal (Scheffler, 2002). The dragline operating cycle is about 60 seconds depending on operator skills (Nikiforuk and Zoerb, 1966; Kemp, 1974; Nichols et al., 1981; Corke et al., 2000; Fry, 2003). It includes the bench digging and bucket loading, simultaneous lifting and

swinging of the loaded bucket, bucket dumping at the spoil pile, and returning of empty bucket to the bank to start a new digging cycle (Nichols et al., 1981).

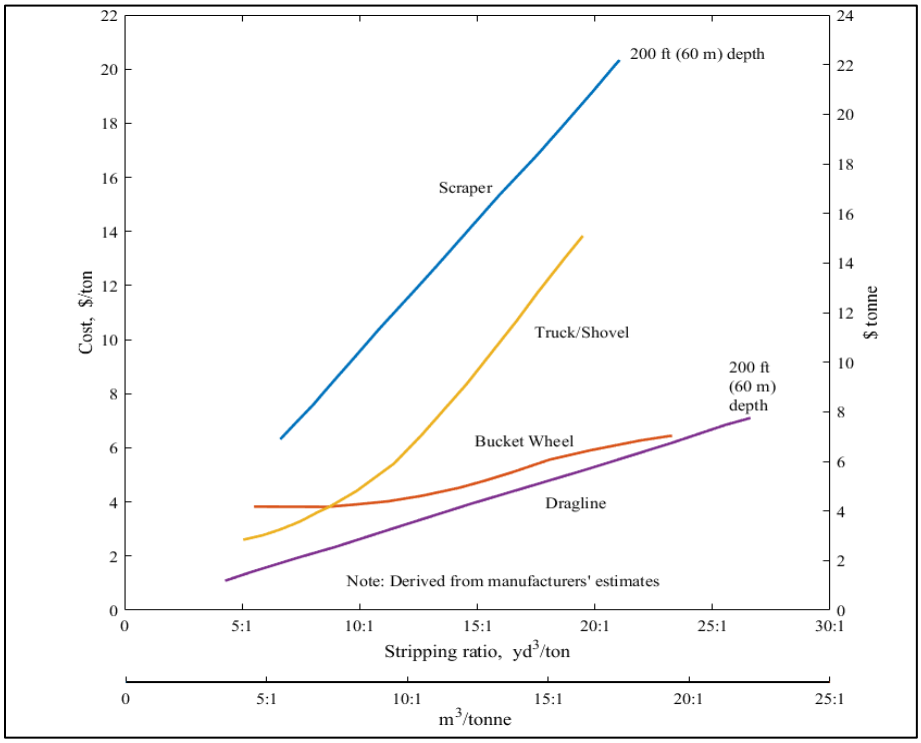

Figure 2.2. Equipment operating cost per ton comparison (Hartman, 1987)

The key structural elements in a dragline are the wire ropes that control the bucket under the boom point sheave. These ropes are subjected to various types of loading (abrasion, corrosion, and fatigue) and they provide the weakest link in the front-end assembly. However, the research on dragline wire ropes focusing on its degradation under these types of loading is not fully understood. Current research on dragline dynamics focuses on bucket design and rigging dynamics, dragline automation, and dragline behavior modelling using machinery kinematics and dynamics theories.

2.2.1. Kinematics and Dynamics Modeling of Excavators. Excavators are one of the great technological advancements of the early 1830s (Fairhurst, 1928). Their design and functionality have greatly been reshaped over many centuries to increase bulk loading capacity, efficiency and longevity. Any excavator can be regarded as a multibody mechanical system with many links that are intertwined to provide specific motion and carry part of the load. Each link of the excavator provides one or several degrees of freedom (DOF) to execute the associated motion. A kinematic analysis is usually performed to study the motion of each link (body) and to track its spatial orientation without the acting forces or loads (Housner and Hudson, 1980; Josephs and Huston, 2002). This branch can be applied to analyze any mechanism in two ways, either forward kinematics or inverse kinematics. The first one is a mapping from excavator joints coordinate to the bucket pose using a predefined transformation and a position vectors of each link and joint. The latter is a reverse process that relies on defining the joint coordinates according to a specific pose of the bucket or link (Corke, 2016).

The kinematics analysis of any excavator is an important process used to assess its maneuverability and its bucket trajectory and to avoid any potential collision among its mechanical components (Vinogradov, 2000). Dynamic modeling is also required to completely analyze the behavior of excavators under the action of transient loading (Housner and Hudson, 1980; Josephs and Huston, 2002; Corke, 2016). This branch, thus, considers the effect of loading variations and describes the periodic machine behavior. The use of kinematics and dynamics modeling allows a complete description of the mechanism behavior using a set of differential-algebraic equations. The fundamental laws that define

the governing mechanical behavior of a rigid body are the Newton's second law and Euler's second law using equations (2.2) and (2.3), respectively (Shabana, 2010).

$$F_i = \sum m_i^R a_i^R \tag{2.2}$$

$$M_i = \sum I_o \ddot{\theta} \tag{2.3}$$

Equations (2.2) and (2.3) can be directly used to develop a set of equations of motion for a single- or multi- body system about a reference point located at its center of mass (Shabana, 2010; Kasdin and Paley, 2011). However, the location of the points of load application can significantly impact the derivation of the mass moment of inertia defined in equation (2.3). The parallel axis theorem must be used to extend equation (2.3) in a case where the reference point of the body is not located at its center of mass. The application of Newton-Euler approach to develop a dynamic model leads to a sparse matrix that can be programmed to solve the accelerations and reactions (Shabana, 2010). The Newton-Euler method requires drawing and analyzing the free body diagram (FBD) for every link and associating the acceleration of its center of mass to forces and torques applied at joints. This technique is very efficient for the dynamics formulation of serial manipulators with limited number of links (less than 10) (de Jalon and Bayo, 1994). The Newton-Euler method can be recursively applied to solve the inverse dynamics of systems (Luh et al., 1980; Saha, 2013).

Lagrange (1788, 1813), in his memoires entitled "Mecanique Analytiques II", credited the seminal work about the theory of motion to earlier philosophers Galileo, Euler, Descartes, and Wallis. Lagrange developed his equations on the basis of the definitions of the generalized coordinates and virtual velocities (Richie, 2012). The Lagrangian

formulation was first used to solve the dynamics of a system of pulleys connected via ropes under a new principle called “The Lagrangian” (Lagrange, 1788). Lagrange’s principle provides a completely different approach to formulate the equations of motion for rigid bodies. The resulting equations of motion are of second order ordinary differential equations. A choice between Newton’s Laws and Lagrange’s equations depends on the type of problem under investigation. If one is trying to analyze the motion of the slider in a slider-crank mechanism to determine the slider displacement, applying the Newtonian mechanics requires solving time-varying constraint forces, which hold the slider in place. However, using Lagrangian mechanics requires only a simple definition of the generalized coordinates that define the motion of the slider.

Although the Lagrangian formulation eliminates the need to work with noncontributing forces (constraint forces), it is problematic when used in systems that have mathematical entities derived in terms of velocity (Kasdin and Paley, 2011). Thus, it is better to describe any system using the velocity-like definition and generalized coordinates. The most acceptable definition is using the angular velocity as will be seen in the next section upon developing the dynamic model of a dragline using Kane’s method. Another short-coming of Lagrangian formulation is due to the nonlinearity that results from the derivations of kinetic and potential energies and the complexity of variables separation. Moreover, the analyst would also sense the difficulty of understanding the equations and it cannot be used to describe dissipative systems (Taylor, 2005). Despite these limitations, Lagrangian formulation started regaining popularity among analysts as a result of the availability of powerful computational resources.

Hamilton (1856) contributed to the field of dynamics by introducing the concept of vectors and extended the work of Lagrange through his discovery of the integrated equations of motion. The transformation of equations of motion expanded by Hamilton received a great attention from Jacobi who considered his results important (Graves, 1889). Both Hamiltonian and Lagrangian formulations are based on the energy methods and can be used instead of Newton's laws as fundamental principles in dynamic analysis. The Hamiltonian, as defined by H, is derived from the Lagrangian using Legendre transformation (Richie, 2012). The Lagrangian, denoted by L, is the difference between the kinetic and potential energies. The Hamiltonian principle is called the principle of least action, which means the variation of a functional S (the integral of Lagrangian over time) is equal to zero over time, as illustrated in equation (2.4).

$$\frac{\delta S}{\delta q(t)} = 0 \tag{2.4}$$

This definition leads to finding the trajectory function $q(t)$ since Lagrange had built his discoveries based on the difference between kinetic energy T and potential energy V. In other words, the minimization of this difference is just the path that an object should follow over time. The remarkable advantage of using the Hamiltonian's formulation is that the integrand of equation (2.4) is invariant to the generalized coordinates (Meirovitch, 1970). However, the function S must be differentiable twice and the boundary conditions must also be known. Luu (2014) applied Hamilton's principle to derive the equations of motion of the BWE boom. The boom was modelled as a 3-D deformable elastic beam using Euler-Bernoulli beam theory. This study addressed the effects of deformation-motion

couplings in the boom on its dynamics response. However, the author did not include the dynamics of the counterbalance arm where inertia loadings are significant.

D'Alembert (1743) had studied the infinitesimal motion of bodies under different geometrical configurations and constraints. The author stated that the sum of all inertia and gravitational forces acting on a body is zero (Kane, 1961). This discovery was used as a starting point by Kane (1961) and Kane and Wang (1964) to develop a new formulation of Lagrangian mechanics. Kane (1968) expanded the Lagrangian mechanics by including the concept of generalized speeds. A new formulation was named after Kane (1968) “The Lagrange’s Form of D’Alembert’s Principle” and Kane’s equations of motion as established in Kane and Levinson (1985).

In the United States, the design of digging excavators, which used the steam engines, was started by Otis Company in the 1836s and continued its developments till the 1920s (Fairhurst, 1928). Despite the advancements in the field of dynamics at that time, the design of these equipment was based on the static analysis and graphical techniques. Peters (1955) and Volkov (1965) studied the design of single bucket excavators (rope shovels and draglines) and established the guidelines based on the static analysis and experimental testing. Pankratov (1967) investigated the dynamics of excavators based on the theory of stability of motion (Lyapunov, 1892). The author developed mathematical models to describe the oscillatory motions of a dragline boom using differential equations of the second order.

Satovsky (1963) highlighted the limitations of the studies that used the separation of working mechanisms when modeling the dynamic of mining excavators. In his approach, the mining excavator machine house, boom, bucket and rope are modeled as

lumped masses connected by elastic springs and dampers. The solutions of the differential equations of these models capture the vibrations in the machine due to unsafe operations and reduced unnecessary increase of safety factor.

The fundamental laws and principles, stated earlier, have also been used for investigating and developing equations of motion in mining machines. Sethna (1962) used the Lagrangian formulation to find the equations of motion of four-wheeled vehicle for the sprung mass. Bakholdin et al. (1967) studied the dynamics of a pit loader mechanism using the Lagrange equations. They found that a geometrical optimization of the geometry of the hoisting mechanism can significantly reduce the driving torque of its motor and can increase the loader productivity. Chang el al. (1989) performed a man-in-the-control-loop simulation on a backhoe excavator in the framework of Newton-Euler formulation. They used relative motion of joint coordinates to derive the equations of motion.

Bullock et al. (1990), Vaha and Skibniewski (1990), Hemami and Daneshmend (1992), and Koivo (1994) developed kinematics and dynamics force/torque models using Newton-Euler formulation. These researchers related the loads at joints to their arm forces through the corresponding joint angles. Koivo et al. (1996) developed a dynamic model of a backhoe excavator in the digging mode and used it for the Proportional-Integral-Derivative (PID) controller design. They used Denavit-Hartenberg (D-H) convention in order to construct the transformations between the excavator links. Newton-Euler technique was used to establish a complete dynamic model of the excavator. A desired trajectory was developed based on the inverse kinematic procedures and the Proportional-Integral-Derivative (PID) controller was used to generate the required torques to be applied on the machine to follow this trajectory.

Frankel (2004) used the Lagrangian formulation to develop the dynamics equations of a backhoe excavator. The author used the inverse kinematics analysis to map the joint space to cylinder space, which is required to calculate the time history of the cylinder length for control tasks. The Lagrangian model of the backhoe was modeled in Simulink using blocks that have information about the joint torques, inverse Jacobian, and joint torques and forces. The direct dynamics process allowed calculating the bucket pose and cylinder lengths according to the input forces. To validate the model, a user-defined digging trajectory was input into the backhoe model and a virtual model and the simulation results were compared to the collected data. Knotz (2007) extended the work by Frankel (2004) and used a minimization of a cost function that includes the bucket angle to avoid the singularity in the backhoe excavator. A constraint method was implemented in the Jacobian and is based on the elimination of the velocity of the link that moves the backhoe bucket in areas where singularity is possible. A force control technique was used to adjust the command velocity in the backhoe links according to forces that resist its motion.

Frimpong and Hu (2004) and Frimpong et al. (2005) and Frimpong and Hu (2008) developed the kinematics and dynamics of cable shovel excavator using Newton-Euler technique. The dynamic model used crowd arm length and its angular displacement as generalized coordinates. A predefined trajectory and a virtual model of the rope excavator were used for validation purposes. The resistive forces to digging used in their calculations are based on the work by Zelenin et al. (1975). Awuah-Offei (2005) developed a dynamic model for a rope shovel based on the simultaneous constraint method (SCM) and Newton-Euler method. The kinematic model considered the boom point sheave in the shovel front-end assembly and used hoist rope and crowd arm angles as generalized coordinates.

Awuah-Offei and Frimpong (2007, 2011) have shown that an optimal digging energy per unit loading rate can be achieved with a digging trajectory produced by 0.7 and 0.25 m/s speeds of hoist rope and crowd arm, respectively.

Frimpong et al. (2005) reported the limitations of Newton-Euler and Lagrangian formulations and contributed to the dynamic analysis of cable shovel excavators based on Kane's Method. Their dynamic model has 2 DOF as generalized speeds, which are the first derivatives of translational and angular displacements of the crowd handle in local and inertial frames, respectively. To maintain higher rope shovel productivity, the authors developed a Proportional-Integral-Derivative (PID) controller that used inputs vectors of desired displacement and velocity. Frimpong and Li (2006), Li and Frimpong (2008), Frimpong and Wardeh (2016) and Raza and Frimpong (2017) published seminal works in the virtual simulation of electric rope shovels. These researchers developed 3-D virtual simulators of the rope shovel and their models were mainly used to study the kinematics and dynamics and to identify zones of high stress loading on an excavator boom.

Shi (2007) developed simplified kinematic and static models of rope shovel and claimed its superiority over its counterparts. A drawback of this model is that the boom point sheave is modeled as a point mass. Another shortcoming is that static equilibrium was used to derive the forces in the hoist and crowd arm. However, the model was capable of generating precise digging trajectories with a hoist speed of 1.7 m/s. Slob (2007) used a load sensing technique to estimate the load at the boom point sheave of a P&H 4100A rope shovel. The dynamics modeling was established in the framework of the Lagrange method and also considered the electrical motors outputs. Awuah-Offei et al. (2009) extended the work by Awuah-Offei and Frimpong (2007) on rope shovel and applied the passive earth

theory to develop the dipper-formation cutting resistance and estimated dipper payload. The authors showed that the horizontal cutting forces are more significant than those in the vertical direction. The estimated payload outweighed the cutting resistance.

Himmelman (2011) studied the dynamics and control of a 2800 XPB P&H electric rope shovel and estimated the inertia and frictions based on data provided by sensors mounted on it. The (D-H) parameters were used in developing the forward kinematics analysis. Euler-Lagrange formulation technique was applied to derive the equations of motions and then estimate the shovel inertia. In his research, an important modeling aspect is based on the inclusion of a complete geometry of the boom-point sheave and shipper shaft. The dynamics model was built in the Simulink environment and used three inputs. These inputs are the torque applied by the swing motor, torque developed in shipper shaft by the hoist rope tension and the force in the crowd arm developed hoist rope and crowd motor. The modeling approach was purposefully applied to control the swinging and hoisting motion and to develop a collision avoidance system. Rasuli (2012) also used the Lagrangian method to derive the equations of motion of a simplified 2 DOF model of cable shovel. The author used the least square technique to search the dynamic parameters under the effects of static and dynamic loadings. The sought-after parameters included the coefficients related to hoist and crowd motors, dynamics payload estimation and inertia.

Raza (2016) and Raza and Frimpong (2017) also used D-H convention and Newton-Euler method to study the kinematics and dynamics of a P&H 4100-XPC electric rope shovel. The authors investigated the fatigue failures of the dipper using linear elastic fracture mechanics. J-integral values of a virtual crack, located in the dipper bottom face, were calculated from a finite element software (ANSYS). It allowed estimating the stress

intensity factor (SIF), which provided valuable information about the crack propagation and service life estimates. The SIF curves were generated using a least square regression and a fitting technique and showed a rapid increase as crack size increases. Research findings also showed that crack growth rate is high at a certain crack length and for a crack length of 75 mm the remaining life is reported 16 days.

2.2.2. Kinematics and Dynamics Modeling of Dragline. Section 2.2.1 has shown extensive research efforts on the kinematics and dynamics of backhoe, hydraulic excavators, and electric rope shovels. However, there is very little research on kinematics and dynamics of dragline excavators, which requires research and development. Dragline kinematics and dynamics must start with proper assignment of geometrical constraints and DOFs to the dragline structural components. These constraints and DOFs must represent reasonably as many working limits and mobility functions as possible to capture the mechanics of the dragline front-end assembly. The arrangement of the structural components of the dragline front-end assembly (boom, ropes, and bucket) have been designed and assembled to maximize bucket maneuverability and reachability. The arrangement has made the kinematics analysis very complex and reduced the fidelity of models reported in the literature due to significant elimination of major mechanical components. As will be seen in Section 3, the digging kinematics are only controlled by two DOFs, which are ropes velocities. The presence of fewer control input variables than DOFs classifies the dragline as an under-actuated mechanical system (Spong, 1998).

Schwedes and Stoetzel (1948) provided valuable information about the rope shovel and dragline power demands in kilowatt-hours per cubic yard according to varied dipper and bucket capacities up to 30.5 m^3 (40 yd^3). Swanson and Meier (1956) reported the

effects of rapid load changes on the performance of a Bucyrus B-22 rope mining shovel. They experimentally tested an engine and torque converter and found that rapid losses in the output power were caused by the engine acceleration and lower torque-converter efficiency. Matuszak (1964) emphasized the importance of static control in the draglines to achieve desirable torque-speed curves for the swing, hoist and drag motions. The author stated that the torque regulated, speed limited controls provide more control and safety in high inertia movements. However, the speed regulated, torque limited controls provide full use of machine capacity at low speed, and thus, increase the useful motion and the excavator productivity.

Drybrough (1965) explained the benefits of using direct current (DC) drives of motor current and generator sets of the hoist motor and compared it to alternative current (AC) drives. Morley (1982) investigated the duty cycle of the dragline and has shown that it can be represented by four quadrants. If any fault occurs during the hoisting quadrant or any other quadrant (motoring, braking, and swing) due to the overload, a high-fault current is generated in the DC motors with high armature current and consequently damage the armature circuit. These abnormalities affect the productivity of rope shovels and draglines, and they were major hurdles that remained unsolved until the development of synchronized AC motors with Insulated Gate Bipolar Transistor (IGBT) inverters controls.

These new technologies are beneficial in many shovels and locomotives (Koellner, 2006). The application of these technologies in dragline started in 2006 by Siemens Inc., and was seen to increase the dragline productivity by 20%, which resulted from reduced maintenance and robust control against perturbations (Koellner, 2006). The dynamic analysis of the electric drives in a dragline is a very broad topic and requires

interdisciplinary collaborative research efforts. However, this research initiative is mainly contributing to the dynamics analysis of dragline using the modern theory of dynamics (Kane's method).

2.3. DYNAMIC LOADS IN DRAGLINE ROPES

Nikiforuk and Ochitwa (1964) and Nikiforuk and Zoerb (1966) might be the first to provide an analytical dynamic model of a dragline. Newton's Law was used to relate the bucket motion to the accelerations of the hoist and drag ropes and their respective hoist and drag forces. The simulation was, however, performed for hoist and drag motions independently. A great emphasis was given to the electrical characteristics of both hoist and drag motors and their respective generators. Jones (1974b) successfully simulated the behavior of dragline ropes using a simplified catenary equation that accounts for rope sag. The unbalanced inertia in the rigging system and the difference between two points on a drag rope allowed the calculation of the drag rope force. The mathematical analysis is very basic and did not include information about position, velocity, and acceleration vectors. However, the results are fairly acceptable from operational point of view.

Kemp (1974) developed a computerized system to analyze the dragline performance. Several sensors were used to automatically measure the cycle times, delays, amperage in the hoist and drag armatures, total power consumption, and bucket loading force. McCoy Jr. and Crowgey (1980) patented an anti-tightline control system that controls the limits of the hoist and drag ropes to reduce the bucket motion in proximity to the machine and to avoid boom collision. A family of curves were proposed based on the hoist and drag drive lengths and speeds that identify the static and dynamic limits. The static limit is defined by dragline manufacturers as a boundary line beneath the boom where

the hoist and drag ropes cannot pass. In other words, it is calculated from the sum of the hoist and drag ropes. Whereas the dynamic limit is found based on the velocities of these ropes, the key idea of anti-tightline system was based on examining the bucket position in 5 seconds and 2 seconds before a collision could happen. These findings are doubtful in a real world when the inertia in the bucket are high and need further investigations.

Godfrey and Susanto (1989) also contributed to the automation and control of dragline and developed a semi-automatic model of dragline drives motions. Drive controllers for hoist and drag systems successfully detected the trajectory of the hoist and drag ropes in a 40-second duty cycle. The swing controller design accounted for the pendulum effect of the bucket motion relative to the boom. Although the simulation models considered this effect, as well as variable inertia, tub inclination, torsional resonance, and external loads; the rope catenaries, centrifugal forces and Coriolis effects were dropped during the analysis. The kinematics results showed good agreement with physical experiments. However, these results cannot be accepted given the stated assumptions. The Coriolis force is significant for a large mass (bucket) translating in a local reference frame and rotating in an inertial reference frame. Its magnitude is given by equation (2.5).

$$F_{Cor} = 2\, m_b v \times \omega \tag{2.5}$$

m_b is the bucket mass, v its velocity or the velocity of drag rope, and ω is the angular velocity of machine house. If the mass of a full bucket is 200,000 kg, its linear velocity in the drag rope reference frame is 1.75 m/s and machine house angular velocity 9 deg/sec, the Coriolis force is 105 KN. The dynamic analysis done by Godfrey and Susanto (1989) is questionable and Coriolis forces cannot be ignored in this kind of machinery.

Ridley et al. (2001) developed a scaled-down model of rigging dynamics of a dragline bucket to study its static pose. The model with 2 DOFs was tested based on the perturbation theory and used velocity inputs of the drag-rope. Several features can be obtained from the model, such as hoist and drag rope angles, and tension in the drag rope. McInnes (2009) applied the Lagrangian to derive a 4 DOFs dynamic model of a dragline front-end assembly with an out-of-digging plane inclination of the bucket. The model considered the rotary motion of the dragline without investigating the digging motion. The slewing torque of the machine was optimized over a simple cycle during peak duty and validated with field data. The fatigue analyses on the boom, based on a FEA, were implemented and have shown that stresses are below the threshold fatigue limits. However, two serious limitations were found, which are due to a point mass modeling of each of the bucket and the boom-point sheave. It is clear that the Lagrangian formulation requires a substantial removal of some DOFs of a system to make the EOMs more compact.

Frimpong and Demirel (2009) and Demirel and Frimpong (2009) developed an advanced kinematic and dynamic model of dragline based on the simultaneous constraint method (SCM). The kinematic model used vector loop method and was a benchmark to develop the dynamic model using Newton-Euler Formulation. The model accounts for the omitted components (boom point sheave and bucket) in the earlier studies and accepts velocity inputs of the hoist and drag ropes. A Simulink based ODE solver was used to integrate the velocities and accelerations and a Gaussian elimination technique was implemented to solve a linear system of equations. The authors successfully calculated forces in the hoist and drag ropes, as well as forces at joints and used them to plot stress contours. However, their contributions were limited to a planar motion and rigid body

kinematics. Since the hoist and drag rope change their lengths during operations, corrections to their corresponding masses should be applied to make these findings more realistic. In the current endeavor, the rigging system is expanded and is modeled as a two-link mechanism rigidly connected with the bucket as point mass located at the free end.

Li and Liu (2013, 2014) provided virtual and analytical models to analyze the kinematic and dynamic behavior of two draglines. They used SCM and Newton's Laws to relate the velocities and accelerations of ropes to the bucket position and mass. The analytical model did not include the rope-sheave motion, nor the rigging dynamics. The authors developed co-simulation in MSC.ADAMS-Simulink-ANSYS to assess the functionality of their design and to predict the stress history and fatigue life. The analysis revealed that the lowest fatigue life was 3.11 years for the largest stresses at boom structural member located at the foot of the boom. The MSC.ADAMS model was superior to the Simulink one and the erroneous results in the Simulink are attributable to the elimination of two major components (sheave and rigging system).

Research findings show that the boom point force reached a maximum of -5,000 KN (Li and Liu, 2013) at the onset of 15 seconds of cycle time and -1,200 KN at time 40 seconds for the CAT 8750 dragline. It also reported -110 KN and -135 KN at 15 seconds and 40 seconds, respectively, for the Marion 7620 model (Frimpong and Demirel, 2009). The maximum allowable load of Marion dragline is 99,400 kg (175,000 lbs) (Demirel, 2007), which is equivalent to 99,400 kg* 9.81 m/s^2 = 974.78 KN. These results are very limited in terms of operational capacity defined in the manufacturer's catalogue. However, very limited information about CAT dragline did not allow conducting a fair comparison. It is important to consider the bucket weight, its payload, the variable weight of the ropes

in dynamics analysis to improve the accuracy of results and avoid unnecessary increase in safety factor during design.

2.3.1. Hoist Rope - Sheave Interactions. Dragline productivity and performance are a function of its components that continuously operate under heavy duty cycles. Hoist, drag, and dump wire ropes, hoist and drag chains, and boom point and fairlead sheaves control the bucket for executing its functions within the normal duty cycle. Figure 2.3 shows the arrangement of ropes and chains that are used to properly control the dragline bucket for loading. A particular concern that hinders the productivity of a dragline is mainly attributed to its unplanned downtime.

Figure 2.3. Komatsu 9020 dragline: (a) physical model, (b) 2D sketch and physical model of ropes (Bridon, 2017), and (c) rigging system

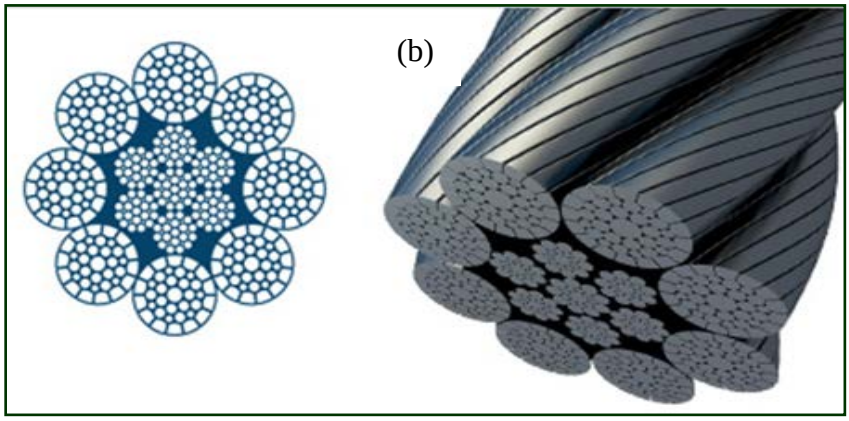

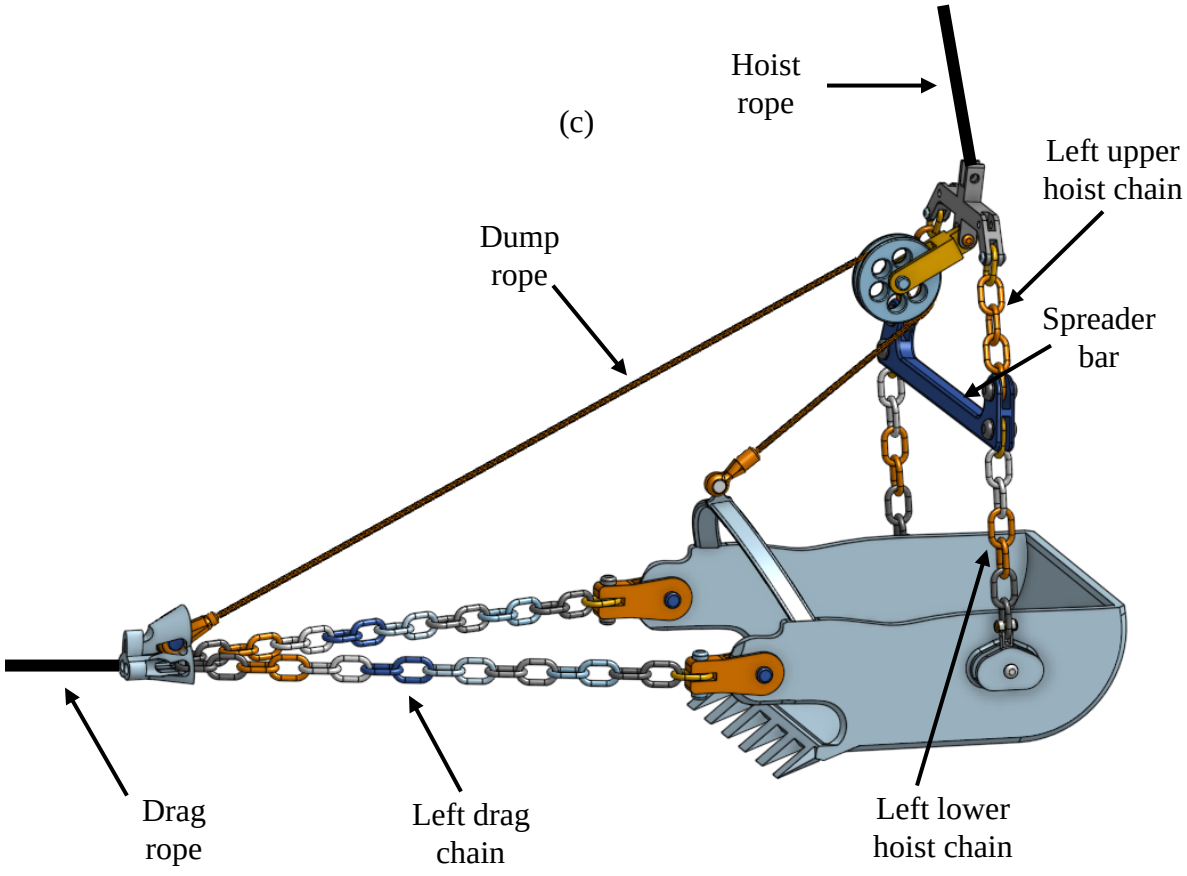

Figure 2.3. Komatsu 9020 dragline: (a) physical model, (b) 2D sketch and physical model of ropes (Bridon, 2017), and (c) rigging system (Cont.)

Ropes and sheaves operate in a direct contact with other parts and the surrounding environment. Thus, wear, tear, and fatigue are more likely to start and develop over time and can cause a complete shutdown of the strip mining process. As a matter of fact, the analyses conducted on the rope-sheave and rope-formation contacts in draglines are rarely given a considerable attention and requires research attention. The hoist rope is used to lift the bucket and payloads off the bank and surmount changes of suspended loads, bending over points-sheave and frictions in its grooves.

Boomsliter and Morgantown (1927) gave an excellent discussion about the effects of the accelerations of mine hoisting systems on loading induced in ropes during service. The authors considered the elasticity of ropes in their analysis of the mine shaft hoisting mechanism that carries loaded skip. They noticed that excessive stresses in the rope could be dropped by the proper selection of wire rope, which could result in a reduction of safety factor by half. Haas (1951) illustrated the designs and features of wire ropes that were mainly used for mining applications at that time. According to the author, the construction of the 6×41 Filler wire was used on large draglines and shovels and made up of 16 outers, 8 small fillers, 8 inners, and a single core wire, as seen in Figure 2.4.

The 16 outers in each strand are of large diameter comparing to the inners, which imply that this construction is confined to large diameter sheaves. This design provides a good flexibility (Haas, 1951) and is not as durable as the current ropes used in the mining industry (Bridon, 2017). The Bridon model is more compact and has excellent wear resistance and higher breaking forces (Bridon, 2017). It is also recommended for draglines that are typically equipped with larger boom point sheaves.

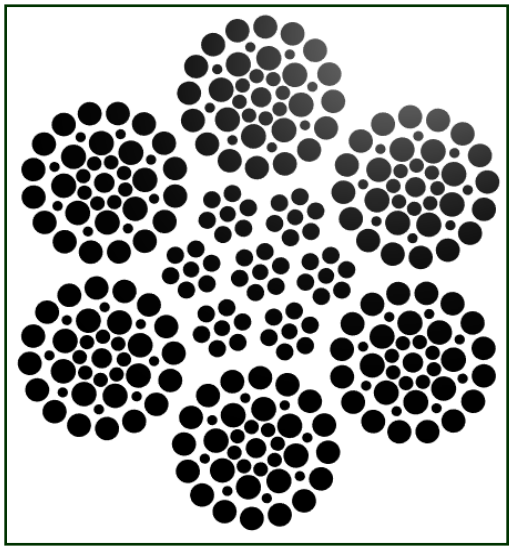

Figure 2.4. 6x41 Filler hoist rope used in dragline (Modified after Haas, 1951)

Heller (1970) studied the static and dynamic contacts of a rope-sheave system under the effects of uniform pressure and angular velocity of sheave (ω). The analytical model differs from the Capstan equation, $T = T_0 e^{\mu\beta}$, and it also accounts for the effects of rope weight on the rope tension, (T) and its contact pressure with sheave (P). Information about the role of every parameter on the tension were furnished in the model and are included in equation (2.6) for an angle of contact that varies between 0 and 180°.

$$\left.\begin{aligned} \frac{T}{T_0} &= M_{it}\left[1 - \frac{M_{av}}{M_{it}}\left(\frac{\rho}{T_0}\right)\left(\omega.\frac{D+d}{2}\right)^2 + \frac{M_{rw}}{M_{it}}\left(\frac{\rho g d}{T_0}\right)\right] \\ P.\frac{dD}{2T_0} &= N_{it}\left[1 - \frac{N_{av}}{N_{it}}\left(\frac{\rho}{T_0}\right)\left(\omega.\frac{D+d}{2}\right)^2 + \frac{N_{rw}}{N_{it}}\left(\frac{\rho g d}{T_0}\right)\right] \end{aligned}\right\} \quad (2.6)$$

$M_{av}, M_{it}, M_{rw}, N_{av}, N_{it}, N_{rw}$ are multipliers for the effects of initial tension, angular velocity, rope weight on rope tensions and contact pressure, respectively. D, d, and ρ are the diameters of sheave and rope and material density of wire rope. The author claimed

that the effects of rope weight and angular velocity are negligible and can be eliminated from equation (2.6). Thus, a simplified form of tension and contact pressure are given in equation (2.7).

$$\left.\begin{aligned} T &= T_0\, e^{-\beta(\emptyset-\emptyset_1)}\left[\frac{\beta}{\alpha}\sinh\alpha\,(\emptyset-\emptyset_1)+\cosh\alpha\;(\emptyset-\emptyset_1)\right] \\ P.\frac{dD}{2T_0} &= 2\;\frac{\beta}{\alpha}\;e^{-\beta(\emptyset-\emptyset_1)}\sinh\alpha\,(\emptyset-\emptyset_1) \end{aligned}\right\} \quad (2.7)$$

$\emptyset-\emptyset_1$ refers to the angle of contact, $\alpha=\sqrt{\beta^2+\frac{D}{d}}$, $\beta=\left(\frac{D}{d}+1\right)/2f$; and f is the coefficient of frictions between rope and sheave. It can be seen that the contact pressure adds an additional force to the tension, at the rope end, due to the friction phenomena. Both the contact pressure and tension are maximum at the point the rope departs the sheave.

Alzheimer et al. (1981) found that the maximum stresses due to bending over sheave double occur when the ratio $\left(\frac{D}{d}\right)$ is reduced by one half because of the added axial linear tension. Depending on the location of wire rope in the sheave groove, every wire strand experiences different tension against the groove, while its twist keeps it tight to the wire rope core. Relative motions between wires in a strand and the motion of strands relative to the core impose a significant friction and cause non-localized deformations. As a result, the damage due to deformation increases over time and some wires break, which reduce the load carrying capacity. Nabijou and Hobbs (1995a) evaluated the frictional performance of heavily loaded ropes and found that the coefficient of friction increases with increasing sheave size. Their research also showed that the type of rope core does not affect the sheave friction coefficient. Nabijou and Hobbs (1995b) analyzed the relative motions and slip between wires of strands and their cores in ropes bent over sheave. They

concluded that the positions of maximum movements of wires are similar to those of failed wires under the experimentation due to high loading.

Schönherr (2005) examined the influence of fleet angle for different construction of ropes and found that for a fleet angle $\varphi = 4°$, the loss of endurance varies between 16% and 48%. The author also claimed that the loss of endurance for four rope constructions occurs when the ratio $\left(\frac{D}{d}\right)$ is reduced and fleet angle increases above 4°. Imanishi et al. (2009) simulated the dynamic contact of rope-winch coupled to a hydraulic system in a tower crane. The dynamic contact was modeled using truss elements of variable length. Their research finding showed that using a hydraulically operated winch-rope system prevented disordered winding.

Kuczera (2012) developed an analytical model to calculate the forces induced in a rope running over a sheave. The dynamic model takes into account the inertia effects of rope, its linear speed and the line of contact pressure with sheave. The results of MSC.ADAMS simulations showed that the contact forces are linearly proportional to the rope acceleration. These forces are higher if the rope enters the sheave at fleet angle higher than 60°. Wang et al. (2013) proposed a time varying length of a hoist rope model to improve the dynamics of winding of rope over a hoisting drum. The MSC.ADAMS model uses angle sensors to capture the friction forces, as the rope is paid out, using the Hertzian contact theory. The sensor is a function that measures the rotation between the COM of the drum and COM of discretized element of the rope within a global reference frame.

The model is depicted in Figure 2.5 and is verified in a numerical simulation experiment using Lagrangian formulation of the hoisting mechanism. Although the virtual

model is computationally efficient and advanced in comparison to the MSC.ADAMS library, the contact model is very basic and based on Coulomb friction.

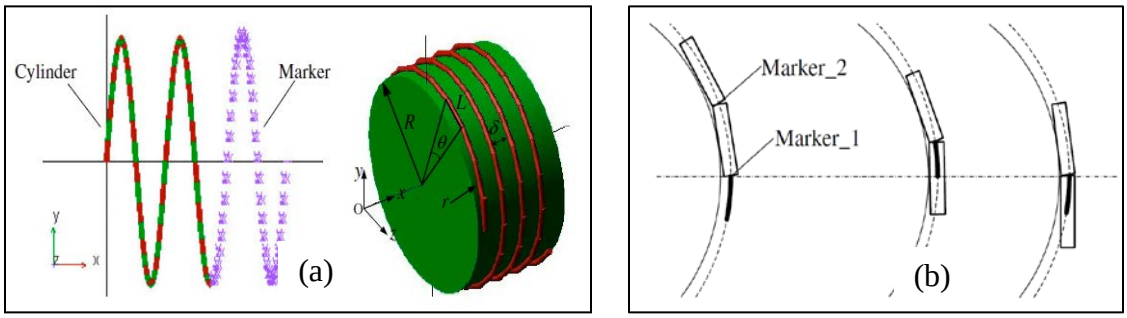

Figure 2.5. Rope-drum contact (a) Mapping process, (b) decomposition process (Wang et al., 2013)

Shi et al. (2017) developed a (6×1) 3D simplified wire rope model to study the rope-sheave interaction. The analytical model uses a V-shape groove and Euler-Eytelwein formula of traction. The simulation results support the claim that the wire core endures tension while the helical wires undergo the effects of friction and pressure. The traction conditions are improved when the angle of grooves is increased and contact pressure get reduced as well. Leonard et al. (2009) designed and tested a scaled-down model of a dragline that uses two hoist sheaves mounted at the boom end. Two hoist ropes are used to maneuver the bucket, which eliminated the need to have the conventional rigging system. The goal was to automate the digging process and reduce the variability of human error.

2.3.2. Drag Rope-Formation Interactions. The dragline digging process is driven by a drag rope, a structural element which is connected to the drag chains and dump rope and reels in/out on fairlead sheaves located near the operator cabin, as seen in Figure 2.3.

The drag rope construction is not different from that for the hoist ropes. However, a drag rope should be designed and engineered to reduce the damage due to wear and abrasive contact with the overburden. The subject of study on bucket-formation interaction remains an active area of research for different kinds of machines (shovels, dragline, backhoes, and wheel loaders). Although research on dragline dynamics has been given fair attention, very little has been done about rope-formation interaction (Alzheimer et al., 1981; Dayawansa et al., 2005; Dayawansa et al. 2008). These research studies show that the drag ropes are prone to damage from abrasive wear more than bending fatigue over fairlead sheaves.

Zelenin (1968) investigated the issues of cutting soils and resistance to cutting under various conditions for different cutting tools. The results showed that resistance to cutting depends on the category of soil, the degree of its saturation and the shape of cutting (Петерс, 1955).

$$P = n.C.h^x = A.h^x \tag{2.8}$$

P is the cutting force at the given cutting width in kg; h refers to the depth of cut (cm); x is an indicator of degree at h (x = 1.35); n is a numerical coefficient depending on the cutting width; C is the number of strokes of Densitometer; A is a coefficient depending on the cutting width and the number of strikes by the densitometer (e.g., 12 DorNII rammer). An improved form of the digging force takes into account the tooth angle of the bucket is given by equation (2.9) (Zelenin et al., 1975 and Kudryavtsev, 2017).

$$P = 10.C.(h)^{1.35}.(1 + 2.6\,l).(1 + 0.0075\,\alpha).z \tag{2.9}$$

l: refers to the bucket width (m); h is the depth of cut (m); h is a function of bucket angular displacement in the hydraulic excavators, and bucket linear displacement in the draglines;

z is a factor that considers the teeth of side bars. The effect of inertia of falling materials, $g(m.s^{-2}).V(m^3).\gamma\left(\frac{kg}{m^3}\right).tg(\emptyset)$, in the bucket is eliminated from equation (2.9) since the boiling effect of soil happens at low constant speed. Konakov and Eliseev (1974) formulated a criterion to improve the diggability of dragline bucket and included variables for the effect of loaded materials, length of digging, and duration. The equation of motion of the drag system was derived and used to find the line of action of drag rope.

Stilwell et al. (1979) showed the effect of location of attachment points of drag chains on the digging energy of a dragline bucket. The authors noticed that the line of action of drag rope depends significantly on locations of the drag hatches (Figure 2.3, c) and on the frictions between the bucket and soil. The presence of friction shifts this line from the center of gravity (C.G) of the bucket to pass through a point located directly beneath it at ground zero level, as seen in Figure 2.6.

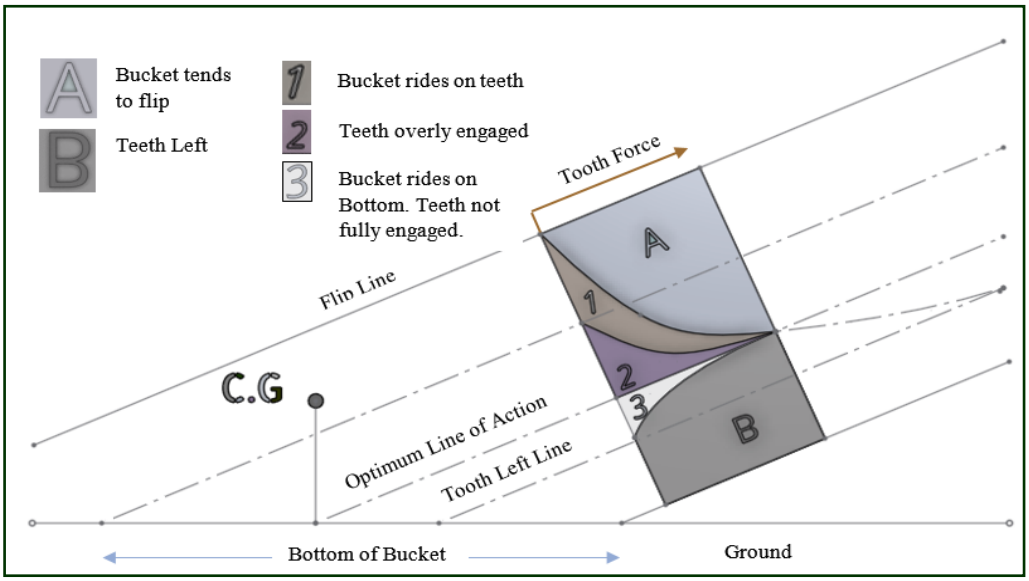

Figure 2.6. Optimum line of action of a drag rope force (Stilwell et al., 1979)

In fact, the wear plates and chains add extra weight to the bucket, which improves its digging efficiency. Their weights, however, constitute about 8% of the dragline payload, which can compromise the productivity. Morgenstern et al. (1980) fabricated load sensors (links) and connected them to drag ropes in a Bucyrus dragline to capture its dynamic loads. To receive data from the sensor, they used radio telemetry (low radio frequency waves), a well-established, reliable technique at that time. The authors found that dynamic loads are more severe in drag ropes than those in hoist ropes and static analysis does not capture their degree of damage.

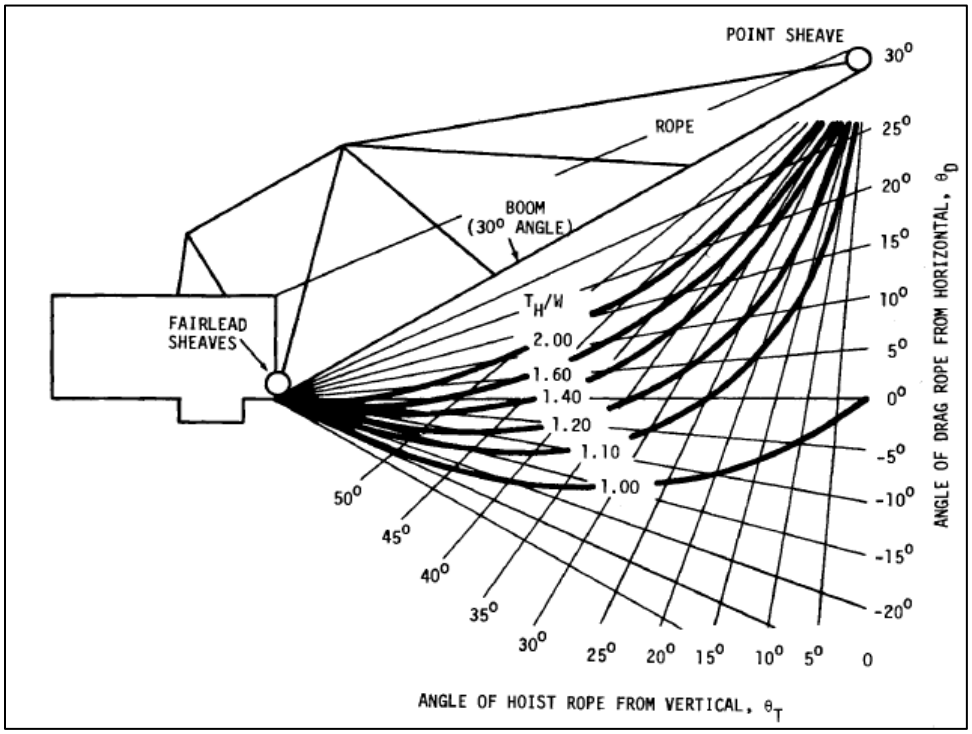

Figure 2.7. Hoist rope tension as function of bucket position (Morgenstern et al., 1980)

Static analysis (Morgenstern et al., 1980) was used to estimate the load magnification factor (the ratio of the hoist rope tension to bucket weight) for different

values of hoist and drag rope angles, as shown in Figure 2.7. This analytical model is not reliable since it ignores inertia effects and rope weights. Hamm (1983) and Golosinski (1995) claimed that retired hoist ropes can be used as drag ropes since its retirement criteria are more stringent. Such scenarios require the analysist to consider drag ropes as pre-deformed structures and would make the dynamics analyses very challenging.

Rowlands (1991) designed and tested three scaled down models of dragline buckets to identify the factors with maximum impact on bucket filling. His experiments showed a great role of bucket geometry and the material type on the specific digging energy. Aspinall (1992) emphasized the effect of rope selection and weights on the bucket payload and productivity. Haneman et al. (1992) evaluated the performance of dragline buckets using small and large scale physical testing. Two hundred experiments were performed on the physical models to estimate the drag force, payload, fill distance, drag peak load, and specific digging energy (SDE). The authors found that the filling behaviors of both buckets are similar to the field data. They also found that drag force at stall was not achieved due to the use of powerful motors, and the SDE of large scale model is less than of a small one due to higher filling efficiency. The large scaled model was successfully verified to potentially increase the productivity by comparing its payload with the field data.

Mclure (1995) also examined the effects of the bucket trunnions and drag and hoist chains lengths on drag rope-ground interaction and on the digging performance. Rowlands (1991) performed experiments that showed that a proper location of the trunnion provides optimum digging where the bucket teeth do not skate over material, nor penetrate it too much and tip the bucket forwards. Mclure (1995) proposed that increasing the length of drag chain reduces drag rope contact with ground. This practice adds more dead loads, due

to longer chains, which move the bucket's CG further to the bucket tip and requires additional dragging distance. It also reduces the carry angle and the filled materials may fall, which results in less carried payloads. Moreover, having longer drag chain imposes an additional operating constraint on the operator to increase dragging distance and to keep a dynamically balanced C.G. of the bucket. Thus, this practice is not recommended as the digging cycle may add two to five seconds, which is disadvantageous to productivity.

Esterhuyse (1997) built and tested a scaled down dragline to study the influence of bucket geometry on its filling performance. Experimental tests revealed that the filling speed of different bucket geometries is the same, when hitch height is fixed, and it is a function of (i) relative position of the teeth, (ii) center of gravity, and (iii) hitch height. Also increasing the hitch height and lowering it increased the drag force, but led to additional wear in the drag rope and drag chains. However, no meaningful conclusions were drawn from the influence of drag angle on the drag force. This limitation is due to the fact that the experimentations were done at a drag angle equivalent to the angle of an inclined, flat digging surface. Schmidt et al. (1998) and Bray (1999) patented rear-dump dragline bucket designs with conventional hoist-trunnion and a tagline instead of a dump rope of adjustable length. These features maximized the dumping radius due to dumping from bucket rear-end, shortened cycle time due to quickly lifting the bucket off the bank, and provided varied carrying attitude of bucket due to varied length of gate-arm chains and tagline.

Crous (2000) used the Newton-Euler method to develop a general framework of the multibody dynamics of a dragline. An experimental model of a rope-pulley was established to model the contact between the dump block and dump rope using simple pulley-chain system. The numerical solution for this subsystem was successful and agreed

with experimental results. However, the entire dragline system was not successfully tested due to many constraints in the multibody dynamics approach and the lack of computational resources (Crous, 2000). Townson et al. (2003) formulated a mathematical model, based on Weibull distribution, to estimate the effect of dragline load on its availability, output yield, and maintenance. The mathematical model used some field data gathered from different maintenance databases. The lack of data from different draglines did not permit a proper validation of the Weibull model. Coetzee et al. (2009) built a scaled model of dragline bucket and simulated the motion of its filling using Discrete Element Method (DEM). The models have two drag ropes and no hoist ropes were considered in this study. The analytical model, with the aid of a particle flow code (PFC), was verified using experimental setup but it was incapable of producing the same drag forces.

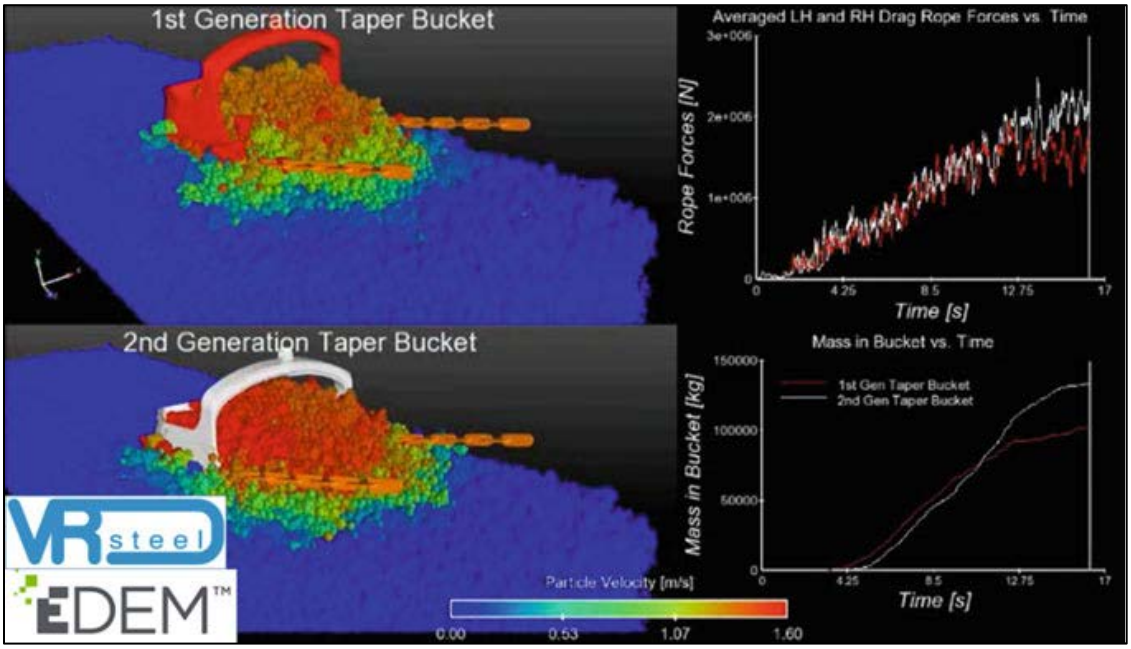

Figure 2.8. MSC.ADAMS-EDEM Co-simulation of a dragline bucket (Curry and Deng, 2017)

Curry and Deng (2017) studied the distribution of loads in a dragline bucket during digging based on efficient MSC.ADAMS-EDEM Co-simulation as shown in Figure 2.8. The coupling allowed real assessment of loads imposed on a 45-ton dragline bucket, reduced the bucket mass, and provided a productivity gain of 2%. The drag rope forces and bucket payload were accurately estimated in real-time. The coupling results were used to optimize equipment design by replacing physical testing and reducing cycle time.

2.4. STRUCTURAL INTEGRITY OF FRONT-END ASSEMBLY

Wheeler (1974, 1976) developed the finite element (FE) software to resolve the structural problem in Bucyrus dragline booms. The author also used NASTRAN to develop a new dragline with longer boom. Manser and Clark (1980) measured the loads on the hoist, drag, and suspension ropes using strain gauges and shear bridges. They reported the disadvantages and uncertainties of using electric motors characteristics (i.e., armature current, armature voltage, and armature speed or field excitation voltage) to estimate rope loads. These disadvantages include (i) friction losses in electric drives, (ii) reduced efficiency of electric motors, (iii) nonlinear relationship of armature current-torque; (iv) damping of dynamic effects, and (v) very high torque of motor shaft.

Test results on drag rope loads were more accurate using shear bridge gauges mounted at fairlead sheave than those based on motor armature current estimation, as shown in Figure 2.9. For the hoist rope load, the dragline bucket and rigging weights were taken and the armature current of hoist drive was recorded during bucket hoisting at constant speed where the drag rope was in a horizontal position. This procedure was repeated for different bucket fills until a correlation was established between the armature

current and load. Unfortunately, there is no information to show these variations but a more appropriate procedure was described in the work by Slob (2007).

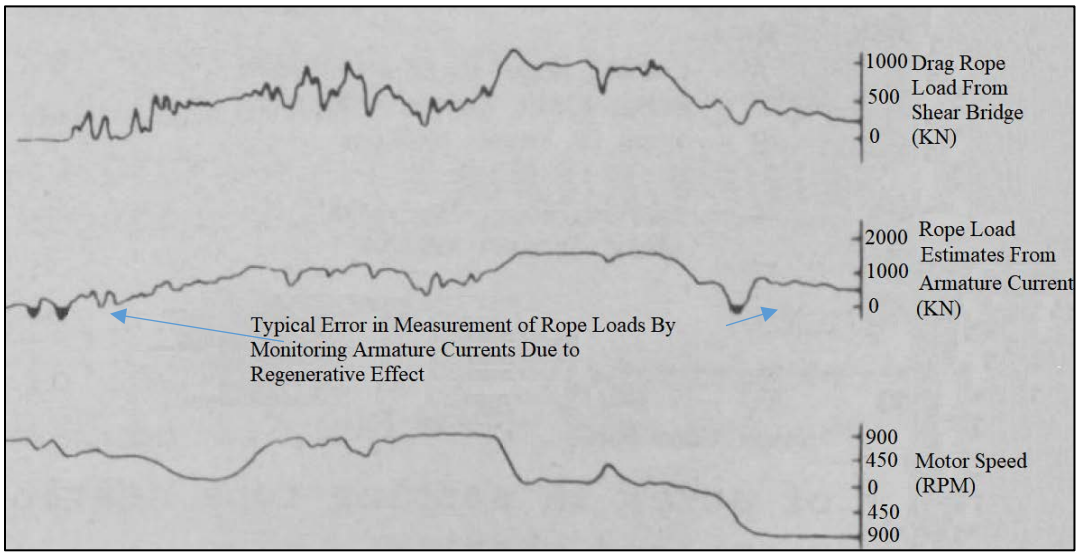

Figure 2.9. Drag rope load measurements for horizontal drags (Manser and Clark, 1980)

Lovass (1982) mentioned that FEA was performed on a Bucyrus dragline in the early 1970s and NASTRAN, developed by NASA, was the software environment for the analysis. The revolving frame and boom structure were successfully modeled and a set of design loads that included inertia effects were developed for the boom and bucket during digging. The results included a representation of maximum and minimum stresses in every member and buckling effect checks. Ehret and Hasse (1992) reported great benefits from using finite element method (FEM) for modeling and analyzing the stresses in a rotating frame, tub, and roller circle of an 8750 Marion dragline. The results showed that cracking developed in the weld joints around mouseholes, buckling of the floor and distortion of the

roller support pad. These results led engineers to modify their designs and rectify some structural components that resulted in a 70% reduction in their stresses.

Gurgenci et al. (2000) introduced the concept of damage point and duty meters to optimize dragline operations under conflicting concerns of productivity and availability. Field tests on a dragline operated by three different operators have shown that the damage in the machine is mainly due to differences in their operational behaviors. Monitoring the stress cycles, at specific joint, has also shown that filling-dumping cycle of a skilled operator is faster than other operators. This observation led to a conclusion that overloading the machine to increase productivity can be done with extensive maintenance efforts based on the severity of damage. Guan et al. (2001) experimentally and numerically tested the dynamic response of a dragline boom-mast using three different excitations for fatigue life predictions. An FE model was used to calculate the first ten modes of the DRE23 dragline. The authors instrumented the dragline front-end assembly with 16 accelerometers located at highest master nodes (DOFs) to assess the first 10 FE modes using the modal assurance criteria (MAC). Their results, however, did not yield an appropriate pairing between the FE modes and those obtained from the experiments except for the first FE mode.

Fry (2003) discussed structural failures of draglines and listed different failure patterns associated with different components. Several failures are weld-related and others are due to either running the machine beyond its capacity or under repeated cycles within its static limits. He investigated a boom collapse that occurred as a result of doubling the buckling effects when a lacing member broke. The breakage of the member was due to a fatigue crack initiation. Improper maintenance failed to address the issue. Thorough material testing and engineering analysis revealed that no defects were present in the boom,

and extensive structural analysis was necessary before restoring the machine to normal operations.

Eggers (2007) applied a computed order tracking method to detect the faults in the drag gear of a Dresser 8200 Marion dragline. An accelerometer was used to measure the vibration and frequency levels and two proximity sensors were used to determine the pinion speed and its rotational directions. The author noticed fatigue cracks opening due to the outward motion of the bucket and this failure was a result of gear misalignment.

Pang et al. (2009) and Pang and Zhao (2009) used FEA to determine the stress intensity factor (SIF) in welded joints of a tubular boom of a dragline. Experimental testing was also done to measure the hot stress spots on 4 full size specimens loaded once at the main chord and then at two bracing members. The values of SIF were found using FEA in a close agreement with those in the experimental analysis and their ratio within [0.94-1.062]. Mashiri et al. (2011) also used the hot stress spots concept to investigate the fatigue in the tubular boom structure of a dragline. The results of their work showed that hot stress spots are more intense in the welds of the lacing members than those in the chords. These results are in agreement with other research findings by Joshi et al. (2009).

2.4.1. Finite Element Analysis of Ropes. Although wire rope efficiently transmits axial loads, its complex construction makes it very difficult to perform multibody dynamics analysis. In many cases, a common approach to study the dynamics of ropes is to discretize them to a finite number of segments allowing some degrees of flexibility. Alzheimer et al. (1981) used the FEM package (ADINA) to analyze the loads on a dragline drag rope since the experimental setup using a load sensor (Morgenstern et al., 1980) did not yield accurate results. The FEM simulations were run on a 35 elements of truss model and resulted in a

maximum tension in the rope of 3,113.7 KN (700,000 lbs) at a drag distance of 33.53 m (110 feet). Cutchins et al. (1987) examined the damping characteristics of wire ropes used as vibration isolators. A model of wire rope with seven strand and one core was modelled using NASTRAN and the assumed modes method was implemented to account for the deformation in the rope. Loading results showed that strands tend to separate due to negative Coulomb friction.

Jiang et al. (1999) used a commercial finite element package (ANSYS) to model the torsional behavior and contact friction in a 7 strand wire rope loaded axially. The simplified model indicated a nonlinearity of stress at contact points between strands. Kamman and Huston (2001) used finite segment approach to develop a multibody dynamics model of a variable length cable system. The model mimics a wire rope partially submerged in water and rope links are connected via spherical joints. One important aspect of their model is the ability to effectively reel in and out on a sheave during the motion of the ship. Moreover, the links masses are lumped at joints, which eliminated the inertia effects of rope segments, increased the number of elements, and increased the computational efficiency. Kyle and Costello (2006) developed a dynamic model of a rope with 20 lumped masses located at joints and connected by springs and dampers. The model is based on Newton's second law and includes the effects of viscos stiffing and viscos damping for each element. Research findings have shown that increasing the number of rope elements resulted in a good agreement between measured and simulated pitch angles of the bucket.

Kuczera (2012) calculated the deformations and stresses in a large diameter sheave using FEM and a dynamic model of rope-sheave developed in MSC.ADAMS. Ropes are

represented as rigid multi-bars and run over sheave. The simulation results of the MSC.ADAMS model made it possible to capture the dynamic contact and maximum forces in the sheave. The results also showed that the spokes in the sheave were more likely to deform under alternating tensile loads. The results also indicated that the maximum stresses exist at the points of attachment of spokes to the sheave. Shi et al. (2017) created a 3-D FE model of a wire rope with a $6 + 1$ construction to analyze its interaction and bending effects over sheave. A contact model based on friction Coulomb was used in a commercial FE software (ABAQUS). The research results indicated that von Mises stress contours depict the real behavior of strands under different tension loads. The authors observed that the contact pressure is higher for a sheave groove angle of 30° than that for a larger angle (40°).

Wokem et al. (2018) studied the bent over sheave for two wire rope constructions (7 wire strand and 19 wire strand) under the effects of cyclic tension. The authors noticed that the SIF reduces when higher forces are applied at the strand end and is independent of sheave groove radius. Their research suggested that increasing the number of wires in a rope from 7 to 19 did not establish a correlation between SIF and applied load.

2.4.2. Fatigue Analysis of Ropes. A skilled dragline operator must maneuver and position the bucket into the bank in a way that improves its diggability and filling efficiency, reduces the loads on drag and hoist motors, and minimizes drag ropes contact with the ground. Although these measures improve the machine availability and productivity, dragline overall performance is controlled by implementing rigorous maintenance practices. Other maintenance factors are reduced probabilities of failure occurrences. For example, the probability of a rope failure is higher than other components and should be concurrently replaced within periods of planned maintenance. Since there

are no criteria replacing dragline ropes, a good engineering judgement and proper periodic inspections play a key role in this process. Many practices set a replacement time while a rope still retain some of its useful life.

Anderson and Brady (1980) investigated the downtime of 17 pieces of draglines and found that the average downtime from rope-related failures constitutes 105.6 hours per year for a 46 m^3 (60 yd^3) dragline operating 6,650 hours of availability per year. If this dragline moves 1.4×10^9 m^3 ($1.8 \times 10^9 yd^3$), a production loss from this failure is estimated to be 19×10^6 m^3 ($25 \times 10^6 yd^3$). The authors found that the average life of hoist rope is twice that of one drag rope. Morgenstern et al. (1980) have tested several wire ropes using bending-over-sheave machine to estimate the fatigue when its strength approached 50% of the breaking strength. Golosinski (1993) mentioned that the performance of hoist and drag ropes varies based on their constructions, operating conditions, and maintenance practices. The author criticized the replacement criterion of drag ropes, which is based on the worn-out by one-third of rope diameter. Other discard criteria were also used by industry depend on the number of broken wires in a rope, wear of the external wires, and deformation in the rope. According to his study, the wear limits should be based on permissible loss of rope strength.

Golosinski (1995) showed the wear factor in hoist and drag ropes and found that hoist ropes outperformed drag ropes. According to the author, surveys revealed that average service life of hoist ropes is 99,000 operating cycles and 55,000 operating cycles for the drag ropes. His assessment of wire rope performance was based on three indicators: (i) work cycle count, (ii) rope wear factor, and (iii) unit work factor. These indicators are of particular importance since they are correlated with the dragline productivity, safety,

cycle time, and rope characteristics (length, unit mass, number of ropes). To complement his analysis, it is fundamental to calculate the transient loads in ropes, define zones of hot stresses, and estimate SIF. These procedures enhance rope replacement practices and reduce the capital cost associated with unnecessary early replacements.

Dayawansa et al. (2006) showed that the average service life is 32 weeks for hoist ropes, 10 weeks for drag ropes and 2 weeks for dump ropes. The authors reported that the cost of maintenance of wire ropes accounts (15%) of the dragline total maintenance costs and is estimated at $300,000 per annum per machine. The research on fatigue failures and expected service lives of large diameter ropes (e.g., 85, 114, 130 mm) is limited (Hanzawa, et al., 1981; Wolf, 1987; Marsh, 1988; Feyrer, 2007; Wokem, 2015). Maintenance practices show that the replacement of hoist and drag ropes is done every 16 weeks and 10 weeks, respectively (Alzheimer et al., 1981). Dayawansa et al. (2008) detailed several maintenance practices that increase service life of ropes. These practices include: (i) maintaining the ratio of sheave groove radius to hoist rope radius as equal to or greater than 1.08, (ii) drag rope area loss due to wear and breaking of wires exceeding 20%, (iii) accommodating larger sheaves and hence larger diameters of ropes, and (iv) improving maintenance practices and understanding rope subsystems carefully.

Wokem (2018) conducted several FE analyses to estimate fatigue life of ropes used in an electric rope shovel. He calculated the SIF and then established a fatigue life estimation based on the reduced endurance limit of a single wire in the rope. This concept considers that the endurance of a structural component is subject to several factors (i.e., surface finish, notch in the wire, tensile strength). The author used the Stress-Number of cycle (S-N) curve and the reduced endurance limit of a wire to deduce the fatigue life of

rope at any level of stress (Thorpe et al., 1985). Figure 2.10 presents the estimated time to first wire failure for a given stress. It can be seen that the diggability of materials affects the stresses and the time to the first failure. It should be noted that this estimation takes into account the availability and utilization of the electric rope shovel.

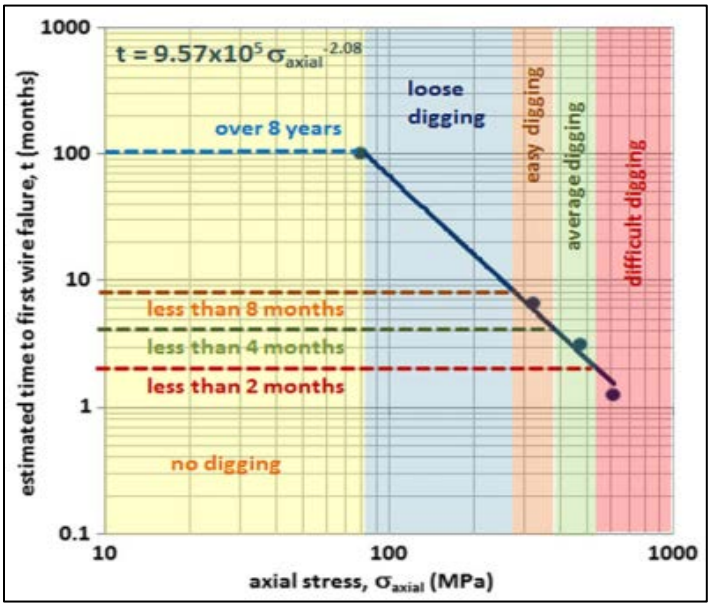

Figure 2.10. Performance of a 6 × 36 wire rope in 4100 rope shovel **(Wokem et al., 2018)**

2.5. RATIONAL FOR PHD RESEARCH

The dragline machinery is used to efficiently excavate and remove overburden and to reduce manpower. Their design and functionality remain unchanged despite the technological advancements. These machines have received major improvements in terms of size and loading capabilities. They are designed and tested under the effect of static loading. However, their performance are not properly tested under dynamic loading

scenarios. The literature contains few studies that did not consider the dynamics of the front-end assembly in details. To the author's knowledge, all the models have major limitations due to the elimination of important structural components from the front-end assembly. To date, there is no computational dynamic model of the dragline front-end assembly that contains all structural components.

The kinematic and dynamic of the front-end assembly in a dragline machinery is one of the most challenging research areas in heavy mining machinery. The multi-link structures make it difficult in developing accurate kinematic and dynamic equations. In addition, the dragline uses only two degrees of freedom during the digging phase and three degrees of freedom in the remaining duty cycle components. There is no model in the literature that can handle digging and swinging simultaneously, which contains all components of the front-end assembly. McInnes (2009) developed a dynamics model that has more degrees of freedom than that in a real dragline. This consideration would result in unnecessary computations and the model cannot be reliably applied to a real dragline.

The current available dynamic models that describe the behavior of the dragline front-end assembly have limited structural systems and cannot accurately predict the forces in the hoist and drag ropes and the swinging torque. Demirel and Frimpong (2009) developed an advanced model that accounts for the digging phase and contains a good representation of the missing structures of the front-end assembly. However, their model is limited to a planar motion and only valid for digging. McInnes (2009) developed a good model for the bucket swinging motion and ignored the digging phase. Many dragline dynamic models have been developed with no boom-point sheave, rigging system, and machine housing (Nikiforuk and Ochitwa, 1964; Nikiforuk and Zoerb, 1966; Jones, 1974a;

Kemp, 1974; McCoy, Jr. and Crowgey, 1980; Godfrey and Susanto, 1989; Shannon, 1990; and Roberts et al., 1999; McInnes, 2009; Li and Liu, 2013).

This research study accounts for the major components that were eliminated from previous research studies, such as the boom-point sheave, bucket rigging, and frictional contact with the ground, as well as the accurate prediction of the cutting resistance force. It describes the digging phase using two input variables and the swinging phase using 3 input variables. The dynamic model also contains all structural components of the dragline front-end assembly, and their material and inertia properties not included in previous research studies. The model is built using the new theory of multibody dynamics derived from the Kane's method. This model results in an advanced dynamic model that eliminates the need to solve unnecessary forces and torques, but increases its accuracy to achieve better load predictions. The dynamic model of the dragline is fully capable of producing accurate numerical results of the spatial kinematics and dynamics. The resulting loads can be used with higher confidence to predict stress concentrations in complex construction of wire ropes running on sheaves under static and dynamic loads.

This research study builds on the current body of knowledge and advances the area of modelling and analysis of dragline. This research initiative is a pioneering effort to solve the problems associated with the kinematics and dynamics of dragline ropes and rigging using the advanced theory of dynamics derived from Kane's method. It entails new concepts and original contributions in the area dragline front-end modelling and analyses. This work resolves the pitfalls of previous models in the literature and provides advanced solutions that address structural safety of dragline wire ropes on a long-term basis. This study also advances a rigorous virtual prototype modelling of the dragline and serves as a

good starting point to evaluate the functionality of other machines (rope shovels, backhoe, cranes, and wire-driven robots).

2.6. SUMMARY

The critical literature review covers the current body of knowledge on dragline front-end assembly kinematics and dynamics and the evolution of equipment design and productivity since the early 1920s. A critical assessment is provided to understand this body of knowledge and to highlight the contributions by researchers in the area of dragline machinery. This literature survey defines new frontiers in this research area. Most of the work cited pertain to the dragline availability, performance, utilization, and productivity. Other indicators were also thoroughly addressed and include: (i) kinematics and dynamics of excavators (backhoe, rope shovel, and dragline), (ii) finite element analysis (FEA) of structural components (boom, sheave, rope), and (iii) fatigue analysis of these structures.

A walking dragline is an expensive mining machine and a vital equipment used for stripping overburden in surface mining operations. The effectiveness of this machine requires rigorous kinematics and dynamics analyses to keep it operating at the highest availability and productivity levels. These analyses also provide a real engineering judgement about the functionality of machine components under variable working conditions. This section provided a review of these measures and underscored the effects of wire ropes failure on machine performance.

This PhD research study advances the frontiers of dragline kinematics and dynamics modeling with stress intensity and fatigue analysis for providing new knowledge and a basis for maximizing efficiency, availability, reliability and maintainability of the front-end assembly.

3. COMPUTATIONAL DYNAMICS MODEL OF A DRAGLINE FRONT-END ASSEMBLY

This section deals with the kinematics and dynamics models of a dragline for strip mining operations. Figure 3.1 shows the main research components, which are mainly related to the dragline front-end assembly. The models describe the motions and constraints imposed on the front-end assembly, as well as forces and torques required to perform the digging task and overburden spoiling. Once the dynamic model is formulated, the resulting forces and torques can then be used to simulate real scenarios using a virtual simulator.

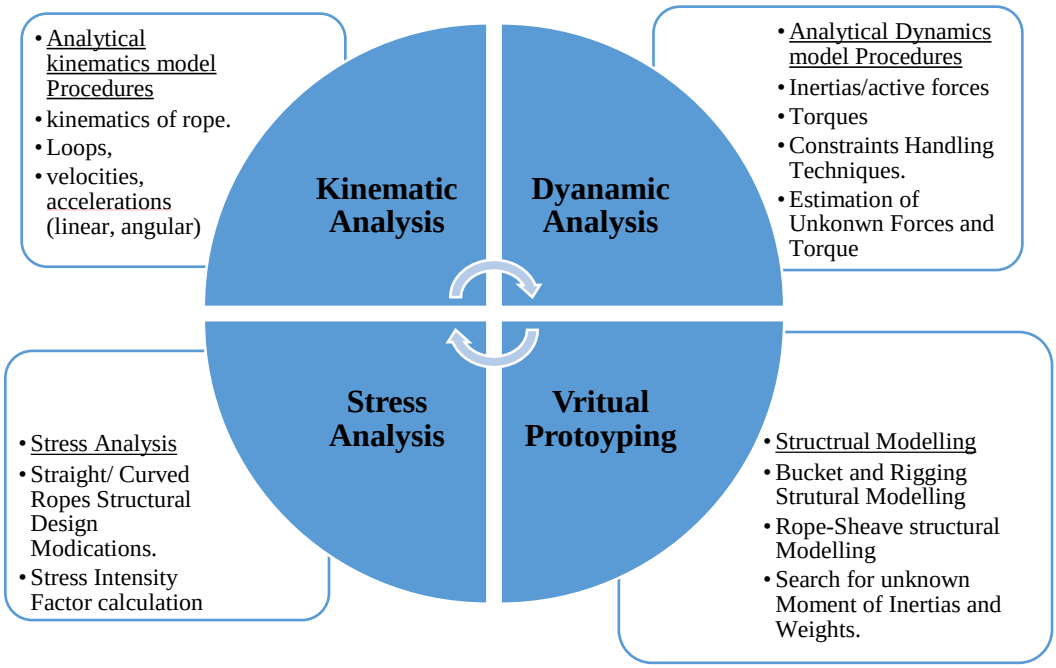

Figure 3.1. PhD research components and flow processes

The virtual simulator contains all the relevant structural components (bucket, chains, ropes, boom, and machine house) that are used to develop the stress fields on any

critical component and estimate its performance. The longevity of the machine parts is estimated from the number of cycles that any structural member can sustain under repeated dynamics loading until failure occurs. The configuration of the dragline vector loop is the most comprehensive one among current models reported in the literature on the dragline machinery. A good understanding of the functionality of each component significantly helps in formulating the kinematics relationships among these components in the inertial reference frame and in a Newtonian reference frame. These analyses form the basis for developing equations of motion of the system under a task of digging in the x-z plane and swinging in the x-y plane (Figure 3.2).

3.1. GEOMETRIC DESCRIPTION OF DRAGLINE MACHINERY

Draglines are massive equipment and vary in size and material excavation capabilities. A dragline equipment contains essential structures to excavate and spoil materials for exposing mineral formations. These structures are mainly the machine house, boom structure, hoist sheave and drag fairlead sheaves, bucket, chains and ropes. An assembly of the boom structure, boom point-sheave, hoist, drag and dump ropes and bucket is called the front-end assembly (Figures 2.1 and 3.2). This combination is a complex design built to control the bucket using hoist and drag ropes only in a 3D operational space. This research contributes to the kinematics and dynamics analysis of this assembly and does not include motions such as propelling of the machine. However, the dragging and swinging motions are developed, which are a major significance of this research in comparison to existing dragline models. The dragline cycle comprises: (i) swinging-back of the machine house with an empty-bucket, (ii) digging by engaging the materials and dragging the bucket into the bank towards the machine, (iii) simultaneous hoisting and

swinging of loaded bucket towards spoiling area, (iv) overburden dumping in the spoil area, and (v) rope reeling-out and swinging simultaneously to reposition the empty bucket in the digging area.

This research study assumes that the dragline machine house and swinging axes are not coincident to permit capturing the significant inertia effects of the machine during swinging. This consideration is very important when developing the dynamics of the front-end assembly, since a loaded bucket weighs hundreds of tons and relatively swings in a short time of about 30 seconds. This study also assumes that machine house, boom structure, chains, and ropes are inextensible and rigid. However, ropes can vary in lengths and inertias to mimic actual motions of the dragline bucket. A complete representation of these components using the vector loop method is shown in Figure 3.2. Constant vectors and angles during the kinematics and dynamic analyses are: (i) machine housing height $\overrightarrow{B_1B_2}$, (ii) boom length ($\overrightarrow{B_2C_1}$) and its orientation (q_2), (iii) boom-sheave interaction represented by vector $\overrightarrow{C_1D^*}$, (iv) the location of bucket, represented by vector ($\overrightarrow{E_1H_1}$), with respect to the center of mass of the dump rope (D^*), and (v) the length of the dump rope, represented by vector ($\overrightarrow{E_1F_1}$). Moreover, ropes are considered as rigid links connected by revolute joints to capture the relative motions among them during the bucket motion.

This representation is required when modelling the hoist rope during digging, as the hoist motor clutch is released to avoid impeding the bucket motion. Hoist, dump, and drag ropes orientations are considered as variables changing with time and are denoted by q_4, q_5 and q_6, respectively. The bucket motion (located at point H_1) over the bank is constrained by a linear motion of the drag rope q_7, its orientation q_6, and a linear motion of the hoist rope q_8 and its orientation q_4. From this vector representation, one can conclude

that the quantities (q_4, q_5, q_6, q_7 and q_8) are numerically related to each other. In other words, there are independent generalized coordinates, such as q_1, q_7 and q_8 and dependent generalized coordinates, such as q_4, q_5 and q_6. The angles are measured from the vertical y-axis and considered positive if the corresponding link rotates clockwise. The directions of vectors that represent the structural elements are arbitrarily chosen from a hinged-point of inward structure toward the center of mass (COM) of outward structure. Their projections in the machine house inertial reference frame (B) guarantee the loop closure.

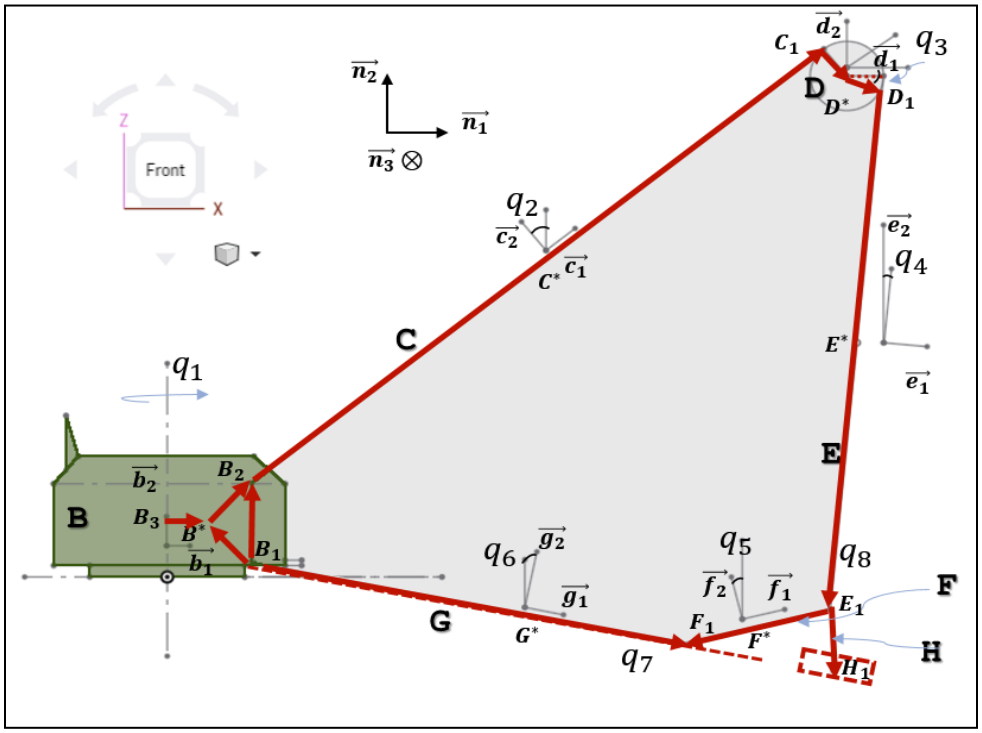

Figure 3.2. Dragline kinematics and its vector loop representation

The configuration of the dragline vector loop is the most comprehensive one among current models reported in the literature on the dragline machinery. A good understanding

of the functionality of each component significantly helps in formulating the kinematics relationships among these components in the inertial reference frame and in a Newtonian reference frame. These analyses form the basis for developing equations of motion of the system under a task of digging in the x-z plane and swinging in the x-y plane (Figure 3.2).

3.2. KINEMATICS OF THE DRAGLINE FRONT-END ASSEMBLY

Kinematics is a prerequisite science for machine dynamics, which deals with system or link motions using vector notation approach. It builds the relationships among positions, velocities, and accelerations of a mechanical system links without regard to the forces or torques causing these motions. Important kinematic parameters in this study are angular velocity of a dragline hoist and drag ropes and their linear displacements in a reference frame. The motion of the dragline bucket is derived from the vector loop method using appropriate kinematics constraints and motion variables related to each element. The dragline bucket slides along the digging face with a defined orientation and digs the materials via a prescribed translational speed ($\dot{q}_7$). The clutch of the hoist rope is released to extend the rope by a translational speed ($\dot{q}_8$). These combined motions dominate the position and trajectory of the bucket being filled through the dragging process. Thus, it is fundamental for the closed loop formulation and subsequent kinematics analysis to take into consideration these characteristics.

The use of vector loop approach results in nonlinear constraints algebraic equations that relate the kinematics quantities (q_1, q_4, q_5, q_6, q_7 and q_8), which are the angular displacement of the machine house and linear and angular displacements of the dragline front-end assembly. The presence of the closed kinematic chain of the front-end assembly also requires that $q_i, (i = 1,..,7)$ are interrelated. It also imposes dependency among the

derivatives of these variables after first and second differentiations. The vector loop method is used to satisfy the kinematics constraints between links and to replace the dependent generalized coordinate $q_5, q_7,$ and $q_8$in terms of q_4 and q_6. Further differentiation of the closed loop equation leads to additional relationships between the derivatives of the independent and dependent generalized velocities. Thus, the kinematic analyses of the dragline front-end assembly can be mainly described using the independent generalized coordinates of q_1, q_4 and q_6 and their time derivatives. The dragline shaking motion q_1, in a vertical axis located in the tub structure, is a given quantity and considered for this model. It can, however, be eliminated from the analysis at any time after developing the kinematics and dynamics models, which greatly simplifies the kinematics and dynamics equations. Torques and forces are transmitted to hoist and drag ropes from points located at the boom-point sheave (D) and point B_2 located in the machine house, respectively.

The definition of measures of vector components of all bodies involved in the front-end assembly and their COM leads to the constraint equations (3.1), (3.2) and (3.3).

$$\left(\overrightarrow{B_1B_2} + \overrightarrow{B_2C_1} + \overrightarrow{C_1D^*} + \overrightarrow{D^*D_1} + \overrightarrow{D_1E_1} + \overrightarrow{E_1F_1} + \overrightarrow{F_1B_1}\right).\overrightarrow{b_1} = 0 \quad (3.1)$$

$$\left(\overrightarrow{B_1B_2} + \overrightarrow{B_2C_1} + \overrightarrow{C_1D^*} + \overrightarrow{D^*D_1} + \overrightarrow{D_1E_1} + \overrightarrow{E_1F_1} + \overrightarrow{F_1B_1}\right).\overrightarrow{b_2} = 0 \quad (3.2)$$

$$\left(\overrightarrow{B_1B^*} + \overrightarrow{B^*B_2} + \overrightarrow{B_2C^*} + \overrightarrow{C^*C_1} + \overrightarrow{C_1D^*} + \overrightarrow{D^*D_1} + \overrightarrow{D_1E^*} + \overrightarrow{E^*E_1} + \overrightarrow{E_1F_1}\right).\overrightarrow{g_1} = q_7 \quad (3.3)$$

One is required to define measures of vector components of all bodies involved in the front assembly. The scalar values of each element and its relevant orientation after introducing the trigonometric abbreviations $\mathrm{s} = \mathrm{Sin}$ and $\mathrm{s} = \mathrm{Cos}$ are given in Tables 3.1 and 3.2. Thus, the equations (3.1) and (3.2) are rewritten as equations (3.4) and (3.5).

$$(L_5 + L_6)c_2 + L_7 s_2 + L_8 c_4 - q_8 s_4 - (L_9 + L_{10})c_5 - q_7 c_6 = 0 \qquad (3.4)$$

$$L_0 + (L_5 + L_6)s_2 - L_7 c_2 - L_8 s_4 + q_8 c_4 - (L_9 + L_{10})s_5 + q_7 s_6 = 0 \qquad (3.5)$$

Projecting equation (3.3) of the drag rope's linear displacement in the machine reference frame (b) yields equations (3.6) and (3.7).

$$-(L_5 + L_6)c_2 + L_7 s_2 - L_8 c_4 - q_8 s_4 + (L_9 + L_{10})c_5 = q_7\, c_6 \qquad (3.6)$$

$$L_0 - (L_5 + L_6)s_2 - L_7 c_2 + L_8 s_4 - q_8 c_4 + (L_9 + L_{10})s_5 = q_7 s_6 \qquad (3.7)$$

Equations (3.6) and (3.7) can be further manipulated to formulate a function of q_7 in terms of other variables q_4, q_5 and q_8. The inclination angle q_5 of the dump rope is considered as a dependent generalized coordinate and unknown. However, it can be derived using the loop closure equations. The vector representation of the hoist rope-sheave interactions provides a way to deduce the angular displacement of the sheave $q_3$in terms of q_4. For this analysis, it is noticed that the orientations of the sheave-radius vector $\overrightarrow{C_1 D^*}$ is constant and measures q_2. It is also observed that the sheave radius vector $\overrightarrow{D^* D_1}$ makes an angle q_3 with a horizontal x-axis and its value equals q_4. These observations are considered in the kinematics analysis and greatly simplify the kinematic functions.

Table 3.1. Vector notation of closed loop of dragline front-end assembly

$L_0 = \overrightarrow{B_1 B_2}.\overrightarrow{b_2}$	$L_4 = \overrightarrow{B^* B_2}.\overrightarrow{b_2}$	$L_8 = \overrightarrow{D^* D_1}.\overrightarrow{e_1}$	$L_{12} = \overrightarrow{F^* H_1}.\overrightarrow{f_1}$
$L_1 = \overrightarrow{B^* B_1}.\overrightarrow{b_1}$	$L_5 = -\overrightarrow{C^* B_2}.\overrightarrow{c_1}$	$L_9 = \overrightarrow{F^* E_1}.\overrightarrow{f_1}$	$L_{13} = -\overrightarrow{F^* H_1}.\overrightarrow{f_2}$
$L_2 = -\overrightarrow{B^* B_1}.\overrightarrow{b_2}$	$L_6 = \overrightarrow{C^* C_1}.\overrightarrow{c_1}$	$L_{10} = -\overrightarrow{F^* F_1}.\overrightarrow{f_1}$	$q_7 = \overrightarrow{B_1 F_1}.\overrightarrow{g_1}$
$L_3 = \overrightarrow{B^* B_2}.\overrightarrow{b_1}$	$L_7 = \overrightarrow{D^* C_1}.\overrightarrow{c_2}$	$L_{11} = \overrightarrow{B_3 B^*}.\overrightarrow{b_1}$	$q_8 = \overrightarrow{E_1 D_1}.\overrightarrow{e_2}$

The current kinematic equations are derived when the dragline machine house has already made the required rotation $q_1.\vec{b}_2$ in order to engage the bank and start excavating the materials. Thus, the transformation matrices, in Table 3.2, provide the orientation of machine house position vectors and other vectors related to the remaining components.

Table 3.2. Transformation matrices of the front-end assembly

	$\vec{b}_1$	$\vec{b}_2$	$\vec{b}_3$
n_1	c_1	0	s_1
n_2	0	1	0
n_3	$-s_1$	0	c_1

	$\vec{c}_1$	$\vec{c}_2$	$\vec{c}_3$
$\vec{b}_1$	c_2	$-s_2$	0
$\vec{b}_2$	s_2	c_2	0
$\vec{b}_3$	0	0	1

	$\vec{d}_1$	$\vec{d}_2$	$\vec{d}_3$
$\vec{b}_1$	c_3	s_3	0
$\vec{b}_2$	$-s_3$	c_3	0
$\vec{b}_3$	0	0	1

	$\vec{e}_1$	$\vec{e}_2$	$\vec{e}_3$
$\vec{b}_1$	c_4	s_4	0
$\vec{b}_2$	$-s_4$	c_4	0
$\vec{b}_3$	0	0	1

	$\vec{f}_1$	$\vec{f}_2$	$\vec{f}_3$
$\vec{b}_1$	c_5	$-s_5$	0
$\vec{b}_2$	s_5	c_5	0
$\vec{b}_3$	0	0	1

	$\vec{g}_1$	$\vec{g}_2$	$\vec{g}_3$
$\vec{b}_1$	c_6	s_6	0
$\vec{b}_2$	$-s_6$	c_6	0
$\vec{b}_3$	0	0	1

3.2.1. Kinematics Constraint Equations. A conventional procedure to relate the velocities of links together is to derive the configuration constraint equations. In this research, the kinematics is developed using the concept of generalized speeds (Kane and Levinson, 1985). The definition of generalized speed allows the description of the system

motion rather than its configurations. The concept of generalized speeds is used in order to facilitate the mathematical description and to solve equations of motion for multibody dynamics of the front-end assembly. Kane's method (Kane and Levinson, 1985) is used to formulate the equations of motion using 40 generalized speeds u_r ($r = 1,..,40$). The method becomes evidently advantageous when a system has several rigid bodies that their configurations, angular velocities, and velocities of their particles can be grouped as equation (3.8).

$$u_r = \sum_{s=1}^{n} Y_{rs}\,\dot{q}_s + Z_r \text{ (r=1…n)} \tag{3.8}$$

Y_{rs} and Z_r are functions of q_1,…: q_n and time t. q_s is the s[th] generalized coordinates. Y_{rs} represents a matrix, the number of rows of which is equal to the number of the generalized speeds and the number of columns represents the number of generalized coordinates q_s. To find $\dot{q}_s$ in terms of generalized speeds u_r, Y_{rs} must be invertible, nonsingular, square matrix, and is given in equation (3.9).

$$\dot{q}_s = \sum_{s=1}^{n} Y_{rs}^{-1}\,(u_r - z_r) \tag{3.9}$$

Equation (3.9) allows the definition of the derivatives of the generalized coordinates of hoist, dump, and drag ropes angular displacements in terms of known generalized quantities ($\dot{q}_7$ and $\dot{q}_8$).

This research defines generalized speeds as angular velocities and velocities of the center of gravity associated with unit vectors and parallel to the central principal axes in each body. Thus, one can now write the angular velocity ω^k of body k, with k = B, C… H, as defined by equation (3.10).

$$\begin{aligned}
\omega^{B} &= u_1\overrightarrow{b_2} \\
\omega^{C} &= u_5\overrightarrow{c_1} + u_6\overrightarrow{c_2} + u_7\overrightarrow{c_3} \\
\omega^{D} &= u_{11}\overrightarrow{d_1} + u_{12}\overrightarrow{d_2} + u_{13}\overrightarrow{d_3} \\
\omega^{E} &= u_{17}\overrightarrow{e_1} + u_{18}\overrightarrow{e_2} + u_{19}\overrightarrow{e_3} \\
\omega^{F} &= u_{23}\overrightarrow{f_1} + u_{24}\overrightarrow{f_2} + u_{25}\overrightarrow{f_3} \\
\omega^{G} &= u_{29}\overrightarrow{g_1} + u_{30}\overrightarrow{g_2} + u_{31}\overrightarrow{g_3} \\
\omega^{F_1} &= u_{38}\overrightarrow{g_1} + u_{39}\overrightarrow{g_2} + u_{40}\overrightarrow{g_3}
\end{aligned} \tag{3.10}$$

The velocity v^{k*} of center of mass of each body (K) are computed by equation (3.11).

$$\begin{aligned}
v^{B^*} &= u_2\overrightarrow{b_1} + u_3\overrightarrow{b_2} + u_4\overrightarrow{b_3} \\
v^{C^*} &= u_8\overrightarrow{c_1} + u_9\overrightarrow{c_2} + u_{10}\overrightarrow{c_3} \\
v^{D^*} &= u_{14}\overrightarrow{d_1} + u_{15}\overrightarrow{d_2} + u_{16}\overrightarrow{d_3} \\
v^{E^*} &= u_{20}\overrightarrow{e_1} + u_{21}\overrightarrow{e_2} + u_{22}\overrightarrow{e_3} \\
v^{F^*} &= u_{26}\overrightarrow{f_1} + u_{27}\overrightarrow{f_2} + u_{28}\overrightarrow{f_3} \\
v^{G^*} &= u_{32}\overrightarrow{g_1} + u_{33}\overrightarrow{g_2} + u_{34}\overrightarrow{g_3} \\
v^{H_1} &= u_{35}\overrightarrow{f_1} + u_{36}\overrightarrow{f_2} + u_{37}\overrightarrow{f_3}
\end{aligned} \tag{3.11}$$

To establish the relationships between the generalized speeds u_r and the generalized coordinates, the constraints motion equations of every element are developed using the golden rule for vector differentiation as defined in equations (3.12).

$$v^{C^*} = \frac{{}^{C}d\vec{r}^{\,B_2C}}{dt} + {}^{B}\omega^{C} \times \vec{r}^{B_2C} \tag{3.12}$$

Thus, the left term of the right hand side of equation (3.12) gives the variation of the position vector of the COM of the boom (C) in its local frame. This variation is zero since the boom is assumed as a rigid body. The second term gives the projection of this vector based on the angular variation of reference frame associated with the same body. If

the dragline is engaged in digging activities, this component vanishes and reappears when swinging from the bank to the spoil area. The COM of machine housing B^* and the rotational axis ($\overrightarrow{n_2}$) are not coincident, but are spaced by a vector position $\overrightarrow{B^*B_3}$. Thus, its velocity in the reference frame (B) is given by equation (3.13).

$$\overrightarrow{v^{B^*}} = {}^{N}\omega^{B} \times \overrightarrow{B_3B^*} \tag{3.13}$$

$$= u_1\overrightarrow{b_2} \times \left(L_{11}\overrightarrow{b_1}\right)$$

$$\overrightarrow{v^{B^*}} = -L_{11}u_1\overrightarrow{b_3} \tag{3.14}$$

The estimation of the generalized speeds u_3 and u_4 is done by comparing equation (3.14) to the velocity vector $\overrightarrow{v^{B^*}}$ defined in equation (3.11). One can deduce that $u_3 = u_4 = 0$, and this analogy is used to produce values of other dependent generalized speeds in the system kinematics. Based on system constraint motion, the boom structure (C) does not rotate relative to B and ${}^{B}\omega^{C} = 0$. Thus, $u_7 = 0$ and the velocity of the boom ω^C equals ω^B. The search for generalized speeds u_5 and u_6 is done by transferring ω^C from a reference frame associated with the machine house (B) to its local reference frame. This yields u_5 and u_6 as defined in equation (3.15).

$$\omega^C = \omega^A + {}^{B}\omega^{C}$$

$$= u_1\overrightarrow{b_2} + u_7\overrightarrow{c_3}$$

$$u_5\overrightarrow{c_1} + u_6\overrightarrow{c_2} = s_2u_1\overrightarrow{c_1} + c_2u_1\overrightarrow{c_2} \tag{3.15}$$

The velocity of COM of the boom in a Newtonian reference frame is provided by equation (3.16).

$$\overrightarrow{v^{C^*}} = v^{B_2} + \omega^C \times \left(\overrightarrow{B^*B_2} + \overrightarrow{B_2C^*}\right)$$

$$= v^{B^*} + \omega^B \times \left(\overrightarrow{B_2B^*}\right) + \omega^C \times \left(\overrightarrow{B^*B_2} + \overrightarrow{B_2C^*}\right)$$

$$= -(L_{11} + L_3 + L_5c_2)u_1.\overrightarrow{c_3} \tag{3.16}$$

The angular velocity and linear velocity of the boom point sheave is defined by equations (3.17) and (3.18), respectively.

$$\omega^D = \omega^B + {}^B\omega^C + {}^C\omega^D$$

$$= u_1\left(-s_4\overrightarrow{d_1} + c_4\overrightarrow{d_2}\right) + \dot{q}_4\overrightarrow{d_3} \tag{3.17}$$

$$v^{D^*} = v^{B^*} + \omega^D \times \left(\overrightarrow{B^*B_2} + \overrightarrow{B_2C^*} + \overrightarrow{C^*C_1} + \overrightarrow{C_1D^*}\right)$$

$$= -(L_3 + c_2(L_5 + L_6) + L_7s_2 + L_{11})u_1 \tag{3.18}$$

The velocity of the point D_1 of the hoist rope from the boom point sheave is required for calculating the linear velocity of its COM in a local reference frame (E). The resulting linear velocity v^{E^*} of the hoist rope and its angular velocities are given in equations (3.20) and (3.21).

$$v^{D_1} = L_8u_{13}\overrightarrow{d_2} - (L_3 + c_2(L_5 + L_6) + s_2L_7 + L_8 + L_{11})u_1\overrightarrow{d_3} \tag{3.19}$$

$$v^{E^*} = v^{D_1} + \omega^E \times \overrightarrow{D_1E^*}$$

$$= 0.5q_8u_{19}\overrightarrow{e_1} + L_8u_{13}\overrightarrow{e_2} - (L_3 + c_2(L_5 + L_6) + s_2\,L_7 + L_8 + L_{11})u_1\overrightarrow{e_3} \tag{3.20}$$

$$\omega^E = \omega^B + {}^B\omega^C + {}^C\omega^D + {}^D\omega^E$$

$$= u_1(-s_4\overrightarrow{e_1} + c_4\overrightarrow{e_2}) + \dot{q}_4\overrightarrow{e_3} \tag{3.21}$$

Equation (3.20) accounts for the variation of the length of the hoist rope, which is defined by the linear displacement input q_8. Equations (3.20) and (3.21) also define the

unknown generalized speeds $u_{17}, u_{18}, u_{19}, u_{20}, u_{21}$, and u_{22}. Point E_1 represents a revolute joint between the hoist rope and the rigging system. It is required to find its absolute linear velocity in order to find the linear velocity of the COM of the dump rope $\overrightarrow{E_1F_1}$, and is given in equation (3.22). c_{45} and s_{45} are trigonometric abbreviation of $\mathrm{Cos}(q_4 + q_5)$ and $\mathrm{Sin}(q_4 + q_5)$.

$$\begin{aligned} v^{E_1} &= v^{E^*} + \omega^E \times \overrightarrow{E^*E_1} \\ &= (c_{45}q_8 + L_8 s_{45})u_{19}\overrightarrow{e_1} + (c_{45}L_8 - q_8 s_{45})u_{19}\overrightarrow{e_2} - \\ &\quad (L_3 + c_2(L_5 + L_6) + L_8 + L_{11} + L_7 s_2)u_1\overrightarrow{e_3} \end{aligned} \tag{3.22}$$

The linear and angular velocities of the dump rope can now be estimated and provided in equations (3.23) and (3.24), respectively.

$$\begin{aligned} v^{F^*} &= v^{E_1} + \omega^F \times \overrightarrow{E_1F^*} = v^{F_1} + \omega^F \times \overrightarrow{F_1F^*} \\ &= (c_{45}q_8 + L_8 s_{45})u_{19}\,\overrightarrow{f_1} + (c_{45}L_8 - q_8 s_{45})u_{19} - L_9 u_{25})\,\overrightarrow{f_2} + (L_9 - L_3 + \\ &\quad c_2(L_5 + L_6) + L_8 + L_{11} + L_7 s_2)u_1\overrightarrow{f_3} \end{aligned} \tag{3.23}$$

$$\omega^F = \omega^B + {}^B\omega^F = u_1\overrightarrow{b_2} + \dot{q}_5\overrightarrow{f_3} = u_1\left(s_5\overrightarrow{f_1} + c_5\overrightarrow{f_2}\right) + \dot{q}_5\overrightarrow{f_3} \tag{3.24}$$

The generalized speed u_{25} is just the angular velocity of the dump rope and it takes another notation $\dot{q}_5$, which is the first derivative of the dump rope angular displacement. It is an unknown quantity and it imposes a great challenge when solving the dynamics of the dragline. This fact led several research studies on the dragline dynamics to omit this link and model the complete rigging system as a point mass. The linear and angular velocities of the COM of the drag rope are shown in equations (3.25) and (3.26), respectively.

$$v^{G^*} = v^{B^*} + \omega^G \times \left(\overrightarrow{B^*B_1} + \overrightarrow{B_1G^*}\right)$$

$$= 0.5q_7u_{31}\overrightarrow{g_2} + (L_1 + L_{11} + 0.5q_7)u_1\overrightarrow{g_3} \quad (3.25)$$

$$\omega^G = \omega^B + {}^B\omega^C = u_1\overrightarrow{b_2} + \dot{q}_6\overrightarrow{g_3} = u_1(-s_6\overrightarrow{g_1} + c_6\overrightarrow{g_2}) + u_{31}\overrightarrow{g_3} \quad (3.26)$$

The bucket is modelled as a point mass $H_1$and is rigidly attached to the hoist chain $\overrightarrow{E_1H_1}$. The absolute velocity of the bucket is calculated in equations (3.27).

$$v^{H_1} = v^{F^*} + \omega^F \times \overrightarrow{F^*H_1}$$

$$= ((c_{45}q_8 + L_8s_{45})u_{19} + L_{13}u_{25})\overrightarrow{f_1} + ((c_{45}L_8 - q_8s_{45})u_{19} + (-L_9 + L_{12})u_{25})\overrightarrow{f_2} - (L_3 + c_2(L_5 + L_6) + L_8 - L_9 + L_{11} + L_{12} + L_7s_2)u_1\overrightarrow{f_3} \quad (3.27)$$

From equation (3.27), it is evident that the motion of the bucket is controlled by the linear displacement of the hoist rope q_8, its angular velocity u_{19}, and the angular velocity of the dump rope. The value of the angular speed of machine house u_1 is zero during the digging motion and can be dropped from the analysis. However, it must appear in the calculations when the dragline bucket is lifted off the bank, where a rotational torque is provided to the front-end assembly, to dump the materials on the spoil area. The drag chain velocity, denoted by v^{F_1}, is also used to facilitate the determination of the relationships between the unknown generalized speeds, and it is given by equation (3.28).

$$v^{F_1} = \dot{q}_7\overrightarrow{g_1} + q_7u_{31}\overrightarrow{g_2} - (L_1 + L_{11} + q_7)u_1\overrightarrow{g_3} \quad (3.28)$$

Equations (3.13) and (3.28) provide a basis for estimating the values of the remaining unknown generalized speeds, as defined in equations (3.10) and (3.11). With appropriate manipulations, these kinematics quantities are sought after using a vector

approach that defines the velocity of a joint with respect to two links located in two adjacent reference frames. An example of this idea is provided in equations (3.29) and (3.30).

$$v^{E_1} = v^{E^*} + \omega^E \times \overrightarrow{E^*E_1} = v^{F^*} + \omega^F \times \overrightarrow{F^*E_1}$$

$$= u_{20}\overrightarrow{e_1} + u_{21}\overrightarrow{e_2} + u_{22}\overrightarrow{e_{13}} + (u_{17}\overrightarrow{e_1} + u_{18}\overrightarrow{e_2} + u_{19}\overrightarrow{e_3}) \times (0.5\, q_8.\overrightarrow{e_2}) \quad (3.29)$$

$$v^{E_1} = u_{26}\overrightarrow{f_1} + u_{27}\overrightarrow{f_2} + u_{28}\overrightarrow{f_3} + \left(u_{23}\overrightarrow{f_1} + u_{24}\overrightarrow{f_2} + u_{25}\overrightarrow{f_3}\right) \times \left(L_9.\overrightarrow{f_1}\right) \quad (3.30)$$

Table 3.3. Dependent generalized speeds as functions of independent ones

$u_2 = u_3 = 0$	$u_{23} = s_6 u_1$
$u_4 = -L_{11} u_1$	$u_{24} = c_5 u_1$
$u_5 = s_2 u_1$	$u_{25} = \dot{q}_5$
$u_6 = c_2 u_1$	$u_{26} = (c_{45} q_8 + L_8 s_{45}) u_{19}$
$u_7 = 0$	$u_{27} = (c_{45} L_8 - q_8 s_{45}) u_{19} - L_9 u_{25}$
$u_8 = u_9 = 0$	$u_{28} = L_9 u_1 - (L_3 + c_2(L_5 + L_6) + L_8 + L_{11} + L_7 s_2) u_1$
$u_{10} = -(L_3 + c_2 L_5 + L_{11}) u_1$	$u_{29} = -s_6 u_1$
$u_{11} = -s_4 u_1$	$u_{30} = c_6 u_1$
$u_{12} = c_4 u_1$	$u_{31} = \dot{q}_6$
$u_{13} = u_{19} = \dot{q}_4$	$u_{32} = 0$
$u_{14} = u_{15} = 0$	$u_{33} = 0.5 q_7 u_{31}$
$u_{16} = -(L_3 + c_2(L_5 + L_6) + L_{11} + L_7 s_2) u_1$	$u_{34} = -(L_1 + L_{11} + 0.5 q_7) u_1$
$u_{17} = -s_4 u_1$	$u_{35} = (c_{45} q_8 + L_8 s_{45}) u_{19} + L_{19} u_{25}$
$u_{18} = c_4 u_1$	$u_{36} = (c_{45} L_8 - q_8 s_{45}) u_{19} + (-L_9 + L_{12}) u_{25}$
$u_{19} = \dot{q}_4$	$u_{37} = -(L_3 + c_2(L_5 + L_6) + L_8 - L_9 + L_{11} + L_{12} + L_7 s_2) u_1$
$u_{20} = 0.5 q_8 u_{19}$	$u_{38} = \dot{q}_7$
$u_{21} = 0$	$u_{39} = q_7 u_{31}$
$u_{22} = -(L_3 + c_2(L_5 + L_6) + L_8 + L_{11} + L_7 s_2) u_1$	$u_{40} = -(L_1 + L_{11} + q_7) u_1$

The approach used in equations (3.29) and (3.30) is applied to establish relationships among the dependent and independent generalized speeds. The resulting generalized speeds of the entire front-end assembly are provided in Table 3.3. Some generalized speeds listed in Table 3.3 still contain unknown kinematics entities like the derivatives of generalized coordinates $\dot{q}_4$, $\dot{q}_5$, and $\dot{q}_6$. Thus, further refinement is needed to express these functions in terms of $\dot{q}_7$, and $\dot{q}_8$. Section 4 provides a systematic approach to handle these kinematics constraints based on the constraint equations (3.4) and (3.5) and their time derivatives.

3.2.2. Nonholonomic System and its Partial Velocities. Vector loop method in Section 3.1 allows the system to be described by quantities $q_i, (i = 1, \dots 8)$ and only requires $q_1, q_4, q_5, q_6, q_7,$ and q_8 to define its configuration. Thus, six generalized coordinates are needed. However, forty generalized speeds, u_r $(r = 1, 2, \dots 40)$, are required to define its motion, as defined in equations (3.10) and (3.11). It was also concluded that these speeds are not independent of each other; three of them are chosen as independent generalized speeds to control the motion. The remaining speeds are represented in terms of these independent generalized speeds. In other words, there are thirty seven motion constraints ($m = 37$), which are expressed as linear combinations of one or more independent generalized speeds.

Finally, the degrees of freedom of the system (P), $n - m = 40 - 37 = 3$, are three independent generalized speeds. The m equations are called non-holonomic constraint equations. The word “nonholonomic” refers to a constraint equation that can be expressed in a form such as provided in equation (3.31). In other words, equation (3.31) is

nonintegrable and its differentiation also yields a nonholonomic differential equation (Kane, 1968).

$$f(q_1, q_2, .., q_n, \dot{q}_1, \dot{q}_2, .., \dot{q}_n, t) \neq 0 \tag{3.31}$$

The use of Kane's method, in developing equations of motion of the dragline, relies on defining other expressions of angular velocity ω^k and linear velocity v^k vectors. These expressions use the independent generalized speeds u_r $(r = 1,2,3)$ explicitly and they are given in equations (3.32) and (3.33) (Kane and Levinson, 1985).

$$\omega^k = \sum_{r=1}^{p} \tilde{\omega}_r \, u_r + \tilde{\omega}_t \qquad \text{(K=A,…E)} \tag{3.32}$$

$$v^k = \sum_{r=1}^{p} \tilde{v}_r \, u_r + \tilde{v}_t \tag{3.33}$$

$\tilde{v}_r$, $\tilde{\omega}_r$ $(r = 1, \dots p)$ are called the rth nonholonomic partial velocity and nonholonomic partial angular velocity vectors. $\tilde{\omega}_t$ and $\tilde{v}_t$ are functions of q_1,… q_n and t, along with $\tilde{v}_r$ and $\tilde{\omega}_r$, $(r = 1, 19, 31)$. Comparing equations (3.32) and (3.33) of every link with its linear and angular velocities vectors, defined in equations (3.10) and (3.11), along with kinematics constraint equations (in Table 3.3), allows the construction of the partial velocities, $\tilde{v}^r$ and $\tilde{\omega}_r$. These partial velocities (in Table 3.4) play a central role in developing the dynamics equations based on Kane's method.

Finding the time derivative of angular displacement of the dump rope u_{25}, based on the vector loop equations (3.5) and (3.6), is the only way to estimate the quantity Z_1. However, u_{25} and Z_1 are given by equation (3.34) and equation (3.35) and their detailed derivation is given in the Appendix A.

Table 3.4. Partial velocities and partial angular velocities of COM of links

	r = 1	r = 19	r = 31
$\widetilde{\omega}_r^B$	$\overrightarrow{b_2}$	0	0
$\tilde{v}_r^{B^*}$	$-L_{11}\overrightarrow{b_3}$	0	0
$\widetilde{\omega}_r^C$	$s_2\overrightarrow{c_1} + c_2\overrightarrow{c_2}$	0	0
$\tilde{v}_r^{C^*}$	$-(L_3 + c_2L_5 + L_{11})\overrightarrow{c_3}$	0	0
$\widetilde{\omega}_r^D$	$-s_4\overrightarrow{d_1} + c_4\overrightarrow{d_2}$	$\overrightarrow{d_3}$	0
$\tilde{v}_r^{D^*}$	$-(L_3 + c_2(L_5 + L_6) + L_{11} + L_7s_2)\overrightarrow{d_3}$	0	0
$\widetilde{\omega}_r^E$	$-s_4\overrightarrow{e_1} + c_4\overrightarrow{e_2}$	$\overrightarrow{e_3}$	0
$\tilde{v}_r^{E^*}$	$-(L_3 + c_2(L_5 + L_6) + L_8 + L_{11} + L_7s_2)\overrightarrow{e_3}$	$0.5\ q_8\overrightarrow{e_1}$	0
$\widetilde{\omega}_r^F$	$s_5\overrightarrow{f_1} + c_5\overrightarrow{f_2}$	$Z_1\overrightarrow{f_3}$	0
$\tilde{v}_r^{F^*}$	$L_9u_1 - (L_3 + c_2(L_5 + L_6) + L_8 + L_{11} + L_7s_2)\overrightarrow{f_3}$	$Z_2\overrightarrow{f_1} + Z_3\overrightarrow{f_2}$	0
$\widetilde{\omega}_r^G$	$-s_6\overrightarrow{g_1} + c_6\overrightarrow{g_2}$	0	$\overrightarrow{g_3}$
$\tilde{v}_r^{G^*}$	$-(L_1 + L_{11} + 0.5q_7)\overrightarrow{g_3}$	0	$0.5q_7\overrightarrow{g_2}$
$\tilde{v}_r^{F_1}$	$-(L_1 + L_{11} + q_7)\overrightarrow{g_3}$	0	$q_7\overrightarrow{g_2}$
$\tilde{v}_r^{H_1}$	$-(L_3 + c_2(L_5 + L_6) + L_8 - L_9 + L_{11} + L_{12} + L_7s_2)\overrightarrow{f_3}$	$Z_4\overrightarrow{f_1} + Z_5\overrightarrow{f_2}$	0

$$u_{25} = \frac{(q_8(-c_{24}(L_5+L_6)+c_{45}(L_9+L_{10})-L_0s_4+L_7s_{24})+L_8(-c_4L_0+c_{24}L_7+(L_5+L_6)s_{24}-(L_9+L_{10})s_{45}))}{(L_9+L_{10})(c_5L_0-c_{25}L_7-c_{45}q_8-(L_5+L_6)s_{25}+L_8s_{45})}u_{19} +$$

$$\frac{q_7\dot{q}_7+(c_4L_0-c_{24}L_7-q_8-(L_5+L_6)s_{24}+(L_9+L_{10})s_{45})q_8\dot{q}_8}{(L_9+L_{10})(c_5L_0-c_{25}L_7-c_{45}q_8-(L_5+L_6)s_{25}+L_8s_{45})} \quad (3.34)$$

$$Z_1 = \frac{q_8(-c_{24}(L_5+L_6)+c_{45}(L_9+L_{10})-L_0s_4+L_7s_{24})+L_8(-c_4L_0+c_{24}L_7+(L_5+L_6)s_{24}-(L_9+L_{10})s_{45})}{(L_9+L_{10})(c_5L_0-c_{25}L_7-c_{45}q_8-(L_5+L_6)s_{25}+L_8s_{45})} \quad (3.35)$$

Equation (3.36) is the linear velocity of the dump rope in terms of its nonholonomic partial linear velocities. It is used to establish the unknown quantities Z_2 and Z_3 as shown in equations (3.37). Their derivation is given in equations (3.38) and (3.39).

$$\tilde{v}_r^{F^*} = \tilde{v}_1^{F^*} u_1 + \tilde{v}_{19}^{F^*} u_{19} + \tilde{v}_{31}^{F^*} u_{31} \tag{3.36}$$

$$u_{26}\overrightarrow{f_1} + u_{27}\overrightarrow{f_2} + u_{28}\overrightarrow{f_3} = (c_{45}q_8 + L_8 s_{45})u_{19}\overrightarrow{f_1} + ((c_{45}L_8 - q_8 s_{45})u_{19} - L_9 u_{25})\overrightarrow{f_2} + (L_9 - (L_3 + c_2(L_5 + L_6) + L_8 + L_{11} + L_7 s_2))u_1\overrightarrow{f_3} \tag{3.37}$$

After substituting u_{25} of equation (3.34) into equation (3.37) and regrouping terms of u_{19}, one finds Z_2 and Z_3, as given in equation (3.38). Z_4 and Z_5 are also used to find the partial velocities of the bucket motion. Their components reflect the complex nonlinear motion behavior during the digging operation and material loading.

$$Z_2 = (c_{45}q_8 + L_8 s_{45}),\ Z_3 = ((c_{45}L_8 - q_8 s_{45}) - L_9\, Z_1) \tag{3.38}$$

$$Z_4 = (c_{45}q_8 + L_8 s_{45} + L_{13} Z_1)\ ,\ Z_5 = (c_{45}L_8 - q_8 s_{45}) + (-L_9 + L_{12})\, Z_1 \tag{3.39}$$

3.2.3. Linear and Angular Accelerations. Equations (3.13-3.30) contain needed linear and angular velocities of all components in the dragline front-end loop and they are used to find the linear and angular acceleration vectors. By differentiating the velocity vector, the resulting acceleration equations are provided in Appendix A. It is important to keep the generalized speeds in explicit evidence during the derivation. The angular accelerations and acceleration of COM points B^*, C^*, … G^*, and H_1 are calculated based on equation (3.40 and 3.41) along with equations (3.10) and (3.11).

$$a^P = \frac{K_d \vec{v}^P}{dt} + \vec{\omega}^K \times \vec{v}^P \tag{3.40}$$

$$\alpha^P = \frac{K_d \vec{\omega}^P}{dt} \tag{3.41}$$

Thus, the left term of the right hand side of equation (3.40) gives the variation of the velocity of a point p in its local frame and the second term gives the projection of

velocity vector based on the angular variation of the reference frame associated with the same body. The angular velocity and the velocity of each body center of mass, taken in their local reference frame, make the derivation of its acceleration a straightforward procedure. At the end, one is required to keep the first derivative of each generalized speed in an explicit form as it will be replaced by the derivative of the corresponding independent generalized speed. The linear acceleration equations of the whole multibody system of the dragline front-end assembly are provided in equation (3.42) and their detailed derivations are provided in the Appendix A.

$$\begin{aligned}
a^{B^*} &= \frac{{}^{B_d}\vec{v}^{B^*}}{dt} + \vec{\omega}^{B} \times \vec{v}^{B^*} \\
a^{C^*} &= \frac{{}^{B_d}\vec{v}^{C^*}}{dt} + \vec{\omega}^{C} \times \vec{v}^{C^*} \\
a^{D^*} &= \frac{{}^{B_d}\vec{v}^{D^*}}{dt} + \vec{\omega}^{D} \times \vec{v}^{D^*} \\
a^{E^*} &= \frac{{}^{B_d}\vec{v}^{E^*}}{dt} + \vec{\omega}^{E} \times \vec{v}^{E^*} \\
a^{F^*} &= \frac{{}^{B_d}\vec{v}^{F^*}}{dt} + \vec{\omega}^{F} \times \vec{v}^{F^*} \\
a^{G^*} &= \frac{{}^{B_d}\vec{v}^{G^*}}{dt} + \vec{\omega}^{G} \times \vec{v}^{G^*} \\
a^{H_1} &= \frac{{}^{B_d}\vec{v}^{H_1}}{dt} + \vec{\omega}^{F} \times \vec{v}^{\,H_1} \\
a^{F_1} &= \frac{{}^{B_d}\vec{v}^{F_1}}{dt} + \vec{\omega}^{G} \times \vec{v}^{\,F_1}
\end{aligned} \qquad (3.42)$$

The acceleration of the bucket COM is taken in a local reference frame (F) associated with the rigging system. The bucket is assumed to be rigidly connected to the drag rope at point E_1 during the excavation process. This means the bucket position and its orientation, with respect to the drag rope, does not change during the digging. This assumption is acceptable based on the observation of the positions variations of both bucket

and dump rope in a real digging cycle of a dragline. Another key point is that the COM acceleration of the drag chain $\vec{a}^{F_1}$ changes in a reference frame (G) associated with the drag rope, as seen in the last part of equation (3.42).

The angular accelerations of every component of the front-end assembly are given by equation (3.43) after a direct differentiation of their correspondent angular velocity vectors.

$$
\begin{aligned}
{N\alpha}^{B} &= \dot{u}_1\,\overrightarrow{b_2} \\
{N\alpha}^{C} &= s_2\,\dot{u}_1\overrightarrow{c_1} + c_2\,\dot{u}_1\,\overrightarrow{c_2} \\
{N\alpha}^{D} &= (-c_4u_1u_{19} - s_4\dot{u}_1)\overrightarrow{d_1} + (-s_4u_1u_{19} + c_4\dot{u}_1)\overrightarrow{d_2} + \dot{u}_{19}\,\overrightarrow{d_3} \\
{N\alpha}^{E} &= (-c_4u_1u_{19} - s_4\dot{u}_1)\overrightarrow{e_1} + (-s_4u_1u_{19} + c_4\dot{u}_1)\overrightarrow{e_2} + \dot{u}_{19}\,\overrightarrow{e_3} \\
{N\alpha}^{F} &= \left(\begin{pmatrix} \frac{(q_8(-c_{24}(L_5+L_6)+c_{45}(L_9+L_{10})-L_0s_4+L_7s_{24}))u_{19}}{(L_9+L_{10})(c_5L_0-c_{25}L_7-c_{45}q_8-(L_5+L_6)s_{25}+L_8s_{45})} + \\ \frac{(+L_8(-c_4L_0+c_{24}L_7+(L_5+L_6)s_{24}-(L_9+L_{10})s_{45}))u_{19}}{(L_9+L_{10})(c_5L_0-c_{25}L_7-c_{45}q_8-(L_5+L_6)s_{25}+L_8s_{45})} \\ \frac{q_7\dot{q}_7+(c_4L_0-c_{24}L_7-q_8-(L_5+L_6)s_{24}+(L_9+L_{10})s_{45})q_8\dot{q}_8}{(L_9+L_{10})(c_5L_0-c_{25}L_7-c_{45}q_8-(L_5+L_6)s_{25}+L_8s_{45})} \end{pmatrix} c_5u_1 + s_5\dot{u}_1\right)\overrightarrow{f_1} + \\
&\quad \left(-\begin{pmatrix} \frac{(q_8(-c_{24}(L_5+L_6)+c_{45}(L_9+L_{10})-L_0s_4+L_7s_{24}))u_{19}}{(L_9+L_{10})(c_5L_0-c_{25}L_7-c_{45}q_8-(L_5+L_6)s_{25}+L_8s_{45})} + \\ \frac{(+L_8(-c_4L_0+c_{24}L_7+(L_5+L_6)s_{24}-(L_9+L_{10})s_{45}))u_{19}}{(L_9+L_{10})(c_5L_0-c_{25}L_7-c_{45}q_8-(L_5+L_6)s_{25}+L_8s_{45})} \\ \frac{q_7\dot{q}_7+(c_4L_0-c_{24}L_7-q_8-(L_5+L_6)s_{24}+(L_9+L_{10})s_{45})q_8\dot{q}_8}{(L_9+L_{10})(c_5L_0-c_{25}L_7-c_{45}q_8-(L_5+L_6)s_{25}+L_8s_{45})} \end{pmatrix} s_5u_1 + c_5\dot{u}_1\right)\overrightarrow{f_2} + \\
&\quad \dot{u}_{25}\overrightarrow{f_3} \\
{N\alpha}^{C} &= (-s_6\dot{u}_1 - c_6u_1u_{31})\overrightarrow{g_1} + (c_6\dot{u}_1 - s_6u_1u_{31})\overrightarrow{g_2} + \dot{u}_{31}\overrightarrow{g_3}
\end{aligned}
\tag{3.43}
$$

3.3. DYNAMICS OF THE DRAGLINE FRONT-END ASSEMBLY

The dynamic analysis of any mechanical system deals with the formulation of its equations of motions. These equations are a set of differential equations that relate the

forces and torques applied to a system to its motion variables. The differential order of an EOM changes according to the theory used to find these equations. In most cases, a second order ordinary differential equations (ODE) of motion are obtained and solved using general ODE solvers. A common practice to formulate the EOM is to use Newton-Euler, Euler-Lagrange, and Hamilton's Equations, which yield very lengthy hand calculations. In addition to that, the fidelity of the model is questionable as a result of eliminating major components. The aim of building a dynamic model is to understand the behavior of the machine under transient loading. The variations in forces and torques over one cycle of operation can be significant and lead to a reduction of the dragline performance. The more loading hysteresis happen, the quicker failure happens. Consequently, the performance becomes unacceptable.

The construction of EOM of the dragline front-end assembly is very problematic as this assembly contains complex structures with a closed loop. To avoid this difficulty, it should be a representative model to capture the essential operations of the dragline. The current research uses Kane's method (Kane and Levinson, 1985) to find the torques and forces of a real dragline operation. The inertia forces and torques of the massive structures are calculated using Newton-Euler equations. The EOM of the dragline are developed for the machine house, hoist rope, and drag rope, which are the control state variables that any real dragline uses to operate. The use of Kane's method yield a compact form of EOM, which are suitable for control purposes. The EOMs are differential algebraic equations of a differential index order 2. The choice of Kane's method eliminates the need for creating free body diagram (FBD) of every link as used in Newton-Euler formulation. In other words, the reaction forces are considered as noncontributing forces and eliminated from

the analysis. Thus, the dragline dynamics is advanced and expanded to provide a more accurate assessment of the dragline performance by the inclusion of accurate contributing forces in the dynamic analysis.

3.3.1. Inertia Torques of the Structural Components. In addition to linear and angular accelerations, inertia torques are required for calculating generalized inertia forces of the machine house, boom structure, boom-point sheave, and hoist, dump, and drag ropes. Kane and Levinson (1985) defined the inertia torques T_K^* of a link K as given in equation (3.43). However, this representation is provided on the basis of derivation of the central angular momentum of a rigid body in a reference frame C. Equation (3.44) may yield misleading results in a case of a massive structure that weighs hundred tons like the rigging system of the dragline. To rectify this limitation, a complete representation of the moment of inertia tensors are used and a 3-D design of the dragline front-end assembly is done in SolidWorks. The CAD design provides an accurate estimate to the central moments of inertia and product of inertia for every structure with a truncated error. Thus, an accurate estimation of the generalized inertia torques can be done based on equation (3.45) and some manipulation. The resulting inertia torque vectors are provided in the Appendix A.

$$\begin{aligned} T_K^* = & -[\alpha_1 I_1 - \omega_2\omega_3(I_2 - I_3)]\vec{c}_1 \\ & -[\alpha_2 I_2 - \omega_3\omega_1(I_3 - I_1)]\vec{c}_2 \\ & -[\alpha_3 I_3 - \omega_1\omega_2(I_1 - I_2)]\vec{c}_3 \end{aligned} \tag{3.44}$$

α_i and ω_i are, respectively, the first derivative of the angular velocity vector in the direction $\vec{c}_i$ and generalized speed u_i of link K. I_i (i=1,2,3) is the inertia dyadic of K. $\vec{c}_1$, $\vec{c}_2$, $\vec{c}_3$ are the dextral set of unit vectors parallel to the principal axes of link K.

$$T_K^* = -\alpha_K . I^{K_i/K_i{}^*} - \vec{\omega}^K \times I^{K_i/K_i{}^*} . \vec{\omega}^K \tag{3.45}$$

$I^{K_i/K_i{}^*}$ is the inertia dyadic of body K_i about its COM $K_i{}^*$.

3.3.2. Kane's Method. The construction of EOM using Kane method is systematic and leads to a compact form of equations. The equations are first order DAE in terms of generalized speeds derivatives ($\dot{u}_1, \dot{u}_{19}$ and $\dot{u}_{31}$), which are the accelerations in the Newton-Euler formulation. It is important to note that the independent generalized speed $\dot{u}_1$ of the machine angular motion is known and can be prescribed as a trapezoidal function of time. However, other quantities $\dot{u}_{19}$ and $\dot{u}_{31}$are unknown and can only be found from the integration of the constraints equations at the acceleration level. When both the hoist and drag ropes change their respective lengths, these values change as well to control the bucket. The integration of these accelerations leads to their angular velocities and a further integration allows the dynamic derivation of the bucket position at each time. Thus, the dynamics model of the dragline using Kane's method is an advanced model that can be used to improve the performance of the machine.

The Kane's method eliminates the non-working forces that are orthogonal to the tangent space of the vector motion. This important property is established by a scalar product of both the partial velocities and Newton-Euler forces (Storch and Gates, 1989; Lesser, 1992). The Newton-Euler method deals with constraint forces in every link and the Lagrange method includes adding and finding unknown Lagrangian multipliers. These formulations make the derivation more complicated and are not always required for the subsequent analysis. Kane's equations of motion use the multiplication of Newton law with the partial velocity, which is called "nonholonomic generalized inertia forces."

3.3.2.1 Generalized inertia forces. The derivations of velocities and accelerations play a prominent role in the construction of Kane's dynamic equations. They are directly

used in the derivation of generalized inertia forces $\left(\tilde{F}_r^*\right)_K$ and partially helps in deriving generalized active forces $\left(\tilde{F}_r\right)_K$. Each body in the dragline front-end assembly contributes to the total generalized inertia force by the following entities defined in equation (3.46).

$$\left(\tilde{F}_r^*\right)_K = -\tilde{v}_r^K . m_K . a^{K^*} + \tilde{\omega}_r^K . T_K^* \tag{3.46}$$

K is the kth body, $K = (B, \dots, H_1)$, and r represents the index of the independent generalized speeds associated with the system ($r = 1, 19, 31$). Spanning equation (3.46) over all bodies in the front-end assembly yields equation (3.47).

$$\begin{aligned}\tilde{F}_r^* = & -m_B . \tilde{v}_r^{B^*} . a^{B^*} + \tilde{\omega}_r^B . T_B^* - m_C . \tilde{v}_r^{C^*} . a^{c^*} + \tilde{\omega}_r^c . T_c^* \\ & -m_E . v_r^{E^*} . a^{E^*} + \tilde{\omega}_r^E . T_E^* - m_G . \tilde{v}_r^{G^*} . a^{G^*} + \tilde{\omega}_r^G . T_G^* \\ & -m_D . v_r^{D^*} . a^{D^*} + \tilde{\omega}_r^D . T_D^* - m_F . \tilde{v}_r^{F^*} . a^{F^*} + \tilde{\omega}_r^F . T_F^* \\ & -m_{H_1} . \tilde{v}_r^{H_1} . a^{H_1} - m_{F_1} . \tilde{v}_r^{F_1} . a^{F_1}\end{aligned} \tag{3.47}$$

m_B represents the mass of the machine housing and its mast; m_C is the mass of the boom structure; m_D is the mass of boom-point sheave; and m_E and m_G are the mass flow of the hoist and drag ropes during the simulation. The mass flow changes as the velocity of each rope changes in magnitude and direction over time. Previous research studies have considered these entities as constants, which are not relevant to a real dragline. m_{F_1} is the mass of the drag chain; and m_F is the dump rope mass. m_{H1} represents the mass of the bucket, which is a function of time, filling factor, and material properties of overburden. The nonholonomic partial velocity vectors, $\tilde{v}_r^{K^*}$, and the nonholonomic partial angular velocity vectors $\tilde{\omega}_r^K$ are defined in Table 3.4. They are used along with accelerations and inertia torques to directly assemble equation (3.47).

For an index $r = 1$, and with the aid of equations (3.42-3.47), the generalized inertia force $\tilde{F}_1^*$ is given in equation (3.48).

$$\tilde{F}_1^* = X_{11}\,\dot{u}_1 + Z_6 \tag{3.48}$$

$$X_{11} = -B_{22} - c_2^2 C_{22} - c_4^2 D_{22} - c_4^2 E_{22} - c_5^2 F_{22} - c_6^2 G_{22} - L_{11}^2 m_B - (L_3 + c_2 L_5 + L_{11})^2 m_C - m_G(L_1 + L_{11} + 0.5q_7)^2 - m_{\mathrm{F1}}(L_1 + L_{11} + q_7)^2 - C_{11}s_2^2 - m_D(L_3 + c_2 L_5 + c_2 L_6 + L_{11} + L_7 s_2)^2 - m_E(L_3 + c_2 L_5 + c_2 L_6 + L_8 + L_{11} + L_7 s_2)^2 - m_F(L_3 + c_2 L_5 + c_2 L_6 + L_8 - L_9 + L_{11} + L_7 s_2)^2 - m_{\mathrm{H1}}(L_3 + c_2 L_5 + c_2 L_6 + L_8 - L_9 + L_{11} + L_{12} + L_7 s_2)^2 - D_{11}s_4^2 - E_{11}s_4^2 - F_{11}s_5^2 - G_{11}s_6^2 \tag{3.49}$$

$$Z_6 = m_E(L_3 + c_2(L_5 + L_6) + L_8 + L_{11} + L_7 s_2)(-0.5c_4 q_8 - L_8 s_4)u_1 u_{19} - m_F(L_3 + c_2 L_5 + c_2 L_6 + L_8 - L_9 + L_{11} + L_7 s_2)(c_4 q_8 + L_8 s_4)u_1 u_{19} - m_{\mathrm{H1}}(L_3 + c_2 L_5 + c_2 L_6 + L_8 - L_9 + L_{11} + L_{12} + L_7 s_2)(c_4 q_8 + L_8 s_4)u_1 u_{19} - m_{\mathrm{F1}}(L_1 + L_{11} + q_7)(c_{456} q_8 + L_8 s_{456})u_1 u_{19} - 2c_5 F_{11} s_5 u_1 u_{25} + 2c_5 F_{22} s_5 u_1 u_{25} - L_9 m_F(L_3 + c_2(L_5 + L_6) + L_8 - L_9 + L_{11} + L_7 s_2)s_5 u_1 u_{25} - m_{\mathrm{H1}}(L_3 + c_2 L_5 + c_2 L_6 + L_8 - L_9 + L_{11} + L_{12} + L_7 s_2)(c_5 L_{13} + L_9 s_5 - L_{12} s_5)u_1 u_{25} - 0.5m_G(L_1 + L_{11} + 0.5q_7)q_7 s_6 u_1 u_{31} + m_{\mathrm{F1}}(L_1 + L_{11} + q_7)u_1(-c_6 L_{13} u_{25} + L_9 s_6 u_{25} - L_{12} s_6 u_{25} - \dot{q}_7) - 0.5m_G(L_1 + L_{11} + 0.5q_7)u_1 \dot{q}_7 \tag{3.50}$$

Trigonometric functions c_{456} and s_{456} refer to the $Cos(q_4 + q_5 + q_6)$ and $Sin(q_4 + q_5 + q_6)$. The generalized inertia force related to the index $r = 19$ is given in equation (3.51).

$$\tilde{F}_{19}^* = -X_{22}\,\dot{u}_{19} + Z_7 \tag{3.51}$$

$$X_{22} = D_{33} + E_{33} + L_8^2(m_E + m_F + m_{\mathrm{H1}}) + (0.25m_E + m_F + m_{\mathrm{H1}})q_8^2 \tag{3.52}$$

$$Z_7 = (0.5c_4m_Eq_8(L_3 + c_2L_5 + c_2L_6 + L_8 + L_{11} + L_7s_2) - c_4D_{11}s_4 + c_4D_{22}s_4 - c_4E_{11}s_4 + c_4E_{22}s_4 + L_8m_E(L_3 + c_2L_5 + c_2L_6 + L_8 + L_{11} + L_7s_2)s_4 + c_5m_F(L_3 + c_2L_5 + c_2L_6 + L_8 - L_9 + L_{11} + L_7s_2)(c_{45}q_8 + L_8s_{45}) + c_5m_{\mathrm{H1}}(L_3 + c_2L_5 + c_2L_6 + L_8 - L_9 + L_{11} + L_{12} + L_7s_2)(c_{45}q_8 + L_8s_{45}) - m_F(L_3 + c_2L_5 + c_2L_6 + L_8 - L_9 + L_{11} + L_7s_2)s_5(c_{45}L_8 - q_8s_{45}) - m_{\mathrm{H1}}(L_3 + c_2L_5 + c_2L_6 + L_8 - L_9 + L_{11} + L_{12} + L_7s_2)s_5(c_{45}L_8 - q_8s_{45}))u_1^2 + (-c_{45}L_8m_F(c_{45}q_8 + L_8s_{45}) - c_{45}L_8m_{\mathrm{H1}}(c_{45}q_8 + L_8s_{45}) + m_Fq_8s_{45}(c_{45}q_8 + L_8s_{45}) + m_{\mathrm{H1}}q_8s_{45}(c_{45}q_8 + L_8s_{45}) + c_{45}m_Fq_8(c_{45}L_8 - q_8s_{45}) + c_{45}m_{\mathrm{H1}}q_8(c_{45}L_8 - q_8s_{45}) + L_8m_Fs_{45}(c_{45}L_8 - q_8s_{45}) + L_8m_{\mathrm{H1}}s_{45}(c_{45}L_8 - q_8s_{45}))u_{19}^2 - L_9m_F(c_{45}q_8 + L_8s_{45})u_{25}^2 - L_9m_{\mathrm{H1}}(c_{45}q_8 + L_8s_{45})u_{25}^2 + L_{12}m_{\mathrm{H1}}(c_{45}q_8 + L_8s_{45})u_{25}^2 - L_{13}m_{\mathrm{H1}}(c_{45}L_8 - q_8s_{45})u_{25}^2 + u_{19}(-0.25m_eq_8\dot{q}_8 - c_{45}m_F(c_{45}q_8 + L_8s_{45})\dot{q}_8 - c_{45}m_{\mathrm{H1}}(c_{45}q_8 + L_8s_{45})\dot{q}_8 + m_Fs_{45}(c_{45}L_8 - q_8s_{45})\dot{q}_8 + m_{\mathrm{H1}}s_{45}(c_{45}L_8 - q_8s_{45})\dot{q}_8) \quad (3.53)$$

The generalized inertia force associated with $r = 31$ is given in equation (3.54).

$$\tilde{F}_{31}^* = -X_{33}\,\dot{u}_{31} + Z_8 \quad (3.54)$$

$$X_{33} = G_{33} + 0.25m_Gq_7^2 + m_{\mathrm{F1}}(1 + q_7^2) \quad (3.55)$$

$$Z_8 = (c_6m_{\mathrm{F1}}(L_3 + c_2L_5 + c_2L_6 + L_8 - L_9 + L_{11} + L_{12} + L_7s_2) - c_6G_{11}s_6 + c_6G_{22}s_6 + 0.25m_Gq_7(2.L_1 + 2.L_{11} + q_7)s_6 + m_{\mathrm{F1}}q_7(L_3 + c_2L_5 + c_2L_6 + L_8 - L_9 + L_{11} + L_{12} + L_7s_2)s_6)u_1^2 + u_{31}(-m_{\mathrm{F1}}(-c_{45}L_8u_{19} + q_8s_{45}u_{19} + (L_9 - L_{12})u_{25}) - 0.25m_Gq_7\dot{q}_7 - m_{\mathrm{F1}}q_7((c_{45}q_8 + L_8s_{45})u_{19} + L_{13}u_{25} + \dot{q}_7)) \quad (3.56)$$

3.3.2.2 Generalized active forces. The construction of equations of motion using KM requires defining the generalized active forces, as well. The generalized active forces are the projection of the contributing forces on a tangent space of motion. This projection

automatically leads to the cancellation of nonworking forces. A mathematical definition of the generalized active forces is given in equation (3.57) (Kane and Levinson, 1985).

$$\tilde{F}_r = \sum_{i=1}^{v} \tilde{v}_r^{p_i} . R_i \qquad (r = 1, \dots, P) \tag{3.57}$$

$\tilde{v}_r^{P_i}$ is the nonholonomic partial velocity of a particle P_i in a reference frame; R_i is the resultant of all contact forces and distance forces acting on p_i. The definition in equation (3.57) allows the calculation of the contribution of all gravity forces acting of each link's COM as provided in equation (3.58).

$$\begin{aligned}\left(\tilde{F}_r\right)_G = \tilde{V}_r^{B^*} . \vec{G}_B + \tilde{V}_r^{C^*} . \vec{G}_C + \tilde{V}_r^{D^*} . \vec{G}_D + \tilde{V}_r^{E^*} . \vec{G}_E + \\ \tilde{V}_r^{F^*} . \vec{G}_F + \tilde{V}_r^{G^*} . \vec{G}_C + \tilde{V}_r^{F_1} . G_{F_1} + \tilde{V}_r^{H_1} . \vec{G}_{H_1}\end{aligned} \tag{3.58}$$

$\vec{G}_B$ represents the resultant gravity force acting on G^*. It acts downward, where the partial velocity, $\vec{V}^{B^*}$, is calculated in the reference frame (B). Thus, one has to express the gravity force of each link in its local reference frame. The gravity force of each link is given in equations (3.59).

$$\begin{aligned}\vec{G}_B &= -g\, m_B \vec{b}_2 & \vec{G}_C &= -g\, m_C(-s_2\vec{c}_1 - c_2\vec{c}_2) \\ G_D &= -g m_D\left(s_3\overrightarrow{d_1} - c_3\vec{d}_2\right) & \vec{G}_E &= -g\, m_E(s_4\vec{e}_1 - c_4\vec{e}_2) \\ \vec{G}_F &= -g m_F\left(-s_5\overrightarrow{f_1} - c_5\vec{f}_2\right) & \vec{G}_G &= -g\, m_G(s_6\vec{g}_1 - c_6\vec{g}_2) \\ \vec{G}_{H_1} &= -g m_{H_1}\left(-s_5\overrightarrow{f_1} - c_5\vec{f}_2\right) & G_{F_1} &= -g\, m_G(s_6\vec{g}_1 - c_6\vec{g}_2)\end{aligned} \tag{3.59}$$

The contribution to the generalized active forces of gravity forces expressed in equation (3.59). There are other forces that contribute to F_r, such as contact forces. To bring their effect into evidence, one can rewrite equation (3.57), such as in equation (3.60).

$$(F_r)_R = w_r.T + v_r^Q.R \tag{3.60}$$

From Kane et al. (1983), equation (3.60) is a replacement of all body and contact forces acting on (R) by the torque T and the force R applied to point *Q* of link *R*. v_r^Q is the partial velocity of point *Q* in *N*. In equation (3.60), one can write $(F_r)_A$, the contribution of all forces acting on body (*B)* to the generalized active forces as equation (3.61).

$$(F_r)_B = \omega_r^B \left(T^{N}/_{B} + T^{C}/_{B}\right) + v_r^{B^*} \left(R^{N}/_{B} + G_B\right) \tag{3.61}$$

In the same manner, for bodies (C and D) these contributions are given in equations (3.62) and (3.63).

$$(F_r)_C = \omega_r^C \left(T^{B}/_{C} + T^{D}/_{C}\right) + v_r^{C^*} \left(R^{B}/_{C} + G_C\right) \tag{3.62}$$

$$(F_r)_D = \omega_r^D \left(T^{D}/_{C} + T^{E}/_{D}\right) + v_r^{D^*} \left(R^{C}/_{D} + G_D\right) \tag{3.63}$$

The contribution of all forces acting on other links *E,…*, H_1 can be derived using equation (3.60) in the same fashion. The relative motion between the drag chain F_1 and the COM (G^*) of the drag rope leads to a contribution $R^{F_1}/_{G}$, acting on link (G) at point (F_1) and constantly coincident with (G), which is given in equation (3.64).

$$\left(v_r^{F_1} - v_r^{G^*}\right).R^{F_1}/_{G} \quad r = (1,19,31) \tag{3.64}$$

and $$R^{F_1}/_{G} = \sigma.\vec{g}_r \tag{3.65}$$

and $$\tau_1 = T^{N}/_{B}.\vec{b}_2 \tag{3.66}$$

$$\tau_2 = T^{E}/_{N}.\vec{e}_3 \tag{3.67}$$

Equations (3.59-3.67) lead to the sum of the contributions to the generalized active forces of all gravity forces and actuator forces acting on the system and is given in equation (3.68). The actuator that controls the motion of the hoist rope, which provides a torque τ_2, is placed at the COM of boom-point sheave. This assumption is acceptable from the control theory and eliminates the need to include the constant length of hoist rope from the machine house to the end of the boom. Thus, the expanded form of the generalized active forces is given in equation (3.68). However, there is also the effect of the friction between the dragline bucket and the overburden at the cutting tip. Another effect plays a role into the generalized forces F_r, which is the frictional contact between the drag rope and digging face. These effects must be included in the final from of the generalized active forces to make the analysis more accurate from operational stand point.

$$\begin{aligned} F_r = {} & \tau_1 . \tilde{\omega}_r^B . \vec{b}_2 + \tau_2 . \tilde{\omega}_r^E . \vec{e}_3 + \sigma\left(V_r^{F_1} - V_r^{G^*}\right) . \overrightarrow{g_1} \\ & + \tilde{v}_r^{B^*} . \vec{G}_B + \tilde{v}_r^{C^*} . \vec{G}_C + \tilde{v}_r^{D^*} . \vec{G}_D + \tilde{v}_r^{E^*} . \vec{G}_E \\ & + \tilde{v}_r^F . \vec{G}_F + \tilde{v}_r^{G^*} . \vec{G}_G + \tilde{v}_r^{F_1} . \vec{G}_{F_1} + v_r^{H_1} . G_{H_1} \qquad (r = 1{,}19{,}31) \end{aligned} \tag{3.68}$$

The drag force (σ) is provided to simulate the effect of the drag motion of the bucket on the top of soil and is established as a result of placing a drag motor at point (B_1). This provides a relative motion of the drag chains and drag rope with respect to the machine house. The cutting force provided by dragging the heavy bucket into the bank should also be considered in the dynamic equations.

3.3.2.3 Dynamics of the dragline bucket. The dragline bucket and its structural elements (drag chains, hoist chains, trunnions, and spreaders) are designed to surmount the

harsh digging environments, speed up the filling and dumping processes, and maximize the productivity. The dump rope is also a critical component in the rigging system and its length affects the bucket carry angle and the direction of the cutting force. The bucket motion is controlled by a constant dragging speed of magnitude of about 1.32 m/s (4.33 ft/s) that guarantees the filling of the bucket in 10 seconds. The rigging system must be operated to orient the bucket properly before the digging starts. Improper bucket-ground engagements cause more vibrations and friction between the rigging system elements. It also reduces the effectiveness of cutting and filling and reduces the longevity of the rigging system. The dynamic nature of bucket-ground contact is a complex phenomenon, and thus, this research is limited to the effect of cutting resistance force on the overall dynamics of the machine.

- **Bucket cutting force.** The motion of dragline bucket into the overburden during digging phase generates cutting forces at its teeth, which vary with the travelling speed of the bucket and the material properties of the soil. In general, except for chop cutting, the dragline bucket digs the overburden at an inclined surface. The cutting force is, thus, a function of the digging face angle, cutting angle ($\mathrm{q_c}$), and the orientation of the dump rope in the machine reference frame ($\mathrm{q_5}$). The components of the bucket cutting resistance force associated with a reference frame (F), located at the COM of dump rope, can be modelled using equation (3.69).

$$\overrightarrow{F_c} = F_{ct}.cos(ca).\cos(q_5)\overrightarrow{f_1} - F_{ct}.cos(ca).\sin(q_5)\overrightarrow{f_2} \tag{3.69}$$

Assuming that the bucket drag velocity is $\dot{q}_7$, which is known and using the formula provided by Poderni (2003), the digging force is given by equation (3.70).

$$F_{ct} = \frac{E_{bucket}\,(1+\lambda_0)\,K_F}{K_{nym}.l_{bucket}.K_p} \tag{3.70}$$

E_{bucket} is the capacity of the dragline bucket (m^3); λ_0 is the ratio of the volume of the prism drawn to the volume of the bucket; K_F is a coefficient of specific resistance to digging; K_{nym} is the ratio of the bucket filling path to the length of the bucket $\frac{l_{path}}{l_{bucket}}$; l_{bucket} is the bucket length; and k_p is a coefficient of loosening of the rock in the bucket (Poderni, 2003). K_F is $0.12 \times 10^6\ N/m^2$ for loose sands and rocks and 0.29×10^6 for a medium type, λ_0 is 0.4 for a loose category of rock and is 0.3 for a medium type, and K_p is 1.25 for a loose type rock and 1.3 for a medium type.

Field observations of the dragline operations show that the dragline bucket rotational motion is very short and takes place when the bucket starts to engage the bank. The translational motion is dominant during material excavation. The cutting resistance force in equation (3.70) accounts for the translational motion on the digging face and the capacity of the bucket. The continuous motion of the bucket under a constant velocity $\dot{q}_7$(m/s) makes the overburden pile up to a height $h(q_7)$. This height can be found from the conditions of static equilibrium as there is no inertia effect of the loaded materials in the bucket. By taking the FBD of the bucket as shown in Figure 3.3, under a static equilibrium condition and no hoist force acts on the bucket, the height of overburden being piled-up in the bucket is given by equation (3.71).

$$h(q_7) = \frac{m_{H_1}.g}{F_c.Cos(q_c)} \tag{3.71}$$

m_{H_1} is the bucket tare mass + overburden mass. Overburden mass changes as a function of digging time t_{dig}, which can be found from an elementary formula

$(q_7/\dot{q}_7)$. The dragging speed $(\dot{q}_7)$ is a known function of time and is related to the diameter of the winding drag drum and its angular velocity. The hoisting force is least during the process of digging since the hoist rope is flaccid during the digging motion. However, it may slightly increase to properly reorient the bucket for facing the bank. In other words, it does not contribute to the cutting resistance force. The line of action of the drag force in the bucket dynamics model (Figure 3.3) intercepts the lines of action of cutting force and bucket weight. Thus, static equilibrium is used to define the height of cut.

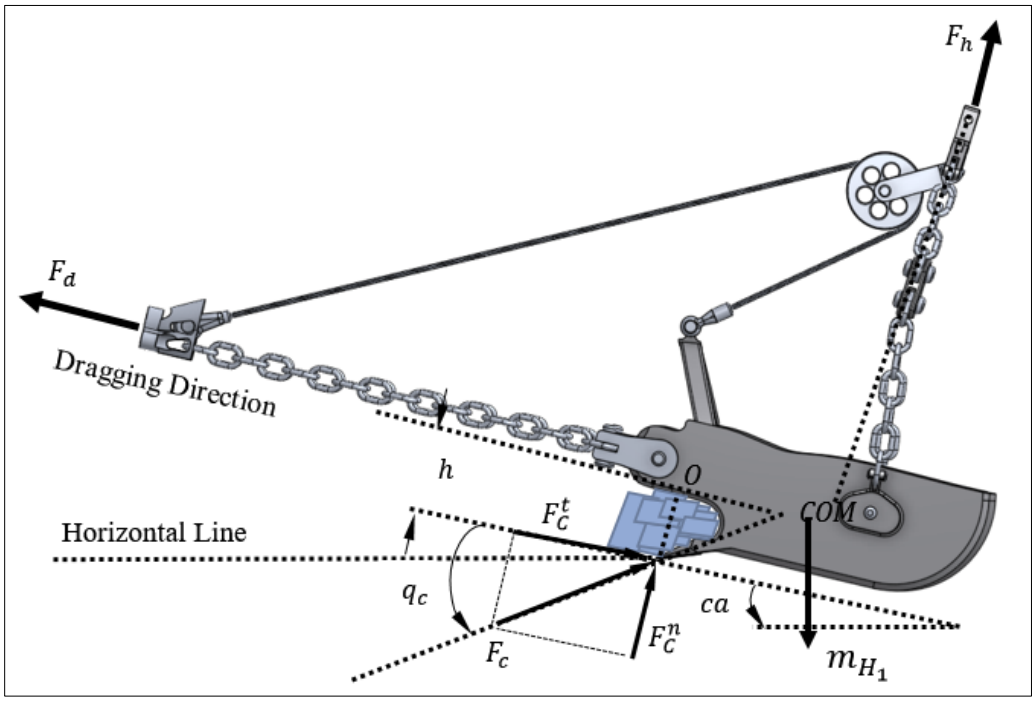

Figure 3.3. Dragline bucket and rigging dynamics

Demirel (2007) estimated the cutting force of a dragline bucket from the dynamics equilibrium of the bucket-rigging system using the hoist and drag forces. It should be

clarified that the cutting force must be developed only based on material properties, cutting tool shape, filling sequence and the bucket capacity. Thus, equations (3.71) and (3.69) are now sufficient to provide a good estimation of bucket cutting force.

- **Payload model of dragline bucket.** The aim for using draglines in strip mining operations is to efficiently and economically dig and dump materials in a short cycle of 60s. To achieve this goal, the dragline bucket design must allow for a quick filling process, reduce the friction between bucket and dirt, and increase the load carrying capacities. Thus, increasing the tare weight of a dragline bucket affects the payloads and has adverse effects on the productivity. A simplified model of the bucket payload is proposed using the simulation results from EDEM package (Li et al., 2017). The equation (3.72) is derived by interpolation and is a linear function of digging time (t_{dig}).

$$m_{H_1} = m_{overburden} + m_{bucket}$$
$$= 3{,}400.18\, t_{dig} + 30{,}000.4(kg) \tag{3.72}$$

The value of 30,000.4 (kg) of the m_{bucket} is accurately estimated using 3D CAD model of a dragline bucket designed in SolidWorks (Figure 3.3). The tare weight of bucket plus the weight of loaded materials and including the breakout forces must be within the allowable dragline load limits provided by the manufacturers.

- **Drag rope and overburden contact model.** The digging process in any dragline should be smooth, stable with as much reduced vibration on drag ropes and chains as possible. Inefficient dragging and digging increase the digging time resulting in low productivity. They also cause much wear and tear on the drag rope and its chains. Thus, the drag ropes and chains may break before their scheduled maintenance periods.

Sometimes the drag ropes come into direct contact with the ground during the bucket filling process. Thus, the dynamic equations of the front-end assembly must include this effect. The drag rope can be partially immersed in the dirt, which results in friction forces that reduce its useful service life. If the end of the drag rope F_1 (Figure 3.2) is partially submerged at a depth of $(d_r.\overrightarrow{b_2})$, a portion of the drag rope $\overrightarrow{F_1F_2}$ is subjected to static and dynamic frictional forces, which acts at the COM of $\overrightarrow{F_2F_1}$. The depth of the submerged part can be estimated from the kinematics of the drag rope established earlier and is given in equation (3.73). The kinematics model of the link-granular material contact is depicted in Figure 3.4 and contains one link. However, multigrid links may be constructed when sufficient boundary conditions about each link orientation exist.

$$y(t) = \left[q_7(0)\sin\left(q_6(0)\right) - q_7(t)\sin(q_6(t))\right] \tag{3.73}$$

$$\overrightarrow{B_1F_3} = q_7(t) - \frac{0.5\,y(t)}{\sin q_6(t)}$$

The position vector $\overrightarrow{B_1F_3}$ defines the location of the COM of the submerged portion of the rope in a reference frame associated with drag rope reference frame (G). The angular and linear velocities of the point F_3 in the drag rope reference do not vary as it is assumed that there is no deformation in this rope. However, its magnitude and direction change with respect to the machine house reference frame as the rope reels in/out on the fairlead sheaves. The area of contact A_c can be estimated as in equation (3.74). d_r represents the diameter of drag rope.

$$A_c = d_r\,\frac{y(t)}{\mathrm{Sin}(q_6)} \tag{3.74}$$

Thus, the horizontal dynamic forces due to friction are estimated by equation (3.75) (Lee and Marghitu, 2011).

$$F_{dh} = -\text{sign}\,(v_h).\,\beta.\,A_c.\,v_{F_{3,h}}^2 \tag{3.75}$$

$$\vec{v}_{F_3} = \omega^G \times \overrightarrow{B_1F_3}$$

$$= (1.5q_7s_6 - 0.5q_{70}s_{60})u_{31}\,\overrightarrow{g_1} + (1.5c_6q_7 - 0.5ct_6q_{70}s_{60})u_{31}\overrightarrow{g_2} +$$

$$(-1.5c_{26}q_7 + q_{70}(0.5c_6ct_6 - 0.5s_6)s_{60})u_1\overrightarrow{g_3}$$

s_{60}, c_{60}, s_{26} and c_{26} are the abbreviated trigonometric functions sin($q_6(0)$), cos($q_6(0)$), sin(2 $q_6(t)$), and cos(2 $q_6(t)$), respectively; β is the drag coefficient of 1569.7 per experimental data (Lee and Marghitu, 2011). The dynamic friction force of the submerged part of the drag rope due to the vertical velocity of dragging is given in equation (3.76).

$$F_{dv} = \text{sign}(v_v).\,\beta.\,A_c V_{F_{3,v}}^2 \tag{3.76}$$

Hill et al. (2005) suggested equation (3.77) to estimate the vertical static friction.

$$F_{sv} = -\text{sign}\,(v_v)\left(\frac{y(t)}{d_c}\right)^{\lambda}\eta_v.\,g.\,\rho.\,V \tag{3.77}$$

The impeding force to the horizontal motion is proportional to the density of the granular material ρ, and V the submerged component of the rope; and it is equal $\frac{y(t)*\pi {d_c}^2}{4*s_6}$; $\eta_v = 10$ for plunging motion; and the submerged depth $d_r(t)$ and d_c. The horizontal friction force is also given as equation (3.78).

$$F_{sh} = -\,\text{sign}(v_h)\,y(t)^2\,.\,\eta_h.\,g.\,\rho.\,d_c \tag{3.78}$$

For plunging motion, $\lambda = 1.4$, $sign(v_h) = 1$, and $sign(v_v) = -1$. Their values indicate that the rope penetrates the medium in a vertical component that matches the direction of dragging and with a rotational displacement acting clockwise at $q_6 > 0$.

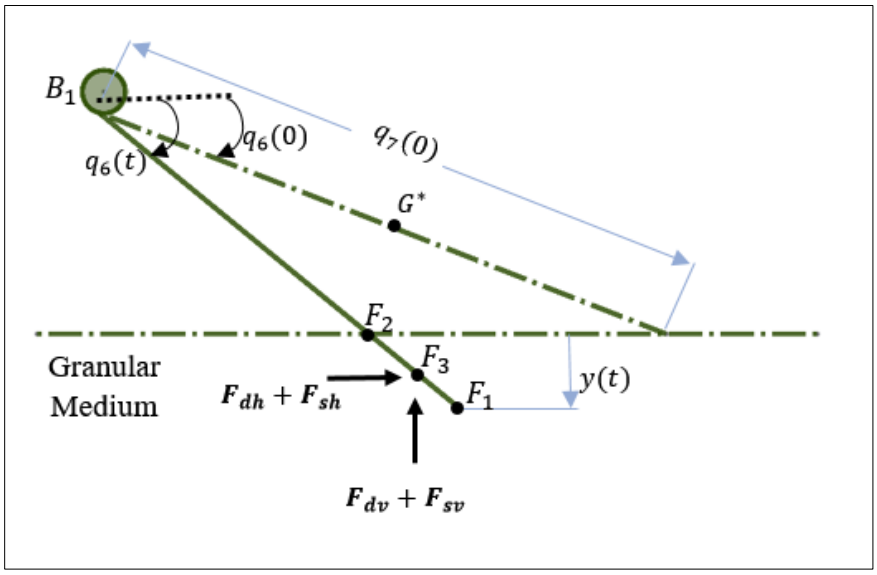

Figure 3.4. Dragline rope and granular medium dynamics

The new form of generalized active forces, defined in equation (3.79), now includes the effects of friction between the drag rope and mine granular matter and effect of cutting forces at bucket tip.

$$F_r = \tau_1 . \tilde{\omega}_r^B . \vec{b}_2 + \tau_2 . \tilde{\omega}_r^E . \vec{e}_3 + \sigma\left(V_r^{F_1} - V_r^{G^*}\right) . \overrightarrow{g_1} + \tilde{v}_r^{B^*} . \vec{G}_B +$$

$$\tilde{v}_r^{C^*} . \vec{G}_C + \tilde{v}_r^{D^*} . \vec{G}_D + \tilde{v}_r^{E^*} . \vec{G}_E + \tilde{v}_r^F . \vec{G}_F + \tilde{v}_r^{G^*} . \vec{G}_G +$$

$$\tilde{v}_r^{F_1} . \vec{G}_{F_1} + v_r^{H_1} . G_{H_1} + \tilde{v}_r^{H_1} . \vec{F}_{cut} + \tilde{v}_r^{F_1} . \vec{F}_{Friction} \qquad (3.79)$$

The friction force equation defined according to equations (3.75-3.79) can now take the form of equation (3.80).

$$\vec{F}_{Friction} = (F_{\mathrm{dh}} + F_{\mathrm{sh}}).\overrightarrow{g_1} + (F_{\mathrm{dv}} + F_{\mathrm{sv}}).\overrightarrow{g_2} \tag{3.80}$$
$$= ((-q_7 s_6 + q_{70} s_{60})\mathrm{sgnV}_h(-2.25\beta d_r s_6(1.\, q_7 s_6 - 0.34 q_{70} s_{60})^2 u_{31}^2 +$$
$$g\rho d_c(q_7 s_6 - q_{70} s_{60})\eta_h).\overrightarrow{g_1} + (\tfrac{1}{4}(-q_7 s_6 + q_{70} s_{60})\mathrm{sgnV}_v(-9.\beta d_r s_6$$
$$(1.\, c_6 q_7 - 0.34\, ct_6\, q_{70} s_{60})^2 u_{31}^2 - g\pi\rho\, \mathrm{csc}_6\, d_c^2(\tfrac{-q_7 s_6 + q_{70} s_{60}}{d_c})^{\lambda}\eta_v)).\overrightarrow{g_2}$$

Constructing the corresponding generalized active forces leads to the generalized active forces associated with index ($r = 1, 19, 31$) in equations (3.81-3.83).

$$\tilde{F}_1 = \tau_1 \tag{3.81}$$

$$\tilde{F}_{19} = \tau_2 + Z_9 \tag{3.82}$$

$$\tilde{F}_{31} = \sigma + Z_{10} \tag{3.83}$$

with

$$Z_9 = g.m_e c_4 L_8 - 0.5 g.m_e q_8 s_4 + g.m_F s_5(c_{45} q_8 + L_8 s_{45}) + g.m_{\mathrm{H1}} s_5(c_{45} q_8 +$$
$$L_8 s_{45}) + g.m_F c_5(c_{45} L_8 - q_8 s_{45}) + g.m_{\mathrm{H1}} c_5(c_{45} L_8 - q_8 s_{45}) +$$
$$\frac{c_{ca} c_5\, E_{\mathrm{bucket}}\, k_F\, k_p\, l_{\mathrm{bucket}}(c_{45} q_8 + L_8 s_{45} + c_{45} L_8 - q_8 s_{45})(1+\lambda_0)}{k_{\mathrm{nym}}} \tag{3.84}$$

$$Z_{10} = g.m_{\mathrm{F1}} c_6 q_7 + 0.5 g.m_G c_6 q_7 - g.m_{\mathrm{F1}} s_6 + (1.5 q_7 s_6 - 0.5 q_{70} s_{60})$$
$$(-q_7 s_6 + q_{70} s_{60})\mathrm{sgnV}_h(-2.25\beta d_r s_6(1.\, q_7 s_6 - 0.34 q_{70} s_{60})^2 u_{31}^2 + g\rho d_c(q_7 s_6 -$$
$$q_{70} s_{60})\eta_h) + \tfrac{1}{4}(-q_7 s_6 + q_{70} s_{60})(1.5 c_6 q_7 - 0.5 ct_6 q_{70} s_{60})\mathrm{sgnV}_v *$$
$$(-9.\beta d_r s_6(1.\, c_6 q_7 - 0.34 ct_6\, q_{70} s_{60})^2 u_{31}^2 - g\pi\rho \mathrm{csc}_6\, d_c^2(\tfrac{-q_7 s_6 + q_{70} s_{60}}{d_c})^{\lambda}\eta_v) \tag{3.85}$$

Equations (3.48, 3.51, 3.54, and 3.80-3.82) are the main elements in the Kane's equations of motion, which are given in the equation (3.86).

$$\tilde{F}_r^* + \tilde{F}_r = 0 \tag{3.86}$$

The final set of EOM of the front-end assembly is given by equations set (3.87).

$$\left.\begin{aligned} X_{11}\,\dot{u}_1 \;+\; Z_6 &= \tau_1 \\ -X_{22}\,\dot{u}_{19} + \; Z_7 &= \tau_2 + Z_9 \\ -X_{33}\,\dot{u}_{31} + \; Z_8 &= \sigma + Z_{10} \end{aligned}\right\} \quad (3.87)$$

Equation (3.87) can be solved after finding appropriate initial values of the generalized coordinates associated with each component and using numerical techniques described in Section 4. The solution is based on the inverse dynamics approach where predefined motion variables are provided for estimating torques, forces and acceleration.

3.4. SUMMARY

This section provided a solid, concise formulation of the kinematics and dynamics of a dragline front-end assembly using vector mechanics and Kane's method. The EOM construction is straight and systematic with the right assumptions to every link in the front-end assembly. This computational dynamic model is a 3D spatial model with 3 DOFs that consider the full dragline motion at any period of operation. The model can be directly reduced to a 2 DOF model by eliminating the generalized coordinate and speed associated with the machine house. The resulting boom point sheave torque τ_2 and drag force σ are used for studying of the stress distribution on different wire rope constructions.

The dynamic analysis using Kane's method was augmented by the consideration of the external forces and their contribution to the generalized active forces. A comprehensive dynamic model was built to account for the friction between the drag rope and the overburden. It also uses an accurate model of cutting resistance force, which was established based on the effective cutting of overburden material. Section 4 contains the

numerical methods for solving the dynamic model. The 3D dragline CAD model is also provided and used to provide good estimates of the front-end weights and inertia. These estimates are used to reduce the error from using mathematical calculations. The model outputs are used in a finite element analysis (FEA) using ANSYS Workbench to generate the maximum equivalent stresses and stress concentrations in the wire ropes.

4. NUMERICAL SOLUTION PROCEDURES AND VIRTUAL PROTOTYPE MODELING

The dynamic model of the dragline front-end assembly developed in Section 3 will be solved using efficient numerical techniques to find the machine housing swinging torque, hoist rope torque, and drag force. The model is an advanced dynamic model and has only three kinematic inputs, which are the linear velocities of hoist and drag ropes and angular displacement of machine house. The equations of motion in equation (3.87) along with a feedforward kinematics analysis are solved using Mathematica (Wolfram, 2018). These equations are solved in a systematic way, based on the initial values of the front-end assembly configuration constraints.

The solution starts with accurate estimations of geometrical quantities that define the COM of machine house, boom, boom-sheave, ropes, and bucket. Central principal moments of inertias of every component are found from the 3D CAD model designed in SolidWorks and used in the numerical solutions. The kinematics constraint equations (3.6) and (3.7) are used to capture the loop closure of the front-end assembly. These equations also contribute to the solution of equations of motion and provide a description of the trajectories of the machine house, bucket, and ropes. The numerical procedures are developed using user-defined functions that contain all relevant details of the dragline front-end geometry. Kinematic constraint equations are also solved independently to find initial conditions, which are used in the dynamics model.

The results of kinematics and dynamic analyses of the model are plotted at the end of the simulation. These results are used as boundary conditions in the finite element analysis of wire ropes using ANSYS. Verification and validation for both the

computational dynamics model and virtual dragline simulator are then carried out in Sections 4.2 and 4.3. These procedures are provided in details and used to establish the accuracy, errors, and robustness of these models. Sections 4.1.1 and 4.1.2 deals with the search of the initial input values of the configuration constraint variables using the closed loop equations (3.6) and (3.7) of the dragline front-end assembly. It also details the process of integration of the dynamics model using the available DAE solver that can handle stiff differential algebraic equations.

4.1. NUMERICAL SOLUTION PROCEDURES

The kinematics and dynamics models of the dragline front-end assembly are a set of differential algebraic equations (DAEs) that describes the physical model of the dragline machinery. DAEs are built using the mutual interactions of the front-end assembly components and their interactions with the mine environment. The configurations constraint equations (3.1), (3.2) and (3.3) in Section 3 are a set of DAEs that contains nonlinear functions of time. The kinematics constraint equations (3.10) and (3.11) are first ordinary differential equations (ODEs) in terms of generalized speeds u_i.

The dynamics equations of motion (3.87) are first DAE in terms $\dot{u}_i$ and second order, nonlinear DAE in terms of q_i. Thus, the solution of the complete model of the dragline system is a numerical solution of combined system of DAEs and ODEs. To establish accurate numerical solution procedures, it is fundamentally required to solve the configuration constraint equations. A unique value of each generalized coordinate must be obtained at one instance of time from the geometrical configuration equations of the front-end assembly and must satisfy these equations at that time. Initial lengths of the hoist and

drag ropes must be input into the equations (3.1), (3.2) and (3.3) and should lie within the actual lengths when a dragline bucket is positioned on the ground to start the digging phase.

The ODEs solver proceeds with the numerical evaluations of the differential kinematics equations that have been developed based on the loop closure equations. The kinematics equations are provided in Appendix A and are derived from the beginning of the starting cycle of the dragline, which is the digging cycle. Once the kinematics quantities are evaluated, the algorithm proceeds to the evaluation of the generalized inertia forces and generalized active forces. An iteration process in the DAEs solver evaluates these forces concurrently with the kinematics quantities based on the initial conditions. The algorithm is developed for the digging phase and full-bucket swinging phase. At maximum bucket capacity, the digging phase ends, and the swing motion starts towards the spoil area.

4.1.1. Kinematics Solution Procedures. The kinematics analysis of the dragline front-end assembly was established on the basis of the DOF and constraints governing the structural member of real draglines. The dragline kinematics model was derived using the concept of generalized speeds in equations (3.10) and (3.11). It also contains all relevant kinematics quantities to perform a full-bucket swinging operation. The model can be extended to account for an empty-bucket, swing-back motion of the machine house with its front-end assembly. This can be done by reversing the direction of the trajectory functions (q_1, q_7 and q_8).

During the kinematics simulation, when the hoist motor clutch is released, the hoist rope length increases and the drag rope reduces in length by retraction. These ropes change their lengths and their respective velocities during the simulation. The orientation and length of the dump rope quickly change at the beginning this phase, but slightly change

during the loaded bucket swinging phase. The orientations of the hoist and drag ropes during these phases change over time in a reciprocal manner. Thus, the kinematics models of these ropes can be mathematically represented by first order ODEs. Also, the nature of the geometrical constraints of the dragline allows the complete kinematics model to be described by a set of multivariable, time-dependent DAEs. The solution of these differential equations can be done by a numerical integration technique that contains the necessary initial conditions for the applications of kinematics constraint and geometrical constraint equations.

Two algorithms are developed for both the digging phase and the loaded bucket swinging phase, where all kinematics quantities ($q_1, q_4, q_5, q_6,\ q_7$ and q_8) change with time. Figure 4.1 shows the algorithm used for the solution of the kinematics model during digging phase. The algorithm uses fixed and variable inputs, which are, respectively, the machine geometrical constraints and hoist and drag ropes linear displacements. The inverse kinematics provides the necessary kinematics functions of the trajectories, q_4, q_5, and q_6, and these quantities are solved during the digging and swinging cycles. The direct differentiations of q_4 and q_6 yield the kinematics differential equations u_{19} and u_{31}, respectively. However, the differential equation of the trajectory function of the dump rope q_5, denoted by u_{25}, was found from the solution of the constraint equations in equations (3.4) and (3.5). This technique provides stability during the numerical integration and reduces the possibility of having singularity in the solution process.

The numerical solver has user-defined functions of the closed kinematics loop, linear displacements of hoist and drag ropes, numerical integration scheme, and outputs.

The initial conditions that represent the hoist and drag ropes lengths, initial values of q_4, q_5, and q_6 are established at the beginning of the integration.

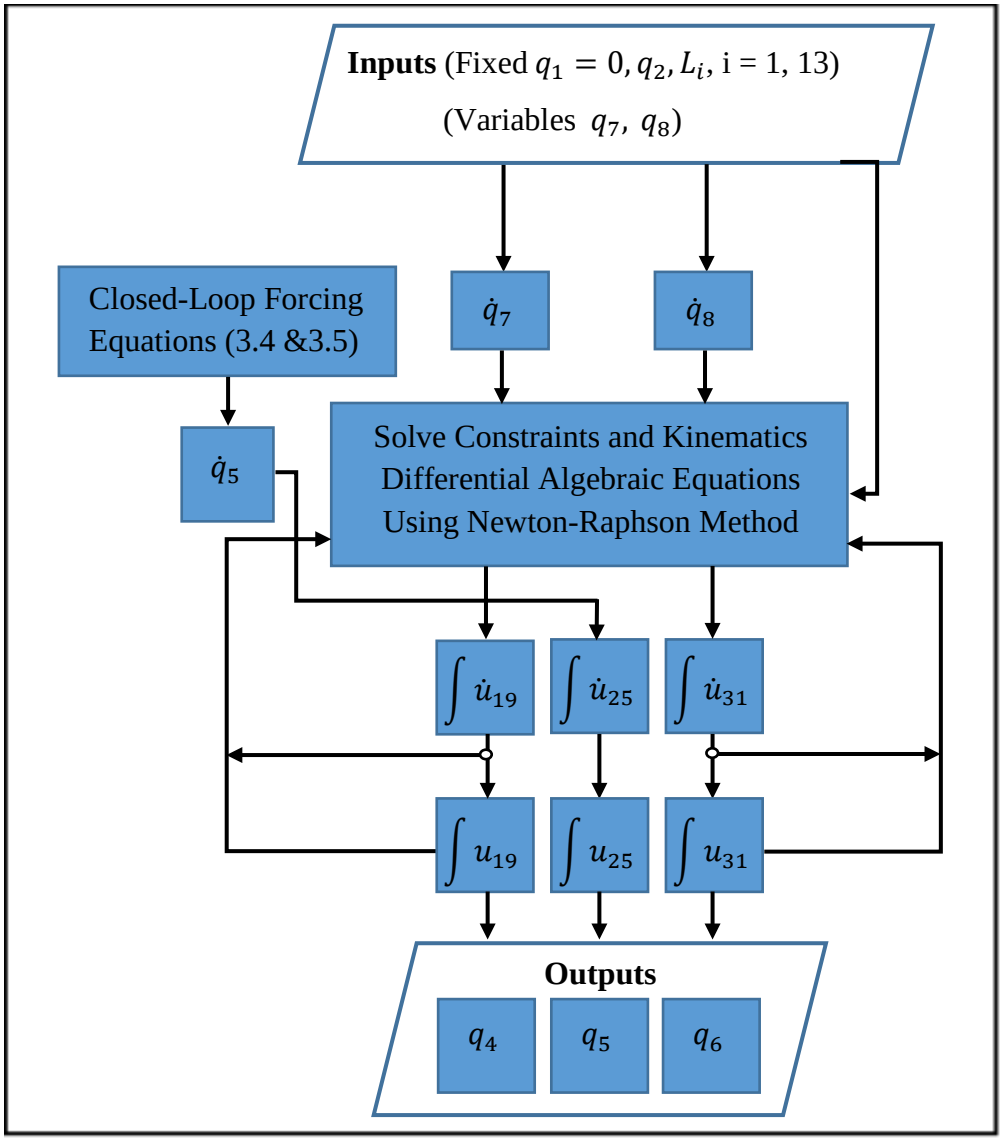

Figure 4.1. Scheme of kinematics procedures algorithm

The results of the first iteration are then used as initial conditions to establish the evolution of the kinematics functions during the entire numerical integration time of the

digging cycle. The results of $q_4, q_5,$ and q_6 of 10 seconds iteration are the output that show the variation of the trajectories of the hoist, dump, and drag ropes over time. The block of an integration sign denotes a numerical integrator that accepts initial conditions for each of u_{19}, u_{25}, and u_{31} and return their respective values $q_4, q_5,$ and q_6. The stability of the numerical integration scheme was established based on the Baumgarte's stabilization technique (Baumgarte, 1972). This technique is used to convert the differential algebraic equations at the velocity level to second order ordinary differential equations at the acceleration level.

4.1.1.1 Initial condition search. The equations resulted from the loop closure and an additional constraint equation for the length of a virtual link D_1F_1 form a set of nonlinear, non-differential, algebraic equations. These equations are used to find the initial conditions of the trajectories and to perform the required kinematics analysis. The nature of these equations makes the direct search for initial conditions a challenging task and requires a special numerical treatment. The differentiation of these equations with respect to time yields a set of DAE that can be solved using advanced numerical methods (Newton-Raphson) since it provides fast convergence to the solution.

- **Full set of constraint equations.** A full representation of the constraint algebraic equations of the trajectories (q_4, q_5, q_6) of the front-end assembly, as well as the linear displacements of the hoist and drag ropes (q_7, q_8) is given in a set of equations (4.1). The symbolic abbreviations, "c" and "s" denote the trigonometric functions, sin and cos, respectively. The linear displacements functions of the hoist and drag ropes are input into the kinematics model and they take the form of the last two rows of equations (4.1).

$$\begin{Bmatrix} 76.60 + 1.715c_4 - 10.5c_5 - c_6q_7 + q_8s_4 = 0 \\ 56.89 + c_4q_8 - 1.715s_4 - 10.5s_5 + q_7s_6 = 0 \\ -11986.81 + 220\,c\left[\frac{37\pi}{180} + q_6\right]q_7 - q_7^2 + q_8^2 - 21\,c[1.57 + q_4 + q_5]\sqrt{2.94 + q_8^2} = 0 \\ -75 + 1.32t + q_7 = 0 \\ -75 - 2.54t + q_8 = 0 \end{Bmatrix} \quad (4.1)$$

To solve the kinematics and dynamics models of the dragline, all of the constraint equations must be satisfied during the numerical integration. Any violation will force the numerical solver to stop the integration, otherwise the numerical results maybe erroneous. These constraint equations define the limits introduced by the machine geometry during the digging phase and are then modified to meet the loaded bucket swinging motion. The initial conditions of (q_4, q_5, q_6) can be resolved by switching these algebraic constraint equations into a set of DAEs that accept initial values of the kinematics entities $(q_4, q_5, q_6, q_7, q_8)$. Equation (4.2) represents a new set of DAEs from the direct differentiation of equation (4.1) with respect to the independent variable (t).

$$\begin{Bmatrix} (\mathrm{c}_4\mathrm{q}_8 - 1.715\mathrm{s}_4)\dot{\mathrm{q}}_4 + 10.5\mathrm{s}_5\dot{\mathrm{q}}_5 + \mathrm{q}_7\mathrm{s}_6\dot{\mathrm{q}}_6 - \mathrm{c}_6\dot{\mathrm{q}}_7 + \mathrm{s}_4\dot{\mathrm{q}}_8 = 0 \\ -(1.715\mathrm{c}_4 + \mathrm{q}_8\mathrm{s}_4)\dot{\mathrm{q}}_4 - 10.5\mathrm{c}_5\dot{\mathrm{q}}_5 + \mathrm{c}_6\mathrm{q}_7\dot{\mathrm{q}}_6 + \mathrm{s}_6\dot{\mathrm{q}}_7 + \mathrm{c}_4\dot{\mathrm{q}}_8 = 0 \\ 21\,\mathrm{s}[1.57 + \mathrm{q}_4 + \mathrm{q}_5]\sqrt{2.94 + \mathrm{q}_8^2}\,(\dot{\mathrm{q}}_4 + \dot{\mathrm{q}}_5) - 220\,\mathrm{s}\left[\frac{37\pi}{180} + \mathrm{q}_6\right]\mathrm{q}_7\dot{\mathrm{q}}_6 \\ +220\,\mathrm{c}\left[\frac{37\pi}{180} + \mathrm{q}_6\right]\dot{\mathrm{q}}_7 - 2\mathrm{q}_7\dot{\mathrm{q}}_7 + 2\mathrm{q}_8\dot{\mathrm{q}}_8 - \frac{21\,\mathrm{c}[1.57+\mathrm{q}_4+\mathrm{q}_5]\mathrm{q}_8\dot{\mathrm{q}}_8}{\sqrt{2.94+\mathrm{q}_8^2}} = 0 \\ 1.32 + \dot{\mathrm{q}}_7 = 0 \\ -2.54 + \dot{\mathrm{q}}_8 = 0 \end{Bmatrix} \quad (4.2)$$

Equation (4.2) takes the form of equation (4.3), which is very common in constrained multibody mechanical systems.

$$F_j(q_i, \dot{q}_i, t) = 0 \qquad (i, j) = (1, .., 5) \tag{4.3}$$

F_j represents the jth DAE, q_i and $\dot{q}_i$ represent the dependent variables or state variables and the time derivative, respectively. An important step to follow when solving the DAEs set in equation (4.2) is to select a good intital value of each dependent variable. This feature defines the difference between the numerical solutions of the DAEs and ODEs. The latter does not necessarily have a good initial value because no hidden constraints must be satisfied at each integration step. A major difficulty in arriving at a quick numerical solution has been attributed to the nature of the dependent variables. In other words, the generalized coordinates do not have the same units and other entities (q_7 and q_8) vary signficantly with time.

Several numerical experiments have been carried out in Matlab and Mathematica to understand the role of every dependent variable on the numerical stability and convergence of the solution algorithm. If no initial values are given to the numerical alogrithm, NDSolve searches for initial values that yields zero DAEs residual. The numerical alogrithm, based on the Newton-Raphson method, achieved a good convergence at 1.52 seconds, but failed to advance the integration due to the presence of singularity at this time step. The trajectories of all ropes based on the initial values are shown in Figure 4.2 (a), with quick changes in their values at the onset of digging. These results show further enhancement of the numerical experiments and can be used as a starting point to construct new values.

Figure 4.2 (b) shows the variations in the lengths of the hoist and drag ropes, with a linear behavior as the bucket penetrates the ground. It can be seen that the initial values of the kinematics parameters, in radians, are $q_{4,1}[0] = 10 * \mathrm{Pi}/180, q_{5,1}[0] = 30 * \mathrm{Pi}/180$, and $q_{6,1}[0] = -30 * \mathrm{Pi}/180$, respectively, and the initial values of the linear displacements of hoist and drag ropes are chosen as 75 m. These linear displacedments are found to reduce the numerical intgeration error. From an operational viewpoint, the rapid change of the angular displacement of the dump rope is unacceptable. This change induces additional vibrations in the rigging system and reduces the machine productivity.

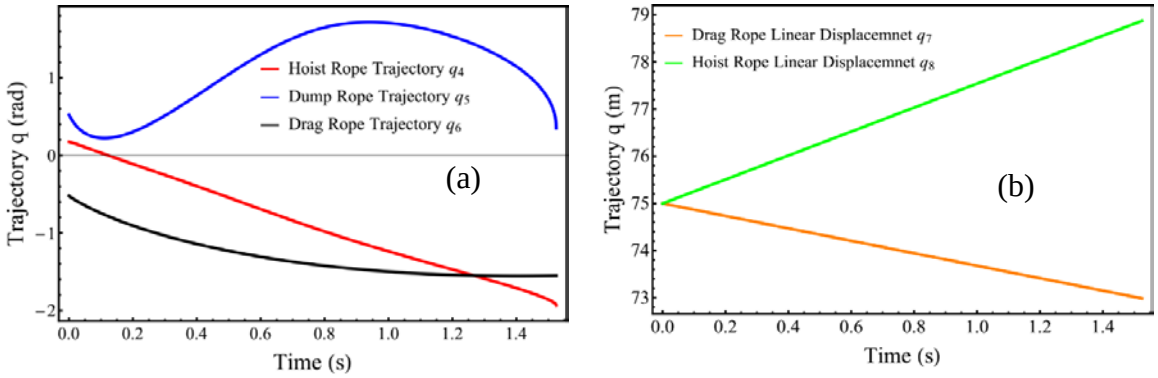

Figure 4.2. Trajectories of hoist, dump, and drag ropes versus time during 1s of digging phase: (a) angular trajectories and (b) linear displacements of hoist and drag ropes

The integration of the DAEs in equation (4.2) with the proposed initial conditions, $(q_{i,1})$ with $i = 0,..,5$, produced a singularity phenomenon shown in Figure 4.3. The second initial values were chosen to minimize the residual values for integrating equation (4.1). This apporach was further used in the calculations to improve the initial values of $(q_{i,n})$, where n is the number of numerical experiments. At each experiment, the solver uses best

values to recalculate the residual at every time step and tries to mimimize it to zero. This kind of numerical study is relevant to an optimization method with inequality constraints.

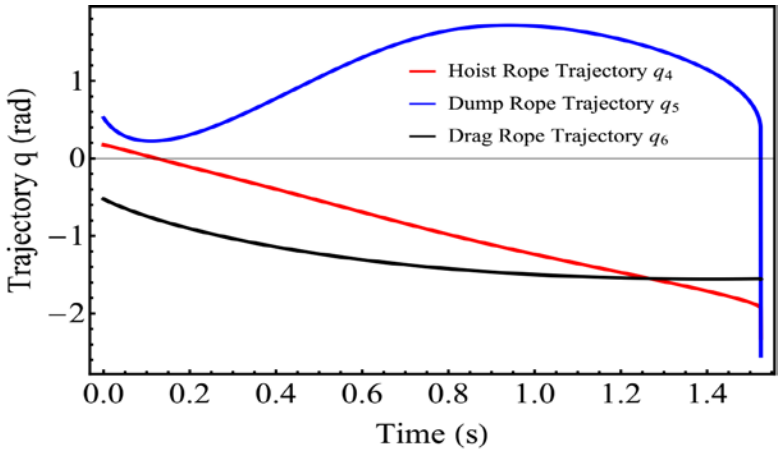

Figure 4.3. Singularity of the kinematics model at time 1.52 s of digging phase

Another method for integrating the DAEs was to start with a zero initial value to every trajectory variable. The alogrithm with a predefined residual minimization embedded option tries to find better values and proceed to the final step. The output of the numerical experiment is shown in Figure 4.4 (a) and another singular location was found at time 7.16 seconds due to the stiffness of equations. Improvements in the numerical integration at time 7.16 seconds of 10-second total digging time do not permit the selection of initial values due to erroneous results in the linear displacements as seen in Figure 4.4 (b). Moreover, the field expirements show that a rapid increase in the trajectory of the hoist rope is not likely to happen during the digging phase. Thus, the numerical stablity of the solution algorithm is not beneficial and cannot be further expanded for finding the actual forces and torques in the front-end assembly.

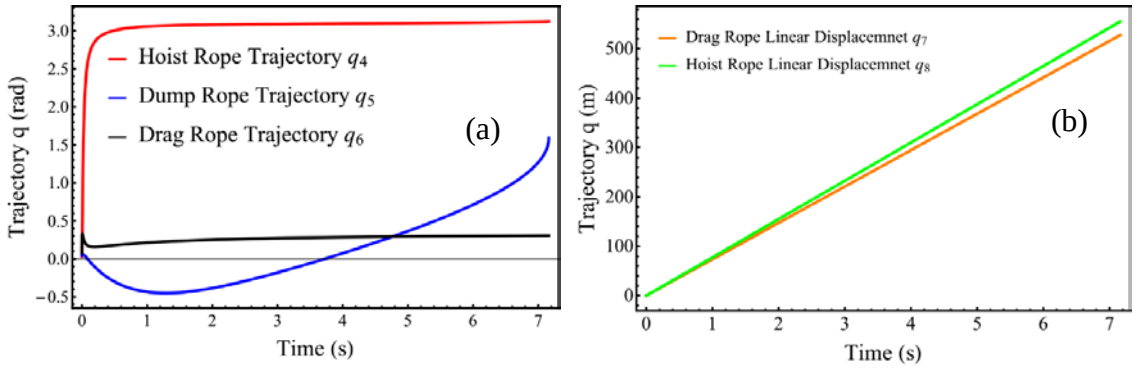

Figure 4.4. Singularity of the kinematics model at time 7.16 s of digging phase: (a) angular trajectories and (b) linear displacements of hoist and drag ropes

- **Minimal set of constraint equations.** The numerical analyses that were done a full set of constraint equations (4.2) resulted in singularity and untable solution process. Numerical stability issues in these analyses are attributed to the fact that the functions of linear displacements cause the integration to fail. In other words, those equations create redundancy that can be avoided by eliminating them. The redundancy means that the excavator has more DOFs available than the number required to do the task. This reason has led to a reduction in the number of the constraint equations to a minimal set as shown in equation (4.4). The numerical solution of these equations is also challenging due to the presence of embedded constraints and the nonlinearities that follow the differentiations. Equation (4.4) forms a set of DAEs that are used to find the initial conditions using FindRoot or NDSolve, which are built-in subroutines in Mathematica. The same analogy is applied to find the initial conditions of all kinematics quantities (q_4, q_5, q_6). It is important to note that the differential kinematics constraint equations (4.4) may yield multiple solutions or may not have any solutions depending the nature of the geometric constraints.

$$
\begin{aligned}
&1.32\,c_6 + 2.54\,s_4 + (75 + 2.54\,t)c_4\dot{q}_4 - 1.715\,s_4\,\dot{q}_4 + 10.5\,s_5\,\dot{q}_5 + \\
&\qquad (75 - 1.32t)s_6\dot{q}_6 = 0 \\
&2.54\,c_4 - 1.32\,s_6 - 1.715\,c_4\,\dot{q}_4 - (75 + 2.54\,t)s_4\dot{q}_4 - 10.5\,c_5\dot{q}_5 + \\
&\qquad (75 - 1.32t)c_6\dot{q}_6 = 0 \\
&2.64\,(75 - 1.32t) + 5.08\,(75 + 2.54t) - \frac{53.34(75+2.54t)\,c[1.57+q_4+q_5]}{\sqrt{2.941+(75+2.54t)^2}} - \\
&290.4\,c\left[\frac{37\pi}{180} + q_6\right] + 21\sqrt{2.94 + (75 + 2.54t)^2}\,s[1.57 + q_4 + q_5](\dot{q}_4 + \dot{q}_5) \\
&\qquad -220(75 - 1.32t)\,s\left[\frac{37\pi}{180} + q_6\right]\dot{q}_6 = 0
\end{aligned}
\tag{4.4}
$$

Equation (4.4) can be rewritten in a matrix form as shown in equations (4.5) and will have a solution only when the Jacobian matrix $\left(J = \frac{\partial F_j(q_i)}{\partial q_i}\right)$ is a full rank matrix.

$$
\begin{bmatrix}
(75 + 2.54\,t)c_4 - 1.715\,s_4 & 10.5\,s_5 & (75 - 1.32t)s_6 \\
-1.715\,c_4 - (75 + 2.54\,t)s_4 & -10.5\,c_5 & (75 - 1.32t)c_6 \\
Z_6 & Z_6 & Z_7
\end{bmatrix}
\begin{bmatrix} \dot{q}_4 \\ \dot{q}_5 \\ \dot{q}_6 \end{bmatrix} =
\begin{bmatrix} -1.32\,c_6 - 2.54\,s_4 \\ -2.54\,c_4 + 1.32\,s_6 \\ Z_8 \end{bmatrix}
\tag{4.5}
$$

The Jacobian is a 3x3 matrix given in the equation (4.6). Thus, the rank of the Jacobian must be 3.

$$
J = \begin{bmatrix}
(75 + 2.54\,t)c_4 - 1.715\,s_4 & 10.5\,s_5 & (75 - 1.32t)s_6 \\
-1.715\,c_4 - (75 + 2.54\,t)s_4 & -10.5\,c_5 & (75 - 1.32t)c_6 \\
Z_6 & Z_6 & Z_7
\end{bmatrix}
\tag{4.6}
$$

$$
Z_6 = 21\sqrt{2.94 + (75 + 2.54t)^2}\,s[1.57 + q_4 + q_5] \tag{4.7}
$$

$$
Z_7 = 220(75 - 1.32t)\,s\left[\frac{37\pi}{180} + q_6\right] \tag{4.8}
$$

$$
\begin{aligned}
Z_8 = {} & 2.64\,(75 - 1.32t) + 5.08\,(75 + 2.54t) - \frac{53.34(75+2.54t)\,c[1.57+q_4+q_5]}{\sqrt{2.941+(75+2.54t)^2}} \\
& -290.4\,c\left[\frac{37\pi}{180} + q_6\right]
\end{aligned}
\tag{4.9}
$$

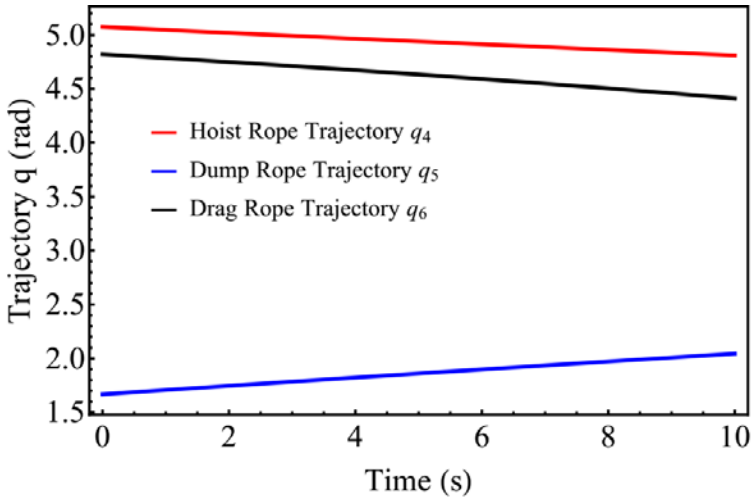

Figure 4.5. Trajectories of hoist, dump, and drag ropes versus time during digging phase

Integration of equation (4.4) was successfully performed using zero initial values of the trajectory functions q_4, q_5 and q_6, in Figure 4.5. The singularity behavior was not an issue and the integration started and ended at the required interval of time $[0, 10]$ seconds. However, the evolution of the trajectory functions through this interval does not meet the limits of the machine's operational space. These responses are due to the fact that the initial values used by the solver at time $t = 0$ second are still out of range. It can be concluded that there is a trade-off between the initial value search and numerical stability of the applied method. To circumvent this problem, subsection (4.1.1.3) highlights the use of Baumgarte Stabilization Technique (BST) to solve a stiff DAE with inequality constraints.

4.1.1.2 Singularity of closed front-end assembly. The singularity behavior is a major issue when attempting to integrate a system of constraint differential equations at different intervals of time $[0, 10]$ seconds. Singularity means that the Jacobian (J) is rank deficient and its determinant is zero. During the integration, the step size becomes very

small at singular positions and the solution algorithm quits without any convergence. From a geometrical viewpoint, singularity means that two or more links in the front-end assembly are coincident and make an angle either (0 or 180) degrees.

Field observations of the dragline operations have shown that the coincidence of dump and drag ropes rarely happens during the digging phase. However, this singular position exists and is depicted in the red-colored vectors in Figure 4.6 (a). The hoisting operations of a loaded bucket swinging require that the drag rope be extended enough at each cycle. As the drag rope extends, the angle between the drag and dump ropes increases and may reach 180 degrees. These positions of the drag and dump ropes cause the closed-loop of the front-end assembly to operate within the proximity of another singularity position. This position is also shown in Figure 4.6 (b), and other positions can be deduced by switching the direction of the short red vector.

Singular positions can be avoided during the numerical integration by applying the appropriate constraints to the solution algorithms. It should be pointed out that the more mathematical constraints are added to the DAE formulation, the stiffer is the mathematical model. Caution should be taken when applying the constraints to the model as it may retard the solution process and reduce the search space. The first inequality constraints applied to the kinematics model are the limits of the hoist and drag rope lengths and are provided in equation (4.10). Other kinematics constraints are chosen in the course of the numerical analysis and were found to be redundant.

$$\left.\begin{aligned} 61.67 \leq q_7 \leq 75.00 \\ 75.00 \leq q_8 \leq 100.18 \end{aligned}\right\} \quad (4.10)$$

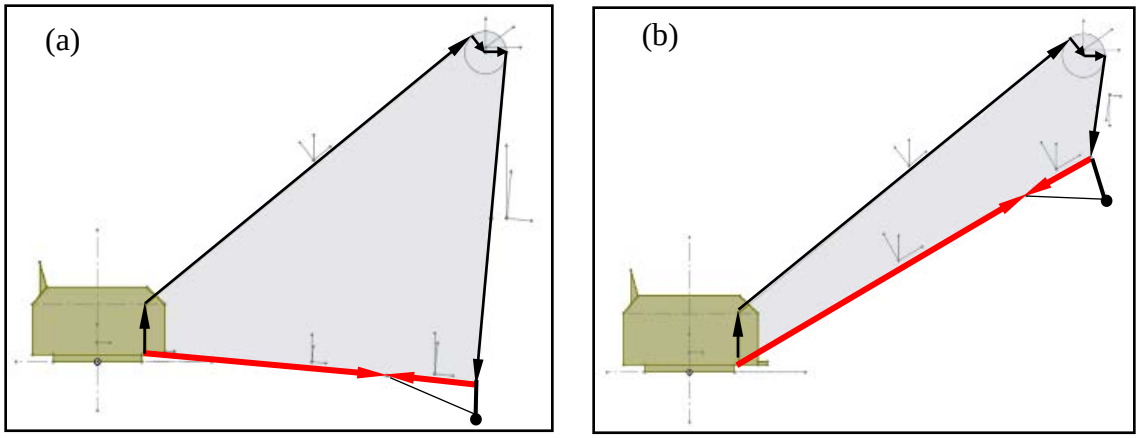

Figure 4.6. Singularity of dragline kinematics models: (a) digging phase (b) full-bucket hoisting phase

4.1.1.3 Baumgarte's stabilization technique (BTS). Although equation (4.4) has shown a higher numerical stability towards the integration over the digging time, it is not sufficient to accurately estimate the trajectories of the ropes and their corresponding initial values. The precedent analyses performed in Section (4.1.1.1) were based on the assumption that the constraint equations (4.1) are smooth and differentiable twice. It was found that the Jacobian matrix is not symmetric and that resulted in singularity at different time steps. Equations (4.1), with the embedded linear displacements of the drag and hoist ropes, is defined by equation (4.11).

$$\mathrm{F}_j(\mathrm{q_i}(t), \mathrm{t}) = 0 \qquad (\mathrm{i}, \mathrm{j}) = (1, .., 3) \tag{4.11}$$

Differentiating equation (4.11) with respect to time results in the constraint equations at the velocity level as shown in equation (4.12). $\mathrm{h}_t(\mathrm{q}, \mathrm{t})$ is called the hidden constraint and is given by the equation (4.13).

$$\frac{d}{dt}\left(\mathrm{F}_j(\mathrm{q_i}(t), \mathrm{t})\right) = J(\mathrm{q(t)}, \mathrm{t}).\dot{\mathrm{q}}(\mathrm{t}) + \mathrm{h}_t(\mathrm{q(t)}, \mathrm{t}) = 0 \tag{4.12}$$

$$\mathrm{h}_t(\mathrm{q(t)},\mathrm{t}) = \frac{\partial(\mathrm{F}_j(\mathrm{q_i}(t),\mathrm{t}))}{\partial t} \tag{4.13}$$

The hidden constraints are just the right-hand side of equation (4.5) and are nonlinear algebraic equations. Differentiating equation (4.12) with respect to time yields the second order differential equation (4.14) at the acceleration level.

$$\frac{d^2}{dt^2}\left(\mathrm{F}_j(\mathrm{q_i}(t),\mathrm{t})\right) = J(\mathrm{q(t)},\mathrm{t}).\ddot{\mathrm{q}}(\mathrm{t}) + \mathrm{J}_q(\mathrm{q(t)},\mathrm{t}).(\dot{q}.\dot{q}) + \mathrm{h}_{tt}(\mathrm{q(t)},\mathrm{t}) + 2\mathrm{h}_{tq}(\mathrm{q(t)},\mathrm{t}) = 0 \tag{4.14}$$

$$\mathrm{J}_q(\mathrm{q(t)},\mathrm{t}) = \frac{\partial \mathrm{J}(\mathrm{q}(t),\mathrm{t}))}{\partial q},\ \mathrm{h}_{tt}(\mathrm{q(t)},\mathrm{t}) = \frac{\partial(h_t(\mathrm{q}(t),\mathrm{t}))}{\partial t},\ \mathrm{h}_{tq}(\mathrm{q(t)},\mathrm{t}) = \frac{\partial(h_t(\mathrm{q}(t),\mathrm{t}))}{\partial q} \tag{4.15}$$

The last two terms in the equation (4.14) are also hidden constraints and their representation is often undesirable due to the complexity of the equations in a constraint multibody system. Equation (4.14) can be rewritten in a simplified form without augmented hidden constraint and is given in equation (4.16).

$$\frac{d^2}{dt^2}\left(\mathrm{F}_j(\mathrm{q_i}(t),\mathrm{t})\right) = J(\mathrm{q(t)},\mathrm{t}).\ddot{\mathrm{q}}(\mathrm{t}) + \mathcal{A}(q,\dot{q},t) \tag{4.16}$$

with

$$\mathcal{A}(q,\dot{q},t) = \mathrm{J}_q(\mathrm{q(t)},\mathrm{t}).(\dot{q}.\dot{q}) + \mathrm{h}_{tt}(\mathrm{q(t)},\mathrm{t}) + 2\mathrm{h}_{tq}(\mathrm{q(t)},\mathrm{t}) \tag{4.17}$$

A central process that follows these derivations is to combine the differential equations (4.12) and (4.16) with the constraint equation (4.11). This combination leads to the Baumgarte's formalism (Baumgarte, 1972), which is given by equation (4.18).

$$\ddot{\mathrm{F}} + \alpha_B.\dot{\mathrm{F}} + \beta_B.\mathrm{F} = 0 \tag{4.18}$$

with,

$$\alpha_B \geq 0\ \ \&\ \ {\alpha_B}^2 = 4\,\beta_B \tag{4.19}$$

α_B and β_B are parameters defined by the user and are more likely selected as stated in equation (4.19) (Baumgarte, 1972). The benefit of using equation (4.18) is that the numerical violations resulted from embedded constraints of velocity and constraint equations are minimized, if not eliminated. The system of equations becomes more stable during integration and the drift error is reduced to a minimum. The drift error can be regarded as the perturbations in the acceleration when the constraint equations and constraint velocity equations are differentiated. Thus, the drift error in equation (4.20) is a quadratic function of time and is related to the constraint equations violation (Simeon, 2010).

$$\kappa = \frac{1}{2}(t - t_0)^2\zeta_a + (t - t_0)\zeta_v + \zeta_p \tag{4.20}$$

ζ_a, ζ_v and ζ_p are constants associated with the error at acceleration, velocity and position levels, respectively. The use of Baumgarte's method has been found to solve the singularity problem and improve the accuracy of resulting trajectories. However, the choice of parameters bigger than 3 did not dampen the errors, but resulted in a stiff DAE system. Correct trajectories are generated after integration for the selected parameters $\alpha_B = 1$ and $\beta_B = 0.25$ and are shown in Figure 4.7 (a). Other trajectories that are not within machine limits are not a part of the solution of the equations of motions. In addition, the applicability of BTS was also evaluated against the errors, which are calculated from the invariants (constraints algebraic equations). Caution must to be taken when choosing the values of Baumgarte's parameters. From Figure 4.7 (b), the selection of $\alpha_B = 6$ and $\beta_B = 9$ meets the conditions of equation (4.19). However, it has changed the structure of the

constraints and their derivatives. Consequently, the numerical analysis has produced inaccurate results.

It can be concluded from Figure 4.7 (a) that the angular displacements of the hoist and drag ropes follow the same behavior and their trajectories vary within the machine limits for the parameters $\alpha_B = 1$ and $\beta_B = 0.25$. The same behavior can be seen for values $\alpha_B = 6$ and $\beta_B = 9$, but the values of the angular displacements of the hoist and drag ropes are around 70 ° and 90 ° and are not within the machine limits. The initial conditions of the angular displacements of the rope angles and their initial angular velocities are listed in Table 4.1.

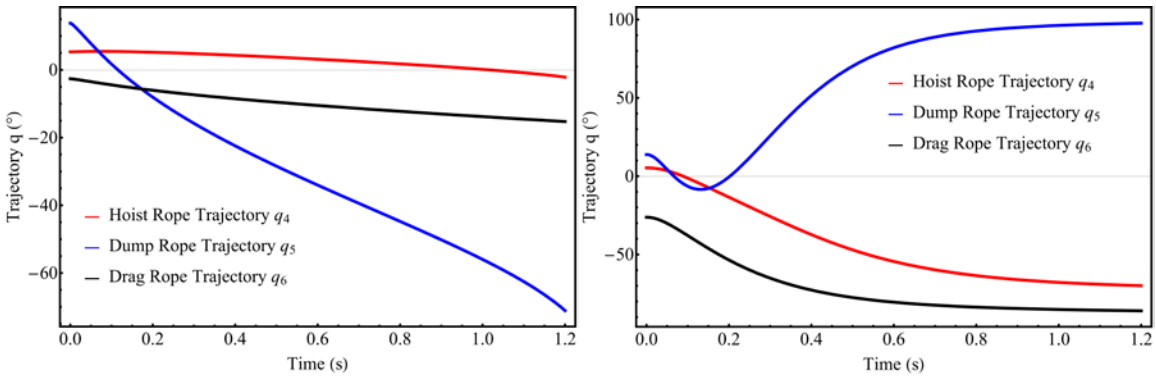

Figure 4.7. Trajectories of ropes using BTS during digging phase: (a) α =1, β =0.25 (b), α =6, β =9

Table 4.1 Initial angular displacements and angular velocities of ropes

Rope	Initial Angle (rad)	Initial Velocity (rad/s)
Hoist rope	$q_4[0] = -0.0437$	$\dot{q}_4[0] = 0.0$
Dump rope	$q_5[0] = \quad 0.2831$	$\dot{q}_5[0] = 0.0$
drag rope	$q_6[0] = -0.4692$	$\dot{q}_6[0] = 0.0$

4.1.2. Dynamics Solution Procedures. The dynamic model of the dragline front-end assembly was formulated based on Kane's method. The mathematical model, in Section 3, has all the relevant information to perform the inverse dynamic analysis. Figure 4.8 shows the flowchart for developing and implementing the simultaneous kinematics and dynamic analyses. The solution of the dynamic model during the digging phase is two-fold: (i) feedforward displacement calculations based on Newton-Raphson method in Mathematica, and (ii) inverse dynamics based on the calculated feedforward displacements from step (i). These procedures are also used for calculating the drag force and hoist and swing torques for the loaded bucket swing motion. The inverse kinematics analysis must be integrated in the solution of the inverse dynamic procedures. The BST used in Section 4.1.1.3 is integrated into the dynamics solution procedures to enforce the constraints of equation (4.4).

It can be seen from Figure 4.8 that the dynamic analysis of a dragline is similar to any multibody dynamic analysis. It starts with a mathematical formulation of the constraint equations, followed by a full kinematics analysis for defining the independent generalized speeds, and finally the formulation of the EOM using Kane's method. The latter are solved simultaneously by enforcing the acceleration constraints using BST to minimize the drift errors. Finally, the outputs of the numerical analysis are plotted and verified based on the machine operational limits. The outputs of the dynamics model during the digging phase include the drag force and hoist torque. In the case of loaded bucket swinging phase, the outputs include the drag force and hoist and swing torques that are used as inputs in the advanced finite element analysis on wire ropes. The errors due to constraint violations are

also plotted and visualized to verify the accuracy of the solution approach and the numerical algorithm.

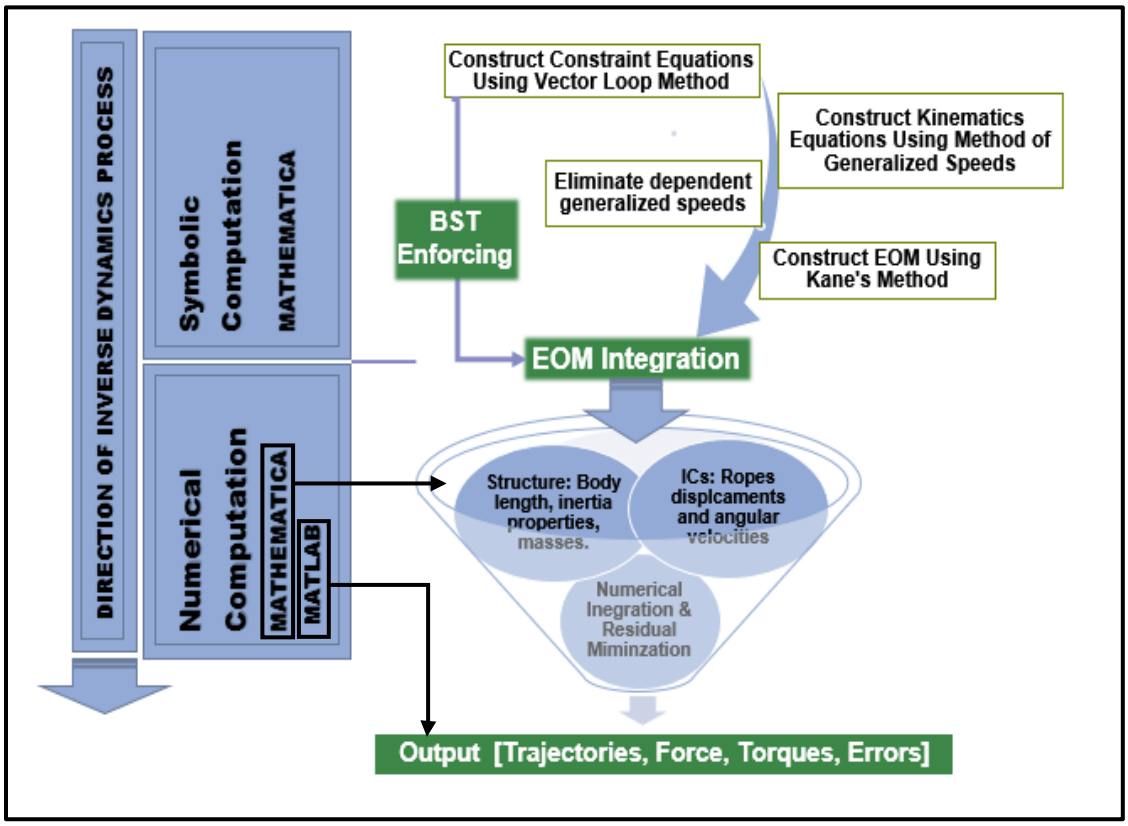

Figure 4.8. Flowchart of the dynamics solution algorithm

The equations of motion in equation (3.87) combined with the acceleration constraint equations in equation (4.4) form a stiff system of highly nonlinear differential equations. The initial conditions found in Section (4.1.1.1) must be consistent and produce minimal errors over the whole integration domain. The derivation of the constraint algebraic equations with respect to time produces a system of equations with a reduced index and it changes the structure of the original equations. As was seen in equations set

(4.5), the derived equations contain additional expressions of nonlinear trajectory functions, which result in drift errors. The DAE solver in Mathematica contains the necessary algorithms to handle a stiff system for a twice-differentiable drift. The reduction of the drift error, in the solution algorithm, is based on using a simplified method that minimizes the residual at each iteration step. In other words, the right-hand side of the complete system, in equation (4.18), is subtracted from the left-hand side to create a residual function. A general type of this residual is given by equation (4.21).

$$\mathrm{F}_j(\mathrm{q_i}(t), \dot{\mathrm{q}}_\mathrm{i}(t), \mathrm{t}) = 0 \tag{4.21}$$

The initial conditions proposed earlier satisfy this residual, as well as its derivative, which is given in the equation (4.22).

$$\frac{d}{d}\,\mathrm{F}_j(\mathrm{q_i}(t), \dot{\mathrm{q}}_\mathrm{i}(t), \mathrm{t}) = 0 \tag{4.22}$$

Inconsistent initial conditions are more likely to violate the residual equations and their derivatives resulting in accumulated errors. Solving DAE with higher index is very challenging because of the requirement to satisfy several equations along with second-to-third degrees of their derivatives. The procedures of the DAE solvers are described in the integrated solution algorithm in Figure 4.9. The algorithm contains a solver for the first order kinematics DAE, a solver for the second order kinematics DAE, and a dynamic solver that integrates the equations of motion. The algorithm starts evaluating the index of the constraints algebraic equations and determines the order of differentiations that is required to relate the variables together. If the index of the DAE1, DAE2, and DAE3 is 1, the equations are solved by integration and their results are passed onto the equations of motion solver.

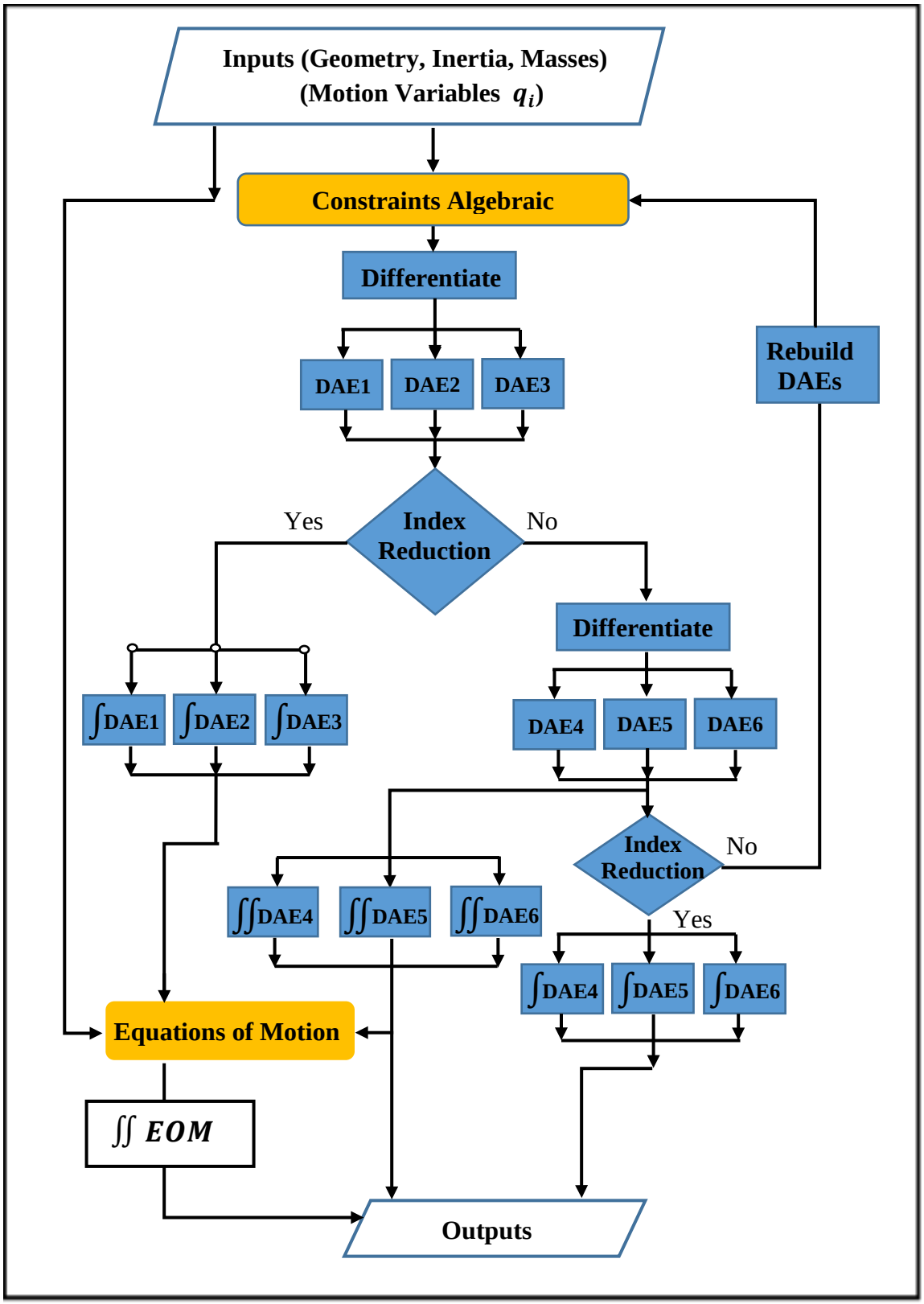

Figure 4.9. Scheme of numerical implementation of the DAE solvers

If the index of the DAE1, DAE2, and DAE3 is 1, the equations are solved by integration and their results are passed onto the equations of motion solver. When the DAE index is 2, a second derivation is performed on the constraints equations and the DAE 4, DAE 5, and DAE6 are then integrated and plotted. In addition, their integration results are passed onto the dynamics solver to calculate the required forces and torques.

The constraint algebraic equations may have an index of three that requires an additional differential order to be carried out to relate the hidden variables. This case is encountered in the vibration and jerky motion of links in the mechanical system. It can be concluded that the formulation of the constraint equations has a profound impact on the numerical solution process. In general, the dynamics of a closed kinematics mechanism that possesses a number of links less than 3 can be done without any difficulty. However, for a multilink mechanism, such as the dragline front-end assembly, it requires a substantial amount of work and fine tuning of the model at all stages of its development. Therefore, it is recommended to start the kinematic and dynamic analyses using a simplified vector loop equation and then expanding it to incorporate additional links. It should be pointed out that the derivations of the kinematic and dynamic models are done in Mathematica and are provided in details in Appendix A.

4.2. VERIFICATIONS OF THE MODELS

The verification of the mathematical model is established based on the technological capabilities and limitations of a real-world dragline machinery. The mathematical model contains the important geometric, structural, and operational features for performing the numerical experimentations. The verification process is three-fold:

4.2.1. Verification of the Symbolic Mathematical Model. The derivations of the kinematic and dynamic models of the dragline front-end assembly are performed by hand using the concept of intermediate variables (Kane and Levinson, 1985). This concept is a good approach for simplifying the work flow of the derivation and reduces the amount of arithmetic calculations in a large multibody dynamic model. The analytical model was then derived using Mathematica, on a step-by-step basis, to generate the same hand-calculations. Both the hand and computer calculations are compared for the resulting symbolic output of all functions and are provided in Appendix A.

4.2.2. Verification of the Virtual Model and Structural Properties. The dragline has several massive structures, such as machine undercarriage, machine housing, and front-end assembly (boom, boom-point sheave, ropes, and bucket and rigging mechanism). These structures weigh thousands to hundreds of thousands tons and have complex geometries that need to be designed properly. A 3-D CAD software, SolidWorks, was used to create the geometries and estimate the masses and inertia properties of each structural system used in the dynamic model. The dragline virtual model, a Marion 7800 dragline, has a working weight of 1,383,457 kg (Nikiforuk and Zoerb, 1966). Thus, all structural systems including the ropes are designed to satisfy this total weight. Figure 4.10 shows the geometry and structural details of the boom.

The inertia property of the multilink structure, such as boom structure, are calculated after grouping all structural members using structural steel (ASTM A36). The central moments of inertia of the corresponding body must be measured in a reference frame that exactly matches its local frame in Figure 3.2. Otherwise, the dynamic model yields erroneous results. Structural steel members of the boom are pipes with inner and

outer diameters 0.206 m and 0.27 m, respectively. Other structural data of the dragline are provided in Figures 4.11-4.15 and in Tables 4.2-4.5. The moments of inertia of the boom are selected according to the values calculated using SolidWorks in Figure 4.11 (see dashed frame). They are calculated with respect to the center of mass (COM) of the boom and aligned with the output coordinate system.

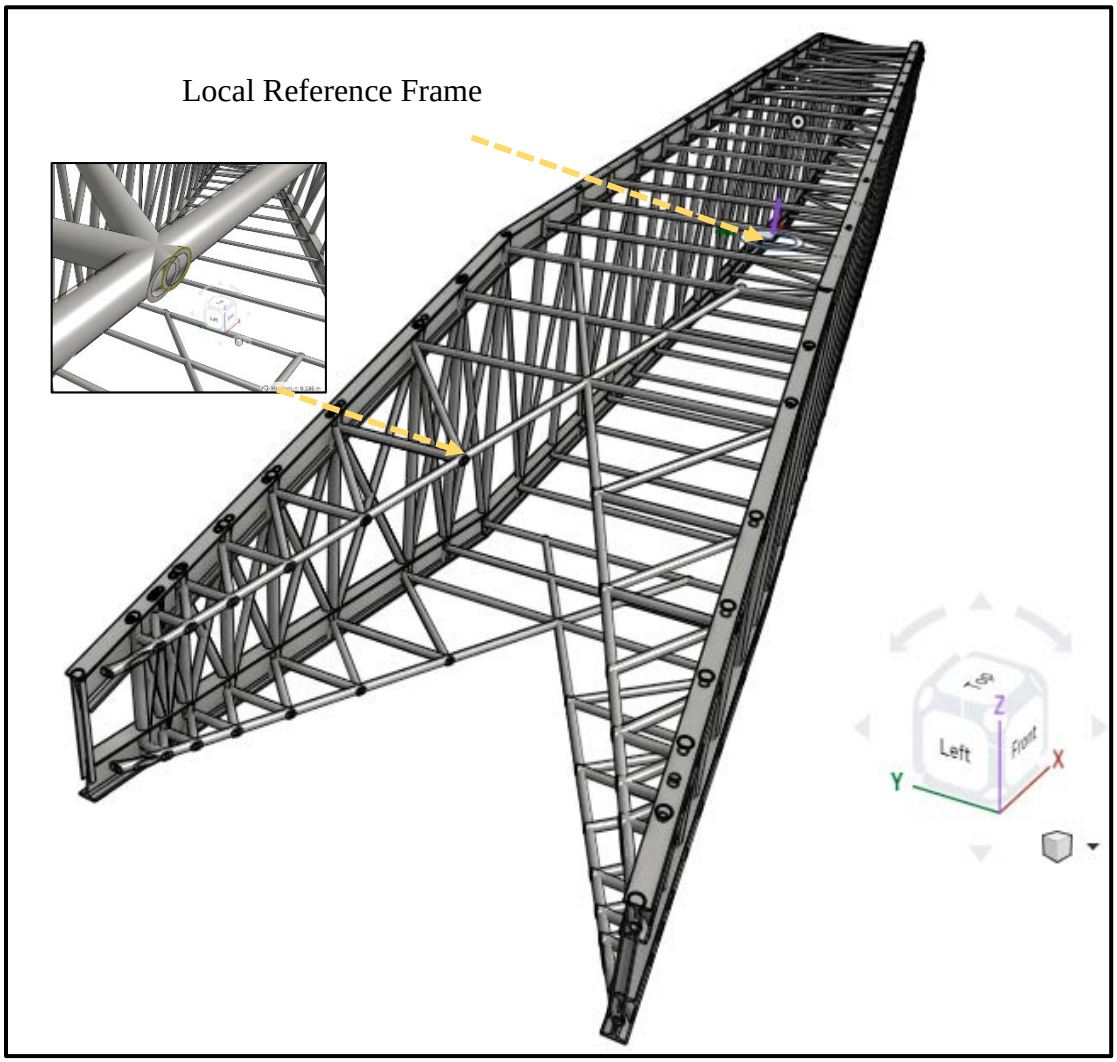

Figure 4.10. Dragline boom and its structural detailing

Table 4.2. Boom structure and its material and structural properties

Density	7,850.00 kg/m³		
Mass	421,149.81 kg		
Moments of Inertia	C_{11}= 13,075,449.73	C_{12}= -2,138,753.88	C_{13}= -43,689.34
	C_{21}= -2,138,753.88	C_{22}= 272,515,394.48	C_{23}= -60,270.76
	C_{31}= -43689.34	C_{32}= -60,270.76	C_{33}= 272,515,394.48

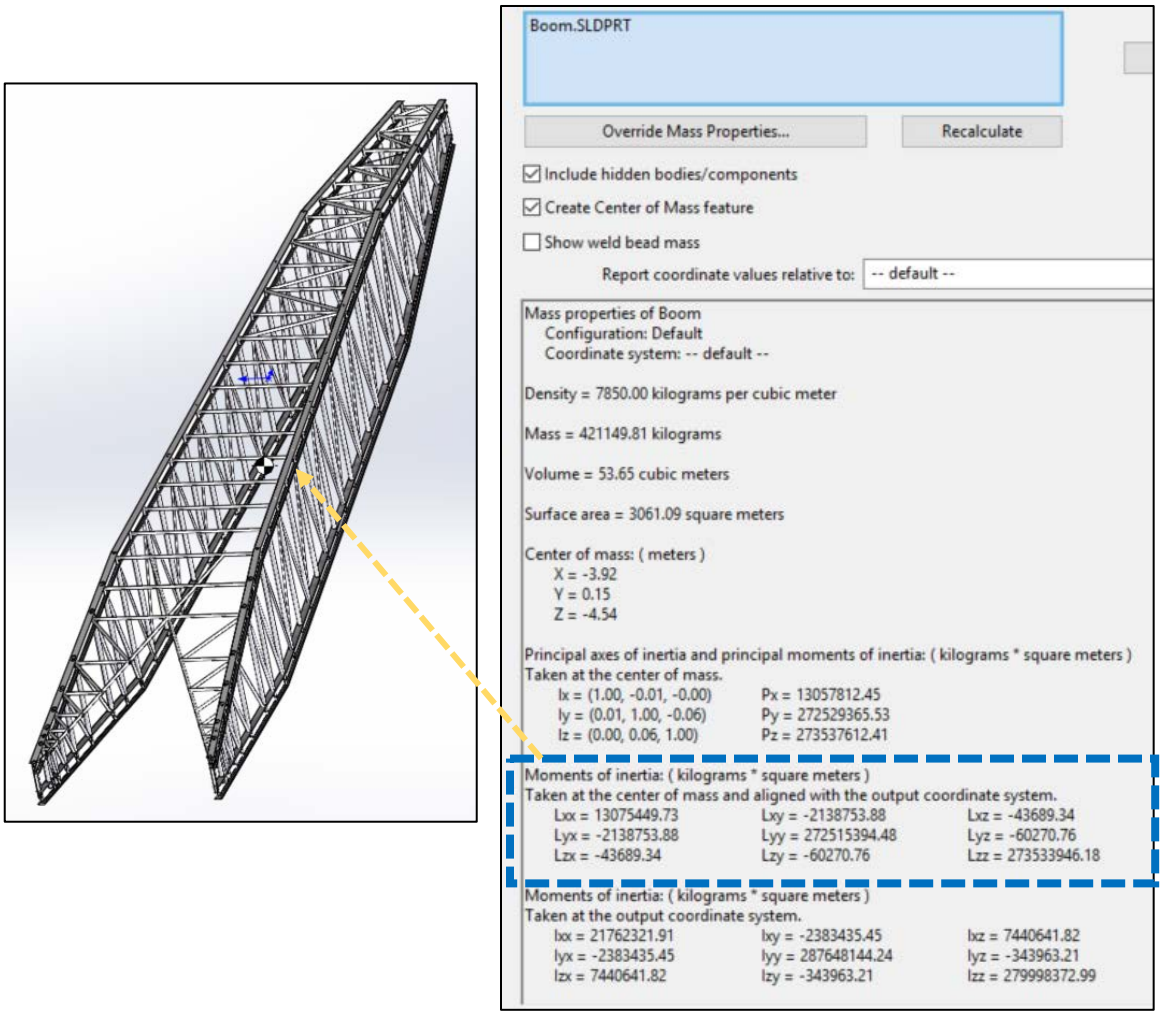

Figure 4.11. Boom structure and its structural properties

The structural system of the machine housing and mast are designed as one structure and it is shown in Figure 4.12. The moments of inertia are taken from Figure 4.12 (see dashed frame) since this coordinate system is aligned with that defined in Figure 3.2. Obviously, this selection results in higher moments of inertia when the machine swings. Moreover, the significant inertia loads that develop during the rotation increase the tension in the drag and hoist ropes. Thus, these values provide a baseline for a better estimation to the forces and torques. The values of these inertia and the structural mass and material density are also given in Table 4.3. The material used for this design is structural steel (ASTM A36).

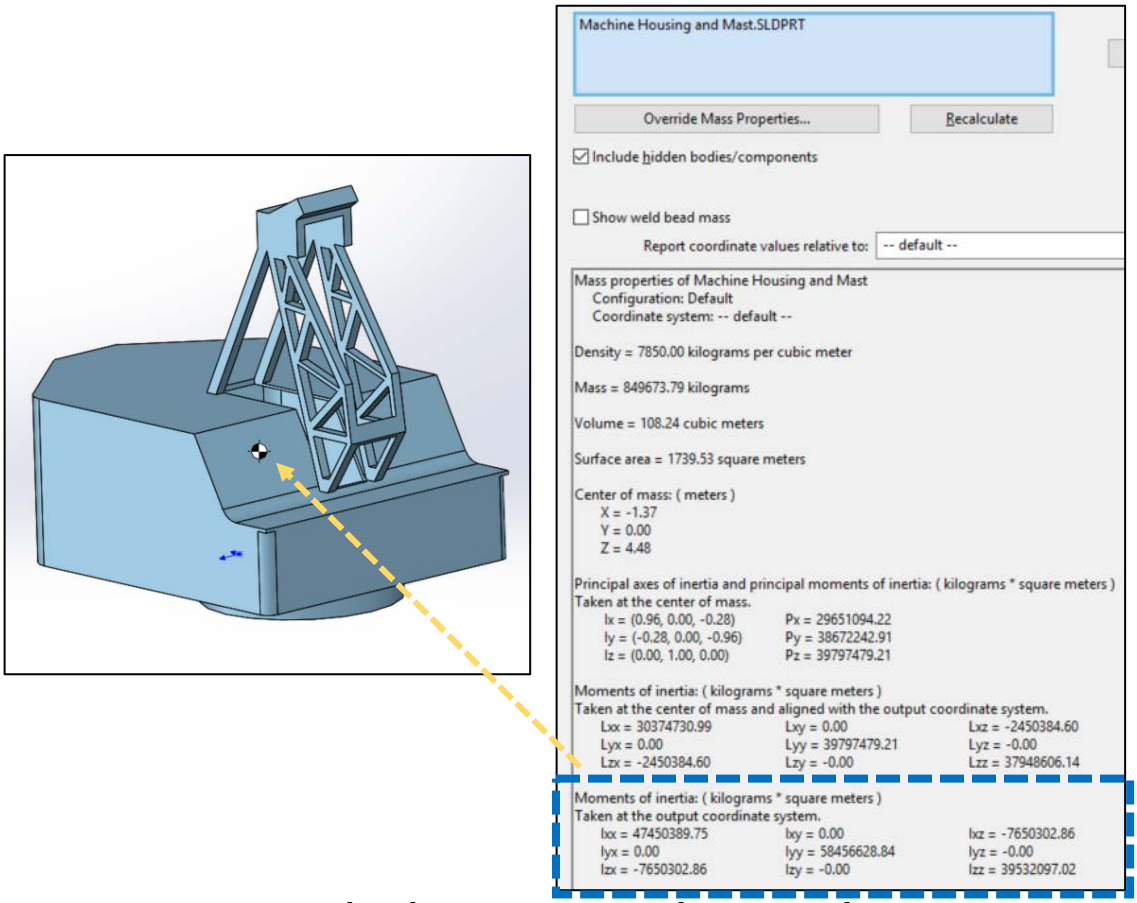

Figure 4.12. Machine housing structure and its structural properties

Table 4.3. Machine housing and mast and their material and structural properties

Density	7,850.00 kg/m³		
Mass	849,673.79 kg		
Moments of Inertia	B_{11}= 47,450,389.75	B_{12} = 0.0	B_{13}= -765,0302.86
	B_{21}= 0.0	B_{22}= 58,456,628.84	B_{23}= 0.0
	B_{31}= -7,650,302.86	B_{32}= 0.0	B_{33}= 39,532,097.02

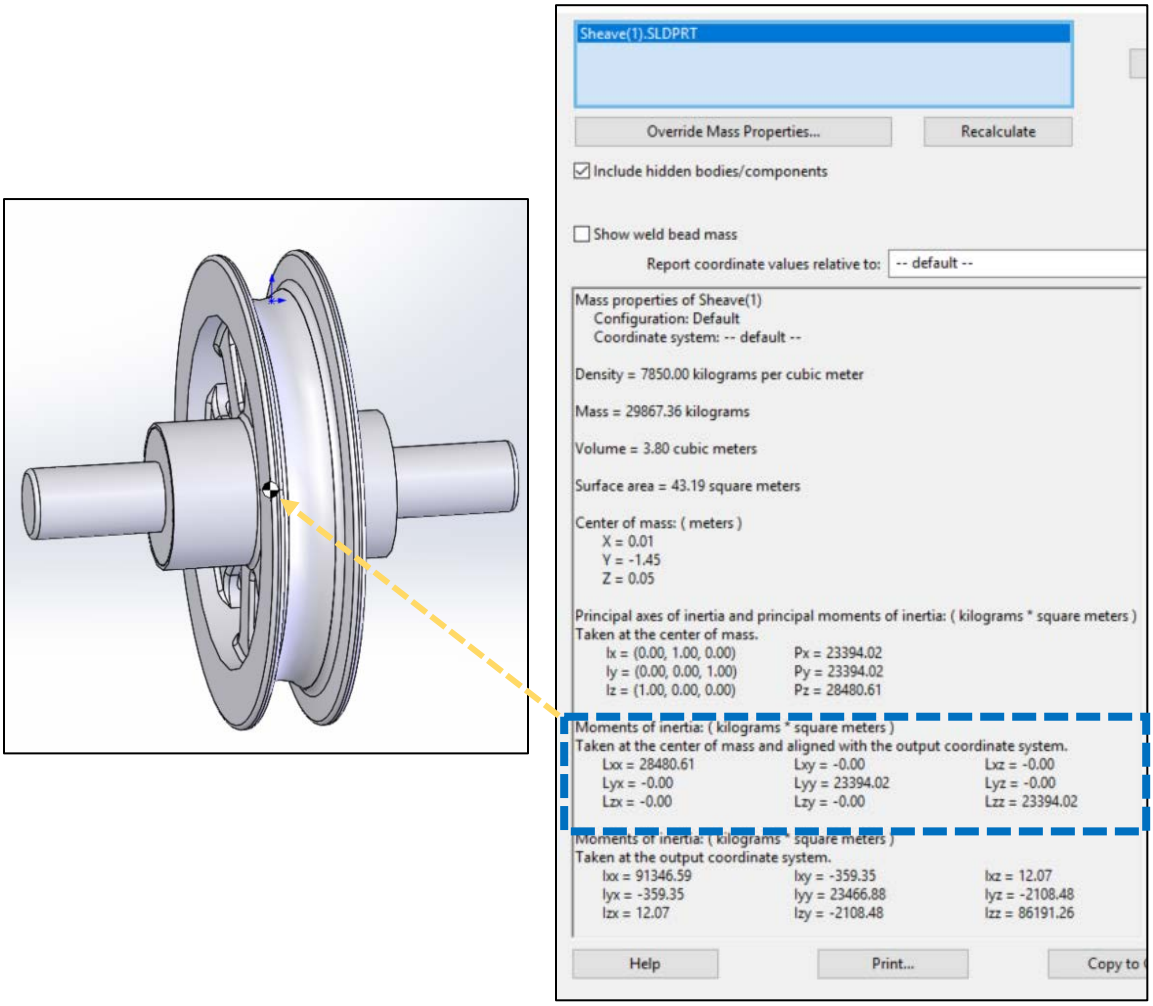

Figure 4.13. Boom point sheave design and its structural properties

The boom point sheave design and its structural and material properties are given in Figure 4.13 and Table 4.4. The sheave has a radius $R_s = 1.715$ m and is made of a structural steel (ASTM A36). The groove width, where the hoist rope runs, is $d = 350$ mm.

Table 4.4. Boom point sheave and its material and structural properties

Density	7,850.00 kg/m³		
Mass	29,867.36 kg		
Moments of Inertia	D_{11}= 28,480.61	D_{12}= 0.0	D_{13}= 0.0
	D_{21}= 0.0	D_{22}= 23,394.02	D_{23}= 0.0
	D_{31}= 0.0	D_{32}= 0.0	D_{33}= 23,394.02

The bucket and rigging design contains several structural elements (bucket, hoist chains, drag chains, dump sheave, trunnions, dump rope, spreaders and connecting pins). The description of this design, as well as its material properties are given in Figure 4.14 and Table 4.5. The same material used for the boom and machine housing is also used for all other structures in the front-end assembly, which a structural steel, type (ASTM A36).

Table 4.5. Bucket and its rigging and their material and structural properties

Density	7,850.00 kg/m³		
Mass	30,000.23 kg		
Moments of Inertia	F_{11}= 1,523,336.30	F_{12}= 18,410.32	F_{13}= 89,651.56
	F_{21}= 18,410.32	F_{22}= 1,346,557.91	F_{23}= 237,263.18
	F_{31}= 89,651.56	F_{32}= 237,263.18	F_{33}= 338,923.45

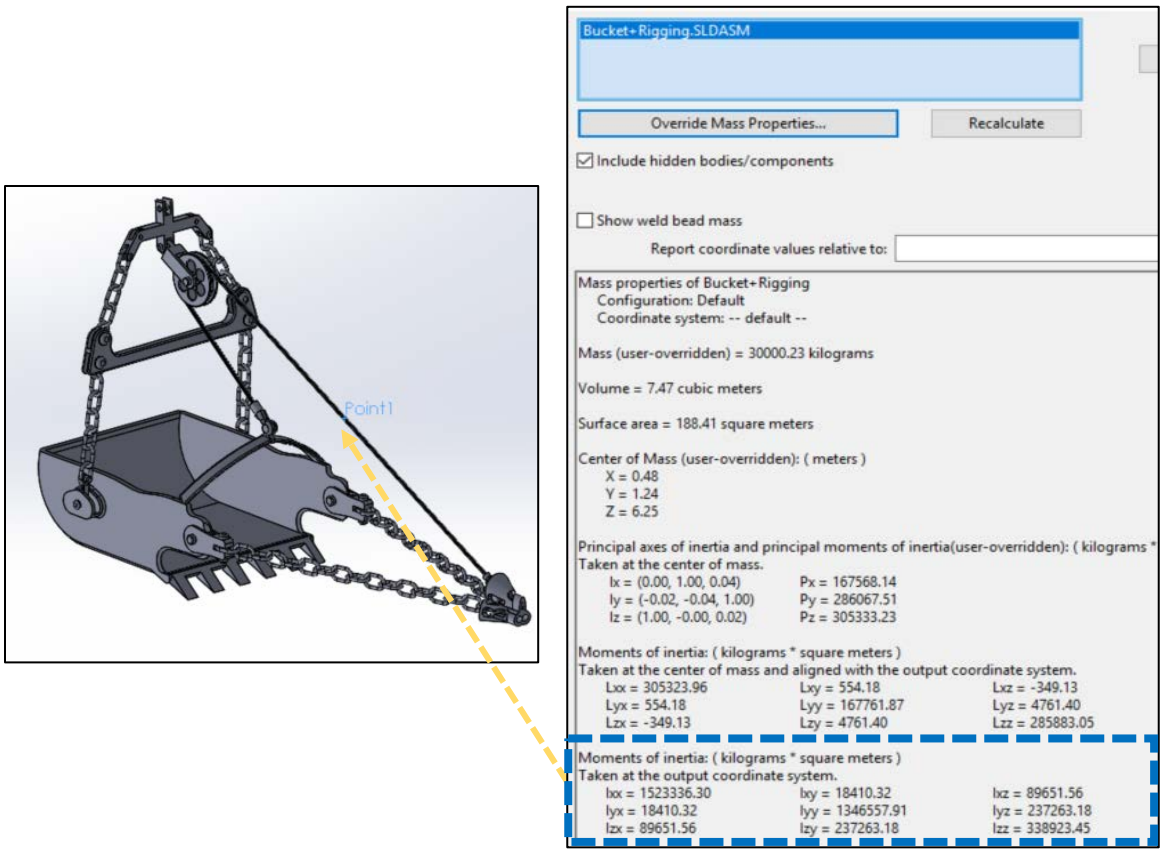

Figure 4.14. Bucket and rigging design and their structural properties

Drag and hoist ropes are considered typical in terms of design and material properties. The initial lengths of both ropes are also equal to 75 m. The resulting structural properties and design of drag and hoist ropes are given in Figure 4. 15 and Table 4. 6.

Table 4.6. Drag and hoist ropes and their materials and structural properties

Density	7870.00 kg/m³		
Mass	2,729.57 kg		
Moments of Inertia	G_{11}= 1,082,956.60	G_{12}= 0.0	G_{13}= 0.0
	G_{21}= 0.0	G_{22}= 1,082,956.60	G_{23}= 0.0
	G_{31}= 0.0	G_{32}= 0.0	G_{33}= 2.18

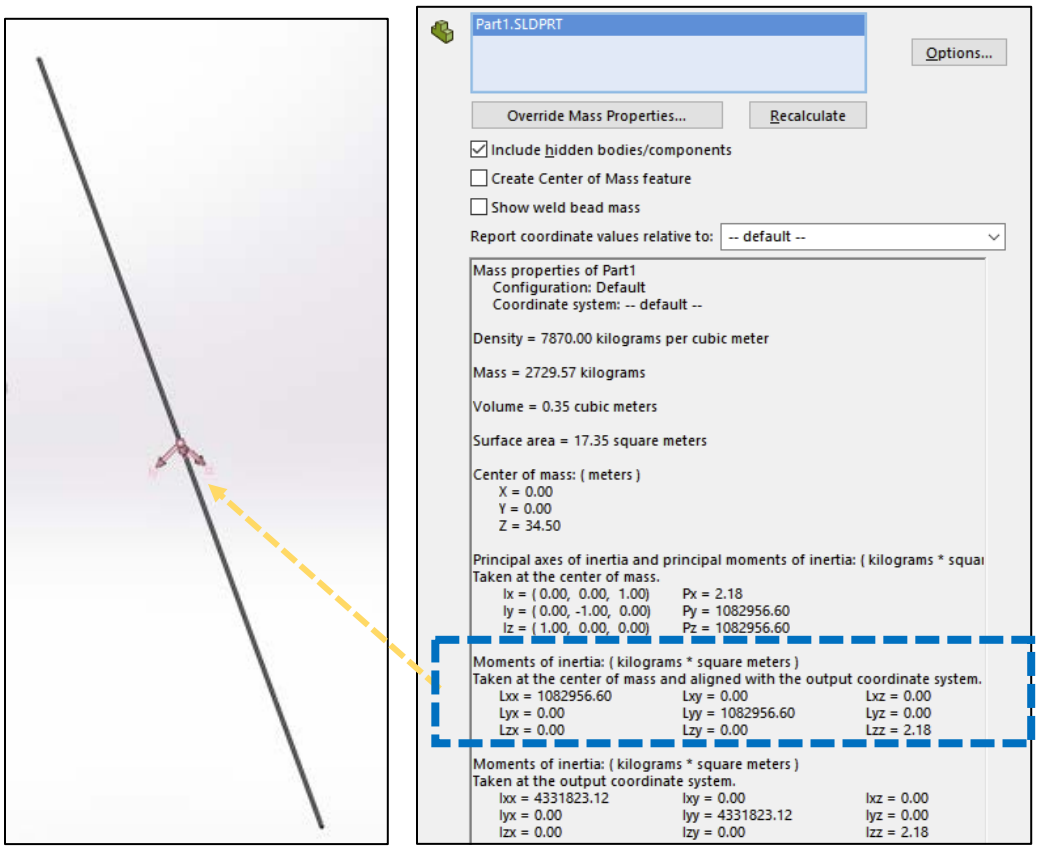

Figure 4.15. Drag and hoist ropes design and their structural properties

The total mass of the dragline machinery is calculated as the sum of the masses of the machine housing and its mast, boom, boom point sheave, bucket and rigging system, and ropes. This weight must not exceed the weight, 1,383,457 kg (Nikiforuk and Zoerb, 1966), is calculated according to equation (4. 23).

$$W_D = W_{M.hosuing} + W_{Boom} + W_{Sheave} + W_{Bucket} + W_{ropes} \quad (4.23)$$

$$= 849{,}673.79 + 421{,}149.81 + 29{,}867.36 + 2 \times 2{,}729.57$$

$$= 1{,}306{,}150.1 < 1{,}383{,}457 \text{ Kg}$$

Thus, this design is acceptable with and an error of 0.055%.

4.2.3. Verification of the Operational Limits. Operational limits are the loading and geometrical constraints that a dragline cannot surpass based on its allowable design load and geometric properties. The linear and angular trajectories of the hoist, dump, and drag ropes are limiting geometries of the dragline despite their flexibilities. In addition, the loading scenarios of a dragline vary from cycle to cycle and must not exceed the allowable designed limits. During the digging phase, the hoist rope extends and drag rope retracts following linear functions of time as prescribed in equation (4.1). Figure. 4.2 (b) shows that the hoist and drag rope operate within the machine limits. Another feature is that their trajectories change with time as the bucket engages the bank and are consistent with the limits of the dragline.

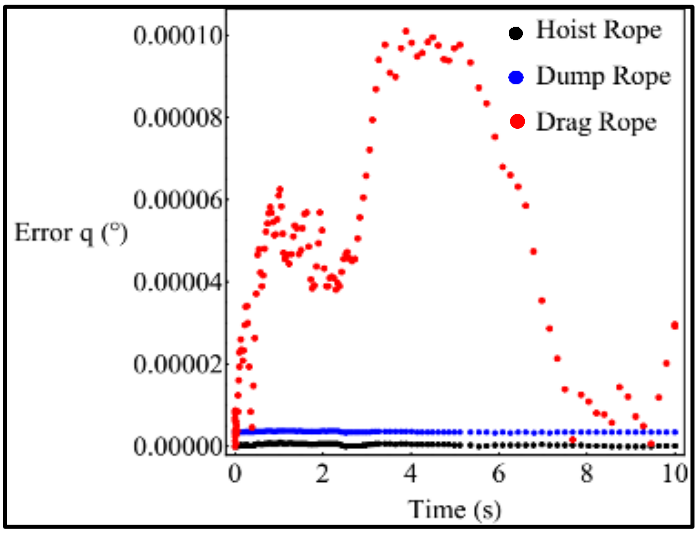

Figure 4.16. Trajectories errors of the hoist, dump, and drag ropes

The angular displacements of the hoist, dump, and drag ropes do not exceed 27°, 26° and 65°, respectively. Thus, the bucket motion is limited by these constraints to prevent

it from hitting the boom or the machine house. The resulting errors of these operational constraints are derived from the constraint equation (4.1) using Mathematica. These functions estimate the changes of each variable and return the absolute error during the numerical experiments. The error associated with each trajectory function is shown in Figure 4.16 and the drag rope has the maximum value. It can be seen that all trajectories errors are less than 10^{-4} degree, which indicate the accuracy of the kinematics analysis and the solution algorithm.

4.3. VALIDATION OF THE DYNAMIC MODEL

After the numerical model is verified using accurate design inputs and design variables, it is validated by checking the evolution of the resulting hoist torque and drag force during the course of simulation in the digging phase using real-world environment. The results are validated using machine capacity and ropes breaking loads. These results are provided in details in Section 5 for the kinematic and dynamic analyses (see Sections 5.1 and 5.2). The resulting forces of the dynamic model are important for the finite element analysis on wire ropes. They are used as boundary conditions for the static and dynamic analyses.

Figure 4.17 (a) shows the maximum drag force, 1.19×10^6N, that was predicted by the dynamic model during the digging phase. Nikiforuk and Ochitwa (1964) stated that the maximum drag load that the dragline machinery can pull, at a rated speed of 1.32 m/s (260 f.p.m), is 136,077.7 kg (300,000 lb). The value of 136,077.7 kg is equivalent to a load (136,077.7 kg $\times$ 9.81 m/s^2), which is 1,334,922.237 N. Thus, the dynamic model is capable of producing right values of the drag load.

In the case of predicting the hoist force, the dynamic model defines a hoist torque as one of its outputs. The maximum hoist torque occurs within the hoist phase when the loaded bucket is hoisted to its closest point to the boom-point sheave. Figure 4.17 (b) shows the resulting hoist torque from the numerical experiment in this phase. It can be seen that the hoist torque is maximum at time 40 seconds, where the swinging-back cycle time has elapsed 10 second. The maximum value of the torque is 922,930.00 N.m. This value is transformed to the form of load, which is 54,857.45 kg on the sheave. The allowable hoist force for the dragline (Nikiforuk and Ochitwa, 1964) is 125,645.1 kg (277,000 lb).

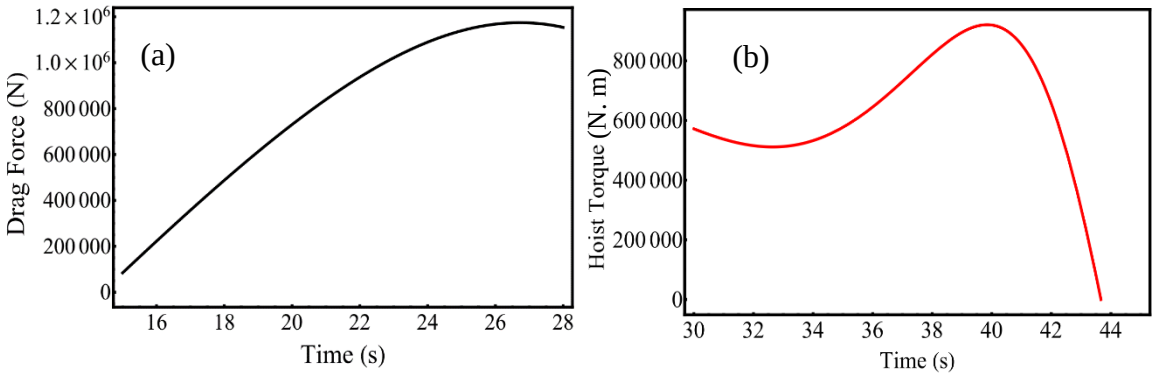

Figure 4.17. Maximum Generated loads on the drag and hoist ropes

4.4. WIRE ROPES STRESS MODELING

The dragline machinery operates in a harsh environment under variable, repeated loading scenarios, which endanger the machine availability, productivity, and its service life. The maximum allowable loads on the hoist and drag ropes in a dragline machinery, such as Marion 7800, can reach up to 136,077 kg (300,000 lb) and 125,645 kg (277,000 lb), respectively, (NikiForuk and Zoerb, 1966). The dragline bucket payload and its dead

weight introduce significant stresses on the drag and hoist ropes and reduce their expected useful life.

This research endeavor provides a stepwise analysis of the stresses generated in ropes of different constructions and diameters. The use of finite element method (FEM) makes such analysis possible in the highly deformable flexible wire ropes. FEM is used to estimate the stresses distribution in a complex structural system that operates under the static and dynamic loading conditions. The structure is discretized into finite segments or elements that may vary in size and shape. The problem space is then defined by a number of nodes whose degrees of freedom (DOF) vary based on the boundary conditions. The application of boundary conditions along with the nodes information constitute a set of PDEs. The solution of the PDEs reveals information about displacements, forces, torques, stresses, and other reactions that capture the response of the system under the load.

Recent advancements in high performance computational environments (solution capabilities, fast processing and visualization techniques) in the last decades have improved the problem solving efficiency and accuracy. However, analyzing a large system using FEM to obtain a closed-form solution, is time-consuming and computationally expensive. For wire rope stress analysis, a rope consisting of 3-5 mm wire diameter and 30-80 mm rope diameter, requires the finite element size to be small enough to realistically capture the deformation during the analysis. The step size also affects the analysis and the solver type (Euler, Lagrangian,) plays a central role in solving the PDEs. The finite element analysis (FEA) has been carried out under the static and dynamic loading using the ANSYS Workbench Version 18.1.

The workflow of the FEA is shown in Figure 4.18, which shows the steps required to perform a complete study. The geometry is imported into ANSYS Workbench after being designed and verified in SolidWorks. Meshing is then applied to the entire geometry using a part or surface depending on the nature of the problem. One is recommended to use a hexahedral mesh on sweepable bodies and a tetrahedral mesh on other bodies. Once the mesh is ready, the physics is applied to different regions of the geometry. The boundary conditions are applied to regions with consistency of units. In this research study, the boundary conditions are mainly related to the drag force and angular velocity, reaction support, frictional contact, and gravity effects.

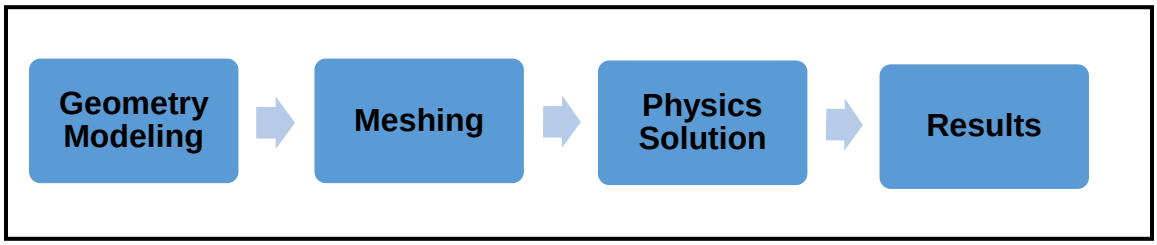

Figure 4.18. FEA workflow of the wire ropes

Material type, which is structural steel (galvanized) is also applied at this step. Static and modal analysis solver options with the Newton-Raphson method could be used for faster convergence of the stiffness matrix. Static analysis means that the inertia effects and damping are not important and are dropped from the analysis. The dynamic analysis means that the applied load varies at each time step and follows a specific function. The results are then plotted and visualized using post-processing viewer. Valuable inputs can

be deduced, such as equivalent stress and strain, displacement, and stress intensity factors. Those results are used to predict wire rope useful life under tension and bent-over sheave.

4.4.1. Ropes Geometry and Material Properties. This research study investigates the stress analysis on several constructions of wire ropes under the effect of direct tensile loading. Three dimensional CAD models of different rope diameters and shapes are designed and analyzed to understand the effects of the geometry, curvature, and diameter of rope and sheave diameter on rope stress distributions. Three dimensional solid models of rope-sheave interactions are constructed and tested under static loading where the rope was modeled as single rod bent over sheave. The rope-sheave solid models are also shown in Figure 4.19. Spiral ropes of diameters 15.00 mm and 13.27 mm of the construction (1×6), and bent over sheave, are analyzed under the effect of static loading and are shown in Figure 4.20.

Figure 4.21 shows spiral wire ropes of diameter 15 and 30.065 mm of construction ($1 \times 6 \times 12 \times 18$) bent over sheave analyzed under the effect of dynamic loading. All ropes and their geometries are designed to provide good contacts (wire-to-wire and rope-to-sheave). The ratio of the sheave diameter to the rope diameter (D/d) is also investigated in FEA to assess its effects on the maximum stresses for different ropes. The construction of straight ropes was used to create curved ropes bent on a sheave of diameter 632 mm. The material type for the ropes and sheave is structural steel with a modulus of elasticity of 2×10^{11}Pa and a Poisson's ratio 0.3. Homogeneous, isotropic behavior of materials was used in the analysis to reduce the computational time. However, each mesh was refined enough to improve the accuracy of the analyses and to obtain meaningful results. Frictional contacts between wires are also included to improve the accuracy of results.

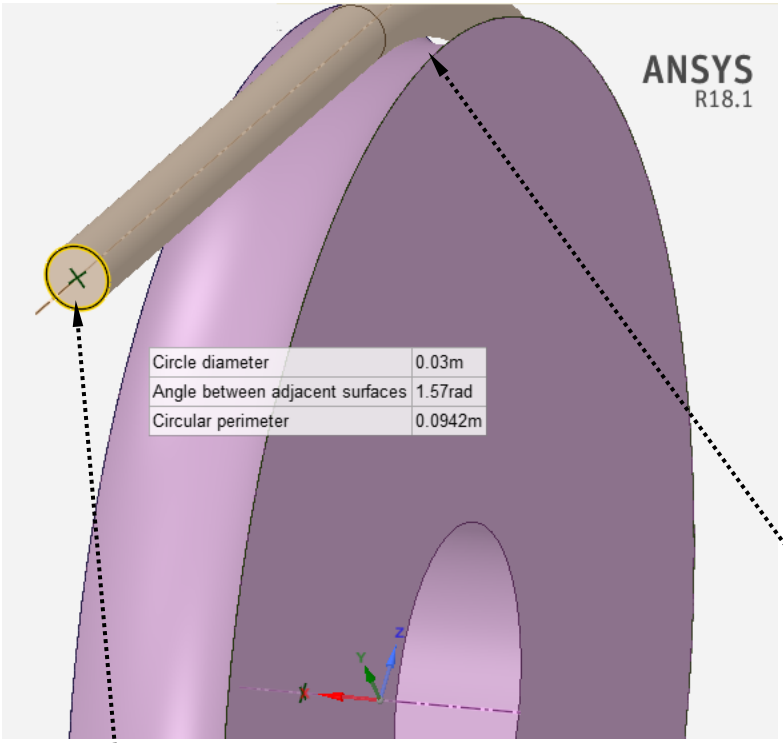

d= 30.00 mm

Gap between the rope and sheave to reduce the elements distortion

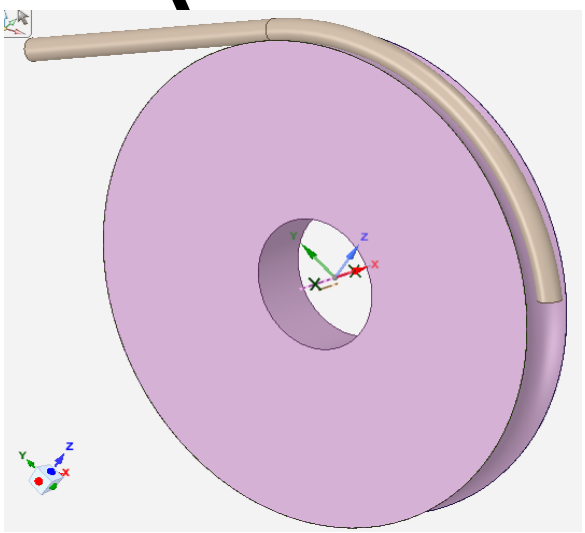

Construction: 1 × 1

Bent over sheave, sheave D = 632 mm

Figure 4.19. Geometry and construction of a wire rope (1×1) bent over sheave

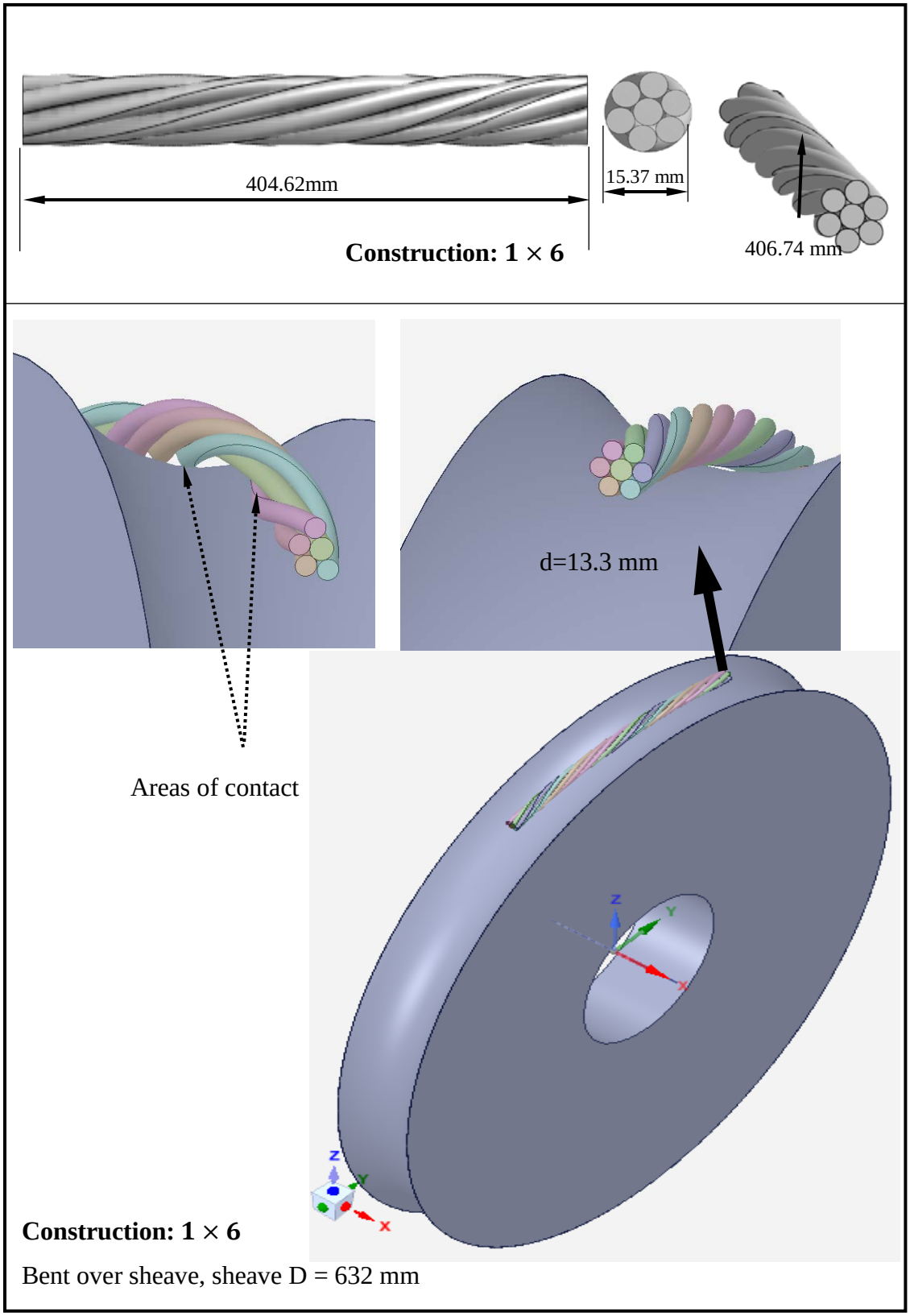

Figure 4.20. Geometry and construction of straight and bent wire ropes (1×6)

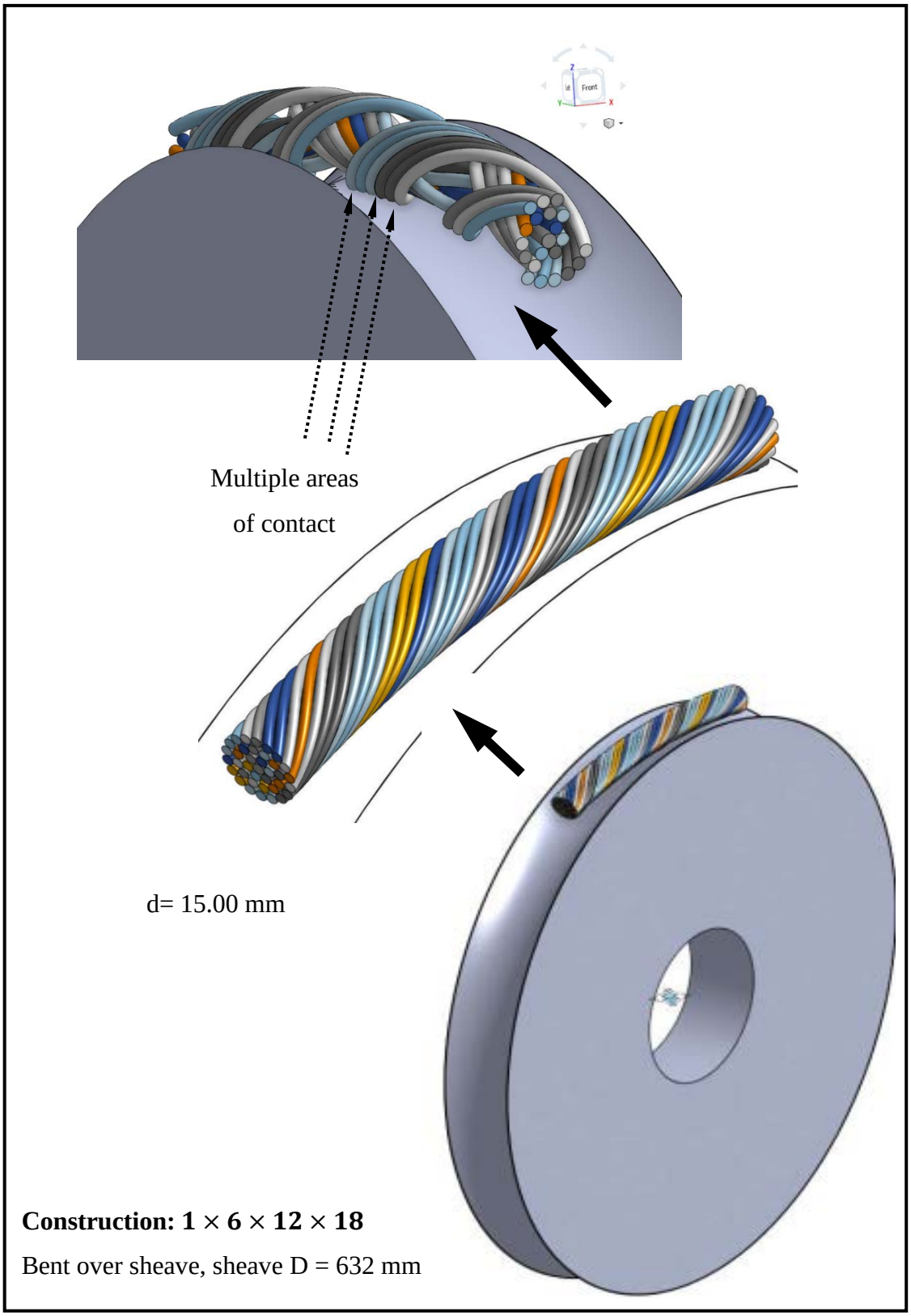

Figure 4.21. Geometry and construction of a 37 wire rope (1×6×12×18)

4.4.2. Meshing, Elements Type, and Size. Meshing is a fundamental step in FEM and its idea relies on dividing the solid geometry or the problem domain into finite elements. The elements in a finite domain are connected via nodes that are partially or completely constrained. The shape and size of the elements determine the FEA fidelity and model refinements may follow in several subsequent steps to reduce the stress localization, material usage and improve the accuracy of results. For this study, hexahedron and tetrahedron element types are chosen with the first geometry for the sweepable bodies, such as the wire ropes, while the second is used for bodies that are not sweepable, such as the sheave. Figure 4.22 shows the mesh for both the rope and sheave using the hexahedral and tetrahedral geometries, respectively. This representation is used to verify the effect of the mesh refinement on the accuracy of the results. The number of elements and other characteristics are described in Table 4.7.

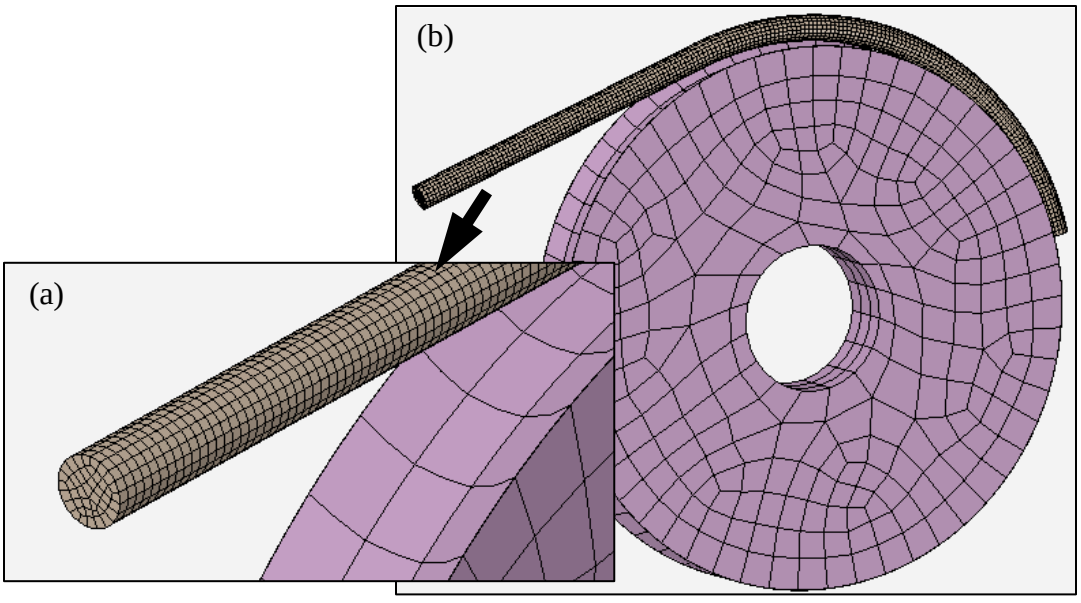

Figure 4.22. Meshing of 30 mm wire rope of construction 1×1: (a) hexahedral element type (b) complete mesh of rope bent-over sheave

Following the mesh refinement on the rod-shape wire rope, the mesh is greatly refined without refining the mesh of the sheave. The results of refinement are depicted in Figure 4.23. The characteristics of this mesh are described in Table 4.7 as well.

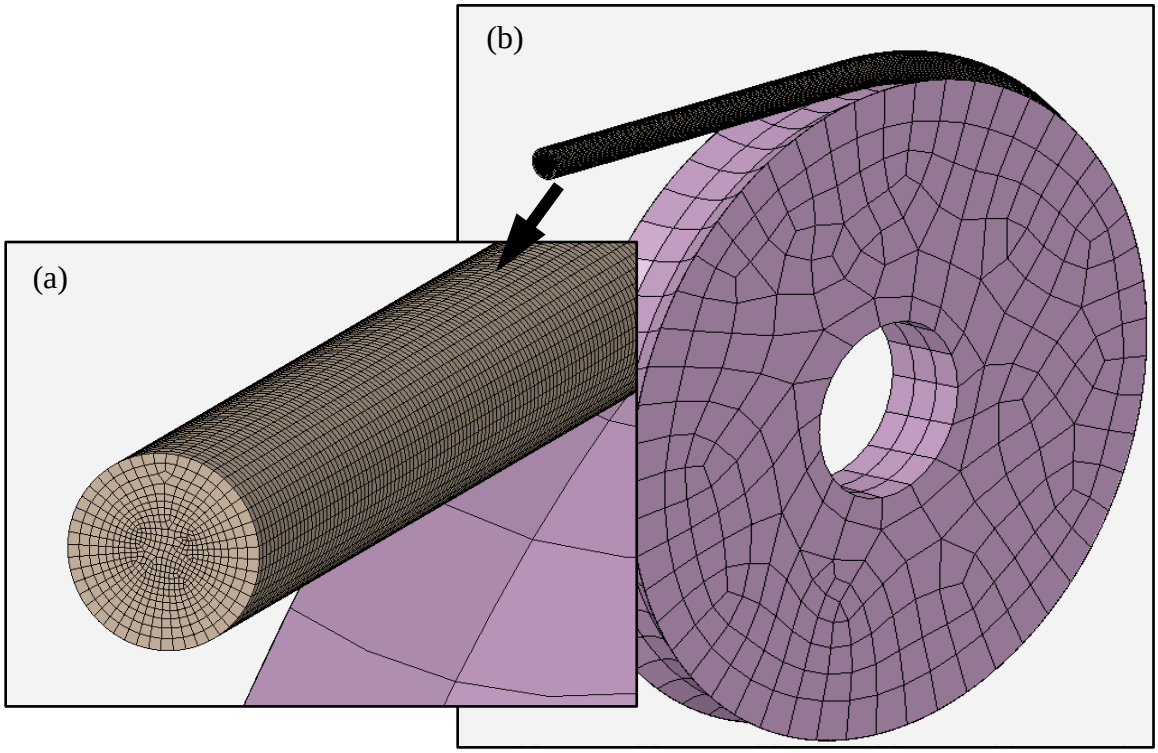

Figure 4.23. Mesh refinement of wire rope of construction 1×1: (a) hexahedral element type (b) complete mesh of rope bent-over sheave

The effect of the mesh refinement on the accuracy of the FEA results are articulated using a straight 7 wire rope with a lay length 404.62 mm. The geometry of the model is shown in Figure 4.20 and the mesh is shown in Figure 4.24. Wokem (2015) used the same geometry and dimensions for the analysis, but with a hexahedral mesh and 1,224,132

elements. The number of element of the FE model shown in Figure 4.24 is 743,280 and is a tetrahedral type.

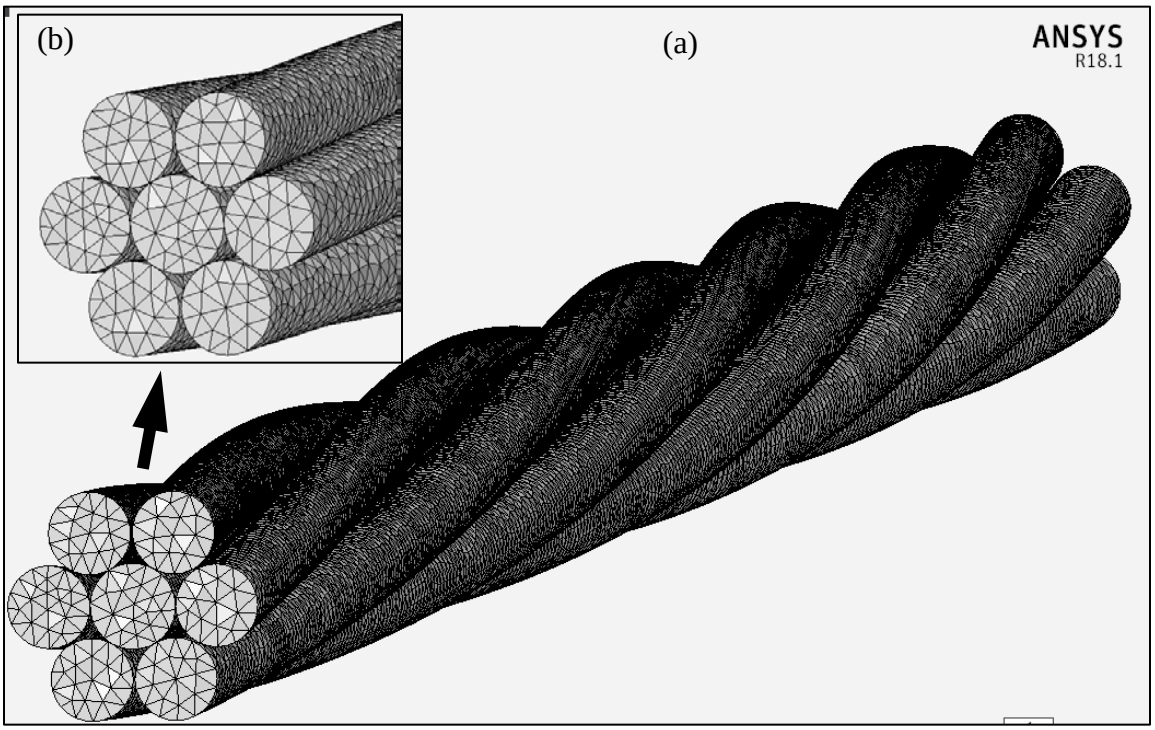

Figure 4.24. Meshing of 7 wire rope (1×6): (a) complete mesh of rope (b) tetrahedron mesh of wire rope

To understand the effect of rope diameter and the type of analysis on the results, a wire rope of construction (1×6), "7 wire rope," is wrapped on a sheave of radius 632 mm. The rope has a hexahedral element type. The results of meshing using ANSYS are shown in Figure 4.25. Mesh characteristics and other information about this experiment are given in Table 4.7. This experiment is also used for comparison purpose with the dynamic experiment of wire rope of construction ($1 \times 6 \times 12 \times 18$).

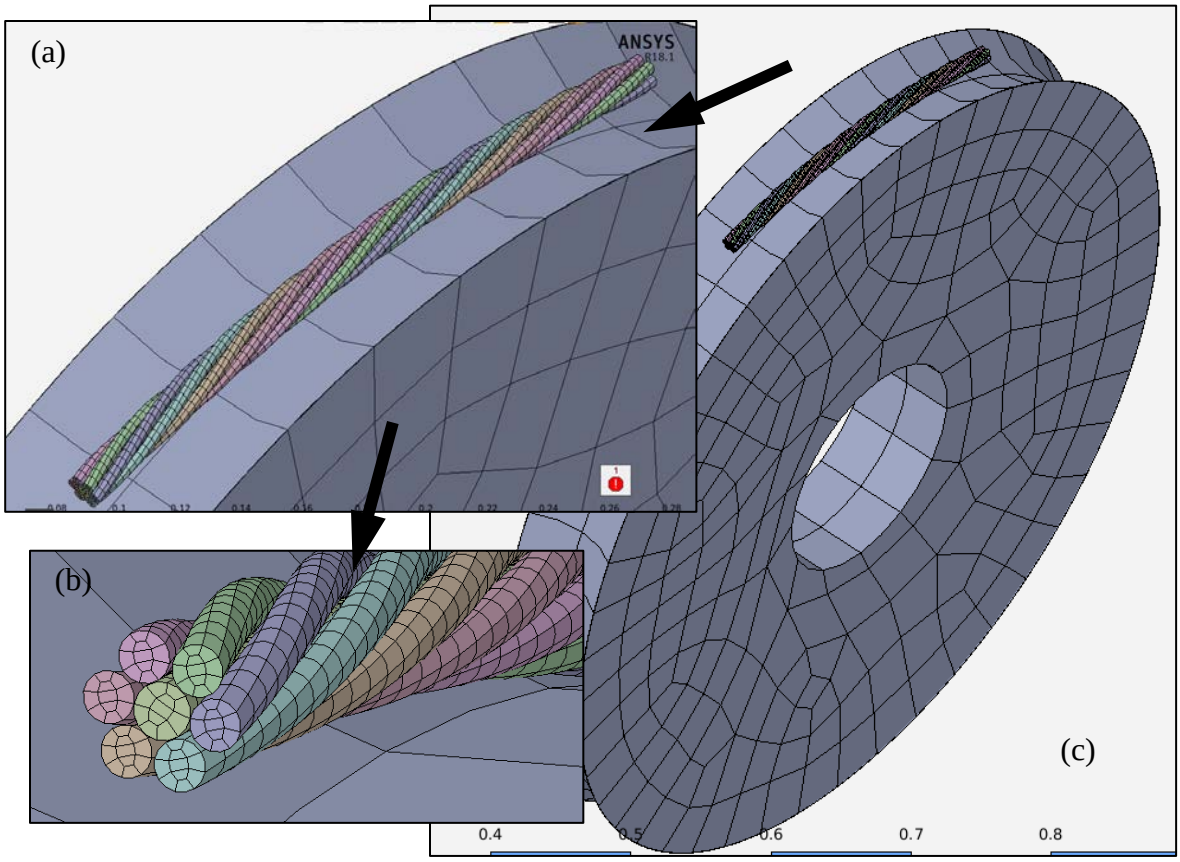

Figure 4.25. Mesh of a 13.3 mm wire rope of construction 1×6: (a, b) wires discretization (with hexahedral elements) (c) complete mesh of rope bent-over sheave

The mesh of the rope-sheave of $D/d = 632/15$ is depicted in Figure 4.26 with an appropriate mesh and mesh quality check. The element size in this FE model is 0.002 m, as it is a starting point for the subsequent FE analysis and further refinements are required to reduce the size of the input file. The number of elements and nodes are 85,904 and 240,085, respectively for the wire rope of 15 mm diameter. Size control and boundary layering are applied in appropriate regions, where the important physics phenomena (such as frictional contact and plastic deformations) are more likely to develop. It can be seen that the wires-sheave contact area and the rope structure require attention.

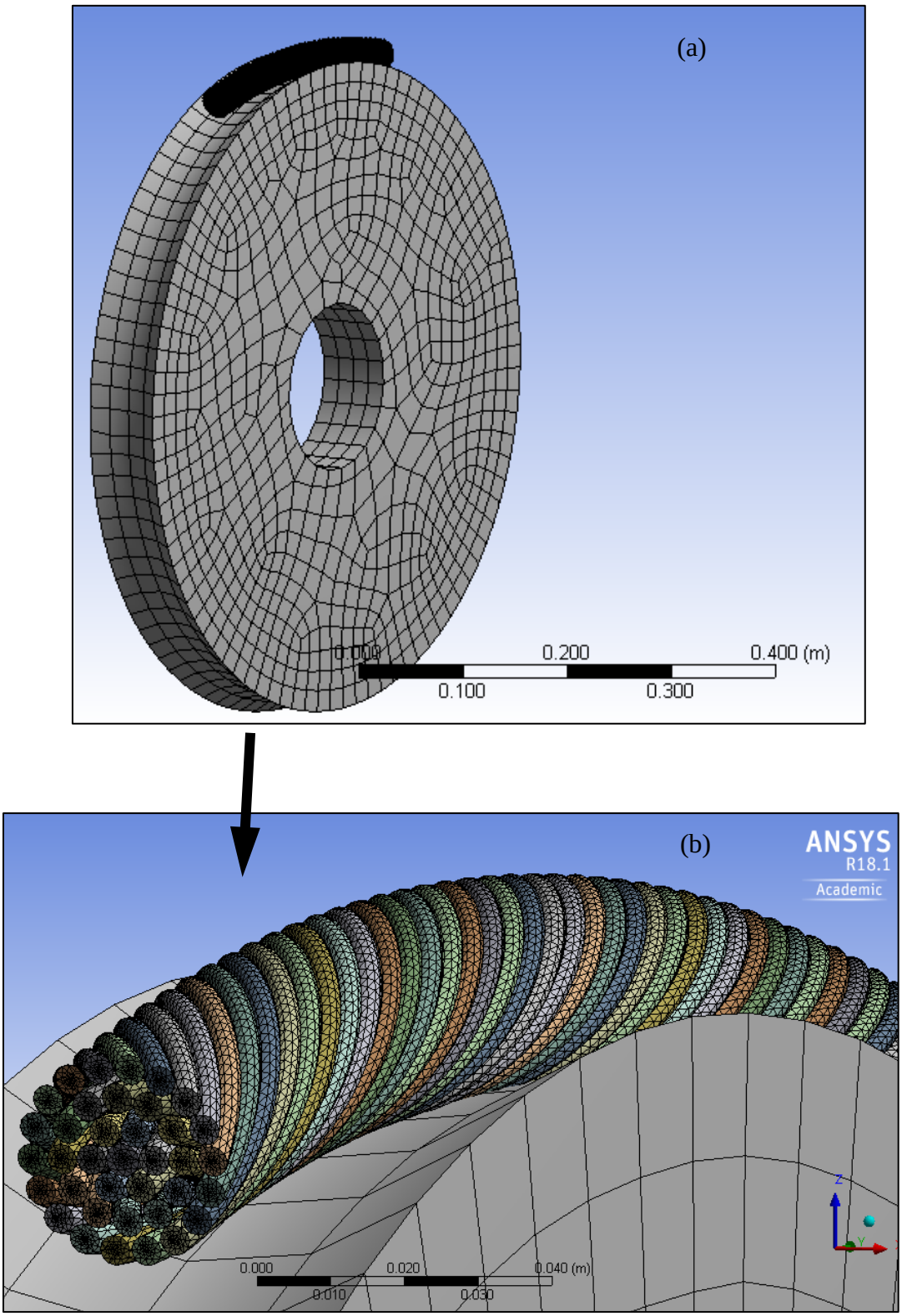

Figure 4.26. Meshing of wire rope of construction 1×6×12×18: (a) complete mesh of rope bent over sheave (b) tetrahedron mesh of wire rope

Table 4.7. FEA experimental setup and mesh characteristics

No	Mesh Characteristics	Parameters	Characteristics of experiment	Rationale for the experiment
	Rope Construction 1×1 bent over sheave			
1	No. total nodes No. elements	= 89379 = 28420	STATIC ANALYSIS	Comparison effect of mesh refinement
2	No. total nodes No. elements	= 977318 = 305838	STATIC ANALYSIS	
	Rope Construction 1×6 straight			
3	No. total nodes No. elements	= 61917 = 23888	STATIC ANALYSIS	Validation purposes
4	No. total nodes No. elements	= 1081978 = 743280	STATIC ANALYSIS	
	Rope Construction 1×6 bent over sheave			
5	No. total nodes No. elements	= 61917 = 23888	STATIC ANALYSIS	Comparison the effects of number of wires and type of experiments on the stress distribution
	Rope Construction 1×6×12×18 bent over sheave			
6	No. total nodes No. elements	= 240,085 = 85,904	DYNAMIC ANALYSIS	

4.4.3. Boundary Conditions and Load Type. A frictional contact behavior was applied between the wires with a frictional coefficient 0.12 for the simple strands and 0.25 for the wires on sheave (Raoof, 1990; Wokem, 2015). The contact behavior was established automatically among all wires and wires and sheave using the contact generator in ANSYS Workbench. ANSYS automatically detected 12 frictional conditions in the 1×6 construction, and 337 contacts for the $(1 \times 6 \times 12 \times 18)$ construction. The straight wire ropes are loaded axially in the case of static analysis and the bent-over sheave. Static

analysis means that the equations of motion of the FE model are solved without the effect of the acceleration ($\sum F = 0$). The FE experiments are also performed on the same structures using explicit dynamics approach as shown in Figure 4.27. In this approach, ANSYS uses Autodyn (a solver with pre/post-processing features), to provide solutions to the problem of the nonlinear dynamics of wire ropes. Explicit dynamics is well suited for the problem of complex contacts and large deformations. The results of the mathematical model, such as the angular velocity of wire rope, which is 0.052 rad/s, and the tension in the drag rope 1,375 KN are used as boundary conditions for the explicit dynamics analysis.

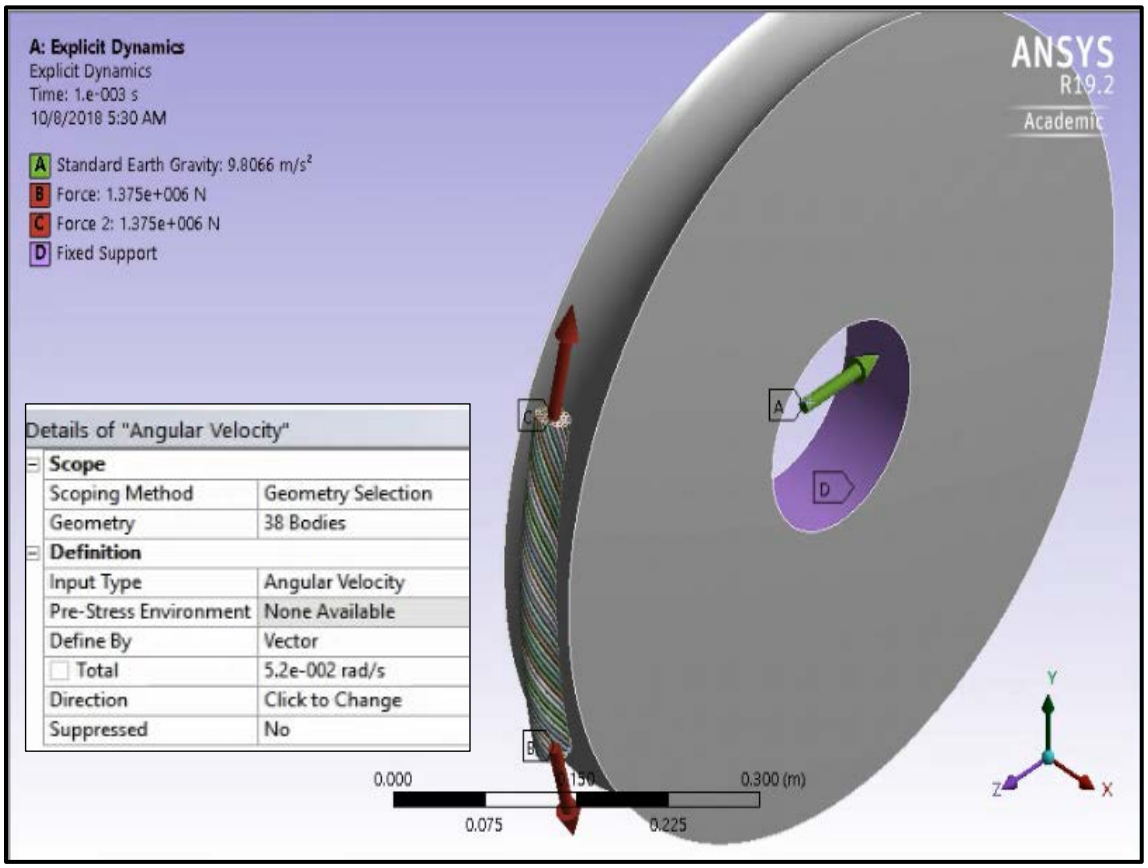

Figure 4.27. Dynamic analysis of rope construction 1×6×12×18 bent over sheave under the effect of boundary conditions

4.5. SUMMARY

In this section, the numerical analysis of an advanced computational dynamic model of a dragline was tested, verified and validated using real-world data. The mathematical formulation of a closed loop multibody mechanism resulted in a set of highly nonlinear differential algebraic equations. The initial conditions search was investigated thoroughly as it is believed to be the first part toward an accurate solution of the equations of motion. The stabilization of the solution algorithms was established using the Baumgarte's Stabilization Technique (BTS), which gave accurate results. The computational dynamic model of dragline was analyzed after generating the right input files in Mathematica. The accurate estimation of the dragline machinery parameters using the 3-D CAD models eliminated the need to input wrong inertia properties and weights. The residual errors, for a digging phase of 10 seconds, were in the magnitude of 10^{-4} degree. Thus, this mathematical model is verified, validated, and significantly improved compared to current models.

The effects of static and transient loading on the wire ropes were also investigated using the ANSYS Workbench. These ropes, the weakest part of the dragline front-end assembly, were subjected to tremendous loading (tensile, frictional, and bending). FEA has been conducted on different wire rope constructions to estimate the maximum stresses and stress intensity factors. The FE models are constructed using SoildWorks and analyzed in ANSYS Workbench. The output of the mathematical model permits the application of the resulting loads on the ropes in static and dynamic analyses. Explicit dynamic modeling approach is very well used in finite element analysis for short-period events. The FE models are enough to capture the rope responses when the dragline bucket is fully loaded.

5. NUMERICAL TESTING AND SIMULATION RESULTS

This section provides a detailed numerical testing of the kinematics and dynamics of the proposed mathematical model of a Marion 7800 dragline. The results of the numerical experimentations are carried out for the digging phase and loaded bucket swinging to dump material on spoil piles. The input data for the mathematical model are provided in Table 5.1. The results of the finite element analyses conducted on the wire ropes are also discussed for the different loading cases. For these analyses, a High Performance Computer (HPC) with 72 logical core processors and a memory capacity of 512 GB was used to carry out the FEA experimentations.

Table 5.1. Input data for the mathematical model

Parameter	Value (m)	Parameter	Value
L_0	7	R_s	1.715 (m)
L_1	10.76	E1H2	5.66 (m)
L_2	10.76	E1E2	6.041(m)
L_3	7.95	E1F1	10.5 (m)
L_4	7.95	DE1	$\sqrt{{R_s}^2 + {q_8}^2}$
L_5	45.7	B1D	110 (m)
L_6	45.7	k_F	0.29×10^6
L_7	1.715	k_p	1.3
L_8	1.715	l_{bucket}	5.2
L_9	5.25	λ_0	0.3
L_{10}	5.25	k_{nym}	3
L_{11}	2.29	ca	$5 * \text{Pi}/180$
L_{12}	7.14	q_2	$32 * \text{Pi}/180$
L_{13}	7.14	λ	$37 * \text{Pi}/180$

5.1. KINEMATIC SIMULATIONS RESULTS AND DISCUSSIONS

The kinematic model of the dragline front-end assembly was built using the concept of generalized coordinates and generalized motion variables (generalized speeds). It was verified and validated in Section 4 using real world data. Section 5 focuses on the numerical implementation of the digging phase and the loaded bucket swinging to dump material on spoil piles. This model contains all the relevant data and information about the linear and angular measurements of displacements, velocities, and accelerations of the machine house and the hoist, dump, and drag ropes. The operational cycle of a dragline usually starts when the dragline machinery, with its empty bucket, begins swinging back from the spoil piles to the digging area. In the kinematic simulations, the time is set to zero at the beginning of the digging phase.

As can be seen in Figure 5.1 (a), during the digging phase the hoist rope extends and the drag rope retracts to move the bucket towards the bank and excavate the overburden. The linear displacements of the hoist and drag ropes are given in equation (4.1). Thus, the linear velocities of the hoist and drag ropes are fixed and are of magnitude 2.54 m/s and -1.32 m/s, respectively. The linear and angular displacements of the drag and hoist ropes govern the motion of the dragline bucket and constrain it from colliding with the machine house or the boom. Figure 5.1 (b) shows an agreement among the linear and angular displacements of both ropes. The hoist rope trajectory increases with the digging time as a result of its extension to permit more mobility to the bucket. Releasing the hoist clutch and engaging the drag motor cause the drag rope to start dragging the bucket. This rope gets shorter as the bucket is partially submerged in the bank under its weight and the weight of the filled materials in the loading process. This occurrence causes

an additional angular displacement to occur in the drag rope and it improves the diggability of the bucket. It can also be seen from Figure 5.1 (b) that the variation of the angular displacement of the hoist rope is less than that for the drag rope and this behavior is also governed by the profile of their linear displacements. The initial angular displacement of the hoist rope is zero and that for the drag rope is -30 °, which is the slope of the digging face. All angular displacements are consistent with the machine operating limits and the model is accurate for simulating the real kinematic operations of a dragline.

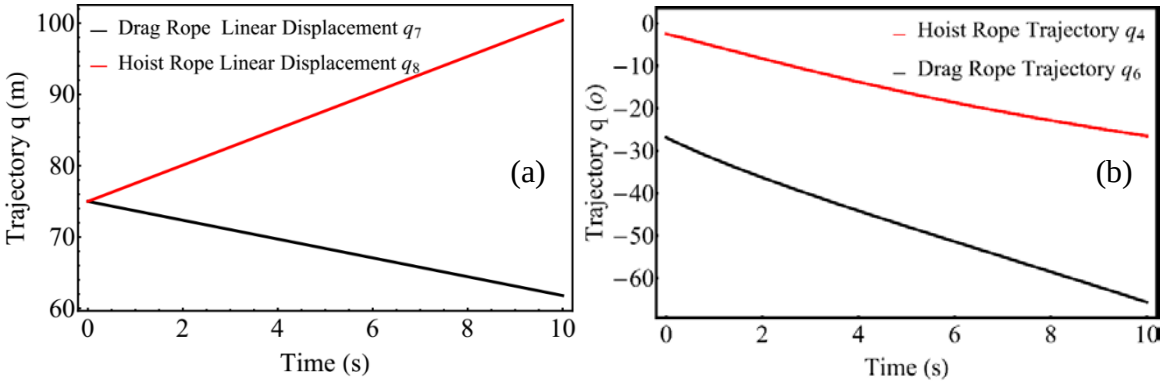

Figure 5.1. Displacements of hoist and drag ropes: (a) linear and (b) angular

The trajectory of the rigging system is characterized by a polynomial function of third order and it is depicted in Figure 5.2. This trajectory was established based on the numerical integration of the nonlinear constraints differential algebraic equation (4.4) at the acceleration level. The trajectory q_5 is also a representative of the bucket trajectory according to the assumption that the bucket is rigidly attached to the rigging system. The variation of the trajectory function of the dump rope q_5 is relevant to its behavior in a real digging event. It begins with positive orientation and changes rapidly to position the bucket

properly against the digging phase. At the end of the digging, it has a steady slow change to eliminate spilling of the filled materials. The field observations have also shown that the orientations of the dump rope slightly change during the hoisting of a loaded bucket. In addition, the dump rope and boom are parallel to each other during the swinging of the loaded bucket onto the spoil piles. This feature plays a key role in stabilizing the bucket carry angle and provides a momentary dynamic balancing until the dumping happens.

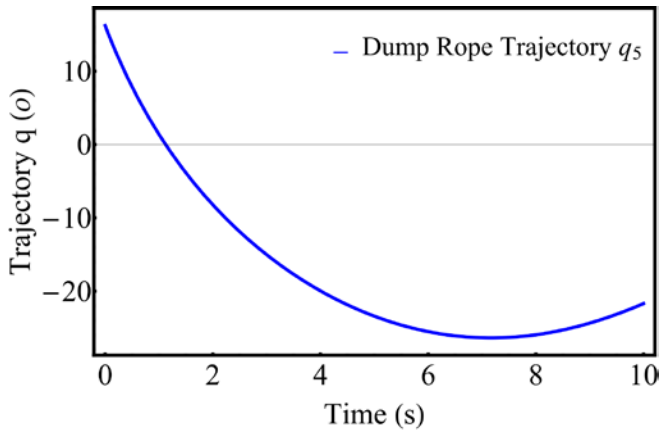

Figure 5.2. Angular displacements of dump rope

The behavoir of the angular velocity of the hoist and drag ropes is shown in Figure 5.3 (a) and it captures the real operation. The hoist rope is not under direct tension from the hoist motor and its velocity changes at a slow rate. On the contrary, the drag rope rotates at higher velocity to peferctly position the bucket during the digging operation. The angular velocity of the dump rope is plotted in Figure 5.3 (b) and it is much higher than that for the hoist and drag ropes. This is because the dump rope has more mobility to rotate than other ropes.

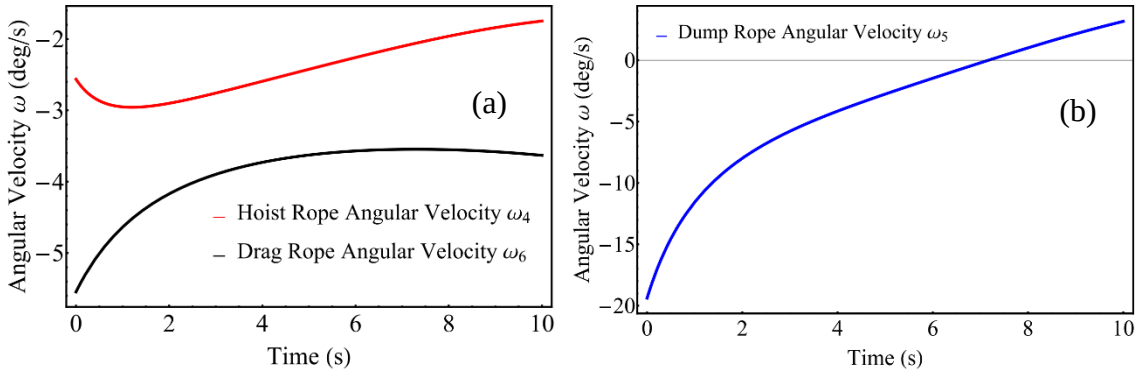

Figure 5.3. Angular velocities: (a) hoist and drag ropes and (b) dump rope

Figure 5.4 shows the variations in the angular accelerations of the hoist, drag, and dump ropes. These accelerations provide valuable information about the dynamics of the dragline machinery during the digging phase. It can be seen that all ropes rapidly change the acceleration within the first 4 seconds of the digging time and then deceleration occurs during the bucket loading process. The acceleration profiles for each rope approximately reaches steady-state after 7 seconds when the bucket is almost filled and is ready to be lifted off the bank.

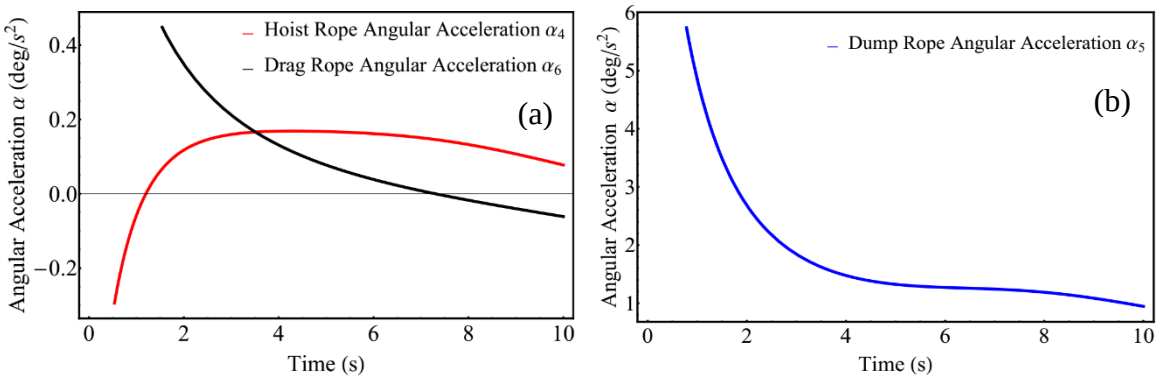

Figure 5.4. Angular accelerations: (a) hoist and drag ropes and (b) dump rope

The acceleration curves for the drag and dump ropes have decreasing profiles at different rates. This behavior indicates that both ropes operate consistently during the digging phase. It can be explained that the dump rope accelerates to quicly respond to the motion of the drag rope. As the bucket slides on the ground, the acceleration of the dump rope gradually decreases to $1\,\mathrm{deg/s^2}$. It was seen in Section 4.1.1.1 that the initial conditions of the trajectory functions q_4, q_5 and q_6 have significant impact on the kinematic solutions. This impact also affects the results of the dynamic simulations. Wrong initial values are more likely to give incorrect solutions, especially when dealing with a stiff mathematical DAE model. The invariants of the kinematic model are a key to performing full and acceptable kinematic and dynamic simulation experiments. They provide consistency in the behavior of the model during the integration and reduce the possibility of increasing the drift error.

The mathematical model also provides information about the velocity and acceleration variations of ropes with respect to their resulting trajectories, as shown in Figure 5.5. The experiment shows that the hoist rope velocity is minimal when its trajectory is – 40 °, as given in Figure. 5.5 (a). The hoist rope, at this angle, is close to the boom and its angular speed is already decreased to avoid collision with it. The angular velocity of the dump rope is much faster than that of the hoist rope allowing for a quick adjustment to the rigging system, as depicted in Figure 5.5 (b). Figure 5.5 (c) shows the variation of the angular velocity of drag rope versus its trajectory and it is similar to that of the hoist rope. When the bucket is filled, the drag rope angle is maximum and the velocity is minimal to prevent the bucket from hitting the machine.

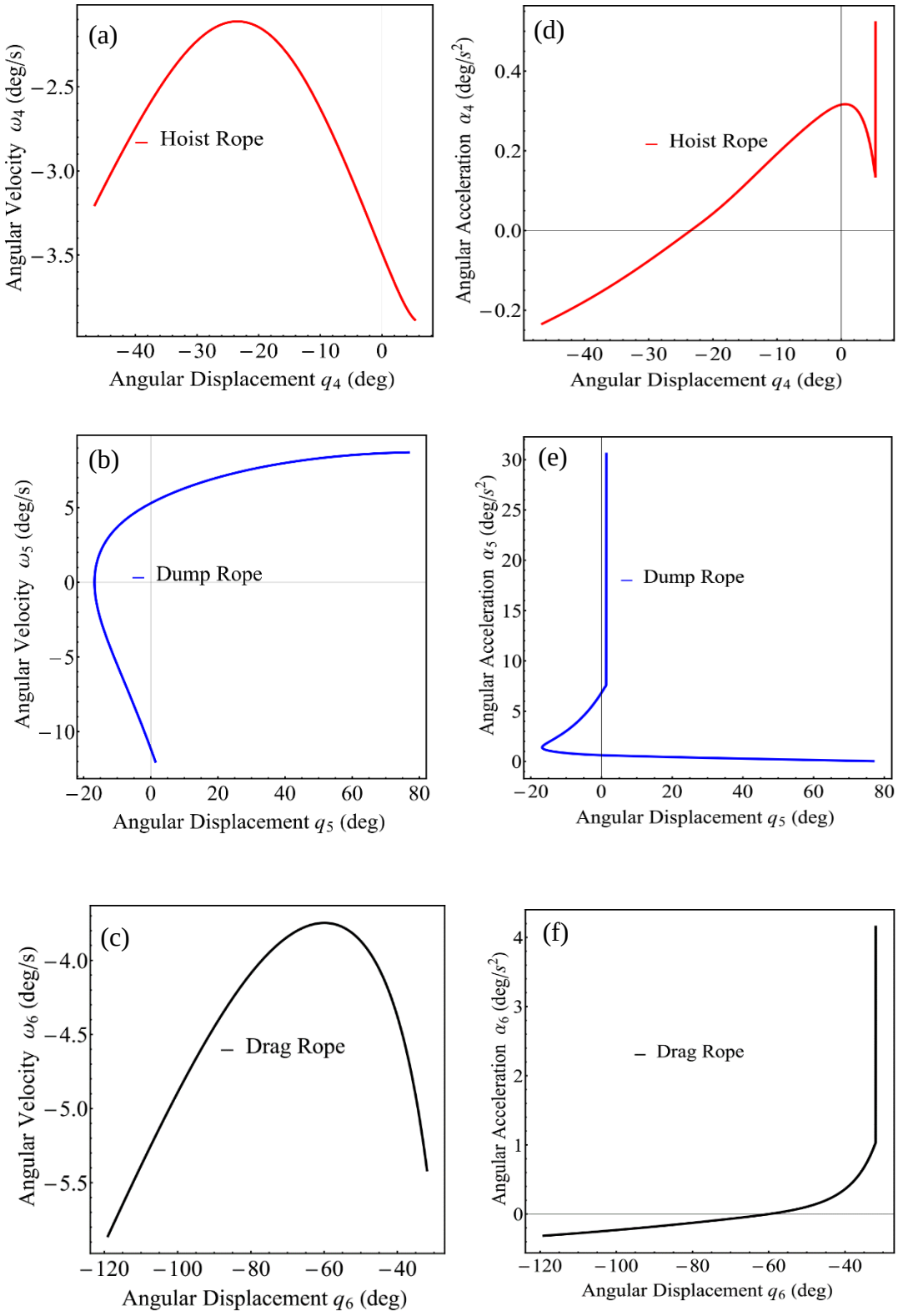

Figure 5.5. Angular velocity versus trajectory: (a) hoist, (b) dump, and (c) drag ropes angular acceleration versus trajectory: (d) hoist, (e) dump, and (f) drag ropes

The behavior of the dynamic model is also investigated during the digging phase for the acceleration and deceleration of the ropes. Figure 5.5 (d, e, f) show the resulting angular acceleration of each rope versus its trajectories at time interval [0, 10] seconds. The angular acceleration profile is steep at the beginning of the excavation process and it gradually decreases through the excavation process. The acceleration is minimal at the end of digging and this behavior is explainable from an operational viewpoint. The rapid change in the accelerations, at the beginning of the digging phase, may be attributable to the stiffness of the constraint, velocity and acceleration equations. The initial conditions of the constraint and velocity functions are also the cause of such behavior. The acceleration of a structural member in the front-end assembly is due to its interaction with other members. Equations (3.42) and (3.43) provide an explanation to this interaction.

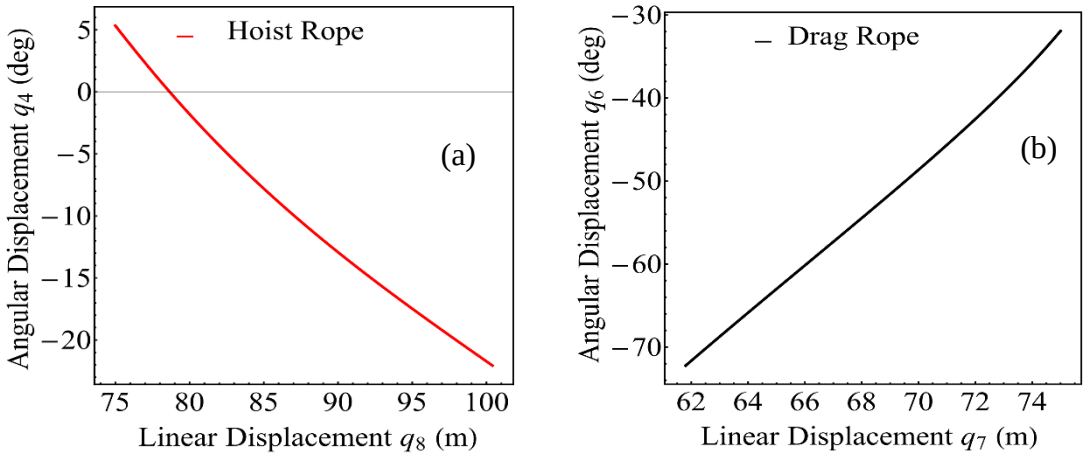

Figure 5.6. Angular displacement versus linear displacement for hoist and drag ropes

The variations in both the hoist and drag rope lengths also affect their trajectories during the digging. They also change the trajectory of the dump rope, whose length is fixed

for all experiments. Figure 5.6 (a) shows that by increasing the hoist rope length q_8, its trajectory increases and it has a maximum magnitude of -22.5° at 100 m. The drag rope trajectory also increases with time and it has a maximum magnitude of -72.5° at 62 m of its length, as given in Figure 5.6 (b). At the end of digging, the operator switches the control from digging to full-bucket swinging motion and the drag rope extends while the hoist rope retracts. Thus, the behavior of the trajectory functions depends on the underlying task that the dragline machinery performs and on its technological limitations.

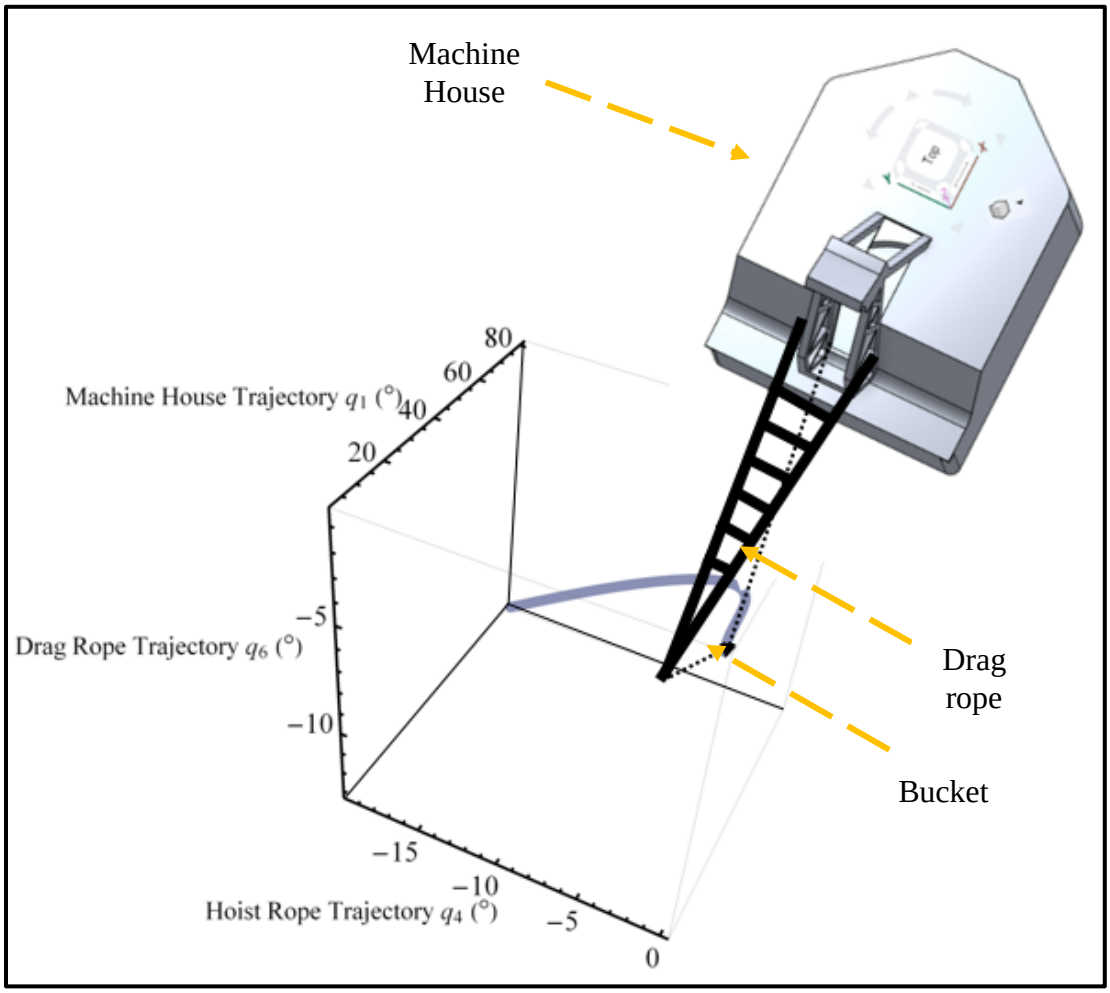

Figure 5.7. Filled bucket trajectory in a 3 D space during swinging-back phase

The front-end assembly of a dragline machinery, with its three ropes (hoist, dump, and drag), governs the bucket motion in a (x-z) plane of digging as shown in Figure (3.2) (see Section 3). The ropes also determine the trajectory of the bucket in a 3D space during a loaded bucket swinging operation. The resulting trajectories of the kinematic model are also used to simulate the bucket motion after completing the digging phase. In a loaded bucket swing motion, the bucket moves in the x-z plane and changes its coordinates in a global reference frame, as depicted in Figure 5.7. The trajectories q_1, q_4 and q_6 simultaneously change with time to return the filled bucket to the dumping area. It can be seen that the machine house makes a rotational displacement of -80°, whereas the trajectories of the drag and hoist ropes make 22.5° and 25°, respectively.

5.2. DYNAMICS SIMULATION RESULTS AND DISCUSSION

The mathematical model of the dragline machinery has been verified and tested using the correct angular displacements as described in Section 4.2. The results of the kinematic simulations generated in Section 5.1 are used as inputs for the dynamics simulation. The dynamic model contains three actuators, which are used to generate the required torques and force and operate the machine in a cycle time of 60 seconds. These actuators may provide simultaneously a swinging torque τ_1, a hoisting torque τ_2, and a dragging force σ or a hoisting and a dragging force depending on the underlying operational task. Thus, a dragline machinery can be regarded as a robotic excavator with three DOF. The solution of the dragline force and torques is a problem of inverse dynamics. The latter requires providing accurate values of the trajectory functions that must meet the machine limits in the course of the solution.

Generally, a loading cycle of a dragline starts when the operator has already positioned an empty bucket and engages the drag motor to begin excavating the materials. In the digging phase, the bucket penetrates the bank with a prescribed dragging velocity $\dot{q}_7$ of approximately -1.32 m/s. The digging extends for 15 seconds and terminates when the bucket is fully loaded with the materials. Previous studies have shown that the maximum loads are more likely to develop, in a dragline machinery front-end assembly, at the end of digging cycle (Nikiforuk and Ochitwa, 1964; Nikiforuk and Zoerb, 1966; Nichols et al., 1981). Thus, the simulation of the digging cycle is of particular interest and would result in valuable information about the dynamic loading of a dragline machinery. The developed dynamic model, in equation (3.87) in Section 3, is a robust model that helps to accurately predict the unknown dynamic loading.

The solution process of the dynamic model was given in Figures (4.8) and (4.9). It starts with the definition of the geometry of the dragline front-end assembly, masses and inertia of components, and prescribed trajectory inputs. The solution of the DAE, in equation (3.87), during digging eliminates the needs for the swinging torque, as the machine house is fixed during this phase. The dynamic solution algorithm includes the kinematic algorithm with its Baumgarte's Stabilization Technique (BTS) and the dynamic equations of motion in equation (3.87). Mathematical functions are developed and contain all relevant information about the dynamic and kinematic analyses. The resistance force to cutting was included in the analysis and it follows the model given in equation (3.70). However, the developed friction model of the drag rope, in equation (3.80), was not included in the dynamic simulation based on the assumption of limited contact with the ground. Its parameters need further research and that is out of the scope of this dissertation.

The bucket payload model was developed using an input function given in equation (3.72). The maximum load (in kg), that the drag rope pulls at the end of the digging phase is depicted in Figure (5.8). It includes the bucket tare mass and the overburden (waste materials) mass, which is a maximum of 80,000 kg per the machine allowable payload (Nikiforuk and Zoerb, 1966).

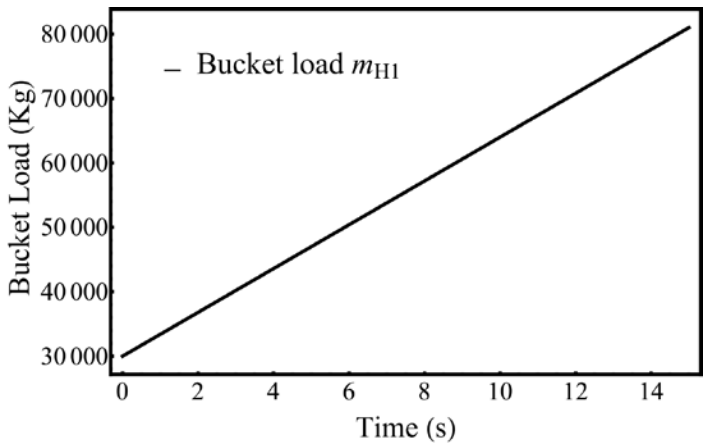

Figure 5.8. Bucket mass variation during digging phase

During the digging operation, the bucket tip interacts with the ground and a resistance force to cutting the material develops and increases with time. The cutting resistance model is included and was developed according to Poderni (2003). It was assumed that the bucket has already made an angle, called “the carry angle ca” with the horizontal and its magnitude is 35°. This value was chosen on the basis that this angle provides a good estimate to the cutting force. It also reduces the bucket tipping-over during the digging and minimizes material spillage during a completely loaded bucket swinging onto the spoil piles. The resulting resistance force to cutting is calculated in accordance

with equation (3.69) and is plotted in Figure 5.9. Two components of the resistant cutting force affect the diggability of materials and the horizontal component is always maximum. The variation of the horizontal cutting resistance force is around 400 KN, whereas the maximum value of the horizontal component, at 4 seconds, is 100 kN. This model captures the complex digging scenarios when the bucket starts penetrating the ground. It can be seen that the vertical cutting force reduces with time and this is an indication of the reduction resistivity of ground to digging. The orientation of the bucket and its carry angle, as well as the fragmentation of the rock and its resistance to cutting and the bucket capacity influence this behavior.

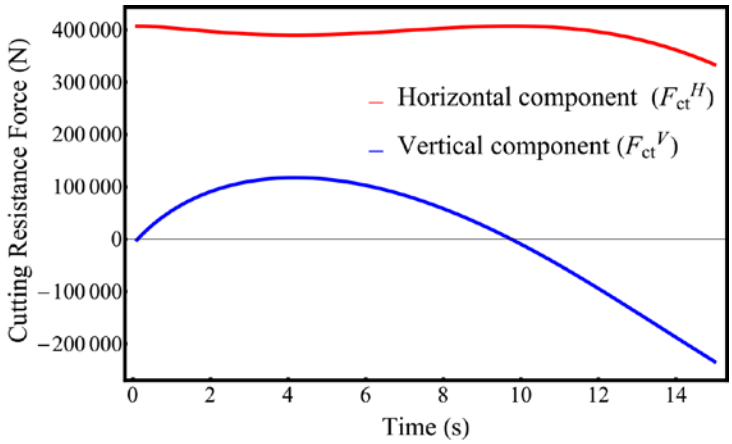

Figure 5.9. Cutting resistance force during digging phase

During the empty-bucket lowering phase, the hoist rope carries most of the load, which includes its own weight, bucket weight, and a partial tension from the drag rope. On the other hand, the drag rope has less load acting on it. The operator releases the hoist clutch quickly and that results in increasing the hoist rope length. The drag motor is also

engaged to position the bucket properly. Both ropes change their lengths and their masses. This change also occurs during the digging phase, in which, the hoist rope becomes longer and the drag rope becomes shorter as in Figure 5.1 (a). This implies that hoist rope mass is linearly increasing with time, whereas the drag rope mass is linearly decreasing with time. In this dissertation, the dynamic simulation takes into account these simple variations to correct the pitfalls of using constant rope mass during the analysis. The variable masses of the hoist and drag ropes are shown in Figure 5.10 for given inputs of q_8 and q_7.

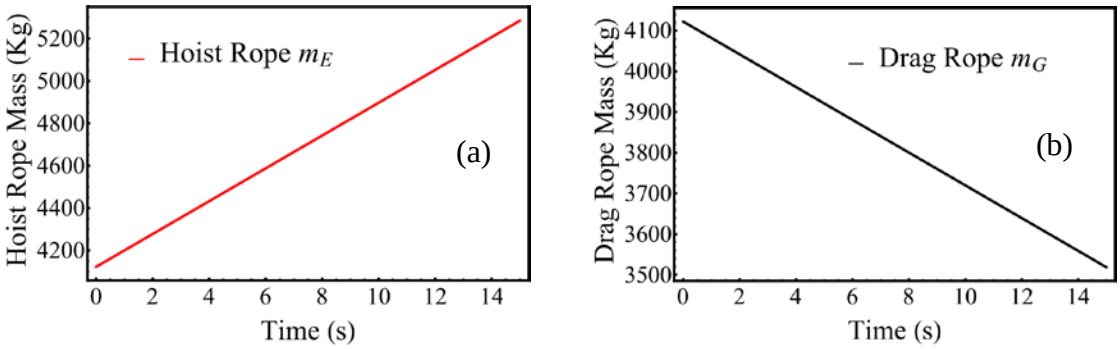

Figure 5.10. Variation of rope mass during digging: (a) hoist rope, and (b) drag rope

The dynamic model is developed to cover an operational period of 40 seconds, which encompasses the digging phase and the loaded bucket swinging phase. However, it can be extended to consider the full cycle with appropriate changes to the input functions. The solution of the dynamic model during digging only includes the drag force and hoist force at the beginning of excavation. That corresponds to the solution of the second and third equations in the complete dynamic model captured by equation (3.87). Figure 5.11 (a) shows the variation of the drag force with time and it follows a polynomial function.

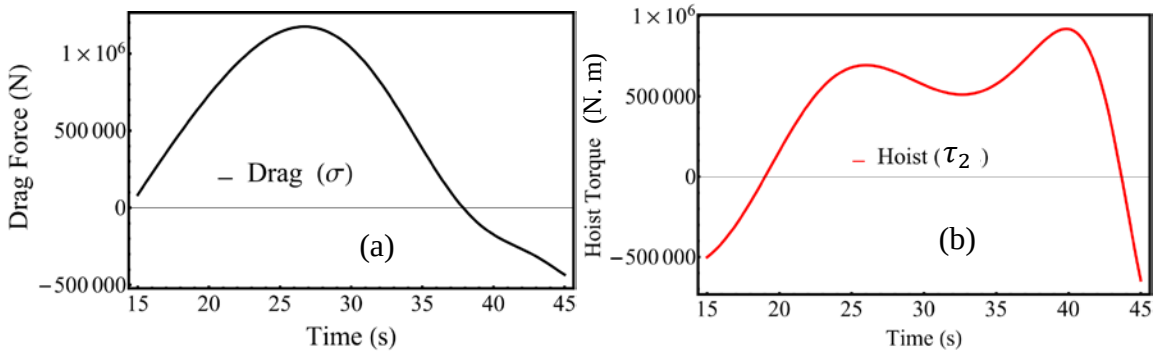

Figure 5.11. Rope loads during digging and full-bucket swinging back motions

It can be seen that the drag rope has some tension at the beginning of digging to allow the orientation of the bucket tip towards the operator. The tension in the drag rope increases rapidly with time as the bucket is being filled with the materials. Also, the resistance to cutting increases, as shown in Figure 5.9, during an operational time span between 15 and 20 seconds. A maximum dragging force, which approximately measures $1.375 \times 10^6\ N$, occurs when the bucket has already moved for a period equivalent to three-quarters of the digging time (27 seconds).

The hoist force is also shown in Figure 5.11 (b) for the digging phase and the loaded bucket swinging onto the spoil piles. At the beginning of the digging phase, the hoist rope has some tension due to the empty- bucket weight. This force decreases with time to allow the bucket to move freely under the effect of the drag force. At 5 seconds of digging, the hoist force changes direction to hosit the bucket and to prevent it from being tipped over. The tension in the hoist rope increases with time until the bucket is filled at time 30 seconds into the digging operation. At the end of the digging phase, the bucket is lifted off the bank, which requires significant hoisting torque to lift a loaded bucket of 80,0000 kg. It can be seen that the maximum hoisting torque, during time interval [15-30] seconds is 690.39

KN.m. However, during the swinging of the loaded bucket onto the spoil pile, at interval of time [30-45] seconds, the maximum hoisting torque is 917.87 KN.m at time 40 seconds.

Nikiforuk and Zoerb (1966) reported the maximum allowabe drag and hoist forces on the dragline Marion 7800. The maximum drag force is 300,000 lb, which is equvailent to 136,077.7 Kg and 1,334 KN and the maximum hoist force is 277,000 lb, which is equvailent to 125,645.1 Kg and 1,232.5 KN. These values (in Figure 5.11) are within the machine limits. Thus, the dynamic model of the dragline front-end assembly is capable of generating accurate results. These values validate the results for the finite element analysis on wire ropes. The maxiumum drag force 1,375 KN was used as a buoundry condition in analyzing the maximum stresses in several wire rope constructions. The results of the stress analysis are provided in the Section 5.3 and for the geometries given in Figures 4.19-4.21 (see Section 4.4.1).

5.3. FINITE ELEMENT MODELS RESULTS AND DISCUSSIONS

The performance and productivity of a dragline machinery are characterized by the amount of drag and hoist forces, as well as the swinging torque, provided by the machine in a full cycle of 60 seconds, to excavate and spoil materials. The hoist and drag forces are applied to the bucket during the entire cycle at varying magnitudes. They greatly affect the machine performance and may reduce the machine availability if the ropes break during operations. These forces and their ropes are, therefore, of paramount importance and require further investigation. A major cause of a wire rope breakage is due to loading the rope beyond its ultimate strength under excessive repeated dynamic loading and unscheduled maintenance.

As was seen in Figures 4.19-4.21, the wire ropes are complex structural elements and their response to the static and dynamic loading is still an area for further research. In this research study, one of the main objectives was to find the stress distribution in an axially loaded straight ropes, and in ropes running on sheaves. The FEM was used to predict the stresses and stress concentrations at different loactions in the rope. The dynamic analysis concluded that a maximum drag force of 1.375 MN is produced and it will be used in the FEA input files. The material for all wire ropes used in the analyses are galvanized structural steel with a Young's modulus 2.00×10^{11}Pa and mass density of $7{,}850$Kg/m^3. The results of the static and dynamic FEA using ANSYS 18.1 are analyzed and discussed for each structural member.

5.3.1. Static Analysis of Simple Wire Ropes. Figure 5.12 (a) shows the static FEA of two wires that were taken from a 7 wire rope construction. The two wire length is 0.404 m and each wire diameter is 2.6 mm. The drag rope load of 1, 375 KN was used in the analysis and it resulted in 4.52×10^{11} Pa von Mises stress and a severe displacement of magnitude 4.65 m as shown in Figure 5.12 (b). These results are limited for predicting the stresses in a multi-strand wire rope of complex construction. It can be seen that the maximum deformation is very significant, the location of which is shown in red color of the loaded rope and corresponds to the location of the applied load. The resulting average stress intensity factor (SIF) for this FE model is 2.738×10^{10} Pa. The 15 mm diameter, 7 wire rope construction was used in this dissertation and it was similar to the rope used by Wokem (2015) for comparison purposes. To further validate the current FEA, the same wire rope used by Costello (1997) and Wokem (2015) is now subjected to the same load

85 KN. The results are given in Figure 5.13 for the maximum von Mises stress and maximum equaivlent strain.

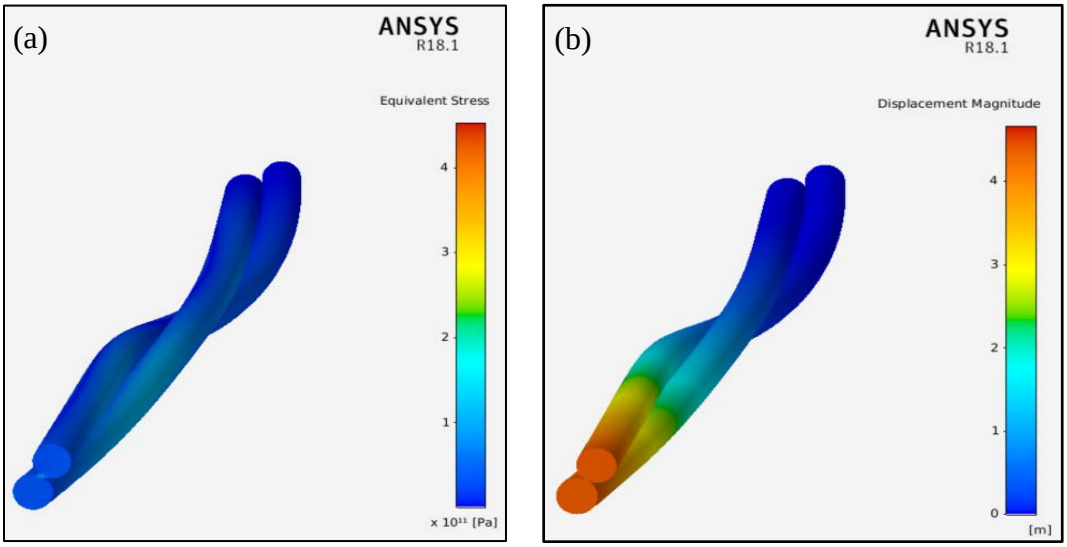

Figure 5.12. Equivalent stress and maximum deformation in two wire rope

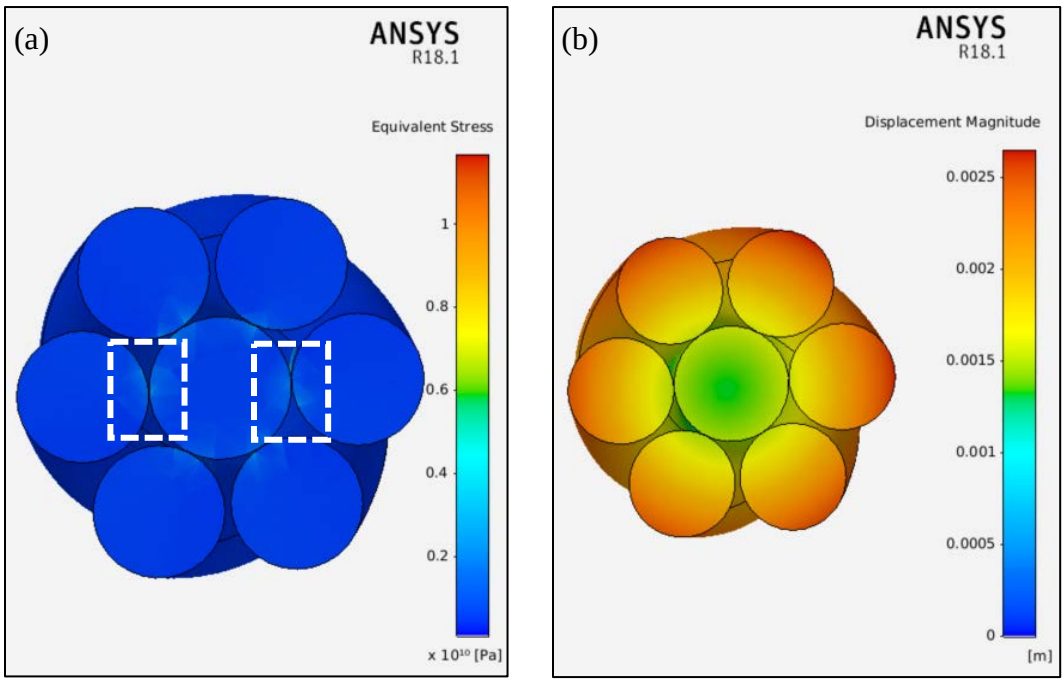

Figure 5.13. Equivalent stress and deformation in a 15 mm, 7 wire rope under F= 85KN

It can be seen that the von Mises stress along the strand, except the white dotted regions, is very close to 7.7×10^8Pa provided by Wokem (2015). The displacement is maximum at the outer layer and its magnitude is 2.5 mm and this value matches the results given in Wokem (2015). It can be concluded that the mesh element type for the simple wire rope construction does not have significant impact on the accuracy of the results.

Now, additional experiment is performed by applying the resultant drag load on the 7 wire rope construction. The stress results of the 15 mm, 7 wire rope, under axial loading of 1.375×10^6 KN, are depicted in Figure 5.14 (a). It can be seen that the maximum equivalent von Mises stress, at points of contact between the wires, is 1.019×10^{10}Pa.

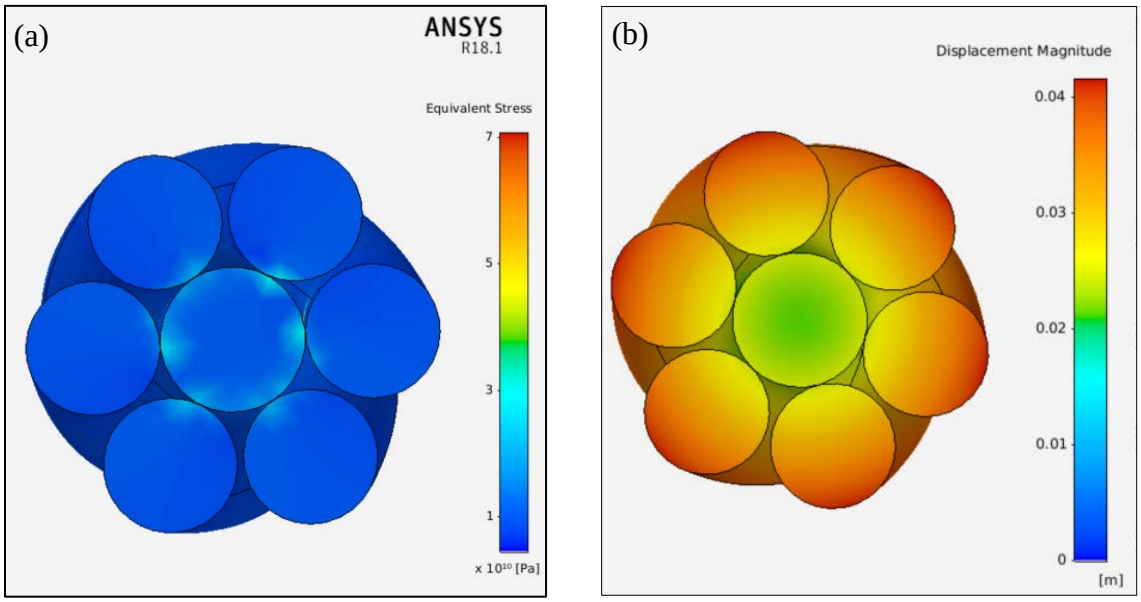

Figure 5.14. Stress and deformation in a 15 mm, 7 wires rope under F= 1,375 KN

Figure 5.14 (b) shows that the outer layer is not fully bonded. That resulted in a higher deformation than the one in the core wire, and its maximum equivalent value is

16.3mm. Wokem (2015) has shown that the maximum equivalent stress for the same construction is approximately 7.7×10^8Pa for an applied load of magnitude 85 KN. The load, he used, was predicted based on the theory of Costello (1997) and his model was used just for validating the effect of mesh refinement of the results. To investiagte the effects of rope diameter and its length on the stress distribtion in the strand, another FE experiment was conducted using 7 wire rope, with diameter 30 mm and reduced length of 200 mm.

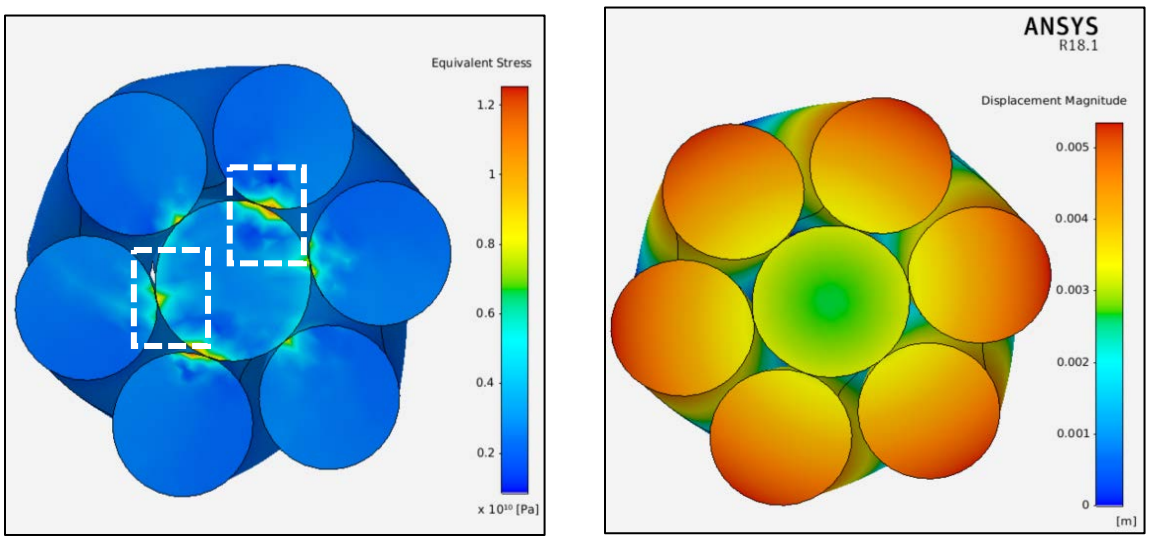

Figure 5.15. Stress and deformation in a 30 mm, 7 short rope under F= 1,375 KN

The results are plotted in Figure 5.15 for the maximum von Mises stress, which is 1.2×10^8Pa, and maximum displacement of magnitude of 5.33 mm. It can be seen that stress concentrations are maximum at points of loading. At these locations, the wire undergoes the effect of tension, twisting, and friction. Obviously, the stresses are less than those developed in the 15 mm wire rope. The results of this analysis indicate that the shorter

the length of the strand is, the lower the deformation in the rope. As the rope becomes longer, its rigidity decreases, and its flexibility becomes more significant. In fact, the short rope behaves similar to a beam when the number of mesh elements in not enough.

The wire rope construction (1×6) bent over sheave, whose geometry and mesh properties are shown in Figure 4.25 and in Table 4.7, is tested under the effect of steady-state applied load. The equaivlent stress and deformation of the FEA are provided in Figure 5.16. The maximum von Mises stress appears in the location of the applied load and its value is 1.25×10^{9}Pa. Maximum displacement also occurs in the same region and its value is 20×10^{-3}m. The FEA results of the 7 wire rope bent over sheave indicate that stress waves significantly exist in the rope and propagate towards the fixed end. The bending of the rope over sheave increases these stresses and the deformation as well.

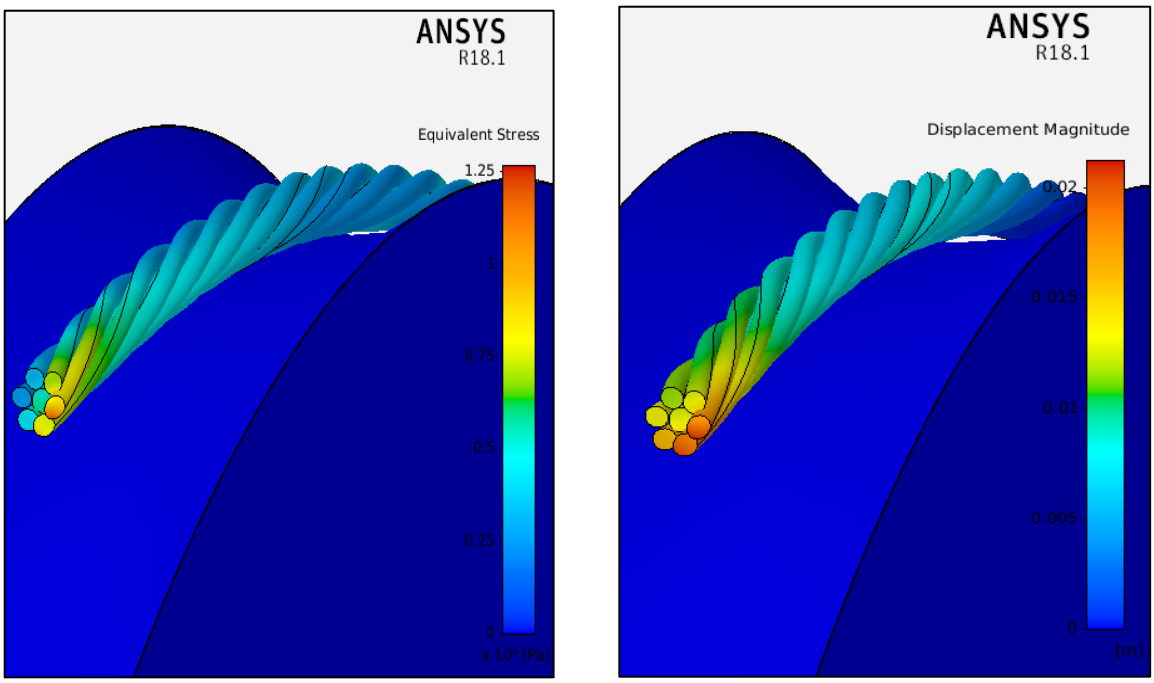

Figure 5.16. Stress and deformation in a 15 mm, 7 wire rope under F= 1,375 KN

It should be noticed that the load applied in this analysis are monotonic load. These results will be compared with that from the 36 wire rope generated under the dynamic analysis (see Section 5.3.2).

The results of the FE model that uses wire rope representation as a single rod are shown in Figure 5.17. The maximum von Mises stress is 8.8×10^8Pa and exists at the fixed support as shown in Figure 5.17a. However, the maximum displacement occurs at the free-end, with a maximum value of 0.04 m Figure 5.17b. This representation is not equivalent to the stress-strain contours that were shown in Figures 5.12-5.16. That means the wire rope construction cannot follow the behavior of a simply supported beam. Thus, more wires are required with an appropriate construction to fully describe the real behavior of a complex rope structure under loading.

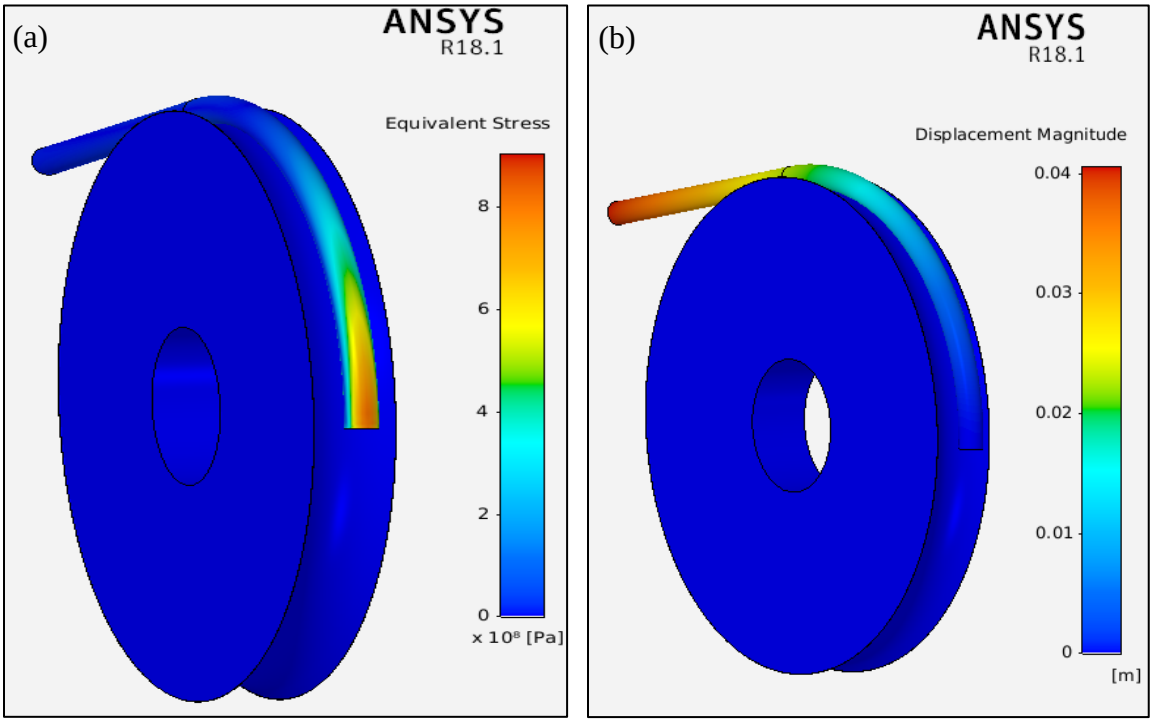

Figure 5.17. Stress and deformation in a 30 mm, 1 wire rope under F= 1,375 KN

5.3.2. Dynamic Analysis of Rope Bent over Sheave. Explicit dynamics has been performed on the ropes running over sheaves. It is well suited for the analysis of wire ropes, where large deformations, geometry nonlinearity, complex contact conditions, and failure can be modeled and captured in a short period of time. The simulations are performed for a short time, in milliseconds, and the angular velocity of rope, its weight and the frictional contacts of its wire are applied.

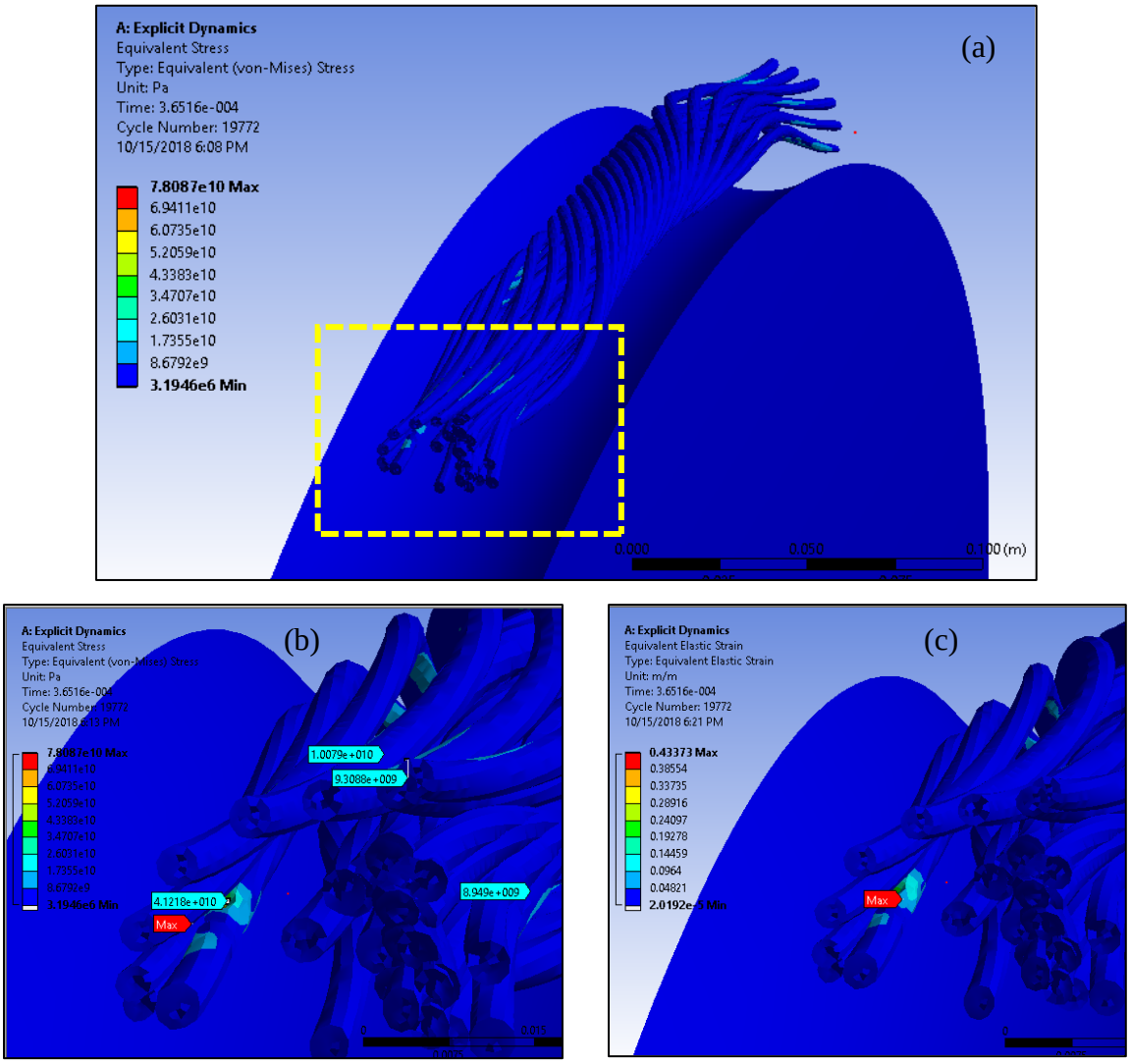

Figure 5.18. Stress and deformation of a 15 mm,1×36 strand wire rope with F= 1,375 KN

The results of the first explicit dynamics experiment on a 1×36 wire rope with diameter 15 mm are shown in Figure 5.18. It can be seen that the maximum equivalent (von-Mises) stress is 4.12×10^{10} Pa in the wires of the outer layer. Other stresses are probed and depicted in Figure 5.18 (b). Figure 5.18 (c) shows that the maximum equivalent strain is 0.433 $[m/m]$, which indicates a large deformation in the strands.

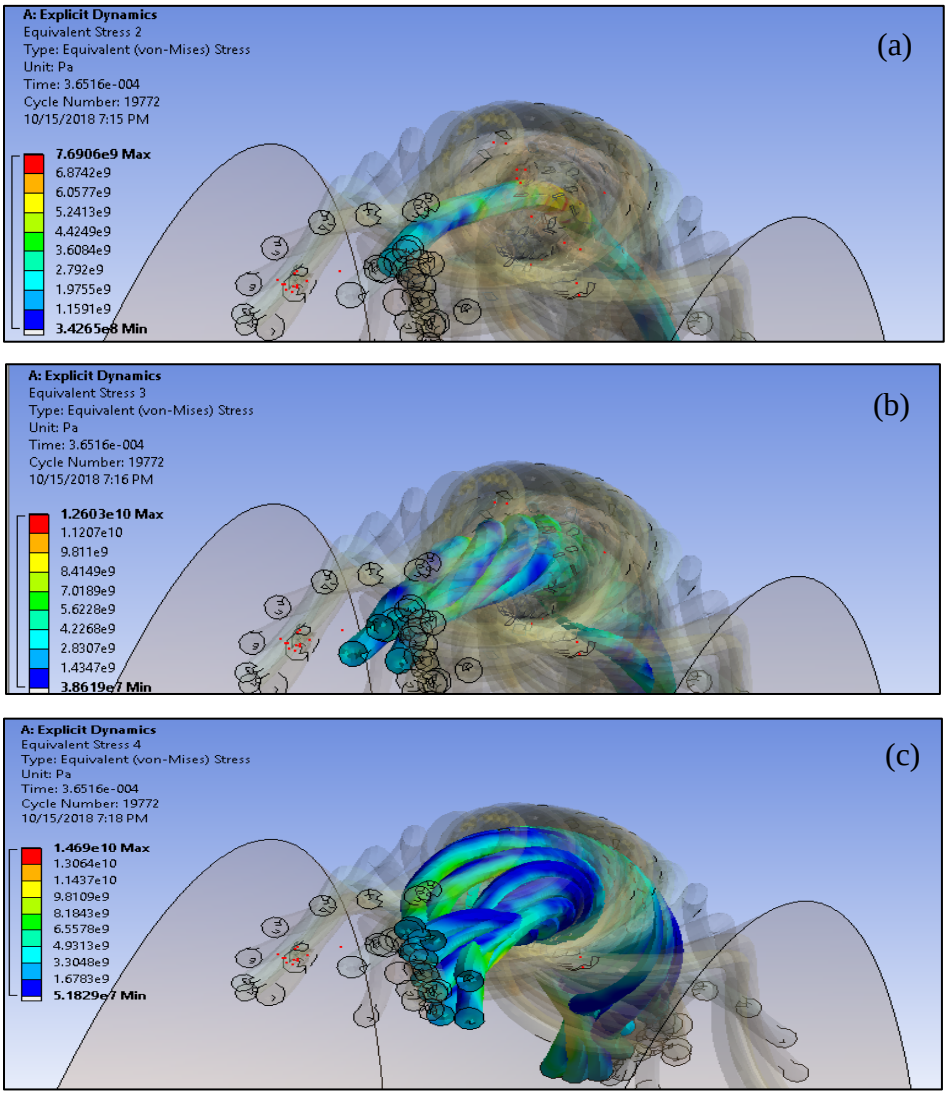

Figure 5.19. Equivalent stress in a 15 mm, 1×36 strand wire rope under F=1,375 KN: (a) core , (b) layer 1, (c) layer 2, and (d) layer 3

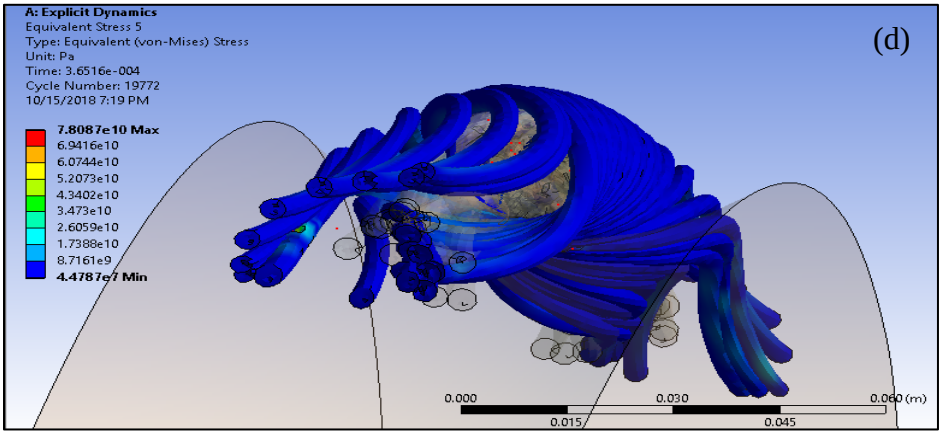

Figure 5.19. Equaivlent stress in a 15 mm, 1×36 strand wire rope under F=1,375 KN: (a) core , (b) layer 1, (c) layer 2, and (d) layer 3 (Cont.)

Figures 5.19 (a-d) show the equivalent von Mises stresses in different layers of the spiral wire rope. The results indicate that the stresses developed in the core are the least, whereas other layers sustain significant stresses. These results are not far from those in the static analyses that have been carried out on simple strands. Thus, the static analysis can be used for analyzing the wire rope stress distribution with a good degree of accuracy.

However, stress distribution cannot be used alone to judge the safe use of wire ropes. In this case, the safety factor of the wire rope was determined for a limited number of cycles.

It can be concluded from Figures 5.19 that the behavior of the wire is anisotropic and the stresses are significant in the zones of contact between the wires. To capture this behavior, each layer responds to the applied load by an extension along its neutral axis and a confinement in the radial direction. As a result, the wires become highly distorted and permanent plastic strain develops indicating irreversible process of deformation and yielding of the steel material. To further investigate the safe operational use of this rope,

the factor of safety was estimated for a number of cycles equivalent to 19,772 cycles. The results are shown in Figure 5.20 (a) and (b) for the core wire and first inner layer.

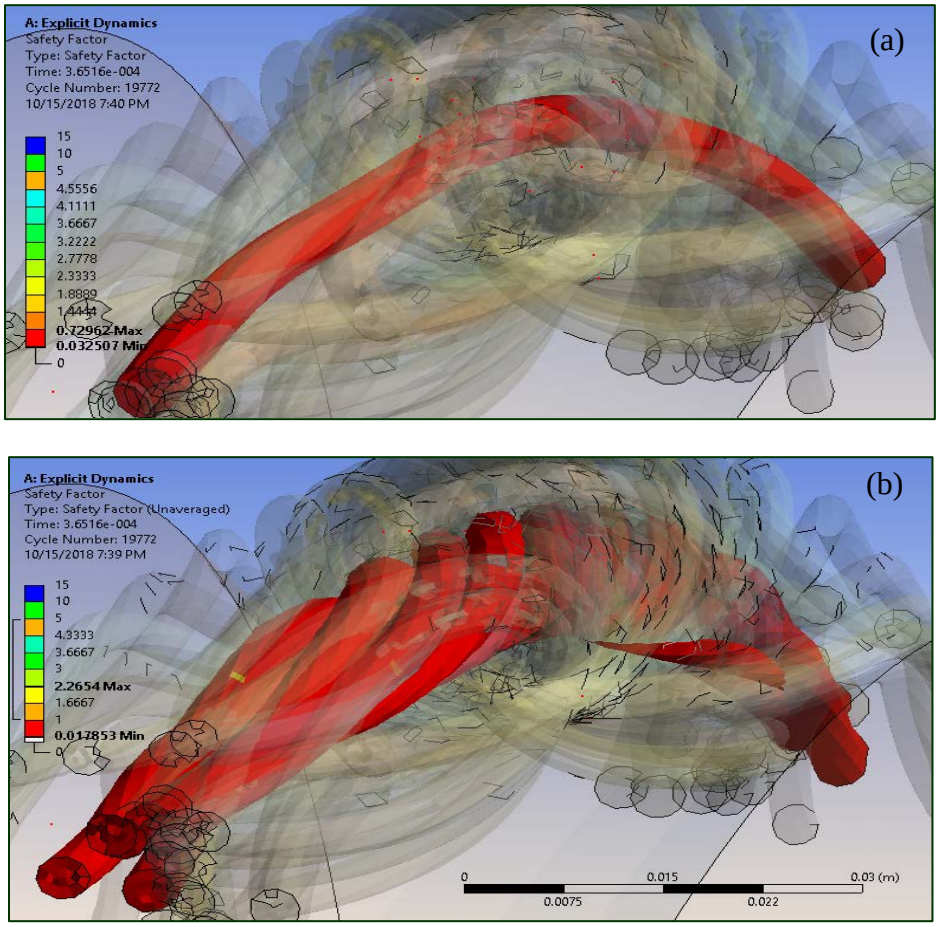

Figure 5.20. Safety factor in a 15 mm, 1×36 wire rope under F = 1,375 KN: (a) wire and (b) first inner layer

5.4. SUMMARY

The kinematic and dynamic analyses of a multibody system provide valuable information about the loads that a structural member is subjected to. In the case of a

dragline machinery, it saves time, money, and personnel required to carry out dynamic experimentations. In this research study, the spatial kinematic functions and dynamic loads associated with dragline operations, are accurately predicted and validated using real-world data in literature and field observations. The formulation of the multibody dynamic model using Kane's method has provided information about the acceleration and the variation of other loads that develop during the operation. The dynamic model of the dragline front-end assembly is a complete model and can be used in any part of the operational cycle of the dragline machinery. This significance is also confirmed by designing and analyzing a virtual dragline model for the kinematics and dynamic analysis.

The kinematic and dynamic of the dragline front-end assembly resulted in a highly nonlinear differential algebraic equations (DAE), which are solved using numerical methods in Mathematica. The results of the computational dynamic model show that the drag rope is the weakest link in the front-end assembly since it carries the maximum load of 1.375×10^6 N. This load was used to perform FEA on wire rope of simple and complex constructions. Static analysis were performed on simple strands to check the feasibility of using static FEA, which can save computational time. The results of the static analyses are compared and validated using the literature on simple strands. In addition, explicit dynamics analysis has been carried out on complex spiral rope of 36 wire rope. The FEA results showed that significant stresses and deformations are more likely to develop in the area of contact between the wires. The wire-wire contact areas are believed to be highly intense localized stress areas. The manufacturing process of the wire ropes can cause high deformation in the layers and it should also be considered in the form of microstructural characterization research. That would help defining the premier cause of wire rope failures.

6. SUMMARY, CONCLUSIONS, AND RECOMMENDATIONS

This section provides a summary of the findings, conclusions, contributions to the current body of knowledge, and recommendations for a new direction in this research. The summary highlights the important steps followed to achieve the research objectives. The conclusions provide the key points that relate the research objectives to the major contributions in the research scope. The original contributions are provided, as well as their potential impact on the current research knowledge and frontiers. The section ends with recommendations for future study to improve the current research results and expand the directions and frontiers of the dragline kinematics and dynamics research.

6.1. SUMMARY

The dragline machinery is a capital-intensive machinery that is primarily used to excavate and move 200+ tons of waste materials in a cycle of about 60 seconds (Kumatso, 2017). The productivity of such machinery is constrained by the performance and the longevity of its components. The payload and the bucket of the Marion 7800 dragline for this study weighs about 30 tons (Nikiforuk and Ochitwa, 1964). These parameters are variable, repeated load and are considered as important indicators of the machine performance and its longevity. These loads, on the other hand, due to their variations, are a source of uncertainty to the dragline performance (Lumley, 2014).

Dragline performance monitoring systems are essential tools in every dragline machinery. They provide critical information about the payload, stresses in the machine boom, and excessive loading. They are, however, built using simplified kinematics and dynamic models since the 80’s (McCoy Jr. and Crowgey,1980; Godfrey and Susanto,

1989). These studies excluded important structural components that can hinder machine availability, performance and productivity. In addition, the dragline simulation models provided in literature are limited to either the digging or swinging phases. That makes the use of current computer models limited in capturing the machine response to the full operating cycle.

As a result of the limitations of current models, dragline kinematics and dynamics have been advanced in this research endeavor by including important structural components within the front-end assembly. The kinematic model of the dragline is a comprehensive model that allows the description of the motion of all dragline front-end assembly in details. The model is built based on a 3-D visualization of the motion of every component in the front-end assembly using the concept of the generalized speeds (Kane and Levinson, 1985).

The dynamic model is a 3 DOF computational model and it incorporates the payloads, formation cutting resistance, and rope-formation friction forces. Numerical simulations have been carried out using Mathematica for simulating the kinematics of the hoist, dump, and drag ropes. The dynamic model is developed to include only the important contributing forces and torques, an important feature of the Kane's method.

A virtual dragline simulator is built using SolidWorks and it highlights the elements of the unknown properties, such as their masses and moments of inertia. Finite element (FE) models of different constructions of wire rope are tested in ANSYS (R18.1) using the output of the dynamic model. The results of the FE models under static and dynamic loading conditions are provided in Section 5 and analyzed thoroughly.

6.2. CONCLUSIONS

This research study was undertaken to address the limitations of the current body of knowledge established via thorough literature review on the kinematics, dynamics and stress intensity of dragline machinery. All the objectives enlisted in Section one have been achieved within the scope defined in Section 1.3. Detailed kinematics and dynamic models of the dragline front-end assembly have been formulated using Kane's method. The kinematics model is based on the concept of generalized speeds (motion variables) and the vector loop method was used as configuration constraints. The kinematics model provides information about the front-end assembly during digging phase, and it also captures the kinematics in the sense of angular rotation of the machine house and the relative motion between components with respect to the machine house.

From the kinematics simulation of the dragline front-end assembly, the following conclusions can be drawn:

1. Vector loop method is not enough to capture the relative motions between different moving components in a multibody mechanical system. The method is important for minimizing constraint violation and it supports the kinematics analysis.
2. Inconsistent initial conditions of the unknown trajectories may produce a singular Jacobian matrix, or yield inaccurate trajectory functions of the ropes.
3. The drift error for using the constraint equations is very small and its value for every trajectory is below 10^{-4}degree, which indicates the accuracy of the kinematics formulation and its solution algorithm.
4. The angular velocity of the dump rope is much higher than that for the hoist and drag ropes since it has higher degrees of freedom than that of other ropes.

5. The linear displacements of the hoist, drag and dump ropes affect their angular displacements. Maximum values of -22.5° at 100 m and -72.5° at 62 m are achieved for the hoist rope and drag rope, respectively.
6. The angular accelerations of the ropes are minimal at the end of digging and they are 0.1 deg/s², -0.05 deg/s², and 1 deg/s² for the hoist, drag, and dump ropes, respectively. This behavior is explainable from an operational viewpoint.
7. The Baumgarte's Stabilization Technique (BTS) reduced the drift error that exists due to constraints violation.

The dynamic formulation focused on finding the unknown contributing forces and torques rather than solving the reaction forces, which are not required for this research study. That resulted in an advanced formulation of the dynamic model and the inclusion of different important aspects in the analysis, such as the friction of the drag rope with the formation, resistance to cutting force, and variable masses in the ropes. The solution of the dynamic model was performed using Mathematica on a compact form of the equations of motion. From the analysis of the dynamic model simulation, the following conclusions can be drawn:

1. Mass and inertia properties of the front-end assembly are important design data and are directly used to estimate the forces and torques. Thus, the accuracy of the dynamic analysis fundamentally depends on these inputs and other engineering inputs.
2. The solution of the dynamic model also depends on the initial condition of trajectory functions and their evolution with time.

3. The horizontal component of the cutting resistance force is always greater than the vertical one. The maximum cutting resistance of 412.31 KN, occurs 5 seconds into the digging time.
4. Hoist rope mass increases 1000 kg, while the drag rope mass decreases 600 kg at the end of digging. Their variations affect the dynamic results and must be accurately factored into the analysis.
5. A maximum dragging force of 1.375×10^6N, occurs when the bucket has already moved for a period equivalent to three-quarters of the digging time.
6. The maximum hoist torque 917.87 KN.m occurs after 10 seconds into the swinging time.

The results of the finite element analysis on wire ropes yield the following conclusions:

1. The deformation of the wires of an axially loaded rope is anisotropic due to their geometric nonlinearity and the load variations along the cross section of the rope.
2. Under the effect of static loading, stress is less in areas of wires that are not in direct contact. However, significant stresses develop at contact zones. A (1×6) wire rope exhibits a maximum contact stress of 6×10^9 Pa, whereas a construction $(1 \times 6 \times 12 \times 18)$ rope bent on sheave exhibits a maximum contact stress of 7.8×10^{10} Pa.
3. Dynamic explicit tests for a rope construction of $(1 \times 6 \times 12 \times 18)$ bent on a sheave showed that maximum stresses are the least in the core wire with a value of 7.6×10^9Pa and are the highest for the outer layers with a value of 7.8×10^{10}Pa.
4. The core layer (wire) exhibits significant stress waves along its length, whereas the outer layers have less stresses along their lengths.

5. The Stress intensity factor (SIF) is the highest at zones of contact, where stress localization is evident, and lower in other regions.
6. The SIF estimates for the rope construction of $(1 \times 6 \times 12 \times 18)$ bent on a sheave showed that this rope fails under the effect of dynamic loading.
7. Contact stresses are the main source of failure mechanisms in wire ropes due to fretting fatigue between wires.

6.3. MAJOR CONTRIBUTIONS

This research is a pioneering effort in dragline front-end assembly kinematics and dynamics modeling and the associated stress analysis. It has expanded research frontiers in these areas and provided knowledge and tools for further research and education for understanding the complex geometric domains of the dragline machinery. The research contributions are as follows:

1. This study is a pioneering effort toward completely modeling and simulating the dragline front-end assembly. Previous research studies ignored the effect of the boom point sheave and the bucket and its rigging system. In this research, an appropriate representation is considered for all front-end elements.
2. The current study introduces new formulation of the kinematics of a multibody system of the front-end assembly. The kinematic equations are not only based on the vector loop method, but on a complete kinematic analysis and coupling of all dragline front-end components using the method of generalized speeds.
3. The solution of the kinematics differential algebraic equations is a three-step approach to accurately solve the initial conditions of the trajectories, reduce the drift error and improve the model response versus the imposed geometrical constraints.

This research is a pioneering effort in advancing the kinematics of closed-loop mechanisms.

4. The dynamic model is a pioneering effort toward formulating the dynamics of the dragline machinery using Kane's method. All previous studies used the Newton-Euler or the Lagrange's formulations, which require major model simplification. The geometry of the dragline front-end assembly is augmented in the current study and is the most complete model to date in dragline dynamics.
5. A significant contribution in dragline machinery research stems from the dynamic modeling of any combination of the dragline operating cycles. The digging phase and full bucket swinging phase are modeled successfully without augmenting the degrees of freedom of the model. No research, to date, has provided such description to the dragline operating cycle.
6. The virtual dragline simulator serves as a platform for training mining engineers and can be used as a tool for education and research initiatives.
7. The stress analysis on wire ropes provides new avenues towards design modifications of complex wire rope construction. The stress intensity calculation has also identified the root cause of failures in the wire rope running under variable loading.

6.4. RECOMMENDATIONS

This research was carried out based on the current body of knowledge and can be improved by considering the following recommendations:

1. Due to proprieties constraints, the virtual model of the dragline was designed based on the operational characteristics of the machine and on scaling a model from

literature (Nikiforuk and Ochitwa, 1964). Thus, the results can be significantly improved by using a CAD model of a real dragline.

2. The Kane's method fits well for rigid body modeling and analysis, and the ropes are modeled as rigid bodies. The current study should include flexible, deformable ropes which produce accurate tension in the ropes.
3. The bucket-ground interactions are limited to the estimation of resistive cutting force and ignored the effect of frictions. The inclusion of the frictional contact forces between the bucket and ground can increase the accuracy of the results.
4. Frictional contact between the drag rope and the ground has been developed, but was not part of the analysis due to limited knowledge of the model parameters.
5. The development of stress analysis framework of the wire rope is significantly constrained by the huge computational cost and the limitation of the current models to run with limited number of licenses on the cluster. Nonlinear contact behavior, large deformation, and mesh refinements, solution step discretization resulted in very large input files that take very long time to load, run and converge. Thus, the stress analyses on wire rope are limited to 3 D wire ropes of construction (1×6) and $(1 \times 6 \times 12 \times 18)$.
6. Future research can include more complex constructions such as the construction described in Figure 2.4. Other constructions can be analyzed such as Bridon model (Figure 2.3b) with polymer infused in the core.
7. Comprehensive fatigue analysis must be carried out using experimental S-N curved, cyclic stresses versus number cycles to failure.

8. Detailed parametric analysis must be carried out to understand the effect of the ratio of sheave to rope diameters on stress distribution and deformation.
9. Experimental analysis must also be carried out to examine the increased length of the wire rope constructions to improve the rope behavior to mechanical loading.
10. Microstructural characterization of the different constructions of the wire rope must be examined to understand its fatigue behavior under static and dynamic loading conditions.

APPENDIX

MATHEMATICA CODE FOR THE FORMULATION OF THE KINEMATIC AND DYNAMIC MODEL USING KANE'S METHOD

```
Clear["Global`*"]
Clear[U]
n1={1,0,0};
n2={0,1,0};
n3={0,0,1};
NRB= {{Cos[q1],0,Sin[q1]},{0,1,0},{-Sin[q1],0,Cos[q1]}};
BRbod1= {{c,-s,0},{s,c,0},{0,0,1}};
BRbod2= {{c,s,0},{-s,c,0},{0,0,1}};
BRC={{Cos[q2],-Sin[q2],0},{  Sin[q2],Cos[q2],0},{0,0,1}}
BRD={{Cos[q3],  Sin[q3],0},{-Sin[q3],Cos[q3],0},{0,0,1}}/.{q3->q4[t]}
BRE={{Cos[q4],  Sin[q4],0},{-Sin[q4],Cos[q4],0},{0,0,1}}/.{q4->q4[t]}
BRF={{Cos[q5],-Sin[q5],0},{   Sin[q5],Cos[q5],0},{0,0,1}}/.{q5->q5[t]}
BRG={{Cos[q6],  Sin[q6],0}, {-Sin[q6],Cos[q6],0},{0,0,1}}/.{q6->q6[t]}
```

```
{{Cos[q2],-Sin[q2],0},{Sin[q2],Cos[q2],0},{0,0,1}}
{{Cos[q4[t]],Sin[q4[t]],0},{-Sin[q4[t]],Cos[q4[t]],0},{0,0,1}}
{{Cos[q4[t]],Sin[q4[t]],0},{-Sin[q4[t]],Cos[q4[t]],0},{0,0,1}}
{{Cos[q5[t]],-Sin[q5[t]],0},{Sin[q5[t]],Cos[q5[t]],0},{0,0,1}}
{{Cos[q6[t]],Sin[q6[t]],0},{-Sin[q6[t]],Cos[q6[t]],0},{0,0,1}}
```

```
NωB[t_]={0,u1[t],0}
NωC[t_]={u5[t],u6[t],u7[t]}
NωD[t_]={u11[t],u12[t],u13[t]}
NωE[t_]={u17[t],u18[t],u19[t]}
NωF[t_]={u23[t],u24[t],u25[t]}
NωG[t_]={u29[t],u30[t],u31[t]}
```

```
{0,u1[t],0}
{u5[t],u6[t],u7[t]}
{u11[t],u12[t],u13[t]}
{u17[t],u18[t],u19[t]}
{u23[t],u24[t],u25[t]}
{u29[t],u30[t],u31[t]}
```

```
VB[t_]={u2[t],u3[t],u4[t]}
VC[t_]={u8[t],u9[t],u10[t]}
VD[t_]={u14[t],u15[t],u16[t]}
```

```
VE[t_]={u20[t],u21[t],u22[t]}
VF[t_]={u26[t],u27[t],u28[t]}
VG[t_]={u32[t],u33[t],u34[t]}
VH1[t_]={u35[t],u36[t],u37[t]}
VF1[t_]={u38[t],u39[t],u40[t]}
VE1[t_]={u41[t],u42[t],u43[t]}
```

```
{u2[t],u3[t],u4[t]}
{u8[t],u9[t],u10[t]}
{u14[t],u15[t],u16[t]}
{u20[t],u21[t],u22[t]}
{u26[t],u27[t],u28[t]}
{u32[t],u33[t],u34[t]}
{u35[t],u36[t],u37[t]}
{u38[t],u39[t],u40[t]}
{u41[t],u42[t],u43[t]}
```

```
NωC[t_]= NωB[t].BRC+{0,0,NωC[t][[3]]}
NωD[t_]= NωB[t].BRE+{0,0,NωD[t][[3]]}/.{q4->q4[t]}
NωE[t_]= NωB[t].BRE+{0,0,NωE[t][[3]]}/.{q4->q4[t]}
NωF[t_]= NωB[t].BRF+{0,0,NωF[t][[3]]}/.{q5->q5[t]}
NωG[t_]= NωB[t].BRG+{0,0,NωG[t][[3]]}/.{q6->q6[t]}
```

```
{Sin[q2] u1[t],Cos[q2] u1[t],u7[t]}
{-Sin[q4[t][t]] u1[t],Cos[q4[t][t]] u1[t],u13[t]}
{-Sin[q4[t][t]] u1[t],Cos[q4[t][t]] u1[t],u19[t]}
{Sin[q5[t][t]] u1[t],Cos[q5[t][t]] u1[t],u25[t]}
{-Sin[q6[t][t]] u1[t],Cos[q6[t][t]] u1[t],u31[t]}
```

```
B1B2={0,L3,0}(* DIDN'T use L17 instead of L2 and (-) is related
to a direction from B3 to COM B^**)
B1B*={-L1,L2 ,0}(* DIDN'T use L1 instead of L2*)
B2B*={-L3,-L4 ,0}
B2C*={L5,0,0}
C1C*={-L6,0,0}
C1D*={0,-L7,0}
D1D*={-L8,0,0}
D1E*={0,-0.5 *q8[t],0}
E1E*={0,0.5 *q8[t],0}
E1F*={-L9,0,0}
F1F*={L10,0,0}
F1G*={-0.5 *q7[t] ,0,0}
B1G*={0.5 *q7[t] ,0,0}
B1F1={q7[t],0,0}
B3B*={L11,0,0}
FH1={L12,-L13,0}
```

```
{0,L0,0}
{-L1,L2,0}
{-L3,-L4,0}
```

```
{L5,0,0}
{-L6,0,0}
{0,-L7,0}
{-L8,0,0}
{0,-0.5 q8[t],0}
{0,0.5 q8[t],0}
{-L9,0,0}
{L10,0,0}
{-0.5 q7[t],0,0}
{0.5 q7[t],0,0}
{q7[t],0,0}
{L11,0,0}
{L12,-L13,0}
VBinB[t_]= Cross[NωB[t],B3B*]
{0,0,-L11 u1[t]}
NωC[t]=NωB[t]+{0,0,NωC[t][[3]]}/.{u7[t]->0}
{0,u1[t],0}
VB2[t_]=VBinB[t]+ Cross[NωB[t], -B2B*]//Simplify
{0,0,-(L3+L11) u1[t]}
VC[t_]= VB2[t]+ Cross[NωB[t],BRC. B2C*]//Simplify (*B2C^*is
projected in B_Frame since NωC = NωB Both B2 and C are fixed on
C*)
{0,0,-(L3+Cos[q2] L5+L11) u1[t]}
VCinCS[t_]=VC[t]//Simplify
{0,0,-(L3+Cos[q2] L5+L11) u1[t]}
NωD[t_]= NωB[t]+{0,0,NωE[t][[3]]}//Simplify
{0,u1[t],u19[t]}
VC1inC[t]= VB2[t]+ Cross[NωB[t],BRC.( B2C*-C1C*)]//Simplify
{0,0,-(L3+Cos[q2] L5+Cos[q2] L6+L11) u1[t]}
VC1inCS[t]= VC1inC[t]//FullSimplify
{0,0,-(L3+Cos[q2] (L5+L6)+L11) u1[t]}
VD[t_]= VC1inCS[t]+ Cross[NωB[t],BRC. C1D*] (*Chosen NωB because
D is fixed in boom frame, which is also fixed in Machine house
frame *)
VDinDS[t_]=VD[t]//FullSimplify
{0,0,-Sin[q2] L7 u1[t]-(L3+Cos[q2] (L5+L6)+L11) u1[t]}
{0,0,-(L3+Cos[q2] (L5+L6)+Sin[q2] L7+L11) u1[t]}
VD1inD[t_]= VDinDS[t]+ Cross[NωD[t],-D1D*] (*No need to transform
VDinDS[t] because it is in the same frame*)
VD1inDS[t_]=VD1inD[t]//FullSimplify
{0,L8 u19[t],-L8 u1[t]-(L3+Cos[q2] (L5+L6)+Sin[q2] L7+L11) u1[t]}
{0,L8 u19[t],-(L3+Cos[q2] (L5+L6)+Sin[q2] L7+L8+L11) u1[t]}
NωE[t]= NωB[t]+{0,0,NωE[t][[3]]}//Simplify
{0,u1[t],u19[t]}
VD1inE= VD1inDS[t](* No need to transfer VD1inE to E ref.frame
```

```
because D and E are rotating in together*)
 {0,L8 u19[t],-(L3+Cos[q2] (L5+L6)+Sin[q2] L7+L8+L11) u1[t]}
VD1inES[t_]= VD1inE//FullSimplify
 {0,L8 u19[t],-(L3+Cos[q2] (L5+L6)+Sin[q2] L7+L8+L11) u1[t]}
VE[t_]=VD1inES[t]+
Cross[NwE[t],D1E*]/.{n_Real/;IntegerPart[n]==n-> IntegerPart[n]}
VEinES[t]=VE[t]//FullSimplify
 {0.5 q8[t] u19[t],L8 u19[t],-(L3+Cos[q2] (L5+L6)+Sin[q2] L7+L8+L11)
u1[t]}
 {0.5 q8[t] u19[t],L8 u19[t],-(L3+Cos[q2] (L5+L6)+Sin[q2] L7+L8+L11)
u1[t]}
VE1inE[t_]=VEinES[t]+Cross[NwE[t],-
E1E*]/.{n_Real/;IntegerPart[n]==n-> IntegerPart[n]}
VE1inES[t_]=VE1inE[t]//FullSimplify
 {q8[t] u19[t],L8 u19[t],-(L3+Cos[q2] (L5+L6)+Sin[q2] L7+L8+L11)
u1[t]}
 {q8[t] u19[t],L8 u19[t],-(L3+Cos[q2] (L5+L6)+Sin[q2] L7+L8+L11)
u1[t]}
NwF[t]=NwB[t]+{0,0,NwF[t][[3]]}
 {0,u1[t],u25[t]}
VE1inB[t_]=VE1inES[t].Transpose[BRE]//FullSimplify(*Return a
vector described in e-frame to a vector in ref (B)*)
 {(Sin[q4[t]] L8+Cos[q4[t]] q8[t]) u19[t],(Cos[q4[t]] L8-Sin[q4[t]]
q8[t]) u19[t],-(L3+Cos[q2] (L5+L6)+Sin[q2] L7+L8+L11) u1[t]}
VE1inFS[t_]=VE1inB[t].BRF//FullSimplify
 {(Sin[q4[t]+q5[t]] L8+Cos[q4[t]+q5[t]] q8[t])
u19[t],(Cos[q4[t]+q5[t]] L8-Sin[q4[t]+q5[t]] q8[t]) u19[t],-
(L3+Cos[q2] (L5+L6)+Sin[q2] L7+L8+L11) u1[t]}
VFinFS[t_]=VE1inFS[t]+Cross[NwF[t],E1F*]//FullSimplify
 {(Sin[q4[t]+q5[t]] L8+Cos[q4[t]+q5[t]] q8[t])
u19[t],(Cos[q4[t]+q5[t]] L8-Sin[q4[t]+q5[t]] q8[t]) u19[t]-L9
u25[t],L9 u1[t]-(L3+Cos[q2] (L5+L6)+Sin[q2] L7+L8+L11) u1[t]}
VB1[t_]= VBinB[t]+Cross[NwB[t],-B1B*]//Simplify
 {0,0,-(L1+L11) u1[t]}
NwG[t]=NwB[t]+{0,0,NwG[t][[3]]}
 {0,u1[t],u31[t]}
VGinGS[t_]=VB1[t].BRG+Cross[NwG[t],B1G*]/.{n_Real/;IntegerPart[n]
==n-> IntegerPart[n]}//FullSimplify
 {0,0.5 q7[t] u31[t],-1. (L1+L11+0.5 q7[t]) u1[t]}
VH1inFS[t_]=VFinFS[t]+Cross[NwF[t],FH1]//FullSimplify
 {(Sin[q4[t]+q5[t]] L8+Cos[q4[t]+q5[t]] q8[t]) u19[t]+L13
u25[t],(Cos[q4[t]+q5[t]] L8-Sin[q4[t]+q5[t]] q8[t]) u19[t]+(-L9+L12)
u25[t],-(L3+Cos[q2] (L5+L6)+Sin[q2] L7+L8-L9+L11+L12) u1[t]}
VF1inGS[t_]=VB1[t].BRG
+Cross[NwG[t],B1F1]+{D[q7[t],t],0,0}//FullSimplify
```

```
(*In Fasseler Thesis, {D[Subscript[q, 7][t],t],0,0} is written
^CV^D= Subscript[u, 15]-Subscript[u, 12]*)
 {Subscript[q, 7]'[t],q7[t] u31[t],-(L1+L11+q7[t]) u1[t]}
NωCT[t_]= NωB[t].BRC+{0,0,NωC[t][[3]]}
NωDT[t_]= NωB[t].BRE+{0,0,NωD[t][[3]]}/.{u13[t]-> u19[t]}
NωET[t_]= NωB[t].BRE+{0,0,NωE[t][[3]]}
NωFT[t_]= NωB[t].BRF+{0,0,NωF[t][[3]]}
NωGT[t_]= NωB[t].BRG+{0,0,NωG[t][[3]]}
 {Sin[q2] u1[t],Cos[q2] u1[t],0}
 {-Sin[q4[t]] u1[t],Cos[q4[t]] u1[t],u19[t]}
 {-Sin[q4[t]] u1[t],Cos[q4[t]] u1[t],u19[t]}
 {Sin[q5[t]] u1[t],Cos[q5[t]] u1[t],u25[t]}
 {-Sin[q6[t]] u1[t],Cos[q6[t]] u1[t],u31[t]}
u1[t]=NωB[t][[2]]//FullSimplify
{u2[t],u3[t],u4[t]}=VBinB[t]//FullSimplify
{u5[t],u6[t],u7[t]}=NωCT[t]//FullSimplify
{u8[t],u9[t],u10[t]}=VCinCS[t]//FullSimplify
{u11[t],u12[t],u13[t]}=NωDT[t]//FullSimplify
{u14[t],u15[t],u16[t]}=VDinDS[t]//FullSimplify
{u17[t],u18[t],u19[t]}=NωET[t]//FullSimplify
{u20[t],u21[t],u22[t]}=VEinES[t]//FullSimplify
{u23[t],u24[t],u25[t]}=NωFT[t]//FullSimplify
{u26[t],u27[t],u28[t]}=VFinFS[t]//FullSimplify
{u29[t],u30[t],u31[t]}=NωGT[t]//FullSimplify
{u32[t],u33[t],u34[t]}=VGinGS[t]//FullSimplify
{u35[t],u36[t],u37[t]}=VH1inFS[t]//FullSimplify
{u38[t],u39[t],u40[t]}=VF1inGS[t]//FullSimplify
{u41[t],u42[t],u43[t]}=VE1inES[t]//FullSimplify
 u1[t]
 {0,0,-L11 u1[t]}
 {Sin[q2] u1[t],Cos[q2] u1[t],0}
 {0,0,-(L3+Cos[q2] L5+L11) u1[t]}
 {-Sin[q4[t]] u1[t],Cos[q4[t]] u1[t],u19[t]}
 {0,0,-(L3+Cos[q2] (L5+L6)+Sin[q2] L7+L11) u1[t]}
 {-Sin[q4[t]] u1[t],Cos[q4[t]] u1[t],u19[t]}
 {0.5 q8[t] u19[t],L8 u19[t],-(L3+Cos[q2] (L5+L6)+Sin[q2] L7+L8+L11)
u1[t]}
 {Sin[q5[t]] u1[t],Cos[q5[t]] u1[t],u25[t]}
 {(Sin[q4[t]+q5[t]] L8+Cos[q4[t]+q5[t]] q8[t])
u19[t],(Cos[q4[t]+q5[t]] L8-Sin[q4[t]+q5[t]] q8[t]) u19[t]-L9
u25[t],L9 u1[t]-(L3+Cos[q2] (L5+L6)+Sin[q2] L7+L8+L11) u1[t]}
 {-Sin[q6[t]] u1[t],Cos[q6[t]] u1[t],u31[t]}
 {0,0.5 q7[t] u31[t],-1. (L1+L11+0.5 q7[t]) u1[t]}
 {(Sin[q4[t]+q5[t]] L8+Cos[q4[t]+q5[t]] q8[t]) u19[t]+L13
u25[t],(Cos[q4[t]+q5[t]] L8-Sin[q4[t]+q5[t]] q8[t]) u19[t]+(-L9+L12)
```

```
u25[t],-(L3+Cos[q2] (L5+L6)+Sin[q2] L7+L8-L9+L11+L12) u1[t]}
 {Subscript[q, 7]'[t],q7[t] u31[t],-(L1+L11+q7[t]) u1[t]}
 {q8[t] u19[t],L8 u19[t],-(L3+Cos[q2] (L5+L6)+Sin[q2] L7+L8+L11)
u1[t]}
Clear[vv];
V= Array[vv,42];
Do[vv[i]=VBinB[t][[i]],{i,1,3}]
Do[vv[i+3]=NwCT[t][[i]],{i,1,3}]
Do[vv[i+6]=VCinCS[t][[i]],{i,1,3}]
Do[vv[i+9]=NwDT[t][[i]],{i,1,3}]
Do[vv[i+12]=VDinDS[t][[i]],{i,1,3}]
Do[vv[i+15]=NwET[t][[i]],{i,1,3}]
Do[vv[i+18]=VEinES[t][[i]],{i,1,3}]
Do[vv[i+21]=NwFT[t][[i]],{i,1,3}]
Do[vv[i+24]=VFinFS[t][[i]],{i,1,3}]
Do[vv[i+27]=NwGT[t][[i]],{i,1,3}]
Do[vv[i+30]=VGinGS[t][[i]],{i,1,3}]
Do[vv[i+33]=VH1inFS[t][[i]],{i,1,3}]
Do[vv[i+36]=VF1inGS[t][[i]],{i,1,3}]
Do[vv[i+39]=VE1inES[t][[i]],{i,1,3}]
V= FullSimplify[V]

 {0,0,-L11 u1[t],Sin[q2] u1[t],Cos[q2] u1[t],0,0,0,-(L3+Cos[q2]
L5+L11) u1[t],-Sin[q4[t]] u1[t],Cos[q4[t]] u1[t],u19[t],0,0,-
(L3+Cos[q2] (L5+L6)+Sin[q2] L7+L11) u1[t],-Sin[q4[t]]
u1[t],Cos[q4[t]] u1[t],u19[t],0.5 q8[t] u19[t],L8 u19[t],-(L3+Cos[q2]
(L5+L6)+Sin[q2] L7+L8+L11) u1[t],Sin[q5[t]] u1[t],Cos[q5[t]]
u1[t],u25[t],(Sin[q4[t]+q5[t]] L8+Cos[q4[t]+q5[t]] q8[t])
u19[t],(Cos[q4[t]+q5[t]] L8-Sin[q4[t]+q5[t]] q8[t]) u19[t]-L9
u25[t],L9 u1[t]-(L3+Cos[q2] (L5+L6)+Sin[q2] L7+L8+L11) u1[t],-
Sin[q6[t]] u1[t],Cos[q6[t]] u1[t],u31[t],0,0.5 q7[t] u31[t],-1.
(L1+L11+0.5 q7[t]) u1[t],(Sin[q4[t]+q5[t]] L8+Cos[q4[t]+q5[t]] q8[t])
u19[t]+L13 u25[t],(Cos[q4[t]+q5[t]] L8-Sin[q4[t]+q5[t]] q8[t])
u19[t]+(-L9+L12) u25[t],-(L3+Cos[q2] (L5+L6)+Sin[q2] L7+L8-L9+L11+L12)
u1[t],Subscript[q, 7]'[t],q7[t] u31[t],-(L1+L11+q7[t]) u1[t],q8[t]
u19[t],L8 u19[t],-(L3+Cos[q2] (L5+L6)+Sin[q2] L7+L8+L11) u1[t]}
U=V//FullSimplify;
U=U/.{u13[t]->u19[t]}
 {0,0,-L11 u1[t],Sin[q2] u1[t],Cos[q2] u1[t],0,0,0,-(L3+Cos[q2]
L5+L11) u1[t],-Sin[q4[t]] u1[t],Cos[q4[t]] u1[t],u19[t],0,0,-
(L3+Cos[q2] (L5+L6)+Sin[q2] L7+L11) u1[t],-Sin[q4[t]]
u1[t],Cos[q4[t]] u1[t],u19[t],0.5 q8[t] u19[t],L8 u19[t],-(L3+Cos[q2]
(L5+L6)+Sin[q2] L7+L8+L11) u1[t],Sin[q5[t]] u1[t],Cos[q5[t]]
u1[t],u25[t],(Sin[q4[t]+q5[t]] L8+Cos[q4[t]+q5[t]] q8[t])
u19[t],(Cos[q4[t]+q5[t]] L8-Sin[q4[t]+q5[t]] q8[t]) u19[t]-L9
```

```
u25[t],L9 u1[t]-(L3+Cos[q2] (L5+L6)+Sin[q2] L7+L8+L11) u1[t],-
Sin[q6[t]] u1[t],Cos[q6[t]] u1[t],u31[t],0,0.5 q7[t] u31[t],-1.
(L1+L11+0.5 q7[t]) u1[t],(Sin[q4[t]+q5[t]] L8+Cos[q4[t]+q5[t]] q8[t])
u19[t]+L13 u25[t],(Cos[q4[t]+q5[t]] L8-Sin[q4[t]+q5[t]] q8[t])
u19[t]+(-L9+L12) u25[t],-(L3+Cos[q2] (L5+L6)+Sin[q2] L7+L8-L9+L11+L12)
u1[t],Subscript[q, 7]'[t],q7[t] u31[t],-(L1+L11+q7[t]) u1[t],q8[t]
u19[t],L8 u19[t],-(L3+Cos[q2] (L5+L6)+Sin[q2] L7+L8+L11) u1[t]}
(*US={For[i=2,i⩽43,i++,Print[Subscript[u, i][t]]];*)
For[i=0;U[[i]][t]=U[i+1],i<42,i++; Print[U[[i]]];
 Set::write: Tag List in {t} is Protected.
 0
 0
 -L11 u1[t]
 Sin[q2] u1[t]
 Cos[q2] u1[t]
 0
 0
 0
 -(L3+Cos[q2] L5+L11) u1[t]
 -Sin[q4[t]] u1[t]
 Cos[q4[t]] u1[t]
 u19[t]
 0
 0
 -(L3+Cos[q2] (L5+L6)+Sin[q2] L7+L11) u1[t]
 -Sin[q4[t]] u1[t]
 Cos[q4[t]] u1[t]
 u19[t]
 0.5 q8[t] u19[t]
 L8 u19[t]
 -(L3+Cos[q2] (L5+L6)+Sin[q2] L7+L8+L11) u1[t]
 Sin[q5[t]] u1[t]
 Cos[q5[t]] u1[t]
 u25[t]
 (Sin[q4[t]+q5[t]] L8+Cos[q4[t]+q5[t]] q8[t]) u19[t]
 (Cos[q4[t]+q5[t]] L8-Sin[q4[t]+q5[t]] q8[t]) u19[t]-L9 u25[t]
 L9 u1[t]-(L3+Cos[q2] (L5+L6)+Sin[q2] L7+L8+L11) u1[t]
 -Sin[q6[t]] u1[t]
 Cos[q6[t]] u1[t]
 u31[t]
 0
 0.5 q7[t] u31[t]
 -1. (L1+L11+0.5 q7[t]) u1[t]
 (Sin[q4[t]+q5[t]] L8+Cos[q4[t]+q5[t]] q8[t]) u19[t]+L13 u25[t]
 (Cos[q4[t]+q5[t]] L8-Sin[q4[t]+q5[t]] q8[t]) u19[t]+(-L9+L12) u25[t]
```

```
 -(L3+Cos[q2] (L5+L6)+Sin[q2] L7+L8-L9+L11+L12) u1[t]
 Subscript[q, 7]'[t]
 q7[t] u31[t]
 -(L1+L11+q7[t]) u1[t]
 q8[t] u19[t]
 L8 u19[t]
 -(L3+Cos[q2] (L5+L6)+Sin[q2] L7+L8+L11) u1[t]
U=Evaluate[Table[ui+1[t],{i,1,42}]]
{{List/@U,List/@V}}//TableForm//FullSimplify

{u2[t],u3[t],u4[t],u5[t],u6[t],u7[t],u8[t],u9[t],u10[t],u11[t],u12[t],
u13[t],u14[t],u15[t],u16[t],u17[t],u18[t],u19[t],u20[t],u21[t],u22[t],u2
3[t],u24[t],u25[t],u26[t],u27[t],u28[t],u29[t],u30[t],u31[t],u32[t],u33[
t],u34[t],u35[t],u36[t],u37[t],u38[t],u39[t],u40[t],u41[t],u42[t],u43[t}

{{u2[t]},   {u3[t]},    {u4[t]},  {u5[t]},   {u6[t]},   {u7[t]},
{u8[t]},    {u9[t]},   {u10[t]},  {u11[t]},  {u12[t]},   {u13[t]},
{u14[t]},   {u15[t]},   {u16[t]},  {u17[t]},  {u18[t]},   {u19[t]},
{u20[t]},   {u21[t]},   {u22[t]},  {u23[t]},  {u24[t]},   {u25[t]},
{u26[t]},   {u27[t]},   {u28[t]},  {u29[t]},  {u30[t]},   {u31[t]},
{u32[t]},   {u33[t]},   {u34[t]},  {u35[t]},   {u36[t]},  {u37[t]},
{u38[t]},   {u39[t]},   {u40[t]},  {u41[t]},   {u42[t]},   {u43[t]}},
{
   {0},
   {0},
   {-L11 u1[t]},
   {Sin[q2] u1[t]},
   {Cos[q2] u1[t]},
   {0},
   {0},
   {0},
   {-(L3+Cos[q2] L5+L11) u1[t]},
   {-Sin[q4[t]] u1[t]},
   {Cos[q4[t]] u1[t]},
   {u19[t]},
   {0},
   {0},
   {-(L3+Cos[q2] (L5+L6)+Sin[q2] L7+L11) u1[t]},
   {-Sin[q4[t]] u1[t]},
   {Cos[q4[t]] u1[t]},
   {u19[t]},
   {0.5 q8[t] u19[t]},
   {L8 u19[t]},
   {-(L3+Cos[q2] (L5+L6)+Sin[q2] L7+L8+L11) u1[t]},
   {Sin[q5[t]] u1[t]},
```

```
   {Cos[q5[t]] u1[t]},
   {u25[t]},
   {(Sin[q4[t]+q5[t]] L8+Cos[q4[t]+q5[t]] q8[t]) u19[t]},
   {(Cos[q4[t]+q5[t]] L8-Sin[q4[t]+q5[t]] q8[t]) u19[t]-L9 u25[t]},
   {L9 u1[t]-(L3+Cos[q2] (L5+L6)+Sin[q2] L7+L8+L11) u1[t]},
   {-Sin[q6[t]] u1[t]},
   {Cos[q6[t]] u1[t]},
   {u31[t]},
   {0},
   {0.5 q7[t] u31[t]},
   {-1. (L1+L11+0.5 q7[t]) u1[t]},
   {(Sin[q4[t]+q5[t]] L8+Cos[q4[t]+q5[t]] q8[t]) u19[t]+L13 u25[t]},
   {(Cos[q4[t]+q5[t]] L8-Sin[q4[t]+q5[t]] q8[t]) u19[t]+(-L9+L12)
u25[t]},
   {-(L3+Cos[q2] (L5+L6)+Sin[q2] L7+L8-L9+L11+L12) u1[t]},
   {Subscript[q, 7]'[t]},
  {q7[t] u31[t]},
   {-(L1+L11+q7[t]) u1[t]},
   {q8[t] u19[t]},
   {L8 u19[t]},
   {-(L3+Cos[q2] (L5+L6)+Sin[q2] L7+L8+L11) u1[t]}
  }}
}
(*UWOt=V/.{Subscript[q, 3]→ Subscript[q, 4],Subscript[q, 4][t]→
Subscript[q, 4],Subscript[q, 5][t]→ Subscript[q, 5],Subscript[q,
6][t]→ Subscript[q, 6],Subscript[q, 7][t]→ Subscript[q,
7],Subscript[q, 8][t]→ Subscript[q, 8],(Subscript[q,
6]^')[t]→Subscript[u, 31][t]}//Simplify*)
UWt= V/.{q4-> q4[t],q5-> q5[t],q6-> q6[t],u13[t]->u19[t]}//Simplify
PartialvelR1= D[UWt,u1[t]]
PartialvelR19= D[UWt,u19[t]]
PartialvelR31= D[UWt,u31[t]]
Partialvel=PartialvelR1+PartialvelR19+PartialvelR31
 0
 0
 0
 0
VBinBN[t]=VBinB[t]//FullSimplify
NωCTN[t]=NωCT[t]//FullSimplify
VCinCSN[t]=VCinCS[t]//FullSimplify
NωDTN[t]=NωDT[t]
VDinDSN[t]=VDinDS[t]
NωETN[t]=NωET[t]
VEinESN[t]=VEinES[t]
NωFTN[t]=NωFT[t]
```

```
VFinFSN[t]=VFinFS[t]
NωGTN[t]=NωGT[t]
VGinGSN[t]=VGinGS[t]
VH1inFSN[t]=VH1inFS[t]
VF1inGSN[t]=VF1inGS[t]/.{Subscript[q, 7][t]→ u31[t]}
VE1inESN[t]=VE1inES[t]
(*VBinBN[t]=VBinB[t]//FullSimplify
NωCTN[t]=NωCT[t]//FullSimplify
VCinCSN[t]=VCinCS[t]//FullSimplify
NωDTN[t]=NωDT[t]
VDinDSN[t]=VDinDS[t]
NωETN[t]=NωET[t]
VEinESN[t]=VEinES[t]
NωFTN[t]=NωFT[t]/.{Subscript[u, 25][t]→ Subscript[Z, 5][t]}
VFinFSN[t]=VFinFS[t]/.{Subscript[u, 25][t]→ Subscript[Z, 5][t]}
NωGTN[t]=NωGT[t]/.{Subscript[u, 25][t]→ Subscript[Z, 5][t]}
VGinGSN[t]=VGinGS[t]
VH1inFSN[t]=VH1inFS[t]/.{Subscript[u, 25][t]→ Subscript[Z, 5][t]}
VF1inGSN[t]=VF1inGS[t]/.{(Subscript[q, 7]^)[t]→ Subscript[u,
31][t]}
VE1inESN[t]=VE1inES[t]*)
```

$\{0,0,-L_{11}\ u_1[t]\}$

$\{\text{Sin}[q_2]\ u_1[t],\text{Cos}[q_2]\ u_1[t],0\}$

$\{0,0,-(L_3+\text{Cos}[q_2]\ L_5+L_{11})\ u_1[t]\}$

$\{-\text{Sin}[q_4[t]]\ u_1[t],\text{Cos}[q_4[t]]\ u_1[t],u_{19}[t]\}$

$\{0,0,-(L_3+\text{Cos}[q_2]\ (L_5+L_6)+\text{Sin}[q_2]\ L_7+L_{11})\ u_1[t]\}$

$\{-\text{Sin}[q_4[t]]\ u_1[t],\text{Cos}[q_4[t]]\ u_1[t],u_{19}[t]\}$

$\{0.5\ q_8[t]\ u_{19}[t],L_8\ u_{19}[t],-(L_3+\text{Cos}[q_2]\ (L_5+L_6)+\text{Sin}[q_2]\ L_7+L_8+L_{11})\ u_1[t]\}$

$\{\text{Sin}[q_5[t]]\ u_1[t],\text{Cos}[q_5[t]]\ u_1[t],u_{25}[t]\}$

$\{(\text{Sin}[q_4[t]+q_5[t]]\ L_8+\text{Cos}[q_4[t]+q_5[t]]\ q_8[t])\ u_{19}[t],(\text{Cos}[q_4[t]+q_5[t]]\ L_8-\text{Sin}[q_4[t]+q_5[t]]\ q_8[t])\ u_{19}[t]-L_9\ u_{25}[t],L_9\ u_1[t]-(L_3+\text{Cos}[q_2]\ (L_5+L_6)+\text{Sin}[q_2]\ L_7+L_8+L_{11})\ u_1[t]\}$

$\{-\text{Sin}[q_6[t]]\ u_1[t],\text{Cos}[q_6[t]]\ u_1[t],u_{31}[t]\}$

$\{0,0.5\ q_7[t]\ u_{31}[t],-1.\ (L_1+L_{11}+0.5\ q_7[t])\ u_1[t]\}$

$\{(\text{Sin}[q_4[t]+q_5[t]]\ L_8+\text{Cos}[q_4[t]+q_5[t]]\ q_8[t])\ u_{19}[t]+L_{13}\ u_{25}[t],(\text{Cos}[q_4[t]+q_5[t]]\ L_8-\text{Sin}[q_4[t]+q_5[t]]\ q_8[t])\ u_{19}[t]+(-L_9+L_{12})\ u_{25}[t],-(L_3+\text{Cos}[q_2]\ (L_5+L_6)+\text{Sin}[q_2]\ L_7+L_8-L_9+L_{11}+L_{12})\ u_1[t]\}$

$\{u_{31}[t],q_7[t]\ u_{31}[t],-(L_1+L_{11}+q_7[t])\ u_1[t]\}$

$\{q_8[t]\ u_{19}[t],L_8\ u_{19}[t],-(L_3+\text{Cos}[q_2]\ (L_5+L_6)+\text{Sin}[q_2]\ L_7+L_8+L_{11})\ u_1[t]\}$

```
aB[t_]= D[VBinBN[t],t]+Cross[NωB[t],VBinBN[t]]
aC[t_]= D[VCinCSN[t],t]+Cross[NωCTN[t],VCinCSN[t]]
aD[t_]= D[VDinDSN[t],t]+ Cross[NωDTN[t],VDinDSN[t]]
aE[t_]=D[VEinESN[t],t]+ Cross[NωETN[t],VEinESN[t]]
```

```
aF[t_]=D[VFinFSN[t],t]+ Cross[NωFTN[t],VFinFSN[t]]
aG[t_]=D[VGinGSN[t],t]+ Cross[NωGTN[t],VGinGSN[t]]
aH1[t_]=D[VH1inFSN[t],t]+ Cross[NωFTN[t],VH1inFSN[t]]
aF1[t_]=D[VF1inGSN[t],t]+ Cross[NωGTN[t],VH1inFSN[t]]
```

{-L11 Subscript[u, 1][t]^2,0,-L11 Subscript[u, 1]'[t]}

{-Cos[q2] L3 Subscript[u, 1][t]^2-Cos[Subscript[q, 2]]^2 L5 Subscript[u, 1][t]^2-Cos[q2] L11 Subscript[u, 1][t]^2,Sin[q2] L3 Subscript[u, 1][t]^2+Cos[q2] Sin[q2] L5 Subscript[u, 1][t]^2+Sin[q2] L11 Subscript[u, 1][t]^2,-(L3+Cos[q2] L5+L11) Subscript[u, 1]'[t]}

{-Cos[q4[t]] L3 Subscript[u, 1][t]^2-Cos[q2] Cos[q4[t]] L5 Subscript[u, 1][t]^2-Cos[q2] Cos[q4[t]] L6 Subscript[u, 1][t]^2-Cos[q4[t]] Sin[q2] L7 Subscript[u, 1][t]^2-Cos[q4[t]] L11 Subscript[u, 1][t]^2,-Sin[q4[t]] L3 Subscript[u, 1][t]^2-Cos[q2] Sin[q4[t]] L5 Subscript[u, 1][t]^2-Cos[q2] Sin[q4[t]] L6 Subscript[u, 1][t]^2-Sin[q2] Sin[q4[t]] L7 Subscript[u, 1][t]^2-Sin[q4[t]] L11 Subscript[u, 1][t]^2,-(L3+Cos[q2] (L5+L6)+Sin[q2] L7+L11) Subscript[u, 1]'[t]}

{-Cos[q4[t]] L3 Subscript[u, 1][t]^2-Cos[q2] Cos[q4[t]] L5 Subscript[u, 1][t]^2-Cos[q2] Cos[q4[t]] L6 Subscript[u, 1][t]^2-Cos[q4[t]] Sin[q2] L7 Subscript[u, 1][t]^2-Cos[q4[t]] L8 Subscript[u, 1][t]^2-Cos[q4[t]] L11 Subscript[u, 1][t]^2-L8 Subscript[u, 19][t]^2+0.5 u19[t] Subscript[q, 8]'[t]+0.5 q8[t] Subscript[u, 19]'[t],-Sin[q4[t]] L3 Subscript[u, 1][t]^2-Cos[q2] Sin[q4[t]] L5 Subscript[u, 1][t]^2-Cos[q2] Sin[q4[t]] L6 Subscript[u, 1][t]^2-Sin[q2] Sin[q4[t]] L7 Subscript[u, 1][t]^2-Sin[q4[t]] L8 Subscript[u, 1][t]^2-Sin[q4[t]] L11 Subscript[u, 1][t]^2+0.5 q8[t] Subscript[u, 19][t]^2+L8 Subscript[u, 19]'[t],-Sin[q4[t]] L8 u1[t] u19[t]-0.5 Cos[q4[t]] q8[t] u1[t] u19[t]-(L3+Cos[q2] (L5+L6)+Sin[q2] L7+L8+L11) Subscript[u, 1]'[t]}

{-Cos[q5[t]] L3 Subscript[u, 1][t]^2-Cos[q2] Cos[q5[t]] L5 Subscript[u, 1][t]^2-Cos[q2] Cos[q5[t]] L6 Subscript[u, 1][t]^2-Cos[q5[t]] Sin[q2] L7 Subscript[u, 1][t]^2-Cos[q5[t]] L8 Subscript[u, 1][t]^2+Cos[q5[t]] L9 Subscript[u, 1][t]^2-Cos[q5[t]] L11 Subscript[u, 1][t]^2-Cos[q4[t]+q5[t]] L8 u19[t] u25[t]+Sin[q4[t]+q5[t]] q8[t] u19[t] u25[t]+L9 Subscript[u, 25][t]^2+u19[t] (Cos[q4[t]+q5[t]] L8 (Subscript[q, 4]'[t]+Subscript[q, 5]'[t])-Sin[q4[t]+q5[t]] q8[t] (Subscript[q, 4]'[t]+Subscript[q, 5]'[t])+Cos[q4[t]+q5[t]] Subscript[q, 8]'[t])+(Sin[q4[t]+q5[t]] L8+Cos[q4[t]+q5[t]] q8[t]) Subscript[u, 19]'[t],Sin[q5[t]] L3 Subscript[u, 1][t]^2+Cos[q2] Sin[q5[t]] L5 Subscript[u, 1][t]^2+Cos[q2] Sin[q5[t]] L6 Subscript[u, 1][t]^2+Sin[q2] Sin[q5[t]] L7 Subscript[u, 1][t]^2+Sin[q5[t]] L8 Subscript[u, 1][t]^2-Sin[q5[t]] L9 Subscript[u, 1][t]^2+Sin[q5[t]] L11 Subscript[u, 1][t]^2+Sin[q4[t]+q5[t]] L8 u19[t] u25[t]+Cos[q4[t]+q5[t]] q8[t] u19[t] u25[t]+u19[t] (-Sin[q4[t]+q5[t]] L8 (Subscript[q,

4]'[t]+Subscript[q, 5]'[t])-Cos[q4[t]+q5[t]] q8[t] (Subscript[q, 4]'[t]+Subscript[q, 5]'[t])-Sin[q4[t]+q5[t]] Subscript[q, 8]'[t])+(Cos[q4[t]+q5[t]] L8-Sin[q4[t]+q5[t]] q8[t]) Subscript[u, 19]'[t]-L9 Subscript[u, 25]'[t],Cos[q4[t]+q5[t]] Sin[q5[t]] L8 u1[t] u19[t]-Cos[q5[t]] Sin[q4[t]+q5[t]] L8 u1[t] u19[t]-Cos[q5[t]] Cos[q4[t]+q5[t]] q8[t] u1[t] u19[t]-Sin[q5[t]] Sin[q4[t]+q5[t]] q8[t] u1[t] u19[t]-Sin[q5[t]] L9 u1[t] u25[t]+L9 Subscript[u, 1]'[t]-(L3+Cos[q2] (L5+L6)+Sin[q2] L7+L8+L11) Subscript[u, 1]'[t]}
{-1. Cos[q6[t]] L1 Subscript[u, 1][t]2-1. Cos[q6[t]] L11 Subscript[u, 1][t]2-0.5 Cos[q6[t]] q7[t] Subscript[u, 1][t]2-0.5 q7[t] Subscript[u, 31][t]2,-1. Sin[q6[t]] L1 Subscript[u, 1][t]2-1. Sin[q6[t]] L11 Subscript[u, 1][t]2-0.5 Sin[q6[t]] q7[t] Subscript[u, 1][t]2+0.5 u31[t] Subscript[q, 7]'[t]+0.5 q7[t] Subscript[u, 31]'[t],-0.5 Sin[q6[t]] q7[t] u1[t] u31[t]-0.5 u1[t] Subscript[q, 7]'[t]-1. (L1+L11+0.5 q7[t]) Subscript[u, 1]'[t]}
{-Cos[q5[t]] L3 Subscript[u, 1][t]2-Cos[q2] Cos[q5[t]] L5 Subscript[u, 1][t]2-Cos[q2] Cos[q5[t]] L6 Subscript[u, 1][t]2-Cos[q5[t]] Sin[q2] L7 Subscript[u, 1][t]2-Cos[q5[t]] L8 Subscript[u, 1][t]2+Cos[q5[t]] L9 Subscript[u, 1][t]2-Cos[q5[t]] L11 Subscript[u, 1][t]2-Cos[q5[t]] L12 Subscript[u, 1][t]2-Cos[q4[t]+q5[t]] L8 u19[t] u25[t]+Sin[q4[t]+q5[t]] q8[t] u19[t] u25[t]+L9 Subscript[u, 25][t]2-L12 Subscript[u, 25][t]2+u19[t] (Cos[q4[t]+q5[t]] L8 (Subscript[q, 4]'[t]+Subscript[q, 5]'[t])-Sin[q4[t]+q5[t]] q8[t] (Subscript[q, 4]'[t]+Subscript[q, 5]'[t])+Cos[q4[t]+q5[t]] Subscript[q, 8]'[t])+(Sin[q4[t]+q5[t]] L8+Cos[q4[t]+q5[t]] q8[t]) Subscript[u, 19]'[t]+L13 Subscript[u, 25]'[t],Sin[q5[t]] L3 Subscript[u, 1][t]2+Cos[q2] Sin[q5[t]] L5 Subscript[u, 1][t]2+Cos[q2] Sin[q5[t]] L6 Subscript[u, 1][t]2+Sin[q2] Sin[q5[t]] L7 Subscript[u, 1][t]2+Sin[q5[t]] L8 Subscript[u, 1][t]2-Sin[q5[t]] L9 Subscript[u, 1][t]2+Sin[q5[t]] L11 Subscript[u, 1][t]2+Sin[q5[t]] L12 Subscript[u, 1][t]2+Sin[q4[t]+q5[t]] L8 u19[t] u25[t]+Cos[q4[t]+q5[t]] q8[t] u19[t] u25[t]+L13 Subscript[u, 25][t]2+u19[t] (-Sin[q4[t]+q5[t]] L8 (Subscript[q, 4]'[t]+Subscript[q, 5]'[t])-Cos[q4[t]+q5[t]] q8[t] (Subscript[q, 4]'[t]+Subscript[q, 5]'[t])-Sin[q4[t]+q5[t]] Subscript[q, 8]'[t])+(Cos[q4[t]+q5[t]] L8-Sin[q4[t]+q5[t]] q8[t]) Subscript[u, 19]'[t]+(-L9+L12) Subscript[u, 25]'[t],Cos[q4[t]+q5[t]] Sin[q5[t]] L8 u1[t] u19[t]-Cos[q5[t]] Sin[q4[t]+q5[t]] L8 u1[t] u19[t]-Cos[q5[t]] Cos[q4[t]+q5[t]] q8[t] u1[t] u19[t]-Sin[q5[t]] Sin[q4[t]+q5[t]] q8[t] u1[t] u19[t]-Sin[q5[t]] L9 u1[t] u25[t]+Sin[q5[t]] L12 u1[t] u25[t]-Cos[q5[t]] L13 u1[t] u25[t]-(L3+Cos[q2] (L5+L6)+Sin[q2] L7+L8-L9+L11+L12) Subscript[u, 1]'[t]}
{-Cos[q6[t]] L3 Subscript[u, 1][t]2-Cos[q2] Cos[q6[t]] L5 Subscript[u, 1][t]2-Cos[q2] Cos[q6[t]] L6 Subscript[u, 1][t]2-Cos[q6[t]] Sin[q2] L7 Subscript[u, 1][t]2-Cos[q6[t]] L8

```
Subscript[u, 1][t]^2+Cos[q6[t]] L9 Subscript[u, 1][t]^2-Cos[q6[t]]
L11 Subscript[u, 1][t]^2-Cos[q6[t]] L12 Subscript[u, 1][t]^2-
Cos[q4[t]+q5[t]] L8 u19[t] u31[t]+Sin[q4[t]+q5[t]] q8[t] u19[t]
u31[t]+L9 u25[t] u31[t]-L12 u25[t] u31[t]+Subscript[u, 31]'[t],-Sin[q6[t]]
L3 Subscript[u, 1][t]^2-Cos[q2] Sin[q6[t]] L5 Subscript[u, 1][t]^2-
Cos[q2] Sin[q6[t]] L6 Subscript[u, 1][t]^2-Sin[q2] Sin[q6[t]] L7
Subscript[u, 1][t]^2-Sin[q6[t]] L8 Subscript[u, 1][t]^2+Sin[q6[t]] L9
Subscript[u, 1][t]^2-Sin[q6[t]] L11 Subscript[u, 1][t]^2-Sin[q6[t]]
L12 Subscript[u, 1][t]^2+Sin[q4[t]+q5[t]] L8 u19[t]
u31[t]+Cos[q4[t]+q5[t]] q8[t] u19[t] u31[t]+L13 u25[t] u31[t]+u31[t]
Subscript[q, 7]'[t]+q7[t] Subscript[u, 31]'[t],-Cos[q6[t]]
Sin[q4[t]+q5[t]] L8 u1[t] u19[t]-Cos[q4[t]+q5[t]] Sin[q6[t]] L8 u1[t]
u19[t]-Cos[q4[t]+q5[t]] Cos[q6[t]] q8[t] u1[t]
u19[t]+Sin[q4[t]+q5[t]] Sin[q6[t]] q8[t] u1[t] u19[t]+Sin[q6[t]] L9
u1[t] u25[t]-Sin[q6[t]] L12 u1[t] u25[t]-Cos[q6[t]] L13 u1[t] u25[t]-
u1[t] Subscript[q, 7]'[t]-(L1+L11+q7[t]) Subscript[u, 1]'[t]}
aBtS[t_]=aB[t]
aCtS[t_]=aC[t]//Simplify
aDtS[t_]=Collect[aD[t],{Subscript[u, 1]'[t],Subscript[u,
19]'[t],u19[t],u1[t]}]//Simplify
aEtS[t_]=Collect[aE[t],{Subscript[u, 1]'[t],Subscript[u,
19]'[t],u19[t],u1[t]}]//FullSimplify
aFtS[t_]=Collect[aF[t],{Subscript[u, 1]'[t],Subscript[u, 19]'[t],Subscript[u,
31]'[t],u31[t],u19[t],u1[t]}]/.{Subscript[u, 25]'[t]-> 0}//FullSimplify
aGtS[t_]=Collect[aG[t],{Subscript[u, 1]'[t],Subscript[u, 19]'[t],Subscript[u,
31]'[t],u31[t],u19[t],u1[t]}]/.{Subscript[u, 25]'[t]-> 0}//FullSimplify
aH1tS[t_]=Collect[aH1[t],{Subscript[u, 1]'[t],Subscript[u, 19]'[t],Subscript[u,
31]'[t],u31[t],u19[t],u1[t]}]/.{Subscript[u, 25]'[t]-> 0}//FullSimplify
aF1tS[t_]=Collect[aF1[t],{Subscript[u, 1]'[t],Subscript[u, 19]'[t],Subscript[u,
31]'[t],u31[t],u19[t],u1[t]}]//FullSimplify
 {-L11 Subscript[u, 1][t]^2,0,-L11 Subscript[u, 1]'[t]}
 {-Cos[q2] (L3+Cos[q2] L5+L11) Subscript[u, 1][t]^2,Sin[q2]
(L3+Cos[q2] L5+L11) Subscript[u, 1][t]^2,-(L3+Cos[q2] L5+L11)
Subscript[u, 1]'[t]}
 {-Cos[q4[t]] (L3+Cos[q2] L5+Cos[q2] L6+Sin[q2] L7+L11) Subscript[u,
1][t]^2,-Sin[q4[t]] (L3+Cos[q2] L5+Cos[q2] L6+Sin[q2] L7+L11)
Subscript[u, 1][t]^2,-(L3+Cos[q2] (L5+L6)+Sin[q2] L7+L11)
Subscript[u, 1]'[t]}
 {-Cos[q4[t]] (L3+Cos[q2] (L5+L6)+Sin[q2] L7+L8+L11) Subscript[u,
1][t]^2-L8 Subscript[u, 19][t]^2+0.5 u19[t] Subscript[q, 8]'[t]+0.5 q8[t]
Subscript[u, 19]'[t],-Sin[q4[t]]] (L3+Cos[q2] (L5+L6)+Sin[q2] L7+L8+L11)
Subscript[u, 1][t]^2+0.5 q8[t] Subscript[u, 19][t]^2+L8 Subscript[u,
19]'[t],-1. (Sin[q4[t]] L8+0.5 Cos[q4[t]] q8[t]) u1[t] u19[t]-(L3+Cos[q2]
(L5+L6)+Sin[q2] L7+L8+L11) Subscript[u, 1]'[t]}
 {-Cos[q5[t]] (L3+Cos[q2] (L5+L6)+Sin[q2] L7+L8-L9+L11) Subscript[u,
```

```
1][t]^2+L9 Subscript[u, 25][t]^2+u19[t] (-(Cos[q4[t]+q5[t]] L8-
Sin[q4[t]+q5[t]] q8[t]) (u25[t]-Subscript[q, 4]'[t]-Subscript[q,
5]'[t])+Cos[q4[t]+q5[t]] Subscript[q, 8]'[t])+(Sin[q4[t]+q5[t]]
L8+Cos[q4[t]+q5[t]] q8[t]) Subscript[u, 19]'[t],Sin[q5[t]] (L3+Cos[q2]
(L5+L6)+Sin[q2] L7+L8-L9+L11) Subscript[u, 1][t]^2+u19[t]
((Sin[q4[t]+q5[t]] L8+Cos[q4[t]+q5[t]] q8[t]) (u25[t]-Subscript[q,
4]'[t]-Subscript[q, 5]'[t])-Sin[q4[t]+q5[t]] Subscript[q,
8]'[t])+(Cos[q4[t]+q5[t]] L8-Sin[q4[t]+q5[t]] q8[t]) Subscript[u,
19]'[t],-u1[t] ((Sin[q4[t]] L8+Cos[q4[t]] q8[t]) u19[t]+Sin[q5[t]] L9
u25[t])-(L3+Cos[q2] (L5+L6)+Sin[q2] L7+L8-L9+L11) Subscript[u, 1]'[t]}
 {Cos[q6[t]] (-1. L1-1. L11-0.5 q7[t]) Subscript[u, 1][t]^2-0.5
q7[t] Subscript[u, 31][t]^2,Sin[q6[t]] (-1. L1-1. L11-0.5 q7[t])
Subscript[u, 1][t]^2+0.5 u31[t] Subscript[q, 7]'[t]+0.5 q7[t]
Subscript[u, 31]'[t],-0.5 Sin[q6[t]] q7[t] u1[t] u31[t]-0.5 u1[t]
Subscript[q, 7]'[t]-1. (L1+L11+0.5 q7[t]) Subscript[u, 1]'[t]}
 {-Cos[q5[t]] (L3+Cos[q2] (L5+L6)+Sin[q2] L7+L8-L9+L11+L12)
Subscript[u, 1][t]^2+L9 Subscript[u, 25][t]^2-L12 Subscript[u,
25][t]^2+u19[t] (-(Cos[q4[t]+q5[t]] L8-Sin[q4[t]+q5[t]] q8[t])
(u25[t]-Subscript[q, 4]'[t]-Subscript[q, 5]'[t])+Cos[q4[t]+q5[t]] Subscript[q,
8]'[t])+(Sin[q4[t]+q5[t]] L8+Cos[q4[t]+q5[t]] q8[t]) Subscript[u,
19]'[t],Sin[q5[t]] (L3+Cos[q2] (L5+L6)+Sin[q2] L7+L8-L9+L11+L12)
Subscript[u, 1][t]^2+L13 Subscript[u, 25][t]^2+u19[t]
((Sin[q4[t]+q5[t]] L8+Cos[q4[t]+q5[t]] q8[t]) (u25[t]-Subscript[q,
4]'[t]-Subscript[q, 5]'[t])-Sin[q4[t]+q5[t]] Subscript[q,
8]'[t])+(Cos[q4[t]+q5[t]] L8-Sin[q4[t]+q5[t]] q8[t]) Subscript[u,
19]'[t],u1[t] (-(Sin[q4[t]] L8+Cos[q4[t]] q8[t]) u19[t]-(Sin[q5[t]]
(L9-L12)+Cos[q5[t]] L13) u25[t])-(L3+Cos[q2] (L5+L6)+Sin[q2] L7+L8-
L9+L11+L12) Subscript[u, 1]'[t]}
 {-Cos[q6[t]] (L3+Cos[q2] (L5+L6)+Sin[q2] L7+L8-L9+L11+L12)
Subscript[u, 1][t]^2+((-Cos[q4[t]+q5[t]] L8+Sin[q4[t]+q5[t]] q8[t])
u19[t]+(L9-L12) u25[t]) u31[t]+Subscript[u, 31]'[t],-Sin[q6[t]]
(L3+Cos[q2] (L5+L6)+Sin[q2] L7+L8-L9+L11+L12) Subscript[u,
1][t]^2+u31[t] ((Sin[q4[t]+q5[t]] L8+Cos[q4[t]+q5[t]] q8[t])
u19[t]+L13 u25[t]+Subscript[q, 7]'[t])+q7[t] Subscript[u, 31]'[t],-u1[t]
((Sin[q4[t]+q5[t]+q6[t]] L8+Cos[q4[t]+q5[t]+q6[t]] q8[t])
u19[t]+(Sin[q6[t]] (-L9+L12)+Cos[q6[t]] L13) u25[t]+Subscript[q,
7]'[t])-(L1+L11+q7[t]) Subscript[u, 1]'[t]}
```

```
NωBt[t_]=D[NωB[t],t]
BωCt[t_]=D[NωCTN[t],t]
BωDt[t_]=D[NωDTN[t],t]/.{Subscript[q, 4]'[t]->u19[t]}
BωEt[t_]=D[NωETN[t],t]/.{Subscript[q, 4]'[t]->u19[t]}
BωFt[t_]=D[NωFTN[t],t]/.{Subscript[q, 5]'[t]->u25[t],Subscript[u,
25]'[t]-> 0}
BωFt[t_]=Collect[BωFt[t],{Subscript[u, 1]'[t],Subscript[u, 19]'[t]}]/.{Subscript[q, 5]'[t]-
```

```
>u25[t],Subscript[Z, 5]'[t]-> 0}
BaGt[t_]=D[NwCTN[t],t]/.{Subscript[q, 0]'[t]->u31[t]}
```

```
 {0,Subscript[u, 1]'[t],0}
 {Sin[q2] Subscript[u, 1]'[t],Cos[q2] Subscript[u, 1]'[t],0}
 {-Cos[q4[t]] u1[t] u19[t]-Sin[q4[t]] Subscript[u, 1]'[t],-Sin[q4[t]]
u1[t] u19[t]+Cos[q4[t]] Subscript[u, 1]'[t],Subscript[u, 19]'[t]}
 {-Cos[q4[t]] u1[t] u19[t]-Sin[q4[t]] Subscript[u, 1]'[t],-Sin[q4[t]]
u1[t] u19[t]+Cos[q4[t]] Subscript[u, 1]'[t],Subscript[u, 19]'[t]}
 {Cos[q5[t]] u1[t] u25[t]+Sin[q5[t]] Subscript[u, 1]'[t],-Sin[q5[t]]
u1[t] u25[t]+Cos[q5[t]] Subscript[u, 1]'[t],0}
 {Cos[q5[t]] u1[t] u25[t]+Sin[q5[t]] Subscript[u, 1]'[t],-Sin[q5[t]]
u1[t] u25[t]+Cos[q5[t]] Subscript[u, 1]'[t],0}
 {-Cos[q6[t]] u1[t] u31[t]-Sin[q6[t]] Subscript[u, 1]'[t],-Sin[q6[t]]
u1[t] u31[t]+Cos[q6[t]] Subscript[u, 1]'[t],Subscript[u, 31]'[t]}
```

```
IB=({
   {B11, 0, 0},
   {0, B22, 0},
   {0, 0, B33}
  });IC=({
   {C11, 0, 0},
   {0, C22, 0},
   {0, 0, C33}
  });ID=({
   {D11, 0, 0},
   {0, D22, 0},
   {0, 0, D33}
  });
IE=({
   {E11, 0, 0},
   {0, E22, 0},
   {0, 0, E33}
  });IF=({
   {F11, 0, 0},
   {0, F22, 0},
   {0, 0, F33}
  });IG=({
   {G11, 0, 0},
   {0, G22, 0},
   {0, 0, G33}
  });


TIB[t_]=-(IB.NaBt[t]+Cross[NwB[t],IB.NwB[t]])
TICc[t_]=-(IC.BaCt[t]+Cross[NwCTN[t],IC.NwCTN[t]]) ;
TIC[t_]= Collect[TICc[t],{u1[t] u19[t],Subscript[u, 1]'[t],Subscript[u,
1][t]2}]
```

```
TIDd[t_]=-(ID.BαDt[t]+Cross[NωDTN[t],ID.NωDTN[t]]) ;
TID[t_]= Collect[TIDd[t],{u1[t] u19[t],Subscript[u, 1]'[t],Subscript[u, 1][t]2}]
TIEe[t_]=-(IE.BαEt[t]+Cross[NωETN[t],IE.NωETN[t]]);
TIE[t_]= Collect[TIEe[t],{u1[t] u19[t],Subscript[u, 1]'[t],Subscript[u, 1][t]2}]
TIFf[t_]=-(IF.BαFt[t]+Cross[NωFTN[t],IF.NωFTN[t]]);
TIF[t_]= Collect[TIFf[t],{u1[t] u19[t],Subscript[u, 1]'[t],Subscript[u, 1][t]2}]
TIGg[t_]=-(IG.BαGt[t]+Cross[NωGTN[t],IG.NωGTN[t]]);
TIG[t_]= Collect[TIGg[t],{u1[t] u19[t],,u1[t] u31[t],Subscript[u, 1]'[t],Subscript[u, 1][t]2}]
```

$\{0,-B_{22}\ \text{Subscript}[u, 1]'[t],0\}$

$\{-\text{Sin}[q_2]\ C_{11}\ \text{Subscript}[u, 1]'[t],-\text{Cos}[q_2]\ C_{22}\ \text{Subscript}[u, 1]'[t],(\text{Cos}[q_2]\ \text{Sin}[q_2]\ C_{11}-\text{Cos}[q_2]\ \text{Sin}[q_2]\ C_{22})\ \text{Subscript}[u, 1][t]^2\}$

$\{(\text{Cos}[q_4[t]]\ D_{11}+\text{Cos}[q_4[t]]\ D_{22}-\text{Cos}[q_4[t]]\ D_{33})\ u_1[t]\ u_{19}[t]+\text{Sin}[q_4[t]]\ D_{11}\ \text{Subscript}[u, 1]'[t],(\text{Sin}[q_4[t]]\ D_{11}+\text{Sin}[q_4[t]]\ D_{22}-\text{Sin}[q_4[t]]\ D_{33})\ u_1[t]\ u_{19}[t]-\text{Cos}[q_4[t]]\ D_{22}\ \text{Subscript}[u, 1]'[t],(-\text{Cos}[q_4[t]]\ \text{Sin}[q_4[t]]\ D_{11}+\text{Cos}[q_4[t]]\ \text{Sin}[q_4[t]]\ D_{22})\ \text{Subscript}[u, 1][t]^2-D_{33}\ \text{Subscript}[u, 19]'[t]\}$

$\{(\text{Cos}[q_4[t]]\ E_{11}+\text{Cos}[q_4[t]]\ E_{22}-\text{Cos}[q_4[t]]\ E_{33})\ u_1[t]\ u_{19}[t]+\text{Sin}[q_4[t]]\ E_{11}\ \text{Subscript}[u, 1]'[t],(\text{Sin}[q_4[t]]\ E_{11}+\text{Sin}[q_4[t]]\ E_{22}-\text{Sin}[q_4[t]]\ E_{33})\ u_1[t]\ u_{19}[t]-\text{Cos}[q_4[t]]\ E_{22}\ \text{Subscript}[u, 1]'[t],(-\text{Cos}[q_4[t]]\ \text{Sin}[q_4[t]]\ E_{11}+\text{Cos}[q_4[t]]\ \text{Sin}[q_4[t]]\ E_{22})\ \text{Subscript}[u, 1][t]^2-E_{33}\ \text{Subscript}[u, 19]'[t]\}$

$\{u_1[t]\ (-\text{Cos}[q_5[t]]\ F_{11}\ u_{25}[t]+\text{Cos}[q_5[t]]\ F_{22}\ u_{25}[t]-\text{Cos}[q_5[t]]\ F_{33}\ u_{25}[t])-\text{Sin}[q_5[t]]\ F_{11}\ \text{Subscript}[u, 1]'[t],u_1[t]\ (-\text{Sin}[q_5[t]]\ F_{11}\ u_{25}[t]+\text{Sin}[q_5[t]]\ F_{22}\ u_{25}[t]+\text{Sin}[q_5[t]]\ F_{33}\ u_{25}[t])-\text{Cos}[q_5[t]]\ F_{22}\ \text{Subscript}[u, 1]'[t],(\text{Cos}[q_5[t]]\ \text{Sin}[q_5[t]]\ F_{11}-\text{Cos}[q_5[t]]\ \text{Sin}[q_5[t]]\ F_{22})\ \text{Subscript}[u, 1][t]^2\}$

$\{(\text{Cos}[q_6[t]]\ G_{11}+\text{Cos}[q_6[t]]\ G_{22}-\text{Cos}[q_6[t]]\ G_{33})\ u_1[t]\ u_{31}[t]+\text{Sin}[q_6[t]]\ G_{11}\ \text{Subscript}[u, 1]'[t],(\text{Sin}[q_6[t]]\ G_{11}+\text{Sin}[q_6[t]]\ G_{22}-\text{Sin}[q_6[t]]\ G_{33})\ u_1[t]\ u_{31}[t]-\text{Cos}[q_6[t]]\ G_{22}\ \text{Subscript}[u, 1]'[t],(-\text{Cos}[q_6[t]]\ \text{Sin}[q_6[t]]\ G_{11}+\text{Cos}[q_6[t]]\ \text{Sin}[q_6[t]]\ G_{22})\ \text{Subscript}[u, 1][t]^2-G_{33}\ \text{Subscript}[u, 31]'[t]\}$

```
GIK1[t_]=- mB*aBtS[t].D[VBinBN[t],u1[t]]-
mC*aCtS[t].D[VCinCSN[t],u1[t]]- mD*aDtS[t].D[VDinDSN[t],u1[t]]-
mE*aEtS[t].D[VEinESN[t],u1[t]]- mF*aFtS[t].D[VFinFSN[t],u1[t]]-
mG*aGtS[t].D[VGinGSN[t],u1[t]]- mH1*aH1tS[t].D[VH1inFSN[t],u1[t]]-
mF1*aF1tS[t].D[VF1inGSN[t],u1[t]]+TIB[t].D[NωB[t],u1[t]]+TIC[t].D[
NωCTN[t],u1[t]]+TID[t].D[NωDTN[t],u1[t]]+TIE[t].D[NωETN[t],u1[t]]+
TIF[t].D[NωFTN[t],u1[t]]+TIG[t].D[NωGTN[t],u1[t]]/.{Subscript[q,
4]'[t]->u19[t]};//ExpandAll
GIK1C[t_]=Collect[GIK1[t],{Subscript[u, 1]'[t], u1[t] u19[t],u1[t]
```

```
u25[t]}]//Simplify
 -1. (L3+Cos[q2] (L5+L6)+Sin[q2] L7+L8+L11) mE (Sin[q4[t]] L8+0.5
Cos[q4[t]] q8[t]) u1[t] u19[t]-1/2 Sin[2 q5[t]] (F11-F22-F33) u1[t]
u25[t]-1/2 Sin[2 q5[t]] (F11-F22+F33) u1[t] u25[t]-(L3+Cos[q2]
(L5+L6)+Sin[q2] L7+L8-L9+L11) mF u1[t] ((Sin[q4[t]] L8+Cos[q4[t]]
q8[t]) u19[t]+Sin[q5[t]] L9 u25[t])+(L3+Cos[q2] (L5+L6)+Sin[q2] L7+L8-
L9+L11+L12) mH1 u1[t] (-(Sin[q4[t]] L8+Cos[q4[t]] q8[t]) u19[t]-
(Sin[q5[t]] (L9-L12)+Cos[q5[t]] L13) u25[t])-0.5 Sin[q6[t]] mG
(L1+L11+0.5 q7[t]) q7[t] u1[t] u31[t]-0.5 mG (L1+L11+0.5 q7[t]) u1[t]
Subscript[q, 7]'[t]+mF1 (-L1-L11-q7[t]) u1[t] ((Sin[q4[t]+q5[t]+q6[t]]
L8+Cos[q4[t]+q5[t]+q6[t]] q8[t]) u19[t]+(Sin[q6[t]] (-
L9+L12)+Cos[q6[t]] L13) u25[t]+Subscript[q, 7]'[t])+(-B22-
Sin[Subscript[q, 2]]2 C11-Cos[Subscript[q, 2]]2 C22-
Sin[Subscript[q, 4][t]]2 D11-Cos[Subscript[q, 4][t]]2 D22-
Sin[Subscript[q, 4][t]]2 E11-Cos[Subscript[q, 4][t]]2 E22-
Sin[Subscript[q, 5][t]]2 F11-Cos[Subscript[q, 5][t]]2 F22-
Sin[Subscript[q, 6][t]]2 G11-Cos[Subscript[q, 6][t]]2 G22-L11^2 mB-
(Subscript[L, 3]+Cos[Subscript[q, 2]] Subscript[L,
5]+Subscript[L, 11])2 mC-(Subscript[L, 3]+Cos[Subscript[q, 2]]
Subscript[L, 5]+Cos[Subscript[q, 2]] Subscript[L,
6]+Sin[Subscript[q, 2]] Subscript[L, 7]+Subscript[L, 11])2 mD-
(Subscript[L, 3]+Cos[Subscript[q, 2]] (Subscript[L,
5]+Subscript[L, 6])+Sin[Subscript[q, 2]] Subscript[L,
7]+Subscript[L, 8]+Subscript[L, 11])2 mE-(Subscript[L,
3]+Cos[Subscript[q, 2]] (Subscript[L, 5]+Subscript[L,
6])+Sin[Subscript[q, 2]] Subscript[L, 7]+Subscript[L, 8]-
Subscript[L, 9]+Subscript[L, 11])2 mF-(Subscript[L,
3]+Cos[Subscript[q, 2]] (Subscript[L, 5]+Subscript[L,
6])+Sin[Subscript[q, 2]] Subscript[L, 7]+Subscript[L, 8]-
Subscript[L, 9]+Subscript[L, 11]+Subscript[L, 12])2 mH1-1. mG
(Subscript[L, 1]+Subscript[L, 11]+0.5 Subscript[q, 7][t])2-mF1
(Subscript[L, 1]+Subscript[L, 11]+Subscript[q, 7][t])2)
Subscript[u, 1]'[t]
 GIK19[t_]=- mB*aBtS[t].D[VBinBN[t],u19[t]]-
mC*aCtS[t].D[VCinCSN[t],u19[t]]- mD*aDtS[t].D[VDinDSN[t],u19[t]]-
mE*aEtS[t].D[VEinESN[t],u19[t]]- mF*aFtS[t].D[VFinFSN[t],u19[t]]-
mG*aGtS[t].D[VGinGSN[t],u19[t]]-
mH1*aH1tS[t].D[VH1inFSN[t],u19[t]]-
mF1*aF1tS[t].D[VF1inGSN[t],u19[t]]+TIB[t].D[NωB[t],u19[t]]+TIC[t].D
[NωCTN[t],u19[t]]+TID[t].D[NωDTN[t],u19[t]]+TIE[t].D[NωETN[t],u19[t
]]+TIF[t].D[NωFTN[t],u19[t]]+TIG[t].D[NωGTN[t],u19[t]]/.{Subscript
[q, 4]'[t]->u19[t],Subscript[q, 5]'[t]-> u25[t]};
GIK19C[t_]=Collect[GIK19[t],{Subscript[u, 19]'[t],Subscript[u,
1][t]2,Subscript[u, 25][t]2,Subscript[q, 8]'[t]}]//Simplify
 (-(1/2) Sin[2 q4[t]] D11+Cos[q4[t]] Sin[q4[t]] D22-1/2 Sin[2 q4[t]]
```

```
E11+Cos[q4[t]] Sin[q4[t]] E22+Sin[q4[t]] L8 (L3+Cos[q2]
(L5+L6)+Sin[q2] L7+L8+L11) mE+0.5 Cos[q4[t]] (L3+Cos[q2]
(L5+L6)+Sin[q2] L7+L8+L11) mE q8[t]+Cos[q5[t]] (L3+Cos[q2]
(L5+L6)+Sin[q2] L7+L8-L9+L11) mF (Sin[q4[t]+q5[t]] L8+Cos[q4[t]+q5[t]]
q8[t])+Cos[q5[t]] (L3+Cos[q2] (L5+L6)+Sin[q2] L7+L8-L9+L11+L12) mH1
(Sin[q4[t]+q5[t]] L8+Cos[q4[t]+q5[t]] q8[t])-Sin[q5[t]] (L3+Cos[q2]
(L5+L6)+Sin[q2] L7+L8-L9+L11) mF (Cos[q4[t]+q5[t]] L8-Sin[q4[t]+q5[t]]
q8[t])-Sin[q5[t]] (L3+Cos[q2] (L5+L6)+Sin[q2] L7+L8-L9+L11+L12) mH1
(Cos[q4[t]+q5[t]] L8-Sin[q4[t]+q5[t]] q8[t])) Subscript[u,
1][t]^2+(-L8 ((-Sin[q4[t]+q5[t]] L12+Cos[q4[t]+q5[t]] L13)
mH1+Sin[q4[t]+q5[t]] L9 (mF+mH1))+((Cos[q4[t]+q5[t]]
L12+Sin[q4[t]+q5[t]] L13) mH1-Cos[q4[t]+q5[t]] L9 (mF+mH1)) q8[t])
Subscript[u, 25][t]^2-0.25 mE q8[t] u19[t] Subscript[q, 8]'[t]-1. mF
q8[t] u19[t] Subscript[q, 8]'[t]-1. mH1 q8[t] u19[t] Subscript[q, 8]'[t]-
1. (D33+E33+L8^2 (me+mF+mH1)+0.25 mE Subscript[q, 8][t]^2+mF Subscript[q,
8][t]^2+mH1 Subscript[q, 8][t]^2) Subscript[u, 19]'[t]
 GIK31[t_]=- mB*aBtS[t].D[VBinBN[t],u31[t]]-
mC*aCtS[t].D[VCinCSN[t],u31[t]]- mD*aDtS[t].D[VDinDSN[t],u31[t]]-
mE*aEtS[t].D[VEinESN[t],u31[t]]- mF*aFtS[t].D[VFinFSN[t],u31[t]]-
mG*aGtS[t].D[VGinGSN[t],u31[t]]-
mH1*aH1tS[t].D[VH1inFSN[t],u31[t]]-
mF1*aF1tS[t].D[VF1inGSN[t],u31[t]]+TIB[t].D[NωB[t],u31[t]]+TIC[t].D
[NωCTN[t],u31[t]]+TID[t].D[NωDTN[t],u31[t]]+TIE[t].D[NωETN[t],u31[t
]]+TIF[t].D[NωFTN[t],u31[t]]+TIG[t].D[NωGTN[t],u31[t]]/.{Subscript
[q, 4]'[t]->u19[t]};
GIK31[t_]=Collect[GIK31[t],{Subscript[u, 31]'[t],u31[t],Subscript[u,
1][t]^2}]//Simplify
 (-(1/2) Sin[2 q6[t]] G11+Cos[q6[t]] Sin[q6[t]] G22+Cos[q6[t]]
(L3+Cos[q2] (L5+L6)+Sin[q2] L7+L8-L9+L11+L12) mF1+Sin[q6[t]]
(L3+Cos[q2] (L5+L6)+Sin[q2] L7+L8-L9+L11+L12) mF1 q7[t]+0.5 Sin[q6[t]]
mG (1. L1+1. L11+0.5 q7[t]) q7[t]) Subscript[u, 1][t]^2+u31[t] (-mF1
((-Cos[q4[t]+q5[t]] L8+Sin[q4[t]+q5[t]] q8[t]) u19[t]+(L9-L12)
u25[t])-0.25 mG q7[t] Subscript[q, 7]'[t]-mF1 q7[t] ((Sin[q4[t]+q5[t]]
L8+Cos[q4[t]+q5[t]] q8[t]) u19[t]+L13 u25[t]+Subscript[q, 7]'[t]))-1.
(G33+0.25 mG Subscript[q, 7][t]^2+mF1 (1+Subscript[q, 7][t]^2))
Subscript[u, 31]'[t]
GB[t_]=-g.mB{0,1,0}
GC[t_]=-g.mC{-Sin[q2],-Cos[q2],0}
GD[t_]=-g.mD{Sin[q4[t]] ,-Cos[q4[t]],0}
GE[t_]=-g.mE{Sin[q4[t]] ,-Cos[q4[t]],0}
GF[t_]=-g.mF{- Sin[q5[t]],-Cos[q5[t]],0}
GG[t_]=-g.mG{Sin[q6[t]],-Cos[q6[t]],0}
GH1[t_]=-g.mH1{- Sin[q5[t]],-Cos[q5[t]],0}
GF1[t_]=-g.mF1{Sin[q6[t]],-Cos[q6[t]],0}
```

```
 {0,-g.m_B,0}
 {g.m_c Sin[q_2],Cos[q_2] g.m_c,0}
 {-g.m_D Sin[q_4[t]],Cos[q_4[t]] g.m_D,0}
 {-g.m_E Sin[q_4[t]],Cos[q_4[t]] g.m_E,0}
 {g.m_F Sin[q_5[t]],Cos[q_5[t]] g.m_F,0}
 {-g.m_G Sin[q_6[t]],Cos[q_6[t]] g.m_G,0}
 {g.m_H1 Sin[q_5[t]],Cos[q_5[t]] g.m_H1,0}
 {-g.m_F1 Sin[q_6[t]],Cos[q_6[t]] g.m_F1,0}
 (*Friction Force*)
y[t_]= q_70Sin[q_60]-q_7[t]Sin[q_6[t]]
B1F3={q_7[t]-(0.5*y[t])/Sin[q_6[t]],0,0}
B1F3.Transpose[BRG]
V_F3=Cross[NωGTN[t],B1F3. Transpose[BRG]]/.{Sin[q_6] ->
Sin[q_6[t]],Cos[q_6] -> Cos[q_6[t]]}//Simplify
A_c=d_r y[t]Sin[q_6[t]]
Vol= (y[t]/Sin[q_6[t]])*d_c^2Pi/4
F_dv=-sgnV_v β A_cV_F3[[2]]^2
F_dh=-sgnV_h β A_c V_F3[[1]]^2
F_sh=-sgnV_h η_hρ g d_cy[t]^2
F_sv=-sgnV_v η_v(y[t]/d_c)^λ g ρ Vol
F_fr= {F_dh+F_sh,F_dv+F_sv,0}/.{ Sin[q_60]-> s_60,Cos[q_60]-> c_60,u_1[t]-
>u_1,u_31[t]->u_31,Cos[q_6[t]]-> c_6,Sin[q_6[t]]-> s_6,q_7[t]-> q_7}//Simplify
F_fr= {F_dh+F_sh,F_dv+F_sv,0}

(*Cutting Force*)
F_ct=E_bucket*(1+λ_0)*k_F/k_nym*l_bucket*k_p
F_Cut={F_ct Cos[ca]Cos[q_5],F_ct Cos[ca]Sin[q_5],0}//Simplify
GAK31[t]/.{ Sin[q_60]-> s_60,Cos[q_60]-> c_60,u_1[t]->u_1,u_31[t]-
>u_31,Cos[q_6[t]]-> c_6,Sin[q_6[t]]-> s_6,q_7[t]-> q_7}//FullSimplify
 Sin[q_60] q_70-Sin[q_6[t]] q_7[t]
 {q_7[t]-0.5 Csc[q_6[t]] (Sin[q_60] q_70-Sin[q_6[t]] q_7[t]),0,0}
 {Cos[q_6[t]] (q_7[t]-0.5 Csc[q_6[t]] (Sin[q_60] q_70-Sin[q_6[t]]
q_7[t])),-Sin[q_6[t]] (q_7[t]-0.5 Csc[q_6[t]] (Sin[q_60] q_70-Sin[q_6[t]]
q_7[t])),0}
 {(-0.5 Sin[q_60] q_70+1.5 Sin[q_6[t]] q_7[t]) u_31[t],(-0.5 Cot[q_6[t]]
Sin[q_60] q_70+1.5 Cos[q_6[t]] q_7[t]) u_31[t],(Sin[q_60] (0.5 Cos[q_6[t]]
Cot[q_6[t]]-0.5 Sin[q_6[t]]) q_70-1.5 Cos[2 q_6[t]] q_7[t]) u_1[t]}
 Sin[q_6[t]] d_r (Sin[q_60] q_70-Sin[q_6[t]] q_7[t])
 1/4 π Csc[q_6[t]] d_c^2 (Sin[q_60] q_70-Sin[q_6[t]] q_7[t])
 -β Sin[q_6[t]] d_r sgnV_v (-0.5 Cot[Subscript[q, 6][t]]
Sin[Subscript[q, 60]] Subscript[q, 70]+1.5 Cos[Subscript[q,
6][t]] Subscript[q, 7][t])^2 (Sin[q_60] q_70-Sin[q_6[t]] q_7[t])
Subscript[u, 31][t]^2
 -β Sin[q_6[t]] d_r sgnV_h (Sin[q_60] q_70-Sin[q_6[t]] q_7[t]) (-0.5
Sin[Subscript[q, 60]] Subscript[q, 70]+1.5 Sin[Subscript[q,
```

6][t]] Subscript[q, 7][t])^2 Subscript[u, 31][t]^2
-g ρ d_c sgnV_h η_h (Sin[Subscript[q, 60]] Subscript[q, 70]-Sin[Subscript[q, 6][t]] Subscript[q, 7][t])^2
-(1/4) g π ρ Csc[q_6[t]] d_c^2 sgnV_v η_v (Sin[q_{60}] q_{70}-Sin[q_6[t]] q_7[t]) ((Sin[Subscript[q, 60]] Subscript[q, 70]-Sin[Subscript[q, 6][t]] Subscript[q, 7][t])/Subscript[d, c])$^\lambda$
{(-q_7 s_6+q_{70} s_{60}) sgnV_h (-2.25 β d_r s_6 (1. Subscript[q, 7] Subscript[s, 6]-0.333333 Subscript[q, 70] Subscript[s, 60])^2 u_{31}^2+g ρ d_c (q_7 s_6-q_{70} s_{60}) η_h),1/4 (-q_7 s_6+q_{70} s_{60}) sgnV_v (-9. β d_r s_6 (1. Subscript[c, 6] Subscript[q, 7]-0.333333 Cot[Subscript[q, 6][t]] Subscript[q, 70] Subscript[s, 60])^2 u_{31}^2-g π ρ Csc[q_6[t]] d_c^2 ((-Subscript[q, 7] Subscript[s, 6]+Subscript[q, 70] Subscript[s, 60])/Subscript[d, c])$^\lambda$ η_v),0}
{-g ρ d_c sgnV_h η_h (Sin[Subscript[q, 60]] Subscript[q, 70]-Sin[Subscript[q, 6][t]] Subscript[q, 7][t])^2-β Sin[q_6[t]] d_r sgnV_h (Sin[q_{60}] q_{70}-Sin[q_6[t]] q_7[t]) (-0.5 Sin[Subscript[q, 60]] Subscript[q, 70]+1.5 Sin[Subscript[q, 6][t]] Subscript[q, 7][t])^2 Subscript[u, 31][t]^2,-(1/4) g π ρ Csc[q_6[t]] d_c^2 sgnV_v η_v (Sin[q_{60}] q_{70}-Sin[q_6[t]] q_7[t]) ((Sin[Subscript[q, 60]] Subscript[q, 70]-Sin[Subscript[q, 6][t]] Subscript[q, 7][t])/Subscript[d, c])$^\lambda$-β Sin[q_6[t]] d_r sgnV_v (-0.5 Cot[Subscript[q, 6][t]] Sin[Subscript[q, 60]] Subscript[q, 70]+1.5 Cos[Subscript[q, 6][t]] Subscript[q, 7][t])^2 (Sin[q_{60}] q_{70}-Sin[q_6[t]] q_7[t]) Subscript[u, 31][t]^2,0}
(E_{bucket} k_F k_p l_{bucket} (1+λ_0))/k_{nym}
{(Cos[ca] Cos[q_5] E_{bucket} k_F k_p l_{bucket} (1+λ_0))/k_{nym},(Cos[ca] Sin[q_5] E_{bucket} k_F k_p l_{bucket} (1+λ_0))/k_{nym},0}
GAK31[t]

```
GAK1[t_]={0,τ1[t],0}.D[NωB[t],u1[t]]+{0,0,τ2[t]}.D[NωETN[t],u1[t]]
+{σ[t],0,0}.D[VF1inGSN[t]-VGinGSN[t],u1[t]]+
GB[t].D[VBinBN[t],u1[t]]+GC[t].D[VCinCSN[t],u1[t]]+GD[t].D[VDinDSN
[t],u1[t]]+GE[t].D[VEinESN[t],u1[t]]+GF[t].D[VFinFSN[t],u1[t]]+GG[
t].D[VGinGSN[t],u1[t]]+GH1[t].D[VH1inFSN[t],u1[t]]+GF1[t].D[VF1inG
SN[t],u1[t]]+Ffr. D[VF3,u1[t]]+FCut.D[VH1inFSN[t],u1[t]]

GAK19[t_]={0,τ1[t],0}.D[NωB[t],u19[t]]+{0,0,τ2[t]}.D[NωETN[t],u19[
t]]+{σ[t],0,0}.D[VF1inGSN[t]-VGinGSN[t],u19[t]]+
GB[t].D[VBinBN[t],u19[t]]+GC[t].D[VCinCSN[t],u19[t]]+GD[t].D[VDinD
SN[t],u19[t]]+GE[t].D[VEinESN[t],u19[t]]+GF[t].D[VFinFSN[t],u19[t]]
+GG[t].D[VGinGSN[t],u19[t]]+GH1[t].D[VH1inFSN[t],u19[t]]+GF1[t].D[
VF1inGSN[t],u19[t]]+Ffr. D[VF3,u19[t]] +FCut.D[VH1inFSN[t],u19[t]]

GAK31[t_]={0,τ1[t],0}.D[NωB[t],u31[t]]+{0,0,τ2[t]}.D[NωETN[t],u31[
t]]+{σ[t],0,0}.D[VF1inGSN[t]-VGinGSN[t],u31[t]]+
GB[t].D[VBinBN[t],u31[t]]+GC[t].D[VCinCSN[t],u31[t]]+GD[t].D[VDinD
```

```
SN[t],u31[t]]+GE[t].D[VEinESN[t],u31[t]]+GF[t].D[VFinFSN[t],u31[t]]
+GG[t].D[VGinGSN[t],u31[t]]+GH1[t].D[VH1inFSN[t],u31[t]]+GF1[t].D[
VF1inGSN[t],u31[t]]+FFr. D[VF3,u31[t]]+FOut.D[VH1inFSN[t],u31[t]]
```

```
 0. +τ1[t]
 Cos[q4[t]] g.mE L8+τ2[t]-0.5 g.mE Sin[q4[t]] q8[t]+g.mF Sin[q5[t]]
(Sin[q4[t]+q5[t]] L8+Cos[q4[t]+q5[t]] q8[t])+g.mH1 Sin[q5[t]]
(Sin[q4[t]+q5[t]] L8+Cos[q4[t]+q5[t]] q8[t])+(Cos[ca] Cos[q5] Ebucket
kF kp lbucket (1+λ0) (Sin[q4[t]+q5[t]] L8+Cos[q4[t]+q5[t]]
q8[t]))/knym+Cos[q5[t]] g.mF (Cos[q4[t]+q5[t]] L8-Sin[q4[t]+q5[t]]
q8[t])+Cos[q5[t]] g.mH1 (Cos[q4[t]+q5[t]] L8-Sin[q4[t]+q5[t]]
q8[t])+(Cos[ca] Sin[q5] Ebucket kF kp lbucket (1+λ0) (Cos[q4[t]+q5[t]]
L8-Sin[q4[t]+q5[t]] q8[t]))/knym
 0. -g.mF1 Sin[q6[t]]+σ[t]+Cos[q6[t]] g.mF1 q7[t]+0.5 Cos[q6[t]]
g.mG q7[t]+(-0.5 Cot[q6[t]] Sin[q60] q70+1.5 Cos[q6[t]] q7[t]) (-
(1/4) g π ρ Csc[q6[t]] dc^2 sgnVv ηv (Sin[q60] q70-Sin[q6[t]] q7[t])
((Sin[Subscript[q, 60]] Subscript[q, 70]-Sin[Subscript[q, 6][t]]
Subscript[q, 7][t])/Subscript[d, c])^λ-β Sin[q6[t]] dr sgnVv (-0.5
Cot[Subscript[q, 6][t]] Sin[Subscript[q, 60]] Subscript[q,
70]+1.5 Cos[Subscript[q, 6][t]] Subscript[q, 7][t])^2 (Sin[q60] q70-
Sin[q6[t]] q7[t]) Subscript[u, 31][t]^2)+(-0.5 Sin[q60] q70+1.5
Sin[q6[t]] q7[t]) (-g ρ dc sgnVh ηh (Sin[Subscript[q, 60]]
Subscript[q, 70]-Sin[Subscript[q, 6][t]] Subscript[q, 7][t])^2-β
Sin[q6[t]] dr sgnVh (Sin[q60] q70-Sin[q6[t]] q7[t]) (-0.5
Sin[Subscript[q, 60]] Subscript[q, 70]+1.5 Sin[Subscript[q,
6][t]] Subscript[q, 7][t])^2 Subscript[u, 31][t]^2)
```

```
(*GIK10[t]=GIK1[t]/.{Subscript[u, 1][t]→0,(Subscript[u, 1]^′)[t]→
0}
GIK190[t]=GIK19[t]/.{Subscript[u, 1][t]→0,(Subscript[u, 1]^′)[t]→
0}
GIK190[t]=Collect[GIK190[t],(Subscript[u, 19]^′)[t]]
 GIK310[t]=GIK31[t]/.{Subscript[u, 1][t]→0,(Subscript[u,
1]^′)[t]→ 0}
GAK10[t]=GAK1[t]/.{Subscript[u, 1][t]→0,(Subscript[u, 1]^′)[t]→
0}
GAK190[t]=GAK19[t]/.{Subscript[u, 1][t]→0,(Subscript[u, 1]^′)[t]→
0}
GAK310[t]=GAK31[t]/.{Subscript[u, 1][t]→0,(Subscript[u, 1]^′)[t]→
0}*)
```

```
 Vol= (y[t]/Sin[q6[t]])*dc^2Pi/4
 1/4 π Csc[q6[t]] dc^2 y[t]
```

BIBLIOGRAPHY

1. Adsero, R. and Lumley, G. (2013), "What Will Halt the Worldwide Decline in Mine Equipment Performance?" SME Annual Meeting.

2. Adsero, R. (2016), "Dragline Step Change; Safer, Greener and Lower Operating Costs Are Possible." Mining Engineering. pp. 32-38.

3. Alzheimer, J. M., Griffiths, J. A., Strope, M. C. C., (1980), "Dynamic Load in Dragline Ropes." U.S.A.: Department of Energy under Contract.

4. Alzheimer, J. M. , Anderson, W. EBeeman, ., G. H. , Dudder, G. B., Erickson, R., Glaeser, W. A. , Jentren, R. L. , Rice, R. R. and Strope, L. A. (1981), "Wire Rope Imporvement Program." Pacific Northwest Laboratory Richland, Washington. 174 p. https://www.osti.gov/servlets/purl/6120963

5. Anderson, R. N., Splitstone, D. C. and Bentley, M. R. (1994), "Method for Measuring the Weight of a Suspended Load". 1994. U.S. Patent No. 5,321,637. 14 Jun. 1994.

6. Anderson, W. E. and Brady, T. M. (1979), "Effects of Maintenance Practice on Wire Rope Life in Dragline Applications." Mining Engineering 31.11: pp. 1610-1614.

7. Arora, V. P., Mukhopadhyay, A. K. and Sikdar, B. (1999), "Condition Monitoring of Dragline Components through Vibration Analysis." Transactions, 306: pp. 95-98.

8. Aspinall, T. (1992), "Use of Draglines - Where to in the 21st Century." Third Large Open Pit Mining Conference.

9. Awuah-offei, K. (2005), "Dynamic Modeling of Cable Shovel- Formation Interactions for Efficient Oil Sands Excavation." PhD Dissertation, Missouri University of Science and Technology.

10. Awuah-Offei, K. and Frimpong, S. (2007), "Cable Shovel Digging Optimization for Energy Efficiency." Mechanism and Machine Theory, 42: 995-1006.

11. Awuah-Offei, K., Frimpong, S. and Askari-Nasab, H. (2009), "Formation excavation resistance modelling for shovel dippers." International Journal of Mining and Mineral Engineering 1: 127-146.

12. Awuah-Offei, K. and Frimpong, S. (2011), "Efficient cable shovel excavation in surface mines." Geotech. Geol. Eng. 29:19-26. doi:https://doi.org/10.1007/s10706-010-9366-9.

13. Baafi, E. Y., Mirabediny, H. and Whitchurch, K. (1995), "A simulation model for selecting suitable digging method for a dragline operation." Conference; 25th, Application of computers and operations research in the minerals industries; Brisbane; Australia.

14. Balsov, I. G. (1975). "Studies of Excavating Equipment." NTIS.

15. Blischke, W. R. and Murthy, D. P. (Eds.). (2003), "Case Studies in Reliability and Maintenance." 480. John Wiley & Sons

16. Bakholdin, B. A., khtyar, D. A. A., Poluyanskii, S. A., and Strashko., V. A. (1968), "Engineering calculation of the main characteristics of the hoisting mechanism of a rock-loading machine with its shovel on a rolling arm." Kluwer Academic Publishers-Plenum. 4: 503 pp.

17. Bandopadhyay, S. (1985), "Simulation of a Dragline Operation in All Eastern Kentucky Mine." University of Alaska.

18. Barbay, J. E. (1979), "Advanced Microprocessor Based Instrumentation for Draglines." Conference record, Industry Applications Society, IEEE-IAS Annual Meeting: 1181-83.

19. Boulter, G. (1968), "Cyclical Methods - Draglines and Clamshells." pp.445-62.

20. Boomsliter, G. P. and Morgantown, W. V., (1927), "Acceleration Stresses in Wire Hoisting-Ropes." New York February Meeting: pp.75-96.

21. Bray, D. (1999), "New Dragline Bucket Improves Stripping Efficiency." Mining Engineering-New York.

22. Bullock, M. D., Apte, M. S., and Oppenheim, I. J. (1990). "Force and geometry constraints in robot excavation." Proc., Space '90, Engrg., Constr. and Operations in Space II, ASCE, New York, N.Y. pp. 960–969.

23. Coetzee, C.J., Els, D.N.J., Dymond, G.F. (2009), "Discrete Element Parameter Calibration and the Modelling of Dragline Bucket Filling." Stellenbosch University.

24. Carter, R. A. (2015), "Moving and Maintaining the World's Biggest Diggers." Dragline Mining 216.11: pp.40-59.

25. Chironis, N. P., (1978a), "Amax to Maximize Dragline Output." Coal Age 83.10: pp.114-19.

26. Chironis, N. P., (1978b), "Computer Aids Dragline Operator." Coal Age 83.3: pp.58-64.

27. Chang, J.L. Lin, T.C. Yae, K.H. (1989) "Man-in-the-control-loop simulation of manipulators." In Jet Propulsion Lab., California Inst. of Tech., Proceedings of the 3rd Annual Conference on Aerospace Computational Control, (2). pp. 688-798.

28. Chatterjee, P.K. Rowlands, D. Siller, K.C. (1977). "Simulation of Dragline Operations." Proceedings XIV International Symposium on the Application of Computer Methods in the Mineral Indus-tries, Ramani, RV Ed., Society of Mining Engineers, AIME.

29. Chrionis, N.P., (1982), "Boomsentry Control Aids Dragline." Coal age 87.5: pp.133-35.

30. Corke, P., Winstanley, G., Dunbabin, M. and Roberts, J., (2006). "Dragline Automation: Experimental Evaluation through Productivity Trial." Manufacturing and Infrastructure Technology: pp.459–68.

31. Corke, P., Roberts, J., and Winstanley. G., (2000). "Experiments and Experiences in Developing a Large Robot Mining System." Manufacturing Science and Technology.

32. Corke, P. Roberts, J. Cunningham, J. and Hainsworth, D., (2008) "Mining robotics" In: Springer Handbook of Robotics, Berlin, Germany: Springer: pp.1127-1150.

33. Corke, P., (2016). "Robotics, Vision and Control Fundamental Algorithms in Matlab®" 2nd Edition, completely revised, extended and updated edition. Springer Tracts Adv. Robot., 118, pp. 1-580.

34. Corke, P. I., Winstanley, G. J. and Roberts, J. M. (1997), "Dragline Modelling and Control." In Robotics and Automation, Proceedings. 1997 IEEE International Conference 2: pp. 1657-1662.

35. Crous, P. G., (2000), "Modelling of Dragline Dynamics." University of Stellenbosch.

36. Cutchins, M.A., Cochran, J.E., Guest, S., Fitz-Coy, N.G. and Tinker, M.L., (1987), "An investigation of the damping phenomena in wire rope isolators." Proceedings of the ASME Design Technology Conference, vol. 5. Boston, Massachusetts. pp. 197–204.

37. Curry, D.R. and Deng, Y. (2017), "Optimizing Heavy Equipment for Handling Bulk Materials with Adams-EDEM Co-simulation." In: Li X., Feng Y., Mustoe G. (eds.) Proceedings of the 7th International Conference on Discrete Element Methods. DEM 2016. Springer Proceedings in Physics, 188. Springer, Singapore.

38. Dayawansa, D., Kuruppu, M. and Mashiri, F. (2008), "Deterioration Mechanisms in Dragline Wire Ropes." Advanced Materials Research, 41-42, pp. 199-204.

39. Dayawansa, P., Chitty, G., Kerezsi B., Bartosiewicz, H. and Price, J. W. H. (2006), "Fracture mechanics of mining dragline booms." Engineering Failure Analysis 13.4: pp.716–725.

40. Deby, G.K. (1980), "Surface Coal Mining Reclamation Equipment and Techniques." 8823: pp.74-80.

41. Demirel, N., (2007), "Dynamic dragline modeling and boom stress analysis for efficient excavation." PhD Dissertation, Missouri University of Science and Technology.

42. Demirel, N. and Frimpong, S., (2009), "Dragline dynamic modelling for efficient excavation." Int. J. Min. Reclam. Environ. 23 (1). pp. 4-20.

43. D'Alembert, J. R. (1743), "Traité de dynamique."239 pp. https://archive.org/details /traitdedynamiqu00dalgoog/page/n13. Accessed, Nov. 2018.

44. Drybrough, R. W., (1964), "The Conversion of a Manual A. C. Hoist to a Semi-Automatic D. C. Hoist at Lynn Lake." Bulletin pp. 31-34.

45. Duan, H., (2001), "Computer Applications in the Minerals Industries." Computer Applications in the Minerals Industries. China. pp. 441-444.

46. Dunbabin, M. and Corke, P. (2006), "Autonomous Excavation Using a Rope Shovel." Journal of Field Robotics: pp. 379-94.

47. Dunfee, J., Leonard, L. and Rumbarger, J. (1980), "Dragline Roller Rack Improvement." U. S. Department of Energy, Contract No. AC01-76ET-12S02.

48. Edmonton, Alberta. (2007), "A New Approach to Improving Cable Shovel Dipper Design for Cutting Soft Rock and Soils." university of Alberta.

49. Edward H. C. B.; Mains D. M. G.; Treiber, J. H., (1976), "Transient Load Damping Circuit for Excavator." Bucyrus-Erie Company, South Milwaukee, Wis. assignee.

50. Erdem, B. H. and Duzgun, S. B. (2004), "Dragline Cycle Time Analysis." Journal of scientific & Industrial Research 64: pp.19-29.

51. Eggers, B. L., (2007), "Dragline Gear Monitoring under Fluctuating Conditions." University of Pretoria.

52. Eggers, B.L., Heyns, P.S. and Stander, C.J. (2007),"Using Computed Order Tracking to Detect Gear Condition on board a Dragline." Transactions Paper 107: pp.115-22.

53. Esterhuyse, S. W. P., (1997), "The Influence of Geometry on Dragline Bucket Filling Performance." University of Stellenbosch.

54. Ehret, J. A. and Haase, W. C. (1992), "New Developments in High Productivity Excavators." The Australasian Institute of Mining and Metallurgy. In the 3rd Large Open Pit Mining Conference. Mackay

55. Fairhurst, T. W. (1928), "Mechanical and electrical design of power excavators." Proceedings of the Victorian Institute of Engineers 1927-1928. http://hdl.handle.net/11343/24686. Accessed, Nov., 2018.

56. Faruquee, M. Z. H., (2001), "Implementation of 0utput-0n Y Identification Methods with Demonstration on the Experimental Boom." University of Queensland.

57. Frimpong, S. and Demirel, N. (2009). "Case Study: Planar Kinematics of Dragline for Efficient Machine Control." Journal of Aerospace Engineering, 22, pp.2.112-122.

58. Frankel, J. G., (2004), "Development of a Haptic Backhoe Testbed." MS thesis, Georgia Institute of Technology, G.W. Woodruff School of Mechanical Engineering,

59. Frimpong, S. and Li, Y., (2006), "Real-Time Monitoring of Cable Shovel Stress Loading for Improved Machine Health." SME Annual Meeting and Conference. St. Louis, MO; SME, Littleton, CO (March).

60. Frimpong, S., and Hu, Y., (2004), "Parametric simulation of shovel-oil sands interactions during excavation." Int. J. Surface Mining, Reclamation and Environment, 18(3), pp.205–219.

61. Frimpong, S, Hu Y. and Awuah-Offei, K., (2005), "Mechanics of cable shovel-formation interactions in surface mining excavations." J. Terramech 42: pp.15–33.

62. Frimpong, S. Hu, Y. and Inyang, H., (2008), "Dynamic modeling of hydraulic shovel excavators for geomaterials." International Journal of Geomechanics, 8(1): pp. 20-29.

63. Frimpong, S. and Hu, Y.F. (2008), "Intelligent cable shoved excavation modeling and simulation." Int. J. Geomechanics. 8(1):1–10

64. Fry, P.R., (2003), "Loads and Stresses -the Real Cause of Failures in Surface Mining Machinery." J Fail Anal Prev, 3 (2) (2003), pp. 7-14.

65. Gentle, C. (2002), "Dragline Productivity Improving Technologies & Their Application at German Creek Coal Mine." University of Queensland.

66. Gerard G., Tuft, R., Yankanich, J., Rumbarger, J., (1980), "Dragline Roller Track Improvement." NTIS: Et/12502-1. pp.48.

67. Gölbaġi, O., (2011), "Investigation of Stress Distribution in a Dragline Bucket Using Finite Element Analysis." Middle East Technical University.

68. Golosinski, T.S., (1993), Performance of Drag and Hoist Ropes of Draglines. SME Annual Meeting: pp.93-111.

69. Golosinski, T.S. "Performance of Dragline Hoist and Drag Ropes." Mining Engineering. (1995). 46. 11: pp.1285-1288.

70. Graeme, F., Dryden, Dd. (2007), "Creation, Optimization and Verification of a Three-Dimensional Numerical Model to Simulate a Dragline Bucket During the Digging Cycle Using Modern Dem Software." University of Stellenbosch.

71. Godfrey, N. and Susanto, A. (1989), "Partial Automation of a Dragline Working in Conjunction with a Hopper/Crusher/Conveyor Overburden Removal System." Second Large Open Pit Mining Conference.

72. Graeme J. Winstanley, Peter I. Corke, Jonathan M. Roberts. (1997), "Dragline Swing Automation." Albuquerque, New Mexico.

73. Guan, Z., Faruquee, Z. and Horton, B. G. (2001), "Dragline Field Testing." Proceedings of IMAC-XIX 4359: pp.1556-60.

74. Gul'ko, F. B., ((1984)), "Synthesis of Quasi-Optimal Control System for the Turning Mechanism of a Walking Dragline Excavator by Prediction Method." Engineering Cybernetics 22.2: pp. 8-14.

75. Gurgenci, H. G., Tpwnson, Z. P. and Muthy, P. (2000), "Managing Damage on Draglines and Other Mining Machines." The Future of Mining: pp. 96-101.

76. Hamm, R. G. (1983), "Selection of Large Diameter Wire Rope for Use on Surface Mining Excavators." CIM Bulletin 76.855: pp. 45-50.

77. Haneman, D. K., Hayes, H., and Lumley, G.I., (1992), "Dragline Performance Evaluations for Tarong Coal Using Physical Modelling." Third Large Open Pit Mining Conference.

78. Hansen, J. (2000). "Dragline Monitoring, Control, and Navigation." Bulletin 93: pp. 59-62.

79. Hass, C. M., (1951), "Wire Rope." The American Institute of Mining, Metallurgical, and Petroleum Engineers. 772-775.

80. Hateley, M. L., (2005). "Chaotic Instability in the Motion of a Dragline Bucket." University of Queensland.

81. Hartman, H.L. (1987) "Introductory Mining Engineering." Wiley, New York. 633 pp.

82. Heller, S. R. (1970). "The contact pressure between rope and sheave." Naval Engineers Journal. pp. 49-57.

83. Hemami, A., and Daneshmend, L. (1992). "Force analysis for automation of the loading operation in a LHD-loader." Proc., 1992 IEEE Int. Conf. on Robotics and Automation, IEEE, Piscataway, N.J., pp.645- 650.

84. Himmelman, N. P. (2006), "Dynamics Modelling of an Electric Rope Shovel for Collision Prediction." The University of British Columbia.

85. Huffman, Joe. (2016). "Dragline Boom and Mast Project." Wyoming Mining Convention. Jackson, Wyoming. http://www.wyomingmining.org/wp content/uploads/2016/06/Joy-Global-Dragline-Boom-and-Mast-Presentation.pdf. Retrieved 11/14/2018.

86. Housner, G. W. and Hudson, D. E. (1980), "Applied Mechanics Dynamics." D. Van Nostrand Company, Inc. pp. 219.

87. Imanishi, E., Nanjo, T. and Kobayashi, T. (2009), "Dynamic simulation of wire rope with contact." Journal of mechanical science and technology 23.4: pp. 1083-1088.

88. Josephs, H. and Huston, R., (2002), "Dynamics of Mechanical Systems." Boca Raton: CRC Press.

89. Jameson, L. (1992), "Selection of P & H 575 Dragline for Stobswood Opencast Mine." Mining Technology pp.74: 36.

90. Jiang, W.G., Yao, M.S. and Walton, J.M., (1999), "A concise finite element model for simple straight wire rope strand." International Journal of Mechanical Sciences, 41. pp. 143-161.

91. Johnson, T. C. (1974), "Surface Mining-Coal New Developments in Dragline Excavators." Society of Mining Engineers. AIME 103D Annual Meeting Dallas, TX.

92. Jones, B. M., (1974a), "Computer Modelling of Excavator Dynamics." Ed. Engineering, Mining. Dallas, Texas: AIME Annual Meeting. pp. 1-14.

93. Jones, B. M., (1974b), "Digital Computer Simulation of a Dragline Mining Machine." MS Thesis. p67.

94. Joshi, S., Semetay, C., Price, J. W.H., and Nied, H. F. (2009), "Weld-Induced Residual Stresses in a prototype Dragline Cluster and Comparison with Design Codes." Thin-Walled Structures. 48: pp. 89-102.

95. Kane, T. R. and Levinson, D. A. (1985) "Dynamics: Theory and Applications," McGraw-Hill Book Co., New York.

96. Kane, T. R. (1968), "Dynamics." Holt, Rinehart and Winston, New York.

97. Kane, T. R. and Wang, C. F. (1965) "On the Derivation of Equations of Motion," Journal of the Society for Industrial and Applied Mathematics, 13, pp. 487-492.

98. Kane, T. R. (1961), "Dynamics of Nonholonomic Systems," ASME Journal of Applied Mechanics, 83, pp. 574-578.

99. Karyakin, A. L. and Osipov, P. A. (2013), "Increased Productivity with Performance Monitoring of the Key Technological Indicators for Power Shovels and Dragline by Means of Electric Drive." 30th International Symposium on Automation and Robotics in Construction (ISARC).

100. Kasdin, N. J. and Paley, D.A. (2011), "Engineering Dynamics: A Comprehensive Introduction." Princeton University Press.

101. Kamman, J.W. and Huston, R.L., (2001), "Multibody Dynamics Modeling of Variable Length Cable Systems." 5(3): pp. 211–221. https://doi.org/10.1023/A:1011489801339.

102. Kemp, K. A. (1974), "Computerized System Analyzed Dragline Performance Prints out Data." Coal Age 79.9: pp. 92-97.

103. Kemp, K. A. (1977). "Excavator Data Logging System." US. Patent, No. 4,035,621.

104. Koivo, A. J. (1994). "Kinematics of excavators (backhoes) for transferring surface material." J. Aerosp. Engrg., ASCE, 7(1), pp.17-32.

105. Koivo, A. J., Thoma, M., Kocaoglan, E. and Andrade-Cetto, J. (1996), “Modeling and control of excavator dynamics during digging operation”, Journal of Aerospace Engineering, 9(1):10–pp.18.

106. Konakov, B. S. and Eliseev, V. V. (1974), "Mathematical Description of the Working Process of Digging by a Dragline." Elsevier: Scopus. pp. 100-103.

107. Kontz, M. (2007), "Haptic Control of Hydraulic Machinery Using Proportional Valves." PhD Dissertation, Georgia Institute of Technology, Atlanta, GA.

108. Kuczera, T. (2012), "Calculation of the stress situation of big rope sheaves." PhD. Dissertation. University of Stuttgart.

109. Kuznetsov, N. K., Iov, I. A., and Iov, A. A. (2018), "Investigation of Control System of Traction Electric Drive with Feedbacks on Load." IOP Conference Series: Materials Science and Engineering 327.5. IOP Publishing.

110. Kuznetsov, N. K., Makhno, D. E., & Iov, I. A. (2017), "Damping Elastic Oscillations of Digging Mechanism." In IOP Conference Series: Earth and Environmental Science 87.2. IOP Publishing.

111. Khorzoughi, M. B., (2017), "A Study of Electric Rope Shovel Digging Effort and Behavior for Diggability Assessment in Open Pit Mines." The University of British Columbia.

112. Knights, P. Liang, X. and Jessett, A. (2013). "Classifying Dragline Swing Dependencies Using Coincident Limit Graphs." Mining Technology 122.1: pp. 46-52.

113. Kudryavtsev, Y. (2017), "Automatic Calculation Techniques for Soil Digging Force Applied by Bucket Swing." Procedia Engineering 206: pp. 1636-1641.

114. Kuruppu, M., Dayawansa, D. and Mashiri, F. (2007), "Strategies for Dragline Rope Life Extension." Mine planning and equipment selection and environmental issues and waste management in energy and mineral production: pp. 234-46.

115. Kyle, J. and Costello, M. (2006), "Comparison of Measured and Simulated Motion of a Scaled Dragline Excavation System." Mathematical and Computer Modelling 44.9–10: pp. 816–833.

116. Learmont, T. (1977), "Fabrication of Large Surface Mining Machinery." Welding Journal 56.1: pp. 21-25.

117. Learmont, T. (1975), "Productivity Improvement in Large Stripping Machines." Society of Mining Engineers of AIME.

118. Leonard, S., Lever, P. and Shekhar, R. (2009), "Development of a Semi-Autonomous Scale Dragline Excavation Research Tool." Australian Mining Technology Conference.

119. Leonard, S. (2011), "Automated UDD Dragline Digging Algorithms." The University of Queensland.

120. Li, Y. and Frimpong, S. (2008). "A hybrid virtual prototype for analyzing cable shovel component stress." The International Journal of Advanced Manufacturing Technology 37.5-6: pp. 423-430.

121. Liang, X. (2015), "The Optimisation of the Digging Sequence of a Dragline." The University of Queensland.

122. Li, X., Feng, Y., and Mustoe, G. (Eds.). (2017), "Proceedings of the 7th International Conference on Discrete Element Methods."

123. Lovaas, M. J. (1982), "Dragline Developments: Past and Future." Journal of Mines, Metals and Fuels 30.6: pp. 297-310.

124. Lumley, G. (2009), "How Can You Get Mining Equipment to Work to Its Real Capacity?" The AusIMM New Leaders' Conference: pp. 29-30.

125. Lumley, G. (2005), "Reducing the Variability in Dragline Operator Performance." Coal Conference.

126. Lumley, G. and McKee, M. (2014), "Mining For Efficiency" PricewaterhouseCoopers, Sydney.

127. Lyaptsev, S. Stepanova, N. Suslov, N. (2014), "Reducing Digger Energy Consumption by Improving the Walking Mechanism." Energy Production and Management in the 21st Century. Department of Finance, Ural Federal University.

128. Luu, K.Q. (2014), "Stability-Oriented Dynamics and Control of Complex Rigid-Flexible Mechanical Systems Using the Example of a Bucket-Wheel Excavator." PhD. Dissertation, Universit¨at Duisburg-Essen.

129. Manser, B. L. and Clark. R. (1979), "Dragline Ropes - Assessment of Rope Loads and other Factors Affecting Rope Life." International Conference on Mining Machinery: pp. 95-101.

130. Marshall, H.S. Coleman P., Bolton, D. and Caldwell, A. (1998), "GPS Applications at Optimum Colliery." The Journal of the South African Institute of Mining and Metallurgy, 98(3). pp. 127-134.

131. Matuszak, R. A. (1964), "What Is "Static" Control?" Society of Mining Engineers of AIME.

132. Mazumdar, J. and Koellner, W., (2007), "Design and Implementation Issues of Active Front End Based Systems in Mining Draglines."

133. Matuszak, R. A. (1978), "Controlled Frequency-the Brushless Electric "Steam Engine." Mining Engineers: pp. 177-82.

134. Matuszak, R. A. (1982), "How Do You Measure Your Dragline Output?" Society Of Mining Engineers of AIME.

135. Mashiri, F., Zhao, X., Price, J. W. H., (2011), "Structural Health Monitoring of a Dragline Cluster Using the Hot Spot Stress Method." Structural Health Monitoring, 10 (2), pp.173-187.

136. Mashiri, F. R., Joshi, S., Pang, N. L., Dayawansa, D. P., and Zhao, X. L., Chitty, G., Hui Jiao, Price, J. W. H., (2011), "Service Loads in Dragline Tubular Structures: A Case Study of Cluster." Structural Control and Health Monitoring, 20 (2), pp. 210-229.

137. McLure, P., (1995),"Efficient Dragline Bucket Design." University of Queensland.

138. McCoy Jr., C. E. and Crowgey, J. L. (1980), "Anti-Tightline Control System for Draglines Used in the Surface Mining Industry." Conference record, Industry Applications Society, IEEE-IAS Annual Meeting: pp. 140-145.

139. McInnes, C. H. and Meehan, P. A., (2010), "Trajectory Optimization of a Mining Dragline Using the Method of Lagrange Multipliers." The University of Queensland.

140. Meehan, Paul A. (2016),"Predicting and Simulating Chaotic Instabilities in an Inclined Furuta Pendulum." Chaotic Modeling and Simulation (CMSIM).

141. Meehan, P. A. and Austin, K. J. (2005),"Prediction of Chaotic Instabilities in a Dragline Bucket Swing." International Journal of Non-Linear Mechanics, 41.2: pp. 304-312.

142. Melvin, W. K. (1969), "Worlds Largest Dragline." Society of Mining Engineering of AIME.

143. McCoy, C. E. J., and Crowgey, J. L., (1983), "Anti-Tightline Control System and Method for Dragline Type Equipment." US Patent No. US4370713A.

144. Mirabediny, H. (1998). "A dragline simulation model for strip mine design and development." Ph.D. Dissertation, University of Wollongong, Australia.

145. Meirovitch, L. (1970), "Methods of analytical dynamics." McGraw-Hill. 524pp.

146. Morris, C W. and Kriby J. K. (1977), "Computer Aided Analysis of Cross-Pit Conveyor Systems." USA: United States Department of the Interior Bureau of Mines.

147. Morgenstern, M. H., Alzheimer, J. M., Anderson, W. E., Beeman, G. H., Rice, R. C., Strope, L. A. and Werry, E. V. (1980), "Wire Rope Improvement Program." Battelle.

148. Morey, P. (1978), "Evaluation of an Area Dragline Mining Project Using Simulation Models." San Mateo, California.

149. Nabijou, S. and Hobbs, R. E. (1995a), "Frictional Performance of Wire and Fibre Ropes Bent over Sheaves." Journal of Strain Analysis 16. pp. 453-460.

150. Nabijou, S. and Hobbs, R. E. (1995b), "Relative Movements within Wire Ropes Bent Over Sheaves." Journal of Strain Analysis 30:2. pp. 155-165.

151. Nikiforuk, P. N. and Ochitwa, D. W. (1964), "Dragline Simulation on Analog Computer." Transactions of the Engineering Institute of Canada.

152. Nikiforuk, P. N. and Zoerb, M. C. (1966), "Analog Computer Simulation of a Walking Dragline." Annual meeting of the American Institute of Mining, Metallurgical, and Petroleum Engineers, Inc., Chicago, Illinois, February. 14.

153. Nichols, S. T., Barton, T. H. and Gunthorpe, G. (1981), "Load Model of a Dragline." IEEE Transactions on Industry Application 17(4): pp. 356-61.

154. Ozdogan, M. and Ozdogan, H. (2015), "Breakout Force of Walking Draglines and Forces Impacting the Stability of Equipment."

155. Pang, N. L. and Zhao, X. L. (2009), "Finite Element Analysis to Determine Stress Concentration Factors of Dragline Tubular Joints." Advances in Structural Engineering. 12: pp. 403-77.

156. Pang, N. L. Zhao, X. L., Mashiri, F. R. and Dayawansa, D. (2009), "Full-Size Testing to Determine Stress Concentration Factors of Dragline Tubular Joints." Engineering Structures: pp. 43-56.

157. Pandey, P., Mukhopadhyay, A. K. and Chattopadhyaya, S. (2017), "Reliability Analysis and Failure Rate Evaluation for Critical Subsystems of the Dragline." Journal of the Brazilian Society of Mechanical Sciences and Engineering: pp. 1-11.

158. Pak, H. A., Rowmau, S., (1990), "Optimal Preview Controllers Based Upon Explicit Trajectory Models." University of Southern California.

159. Porter, T. (2011), "Investigation of Dragline Swing Instabilities." University of Queensland.

160. Pretorius, C. B. (2016), "Development of a Demand Response Programme for the Coal Mining Industry." Doctoral dissertation, Stellenbosch: Stellenbosch University.

161. Pundari, N. B. (1981), "Selecting and Using Large Walking Draglines for Deeper Overburden Stripping." Mining Engineering, AIMMPE.

162. Puchkov, L. A. and Pevzner, L. D. (1992), "Automatized Excavator-Dragline." Russia: Moscow Mining Institute: pp. 324-34.

163. Pandit, P., Mazumdar, J., May, T. and Koellner, W. G. (2010), "Real-Time Power Quality Measurements from a Conventional AC Dragline." IEEE Transactions on Industry Applications 46.5: pp. 1755-1763.

164. Pathak, K., Dasgupta, K. and Chattopadhyay, A. (1992), "Determination of the Working Zone of Dragline Bucket - a Graphical Approach." Mining Technology 74.852: pp. 47-49.

165. Pankratov S.A and Ryakhin V.A. (1967), "Elements of the design of the construction machines metal structures." Moscow: Mashinostroenie; (in Russian)

166. Peters, E. R. (1955), "Principles of the theory of single-bucket excavators," Mashgiz.

167. Ridley, P. and Algra, R. (2002), "Dragline Bucket Carry Angle Control." Australasian Conference on Robotic and Control.

168. Rasuli, A. R. (2012), "Dynamic Modeling, Parameter Identification, Payload Estimation, and Non-Contact Arm Geometry Sensing of Cable Shovels." PhD Dissertation, the University of British Colombia.

169. Raza, M. A. (2016), "Cable shovel dipper stress and fatigue failure modeling in formation excavation engineering". PhD. Dissertation, Missouri University of Science and Technology.

170. Raza, M. A. and Frimpong, S. (2017), "Mechanics of Electric Rope Shovel Performance and Reliability in Formation Excavation, Lagrangian Mechanics." In: Canbolat, H. (ed). Lagrangian-mechanics: pp. 107-133.

171. Ridley, P. and Algra, R. and Corke, P. (2001). "Dragline Bucket and Rigging Dynamics." Proc. Australian Conference on Robotic and Automation. Sydney, pp. 14-15.

172. Richie, R. (2012). "Lagrangian mechanics." First Ed., New Delhi : Orange Apple.

173. Rowlands, J. C., Just, G. D., (1992), "Performance Characteristics of Dragline Buckets." Third Large Open Pit Mining Conference.

174. Roberts, J.M., Corke, P.I. and Winstanley, G. J., (1999). "Development of a 3500-Tonne Field Robot" The International Journal of Robotics Research, 18: 739-52.

175. Roberts, J., Winstanley, G. and Corke, P. (2003), "Three-Dimensional Imaging for a Very Large Excavator." The International Journal of Robotics Research. p. 22.

176. Rowlands, J. C. (1991), "Dragline Bucket Filling." University Of Queensland.

177. Rumfelt, H. (1961), "Computer Method for Estimating. Proper Machinery Mass for Stripping Overburden." Mining Engineering: pp. 480-487.

178. Ruff, T. (2006), "Recommendations for evaluating & implementing proximity warning systems on surface mining equipment." DHHS (NIOSH) Publication No. 2007-146, Report of Investigations 9672, 2007 June: 1-80.

179. Satovskiy B. (1963), "Designing large machines. Excavators." Collection of articles, M.: MASHGIZ, 204 pp.

180. Sethna, P. R. (1962), "Dynamics of a four-wheeled vehicle and the effects of suspension geometry." Proc. Auto. Div. Imtn mech. Engrs (6), 201.

181. Shabana, A. A. (2010), "Computational dynamics," third edition, (John Wiley & Sons, New York).

182. Schönherr, S. (2005), "Influence of the Fleet Angle on the Service Life of Wire Ropes Running over Sheaves." PhD. Dissertation, University of Stuttgart.

183. Schmidt, D. F., Marthaller, D. A., Lemmerman, K., Bray, D., Lengenfelder, W. and Metzger, R. S. (1998), "Rear dumping dragline bucket and rigging system." US Patent No.: US6272775B1.

184. Schiffbauer, W. H. (2001), "An Active Proximity Warning System for Surface and Underground Mining Applications." At the SME Annual Meeting, Feb. 26-28, 2001 Denver, Colo.

185. Scheffler, M. (2002). "Earthworks and surface mining machines." Baumaschinen. Erdbau- und Tagebaumaschinen" Springer, Germany. doi.org/10.1007/978-3-663-09352-7

186. Stoner, T. A. (1973), "Method and Means for Measuring the Torque Delivered by an Electric Motor." U.S. Patent No. 3,965,407.

187. Sharrock, G. (1996), "An Investigation into Block Design and Dragline Operating Methods in Australian Coal Strip Mines." The University of Queensland, 1996.

188. Shi, X., Pan, Y., and Ma, X. (2017), "Modeling and Analysis of the Rope–Sheave Interaction at Traction Interface." Journal of Applied Mechanics 84.3: pp. 031005-1-9.

189. Slob, J. J. (2007), "Payload Estimation for Electric Mining Shovels Using a Load Sensing Pin." MS Thesis, Universiteit Eindhoven.

190. Stevens, P. S. (1948), "Evolution of Ward-Leonard Control for Shovels and Dragline." 67: pp. 1491-97.

191. Stilwell, T., Kelly, H., Rumbarger, J. and Dowling, M. (1979), "Dragline bucket improvement survey." Final report, September 30, 1977-September 29, 1979; United States.

192. Strand, F. J. (1957), "The Torque Converter in Shovels, Draglines, Cranes." No. 570135. SAE Technical Paper.

193. Swanson, P. "S.A.E. Transactions." Vol. 641956. pp. 534-541.

194. Schwedes, W. H. and Stoetzel, D. (1948), "Electric Equipment for Power Shovels and Dragline." AIEE TRANSACTIONS 67 (1948): pp. 1498-507.

195. Scoble, M.J., Muftuoglu Y.V. (1984), "Derivation of a diggability index for surface mine equipment selection." Mining Science and Technology, 1, pp. 305-322.

196. Scoble, M.J., Peck, J. and Hendricks, C. (1991), "A study of surface mine equipment monitoring', Int. J. Surf. Mining and Reclamation, 5, 1991, pp. 111-116.

197. Szczuka, A. E., Contor, K. L., Morris, C. W (1976). "Concept Feasibility Study for Training Equipment to Improve Coal Productivity."

198. Sahu, A.R., Naik, H. (2015), "Economical Operation & Estimation of Operating Cost of Draglines in Open Cast Mines. The Indian Mining & Engineering Journal.

199. Tas, S. V. D. (2008), "Data Acquisition for an Electric Mining Shovel Pose Estimator." *DCT* 2008: 47 pp.

200. Taylor, J. R. (2005). Classical Mechanics. University Science, Sausalito, CA.

201. Townson, P. G. A. L. (2002), "Load – Maintenance Interaction: Modelling and Optimisation." University of Queensland.

202. Townson, P. G., Murthy, D. N., & Gurgenci, H. (2003), "Optimization of Dragline Load." Case Studies in Reliability and Maintenance 517: 544.

203. Vähä, P.K. and Skibniewski, M.J. (1993),"Dynamic model of excavator." Journal of aerospace engineering, 6(2), pp.148-158

204. Vinogradov, O. (2000). "Fundamentals of kinematics and dynamics of machines and mechanisms." Boca Raton, FL: CRC Press

205. Vynne, J. F. (2008), "Innovative Dragline Monitoring Systems and Technologies." CIM Conference.

206. Volkov, D.P. (1965), "Dynamics and strength of one-bucket excavators." Moscow: Mashinostroenie

207. Wang, J., Cao, G., Wang, Y., and Wu, R. (2013), "A Novel Driving Strategy for Dynamic Simulation of Hoisting Rope with Time-Varying Length." International Journal of Modeling, Simulation, and Scientific Computing, 4.03, pp. 1–17.

208. Wardeh, M. and Frimpong, S. (2016), "Virtual Prototype Modeling and Simulation of an Electric Shovel for Efficient Excavation." In: SME Annual Meeting. Phoenix. AZ.

209. Watwood, V. B. (1979), "Equation of Motion of a Revolving Dragline Boom." Electronic Computation, pp. 803-812. ASCE.

210. Wheeler, O. E. (1974), "Finite Elements and Strip Mining Equipment." Dallas, Texas. pp. 1-14.

211. Wheeler, O. E. (1976), "Long Boom Design Consideration." AIME Annual Meeting, Las Vegas, Nevada.

212. Williams, G. (2005), "Achievements through the Dragline Improvement Group (Dig) in Anglo Coal." Institute of quarrying southern Africa (36th conference & exhibition).

213. Winstanley, G.J., Usher, K., Corke, P.I., Dunbabin, M. and Roberts, J.M. (2007), "Dragline automation: a decade of development: shared autonomy for improving mining equipment productivity." IEEE Robotics and Automation Magazine, 14(3): pp.52-64.

214. Wokem, C. Joseph, T. and Curley, M. (2018), "Fatigue life prediction for cables in cyclic tension." The Journal of Strain Analysis for Engineering Design 53.3: pp. 141-155.

215. Wokem, C. (2015), "Fatigue prediction for strands and wire ropes in tension and bent over sheave wheels." PhD Dissertation, University of Alberta, Canada.

216. Wolfram Research, Inc., (2018), Mathematica, Version 11.3, Champaign, IL.

217. Wu, Y. (1990), "Advanced Simulation Concepts Applied to Dragline Operations." University of California.

218. Wusaty, E, and Paulhus, L. (1995), "Mining`s new frontier: the Fording Coal G.P.S. experience." Canada: Conference: 97. Annual general meeting of the Canadian institute of mining, metallurgy and petroleum, Halifax (Canada), 14-18 May 1995. pp.23.

219. Zelenin, A. N., Balovnev, V. I. and Kerov, I. P. (1975), "Earth Moving Machines." Moscow. 423 pp.

220. Zelenin, A. N. (1968), "Fundamentals of soil destruction by mechanical methods." Monograph. 2nd Edition: Mashinostroenie. 376 pp.

VITA

Muhammad Wardeh was born and grew up in Damascus, Syria. He graduated with a BSc in mechanical engineering from Damascus University in 2007. He also graduated with two Master's Degrees in Material Sciences and Structures from the University of Paris VI and Polytechnic School in Paris, France in 2011 and 2012, respectively. He moved to the United stated to pursue a PhD degree in civil engineering. He attended the University of Alabama in Huntsville for two years, finished all graduate course work, and successfully passed the PhD preliminary examination. He later transferred from the University Alabama in Huntsville to Missouri University of Science and Technology in spring 2015 to start a new PhD program in mining engineering. There, he started working under the supervision of Dr. Samuel Frimpong in the area of heavy mining machinery design and testing. He won graduate research showcase in 2016 for his studies on electric rope shovels modeling. He became a member of the Society for Mining, Metallurgy & Exploration (SME). He received his PhD degree in Mining Engineering from Missouri University of Science and Technology in December 2018.